The mechanism of the water oxidation reaction catalyzed by an amorphous Co-based catalyst is revealed using operando Raman and time-resolved X-ray absorption spectroscopy

Dissertation

zur Erlangung des Grades einer Doktorin der
Naturwissenschaftenn

am Fachbereich Physik der Freien Universität Berlin

vorgelegt von

Chiara Pasquini

Berlin 2021

Erstgutachter: Prof. Dr. Holger Dau
Zweitgutachter: Prof. Dr. Peter Hildebrandt

Tag der Disputation: 24 May 2022

Abstract

Hydrogen production from water via electrolysis has raised considerable interest in recent years as a tool to help the decarbonization of our society. Currently, the bottleneck for a wider application of this technology is the efficiency of the water oxidation reaction, thus, a lot of effort has been directed in the investigation of catalysts and reaction mechanisms. The subject of this thesis is the amorphous Co oxide catalyst (CoCat). The catalyst is formed by electrodeposition from low-cost materials and can be operated at neutral pH. The CoCat is composed of fragments of 14-19 Co atoms, which are surrounded by the electrolyte. Amorphous transition-metal catalysts are particularly active for the water oxidation reaction, thanks to their bulk activity and ability to accumulate oxidizing equivalents by changing their oxidation state, the CoCat can be taken as a model for this class of materials.

The simultaneous coupling of electrochemistry with spectroscopic techniques, which are sensitive to oxidation state changes, allows direct insight into the reaction mechanism. Operando X-ray absorption spectroscopy at a fixed incoming beam energy is adapted and employed in this thesis to obtain time-resolved information on oxidation state changes. The potentiality and limits of this technique are illustrated. Operando Raman spectra are collected at various applied potentials and show spectral changes, which can be assigned to two distinct Co oxidation reactions, establishing Raman spectroscopy as a novel tool to study metal oxidation states. Peak assignment reveals the presence of $H_2PO_4^-$ polymers in CoCat interlayers.

Operando techniques are also employed to study the release of the products of the reaction and their influence on catalyst efficiency and stability. Operando Raman spectroscopy reveals the presence of local acidification at the catalyst surface due to proton transfer limitations. The local acidification affects the catalyst efficiency by increasing the value of the Tafel slope, an inverse relationship between the Tafel slope and the electrolyte buffer capacity is found. Operando microscopy reveals that molecular oxygen can form microbubbles in the bulk of the catalyst for sufficiently thick films, causing catalyst destruction.

X-ray absorption spectroscopy is employed, together with H/D and $^{16}O/^{18}O$ isotopic substitution to unravel details on the reaction mechanism at neutral pH. The mechanism involves a pre-equilibrium oxidation state change, with a rate-determining electron transfer coupled with a proton transfer, which influences the reaction overpotential. The pre-equilibrium step is followed by the rate-limiting oxygen-oxygen bond formation, which is a pure chemical step and depends on the applied potential only indirectly, through the Co oxidation state. When a higher average Co oxidation state is reached in a Co-oxo fragment, the interaction between Co atoms gives rise to a higher energy state, which lowers the barrier for oxygen-oxygen bond formation.

The reaction mechanism differs in alkaline electrolytes, where the catalytic efficiency is higher and the Tafel slope decreases, likely due to an electron transfer step becoming rate-determining. The differences between the two pH regimes were investigated using operando X-ray absorption to unravel the key factors for catalyst efficiency. In alkaline electrolyte, the oxidation state change is shifted to lower potentials, likely due to a change in the Co coordination environment, and proton release is facilitated by the presence of OH^-. The analysis of CoCat and other Co-based catalysts revealed an irreversible structural transformation in the direction of crystalline CoOOH, which is coupled with Co oxidation and happens spontaneously upon exposure to alkaline electrolytes. The transformation results in better electron transfer but a lower concentration of active sites. A method is proposed to keep the catalyst amorphous by applying an oxidative potential just after exposure of the catalyst to the alkaline electrolyte.

In summary, operando spectroelectrochemical techniques are adapted to the study of oxidation state changes and employed to reveal insights into the reaction mechanism and suggest routes to improve the stability and efficiency of water oxidation catalysts.

Zusammenfassung

Die Wasserstoffproduktion aus Wasser mittels Elektrolyse hat in den letzten Jahren erheblich an Interesse gewonnen, um die Dekarbonisierung unserer Gesellschaft zu unterstützen. Derzeit ist der Engpass für eine breitere Anwendung dieser Technologie die Effizienz der Wasseroxidationsreaktion, daher wird viel Aufwand in die Untersuchung von Katalysatoren und Reaktionsmechanismen gesteckt. Das Thema dieser Arbeit ist der amorphe Co-Oxid-Katalysator (CoCat). Der Katalysator wird durch Elektrodeposition aus kostengünstigen Materialien gebildet und kann bei neutralem pH-Wert betrieben werden. Der CoCat besteht aus Fragmenten von 14-19 Co-Atomen, die vom Elektrolyten umgeben sind. Dank ihrer Massenaktivität und der Fähigkeit oxidierende Äquivalente durch Änderung ihres Oxidationszustandes zu akkumulieren sind amorphe Übergangsmetallkatalysatoren besonders aktiv für die Wasseroxidationsreaktion, der CoCat kann als Modell für diese Klasse von Materialien verwendet werden.

Die simultane Kopplung der Elektrochemie mit spektroskopischen Techniken, die empfindlich auf Oxidationszustandsänderungen reagieren, ermöglicht einen direkten Einblick in den Reaktionsmechanismus. Die Operando-Röntgenabsorptionsspektroskopie bei einer festen einfallenden Strahlenergie wird in dieser Arbeit eingesetzt und angepasst, um zeitaufgelöste Informationen über Oxidationszustandsänderungen zu erhalten. Die Möglichkeiten und Grenzen dieser Technik werden aufgezeigt. Operando-Raman-Spektren bei verschiedenen angelegten Potentialen werden aufgenommen und zeigen spektrale Veränderungen, die zwei unterschiedlichen Co-Oxidationsreaktionen zugeordnet werden können. Damit wird die Raman-Spektroskopie als neuartiges Werkzeug zur Untersuchung von Metalloxidationszuständen etabliert. Die Peakzuordnung zeigt die Anwesenheit von $H_2PO_4^-$-Polymeren in CoCat-Zwischenschichten.

Operando-Techniken werden auch eingesetzt, um die Freisetzung der Reaktionsprodukte sowie deren Einfluss auf die Effizienz und Stabilität des Katalysators zu untersuchen. Die Operando-Raman-Spektroskopie zeigt das Vorhandensein einer lokalen Versauerung an der Katalysatoroberfläche aufgrund von Protonentransferbeschränkungen. Die lokale Versauerung beeinflusst die Katalysatoreffizienz, indem sie den Wert der Tafel-Steigung erhöht. Es wird eine inverse Beziehung zwischen der Tafel-Steigung und der Elektrolytpufferkapazität gefunden. Die Operando-Mikroskopie zeigt, dass molekularer Sauerstoff bei ausreichend dicken Filmen Mikrobläschen in der Masse des Katalysators bilden kann, was zu einer Zerstörung des Katalysators führt.

Röntgenabsorptionsspektroskopie wird zusammen mit H/D- und $^{16}O/^{18}O$-Isotopensubstitution eingesetzt, um Details des Reaktionsmechanismus bei neutralem pH zu entschlüsseln. Der Mechanismus beinhaltet eine Oxidationszustandsänderung vor dem Gleichgewicht, mit einem geschwindigkeitsbestimmenden Elektronentransfer, der mit einem Protonentransfer gekoppelt ist, der das Reaktionsüberpotential beeinflusst. Dem dem Gleichgewicht vorgelagerten Reaktionsschritt folgt die ratenlimitierende Sauerstoff-Sauerstoff-Bindungsbildung, die ein rein chemischer Schritt ist und nur indirekt, über die Co-Oxidationsstufe, vom angelegten Potential abhängt. Wenn ein höherer durchschnittlicher Co-Oxidationszustand in einem Co-Oxo-Fragment erreicht wird, führt die Wechselwirkung zwischen den Co-Atomen zu einem höheren Energiezustand, der die Barriere für die Bildung der Sauerstoff-Sauerstoff-Bindung senkt.

Der Reaktionsmechanismus unterscheidet sich in alkalischen Elektrolyten, wo die katalytische Effizienz höher ist und die Tafel-Steigung abnimmt, was wahrscheinlich darauf zurückzuführen ist, dass ein Elektronentransferschritt geschwindigkeitsbestimmend wird. Die Unterschiede zwischen den beiden pH-Regimen wurden mittels operando-Röntgenabsorption untersucht, um

die Schlüsselfaktoren für die Katalysatoreffizienz zu ermitteln. Im alkalischen Elektrolyt ist der Wechsel des Oxidationszustands zu niedrigeren Potentialen verschoben, was wahrscheinlich auf eine Änderung der Co-Koordinationsumgebung zurückzuführen ist, sowie darauf, dass die Protonenfreisetzung durch die Anwesenheit von OH^- erleichtert wird. Die Analyse von CoCat und anderen Co-basierten Katalysatoren ergab eine irreversible strukturelle Umwandlung in Richtung kristallinem CoOOH, die mit der Co-Oxidation gekoppelt ist und spontan bei Exposition mit alkalischen Elektrolyten stattfindet. Die Umwandlung führt zu einem besseren Elektronentransfer, aber zu einer geringeren Konzentration an aktiven Zentren. Es wird eine Methode vorgeschlagen, um den Katalysator amorph zu halten, in welcher ein oxidatives Potential direkt nach der Exposition des Katalysators gegenüber dem alkalischen Elektrolyten angelegt wird.

Zusammenfassend, es werden operando-spektroelektrochemische Techniken an die Untersuchung von Oxidationszustandsänderungen angepasst und dafür eingesetzt, um Einblicke in den Reaktionsmechanismus zu erhalten sowie Wege zur Verbesserung von Stabilität und Effizienz der Wasseroxidationskatalysatoren vorzuschlagen.

Contents

List of Abbreviations

BESSY	Berliner Elektronenspeicherring-Gesellschaft für Synchrotronstrahlung.
CFP	Carbon fiber paper.
CoCat	Cobalt oxide catalyst, by default deposited in KPi.
CV	Cyclic voltammetry or cyclic voltammogram.
EXAFS	Extended X-ray absorption fine-structure.
FT	Fourier Transform.
FWHM	Full-width-at-half-maximum.
GC	Glassy Carbon.
ITO	Indium tin oxide.
KBi	Potassium borate buffer, by default at pH 9.2.
KPi	Potassium phosphate buffer, by default at pH 7.
NHE	Normal hydrogen electrode.
OCP	Open Circuit Potential.
OER	Oxygen evolution reaction.
pL	Indicates both pH and pD.
RHE	Reversible hydrogen electrode.
TXRF	Total reflection X-ray fluorescence.
XANES	X-ray absorption near-edge structure.
XAS	X-ray absorption spectroscopy.

1 Introduction

> — Et qu'est-ce qu'on brûlera à la place du charbon?
> — L'eau, répondit Cyrus Smith.
>
> *Julius Verne, 1874*

1.1 Why hydrogen is key for the energy transition?

The energy production model that sustains our society is mostly based on fossil fuels, which provide 86% of the energy supply.* The world energy consumption increased by 55% during the last 20 years, leading to the emission of 33 Gt of CO_2 per year, compared to 20.5 Gt in 1990.* This trend is unsustainable and incompatible with the goal of an emission-neutral world by 2050, which is needed to limit global warming to 1.5°C (Masson-Delmotte, 2018). Thus, developing and implementing a new sustainable energy production system is one of the biggest challenges of our century (Armaroli, 2016; Lewis, 2006; Abbott, 2010).

The quest for renewable and carbon-neutral energy sources, which could replace fossil fuels, started already in 1912 (Ciamician, 1912) and lead to technological advancements and price lowering, especially for solar and wind. For example, the price of solar photovoltaic dropped 9-fold in the last decade (Lazard, 2019a). In 2019, the average levelized cost of energy, which includes construction and operation costs, from (unsubsidized) solar (40 $/MWh) and on-shore wind (41 $/MWh) power plants was lower than the one from coal (109 $/MWh), nuclear (155 $/MWh) and natural-gas (56 $/MWh) power plants, although prices have a strong regional variation (Lazard, 2019a; REN21, 2019). As a result, the construction of renewable power plants increased exponentially and from the ca. 300 GW additional power capacity installed in 2018, 100 GW came from solar and 50 GW from wind (REN21, 2019). Although these numbers reveal a promising trend, the energy transition is still far from completion, considering that renewable energy sources only account for 26% of electricity production (with the 16% produced by hydropower, REN21, 2019) and 14% of total energy production (with the 9% produced from biofuel and waste).*

The main factor that is still limiting the widespread adoption of renewable energy technologies is their variable nature. Since they exploit weather-dependent resources, their availability variate greatly, leading to periods of oversupply, when energy production needs to be curtailed, and periods of shortfall when we rely on energy generation by other sources (Barnhart, 2013; Denholm, 2007; Mai, 2012). The adaptation of the electricity grid to fluctuating and nonadjustable energy supply has become a priority in recent years. Adaptation efforts included the development of a smart grid able to exchange information between customer and utility and the incorporation of energy storage units in the system, which lead to nearly a doubling of the annual storage

---

*Data of the International Energy Agency based on the year 2017.

capacity in 2018 (Munuera, 2019). A large variety of storage options have been investigated and employed: pumped hydroelectric storage (which accounted for 96% of installed storage capacity in 2017), compressed air storage, flywheels, capacitors, but, mostly, research focused on batteries and regenerative hydrogen fuel cells (Armaroli, 2011; Ralon, 2017; Anderson, 2004).

Lithium batteries have reached efficiency and durability performances which make them suitable for local (off-grid) and short-term energy storage, during 2016 they represented 88% of the total installed storage capacity (excluding pumped hydro) (Munuera, 2019; Lazard, 2019b). Although prices strongly decreased in the last years, the technology is still not suitable for installment in the grid, because of the high cost of the materials and is mostly used off-grid in combination with rooftop solar panels (Lazard, 2019b; Ralon, 2017; Pellow, 2015). Regenerative hydrogen fuel cells convert electricity to chemical energy by producing hydrogen from water, store the hydrogen and feed it to a fuel cell to obtain back the electricity. The sum of these processes leads to a round-trip efficiency of 30-50% (Regmi, 2020; Park, 2019), meaning that the energy recovered per input energy is quite low, while batteries have a round-trip efficiency of 75-90%. Nevertheless, since hydrogen can be stored in large quantities at very low prices, it can provide long-term storage. Regenerative hydrogen fuel cells can be profitably matched, as an alternative to curtailing, with highly fluctuating energy sources, like wind (Pellow, 2015; Mohammadi, 2018). To provide wider applicability to this technology an increase in the energy efficiency is mandatory (Shaner, 2016).

However regenerative hydrogen fuel cells are not the main target. The high potentiality of hydrogen relies upon the replacement of fossil fuels in transportation, heating and in energy-intensive chemical processes. Currently, emissions linked to transportation accounts for 25% of the total CO_2 emissions.* Ideally power generated by renewable sources during high-peak hours can be stored or converted to hydrogen for use in transportation (Finn, 2012). The electric car market is expanding fast, in 2018 the number of electric cars doubled, reaching 5 million (Bunsen, 2019); the number of fuel cells vehicles, which use hydrogen as a fuel, is also increasing but is still in its infancy, reaching 11200 units in 2018, including buses (Munuera, 2019). This is mostly due to a lack of infrastructure for recharging, while in principle fuel cells are superior to batteries for long distances (Thomas, 2009). Fuel cells have also been used in the aerospace sector and prototypes of airplanes powered by hydrogen are currently being tested (Baroutaji, 2019). Furthermore, the hydrogen produced from renewable energy could be used for domestic heating and could replace the 70 million tonnes of hydrogen currently produced (at very low prices) by fossil fuels and used mostly for oil refining and chemical production (Munuera, 2019). In summary, batteries and hydrogen production technologies play a critical role in the decarbonization of transportation and of the energy and chemicals production sectors (Armaroli, 2016; Victoria, 2019). However, the transition to a hydrogen economy has to be supported by a political decision, because a targeted investment plan is required to adapt the existing infrastructure based on fossil fuels to hydrogen (Brandon, 2017).

1.2 Hydrogen production using the water oxidation reaction

The devices which can produce hydrogen from water, using electricity, are called electrolyzers (Fig. 1.1) and are commercially available since the late 1800s. They are composed of two electrodes, separated by a membrane and immersed in an electrolyte. On the anode side, the water oxidation reaction (also referred to as oxygen evolution reaction or OER) occurs and water is divided into molecular oxygen and protons.

$$2H_2O \rightarrow O_2 + 4H^+ + 4e^- \tag{1.1}$$

On the cathode side, the protons are combined with electrons to produce molecular hydrogen (H_2). The overall reaction requires an energy input of 286 kJ $mol^{-1}{}_{H_2O}$, which is stored in form of chemical bonds and can be recovered (minus losses determined by the process efficiency) using a fuel cell (Dau, 2010; Lewis, 2006). It is particularly difficult to find good catalysts for the water oxidation reaction because it requires the subsequent removal of four electrons and, thus, the stabilization of a series of reaction intermediates. The water oxidation reaction is considered the bottleneck which is currently limiting the overall efficiency of the hydrogen production process (Song, 2018; Dau, 2010). Driven by the need for an efficient technology for renewable energy storage a massive research effort took place in recent years to find more efficient catalysts (Suen, 2017; Roger, 2017; Doyle, 2013).

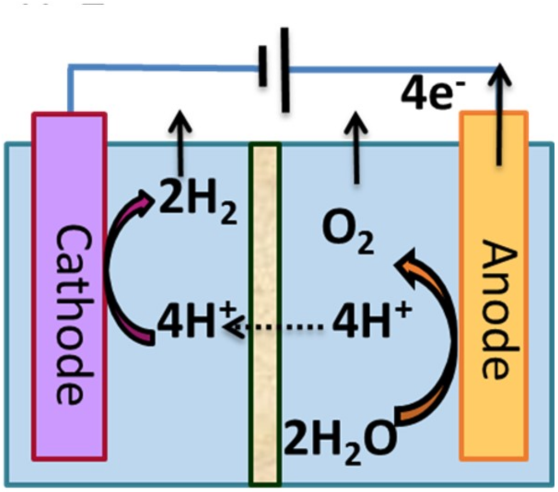

Figure 1.1: Schematic representation of an electrolyzer operating at neutral pH.

Two types of electrolyzers are commercially available: polymer electrolyte membrane (PEM) electrolyzers, which work at acid pH, and alkaline electrolyzers, which work at basic pH, in both cases the extreme pH favors efficient charge transport (Schalenbach, 2018). PEM electrolyzers use a membrane, permeable to protons, to separate the two electrodes, which allows excellent product separation. However, they require the use of rare and expensive metals, usually Ir, as water oxidation catalysts, because the others are not stable at acidic pH (Reier, 2016; Carmo, 2013). In alkaline electrolyzers, cheap and Earth-abundant catalysts, such as Ni, Co and Fe can be used (Roger, 2017; Zeng, 2010). Despite being discovered earlier, only recently alkaline electrolyzers have reached performances comparable to the ones of PEM electrolyzers (Schalenbach, 2016), mostly thanks to strong improvement in catalysts efficiency (Suen, 2017; Song, 2018).

A series of other technologies involving the water oxidation reaction are not yet at the commercialization level, but are the subject of intense research. One is the production of hydrogen or other fuels via natural photosynthesis, which uses energy from the sun to perform the water oxidation reaction. Natural photosynthesis combines very efficient reaction steps with low overall metabolic efficiency (Blankenship, 2011). Research branches in this area include farming of algae and cyanobacteria and semi-artificial photosynthesis. The first can be coupled with genetic or metabolic engineering to maximize fuels production. The latter utilizes enzymes in combination with synthetic materials (Catal, 2020; Kornienko, 2018; Rögner, 2013; Lin, 2018).

Another technology is artificial photosynthesis performed by photoelectrolyzers, which combine the functions of solar panels and electrolyzers. They can absorb sunlight and use it to convert water into hydrogen or other fuels (Nocera, 2012; Ismail, 2014; Hisatomi, 2014; McKone, 2014; Roger, 2017), the direct conversion should increase the device efficiency. However, the combination of the two processes adds requirements to the photocatalyst, which is usually composed of a light absorber and a co-catalyst for water oxidation, resulting, at the moment, in a lower solar-to-hydrogen efficiency (Armaroli, 2016; Qiu, 2018; Kim, 2019). Another possibility is to combine the protons and electrons obtained from water oxidation, with CO_2 or N_2 extracted from the atmosphere. These processes allow the production from renewable energy sources of chemicals and fuels, such as carbon monoxide, formic acid, methane, methanol, C_{2+} hydrocarbons and oxygenates (from CO_2 reduction) and ammonia (from nitrogen reduction) (Luna, 2019; Jones, 2014; Seh, 2017). The fuels produced are carbon-neutral, meaning that the same quantity of CO_2 is emitted during their burning as it is sequestrated during their synthesis and could replace fossil fuels without any need for infrastructural change. Research is now focused on developing catalysts with good product selectivity towards one or more of the desired products (Bagger, 2017; Garg, 2020). Both these technologies require a water oxidation catalyst, that is stable and efficient in near-neutral electrolyte, unlike the catalysts usually employed in electrolyzers. This is due to the fast degradation of light absorbers at extreme pH (Roger, 2017) and to the effect of CO_2 dissolved in solution, which decreases the electrolyte pH.

This thesis work will focus on a Co oxide catalyst for water oxidation, which is stable at near-neutral pH. A better understanding of the catalyst mechanism will be beneficial for a large series of applications including:

- Photoelectrolyzers for direct hydrogen production from solar energy. Co oxides are among the most used co-catalyst (Takata, 2020; Zhong, 2010).
- Electrolyzers for the production of carbon-neutral fuels and chemicals.
- Alkaline electrolyzers for renewable energy storage via hydrogen production.

1.3 An amorphous Co oxide catalyst

In the previous sections, we established that the energy transition would greatly benefit from the development of an efficient water oxidation catalyst. The desirable wide adoption of this technology requires a catalyst that is easy-to-assemble from Earth-abundant and cheap materials (Roger, 2017; Kim, 2019). The water oxidation reaction (Eq. 1.1) entails the progressive removal of four protons and four electrons. Transition metal oxide catalysts are particularly apt for this task, because they can reversibly change their oxidation state. Thus, electrons can first be extracted from the catalyst, which increases its oxidation state and, then, extracts electrons from water, reducing its oxidation state (Hoganson, 1997; Fujishima, 1972; Hunter, 2016b; Dau, 2010;

Nong, 2020). Several first-row transition metals, like Mn, Fe and, to a lesser extent, Co and Ni, satisfy the requirement of Earth abundance and have a high efficiency for water oxidation catalysis (Roger, 2017). It is not by chance that photosynthetic organisms use a metal-oxo center, formed by four Mn atoms, to catalyze the water oxidation reaction (Nelson, 2006; Dau, 2012).

The quest to improve catalyst efficiency involved the study of new synthesis methods (Suen, 2017; Anantharaj, 2016; Doyle, 2013; Roger, 2017), along with knowledge-guided design (Hong, 2015; Seh, 2017; Jiao, 2015; Man, 2011; Stamenkovic, 2017; Hunter, 2016b). Catalysts used in applications are normally heterogeneous, meaning that they are solid-state materials immersed in a liquid electrolyte. Conversely, homogeneous catalysts are composed of molecules solved in solution and are often employed to investigate the reaction mechanism (Hadt, 2016; McAlpin, 2011; Brodsky, 2017). Heterogeneous catalysts have higher activities and are easier to separate from the products, but they are usually only active at the catalyst-electrolyte interface (Fukuzumi, 2013). Amorphous metal oxides are a class of hydrated (water-containing) heterogeneous catalysts, which are formed by fragments or layers of catalyst material surrounded by the electrolyte and, thus, maintain molecular properties and can perform catalysis in all their bulk (Klingan, 2014; González-Flores, 2015; Farrow, 2013). They can be readily prepared by a variety of fabrication techniques, including precipitation (King, 2017; Gorlin, 2017), electrodeposition (Kanan, 2008; Dincă, 2010; Huynh, 2014; Burke, 2015b), laser ablation (Hunter, 2014) or photochemistry (Smith, 2013b; Smith, 2013a). At the state of the art, layered NiFe oxides are considered the most active catalyst, based on not-noble metals, for alkaline electrolytes (McCrory, 2013; Zhu, 2018). Instead, amorphous Co oxide is one of the most investigated catalysts for neutral pH electrolytes. The subject of this thesis is an amorphous Co oxide catalyst, referred to as CoCat, which can be taken as a model system for the class of amorphous transition metal catalysts.

The first mention of an amorphous cobalt oxide for water oxidation appeared 120 years ago (Coehn, 1902), however, the catalyst raised wide research interest starting in 2008 (Kanan, 2008; Risch, 2014; Bediako, 2015), when it was presented by Nocera as the key to artificial photosynthesis (Nocera, 2012). The catalyst has a reasonable efficiency at room temperature and in neutral pH and can operate in river and sea water (Esswein, 2011). The CoCat is usually prepared by electrodeposition by applying an electric potential to a pH-neutral solution containing Co^{II} ions and a buffer. During the deposition process, the Co^{II} ions are oxidized to Co^{III} and react with oxygen from water molecules forming an oxide material (Kanan, 2008; Surendranath, 2012; Surendranath, 2009; Klingan, 2014; Costentin, 2017). Since deposition and operation conditions are the same, the catalyst benefits from a self-repair mechanism, which ensures stability at neutral pH. Provided that the electrolyte is a buffer and has a pH higher than 6, the Co atoms that leach in solution during operation can be redeposited (Lutterman, 2009; Surendranath, 2012; Costentin, 2017; Mohammadi, 2020). However, a decrease in catalytic activity on a per-cobalt basis is observed over time, which is linked to an increase in structural order (Mohammadi, 2020).

Typically, the CoCat is electrodeposited and operated in 0.1 M potassium phosphate buffer at pH 7. Increasing the concentration of phosphate increases the disorder and has a negative effect on catalyst performances (King, 2017). Exchanging phosphate with methyl phosphonate or borate and potassium with sodium does not appreciably affect the activity (Surendranath, 2009; Lutterman, 2009). On the contrary, when phosphate is exchanged with weakly or non-buffering anions, like acetate and chloride, the activity decreases and the deposited film appears more ordered (Risch, 2012). The level of disorder is linked to the size of the molecular Co-oxo fragments which compose this amorphous material and contain 14-19 Co atoms each, for Co deposited in phosphate buffer (Du, 2012; Farrow, 2013). Since water oxidation takes place in the bulk of the film (Surendranath, 2010; Klingan, 2014) at the periphery of the Co-oxo fragments (Kwon, 2018; Farrow, 2013; Risch, 2012; Bediako, 2015), the size of the fragments has a direct impact on catalyst performances.

The amorphicity of CoCat prevents the use of X-ray diffraction techniques, thus its local structure was investigated using X-ray absorption spectroscopy (XAS). The CoCat consists of edge-sharing CoO_6 octahedra, where oxygen atoms form μ-oxo bridges between Co atoms (Risch, 2009; Kanan, 2010; Risch, 2015; Mattioli, 2011). The structure has a strong similarity with the Mn-complex of natural photosynthesis (Zaharieva, 2011; Dau, 2007) and with the structure of other transition metal catalysts (Risch, 2011; Zaharieva, 2012). Furthermore, it was shown that a series of crystalline Co-based catalysts, convert into the amorphous CoCat under water oxidation conditions (González-Flores, 2015; Bergmann, 2018).

The CoCat resting state is composed of a Co^{II}-Co^{III} mixture, with Co^{IV} species appearing at potentials relevant to catalytic water oxidation (Kanan, 2010; Risch, 2015; Gerken, 2011; McAlpin, 2010). Co oxidation state changes are coupled to the release of a proton to the buffer species in solution and represent a pre-equilibrium preceding the rate-determining step, which has been proposed to be the formation of an oxygen-oxygen bond (Surendranath, 2010; Risch, 2015; Mattioli, 2013). CoCat has been the subject of numerous mechanistic studies, involving both proton and electron transfer kinetics (Bediako, 2013; Symes, 2011; Ahn, 2015) and different hypotheses for oxygen-oxygen bond formation (Zhang, 2014; Koroidov, 2015; Costentin, 2017; Ullman, 2016; Mattioli, 2013), which are reviewed in detail in section 6.3.1. However, several mechanistic details are still unclear and are the subject of this thesis work.

1.4 Scope and organization of this thesis

The thesis has two main objectives: the advancement of operando methods for the study of transition metal oxides and the mechanistic investigation of the water oxidation reaction, with the aim of obtaining improvements in catalyst efficiency and stability.

The chapters are organized as follows:

> *Chapter 2* presents three exemplary experiments on CoCat, in which time-resolved metal oxidation state changes driven by electrochemical operation are tracked by X-ray absorption spectroscopy. The time-resolved X-ray signal, collected at a single energy, is converted to a metal oxidation state. The procedure for this conversion and the challenges and potentialities of this approach are illustrated in detail. A brief theoretical introduction to X-ray absorption spectroscopy is included.
>
> *Chapter 3* presents an operando Raman spectroscopy study of CoCat, addressing changes in the electronic and atomic structure of the catalyst material. It illustrates Raman spectroscopy's potentiality in the study of amorphous oxides and oxidation state changes. A brief theoretical introduction to Raman spectroscopy is included.
>
> *Chapter 4* establish Raman spectroscopy as a method to measure local pH changes, due to proton transport limitations; investigates the effects of local pH changes on the catalyst activity and efficiency (studies of the Tafel slope).

Chapter 5 employs operando microscopy to study the phenomenology of O_2-bubbles formation and the consequences on catalyst stability and life-time. Videos depicting bubbles formation and bubbles-induced damages are included.

Chapter 6 investigates the water oxidation reaction mechanism at neutral pH, using isotopic substitution and energetic and kinetic analysis. It contains a mechanistic proposal inserted in the framework of previous literature.

Chapter 7 employs operando X-ray absorption spectroscopy to investigate the reasons behind the higher catalytic activity observed in alkaline electrolyte in respect to neutral. It also reveals a spontaneous oxidation and crystallization process, observed upon exposure of the catalyst to an alkaline electrolyte, and proposes a technique to stop this process and maintain the catalyst amorphous.

All the chapters in this thesis are self-contained with regard to scientific content. Each chapter refers to a first author publication, either already published or in the process of writing. Each chapter starts with a "Context and motivation" section, which presents the relevant literature and scientific background and explains the chapter's scope and organization. At the end of each chapter, a summary and experimental details are given.

2 Operando tracking of Co oxidation-state changes by coupling electrochemistry with time-resolved X-ray absorption spectroscopy

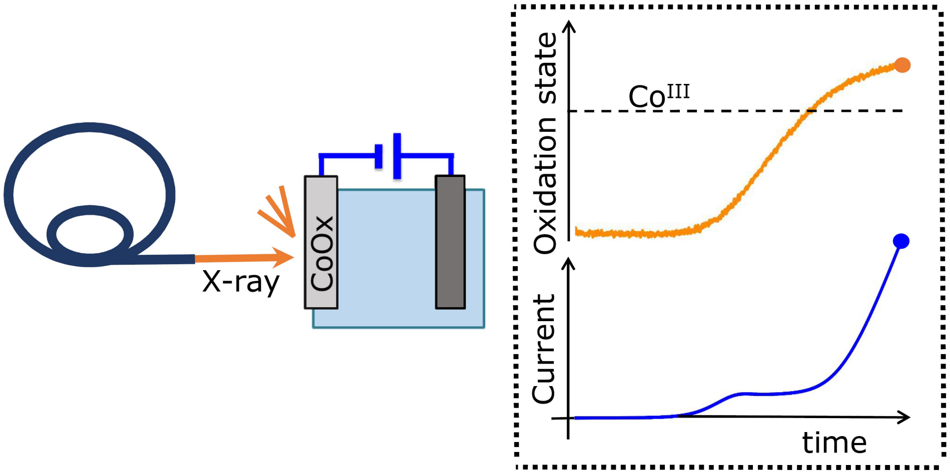

Reproduced in part from

Pasquini, C.; Liu, S.; Chernev, P.; Gonzalez-Flores, D.; Mohammadi, M. R.; Kubella, P.; Jiang, S.; Loos, S.; Klingan, K.; Sikolenko, V.; Mebs, S.; Haumann, M.; Beyer, P.; D'Amario, L.; Smith, R. D. L.; Zaharieva, I.; Dau, H., Operando tracking of oxidation-state changes by coupling electrochemistry with time-resolved X-ray absorption spectroscopy demonstrated for water oxidation by a cobalt-based catalyst film. *Anal. Bioanal. Chem.* **2021**.
DOI: 10.1007/s00216-021-03515-0

Author Contributions: Design of the investigation, C.P., I.Z. and H.D.; data analysis, C.P. (mostly) and I.Z. (data of Figure S6, not included in this thesis); preparation of catalyst films, C.P. (mostly) and S.L. (data of Figure 1, not included in this thesis); contributions to method developments and data collection, C.P., S.L., P.C., D. G.-F., M.R.M., P.K., S.J., S.L., K.K., V.S., S.M., M.H., P.B., L.D., R.D.L.S. and I.Z.; software development, P.C.; writing C.P.,[*] I.Z. and H.D.

---

[*] This chapter was used as the first draft when writing the manuscript.

2.1 Context and motivations

The catalytic role of transition metal oxides in water oxidation consists in the accumulation of oxidizing equivalents, which can be used to oxidize water molecules (Hoganson, 1997; Fujishima, 1972; Hunter, 2016b; Dau, 2010; Nong, 2020). Transition metal oxides can accumulate oxidizing equivalents by changing their oxidation state. As a result, the active site for water oxidation usually entails a highly oxidized metal species. For example, the proposed reaction mechanism for OER on Co catalysts consists of two proton-coupled electron transfer reactions linked to $Co^{II} \rightarrow Co^{III} \rightarrow Co^{IV}$ oxidation, before the rate-limiting O-O bond formation (Surendranath, 2010; McAlpin, 2010; Risch, 2015).

X-ray absorption spectroscopy (XAS) can be used to determine the metal oxidation state of a specific sort of atom with a precision of up to 0.1 oxidation-state units (Kasrai, 1991; Dau, 2003). This makes it well-suited, when coupled with electrochemistry, for the investigation of catalytic intermediates and reaction mechanisms in transition-metal oxides. Other advantages are that XAS is a bulk technique, therefore appropriate for bulk active materials like CoCat, it is element specific and x-rays can cross various substrates and thin layers of water, enabling operando measurements (Bokhoven, 2016; Newville, 2004). An XAS spectrum is composed of the X-ray Absorption Near-Edge Structure (XANES), which provides information on the ligand-geometry and oxidation state of the absorber atom, and the Extended X-ray Absorption Fine Structure (EXAFS), which provides information about the atomic environment of the absorber atom (Penner-Hahn, 1999).

XAS can be coupled with electrochemistry measurements by quasi-in-situ or operando methods (van Oversteeg, 2017). The quasi-in-situ freeze-quench method consists in freezing the sample while performing an electrochemical experiment and later measuring it at a synchrotron facility (Risch, 2015 and section 6.2.3). This method has no time resolution, but performing the X-ray measurement at cryogenic temperature (e.g. 20 K) gives several advantages: the spectral resolution is higher and radiation damage is reduced. During operando experiments (also referred to as in-situ experiments) the X-ray fluorescence is recorded at the same time as the electrochemical measurement. It can be achieved with the use of a flow-cell with a thin water layer (Nagasaka, 2015, since a thick layer would stop the X-ray beam) or with back-side illumination of the sample (Favaro, 2017; King, 2019) and can be made surface-sensitive (Farmand, 2019).

The main factor limiting the combined use of operando XAS and electrochemical experiments with typical CV scan rates is the data collection time required for a complete XANES spectrum, which decreases the temporal resolution of the technique. The acquisition of an X-ray absorption spectrum, including the EXAFS region, usually takes from minutes up to hours depending on: the brilliance of the beam-line, the concentration of the investigated element in the sample and the desired quality of the spectrum. Operando studies of the kinetics of chemical reactions require shorter time scales, which can be achieved using special techniques (Fracchia, 2018). These techniques include: fixed-energy XAS (Minguzzi, 2013); energy-dispersive XAS (EDXAS) (Pascarelli, 1999; Achilli, 2017), which requires a special monochromator; quick scanning EXAFS (QEXAFS) (Müller, 2016; Clark, 2020; Lin, 2020) and pump & probe experiments (Hu, 2020; Haumann, 2005), which must be combined with high brilliance beam-lines or X-ray free-electron lasers (XFEL). These techniques have noteworthy limitations: QEXAFS is limited by the mechanical stability of the monochromator, which can affect the spectral quality; energy-dispersive XAS is applicable only in transmission mode, which often hampers the performance of operando experiments and pump & probe experiments can only be applied to light-driven reactions.

Between the mentioned techniques, fixed-energy XAS is, at the time of writing, the only one that can be employed at a conventional bending-magnet beamline, equipped with a standard double-crystal monochromator. Fixed-energy XAS (often referred to as fixed-energy X-ray absorption voltammetry, FEXRAV) consists in recording the X-ray absorption coefficient at a fixed energy of the incoming beam, while performing cyclic voltammetry or another electrochemical experiment (Minguzzi, 2013). The variations in the absorption coefficient caused by changes in the metal oxidation states are recorded in real-time during the experiment and are related to changes in the oxidation state. Since its first application (Filipponi, 1998), this technique has been successfully used to investigate operando oxidation state changes, including in materials for electrolysis of water (Zaharieva, 2016; Smith, 2017; González-Flores, 2018; Mohammadi, 2020). An outlook on the advantages and limitations of the fixed-energy XAS method is given in Tab. 2.1.

Table 2.1: Summary of the advantages, requirements and limitations of the fixed-energy hard/tender X-ray absorption method presented in this chapter.

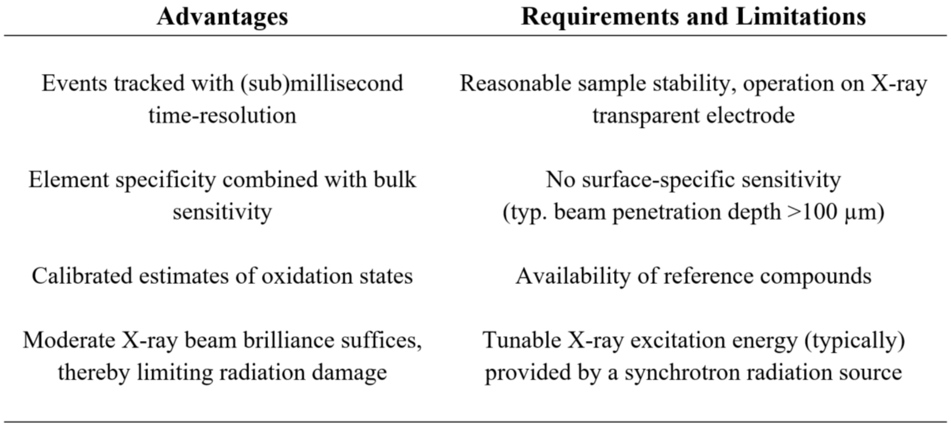

Advantages	**Requirements and Limitations**
Events tracked with (sub)millisecond time-resolution	Reasonable sample stability, operation on X-ray transparent electrode
Element specificity combined with bulk sensitivity	No surface-specific sensitivity (typ. beam penetration depth >100 µm)
Calibrated estimates of oxidation states	Availability of reference compounds
Moderate X-ray beam brilliance suffices, thereby limiting radiation damage	Tunable X-ray excitation energy (typically) provided by a synchrotron radiation source

This chapter is focused on the methodological development of fixed-energy XAS and its application to the study of the CoCat as a water oxidation catalyst. The first section contains a brief introduction to X-ray absorption spectroscopy. Then, a time-resolved operando XAS technique (fixed-energy XAS) is presented, including a detailed explanation of how the time-resolved fluorescence signal can be converted in an oxidation-state value, using two calibration lines. To the best of our knowledge, this explanation is provided here for the first time. Afterward, the technique is applied to three different operando electrochemical experiments (Cyclic Voltammetry, "potential jumps" and "potential stairs") as proof-of-concept. The experiments investigate Co oxidation state changes with 10 ms time resolution and reveal different aspects of water oxidation in neutral pH illustrating the wide information content provided by fixed-energy XAS. Then, a systematic investigation of possible problems is presented, strategies to avoid data misinterpretation are demonstrated and an error range is estimated. At the end of the chapter, UV-vis spectroscopy is presented as a complementary method to XAS. Other applications of fixed-energy XAS to water oxidation at alkaline pH can be found in chapter 7.

2.2 Theory of X-ray absorption spectroscopy (XANES and EXAFS)

The energy of an X-ray photon (few to 100 KeV) is in the same range as the binding energy of core-electrons in an atom. Electrons can absorb the X-ray photon and transition to a higher unoccupied energy level or to the continuum (i.e. the electron is expelled from the atom). X-ray absorption spectroscopy (XAS) studies the probability of the absorption process, which depends on the electronic density of states of the absorbing atom and its local atomic environment. Since the core electron energies are different for each element, XAS is an element-specific technique (Bokhoven, 2016; Newville, 2004).

Atomic energy levels are quantized, thus when varying the incident photon energy abrupt increases in absorption are observed (so-called edges). Each edge corresponds to a dipole-allowed transition from a core-electron energy level to an unoccupied level. Edges are named by the quantum numbers of the initial electron energy level: n (indicated by a letter) and l (indicated by a number). For example, the K-edge will be a transition from the 1s level, the L_2-edge from the 2p level and so on. Following the dipole-selection rules (Δl= ±1, Δj= ±1, Δs=0) a K-edge can only represent a transition to a p-state. However, there are exceptions to these rules, e.g. due to orbital mixing, which allow forbidden transitions, which are visible in the absorption spectrum as small pre-edges. For example, a typical Co K-edge absorption spectrum (Fig. 2.1) has a pre-edge peak that is formally assigned to the 1s→3d and a main absorption edge corresponding to the 1s→4p transition.

When dealing with thin samples the direct measurement of the absorption signal often results in low-quality spectra. A better option is to measure the fluorescence, which is emitted when the core-electron hole, left by the absorption event, is filled by an electron from a higher orbital. If the number of absorber atoms is relatively small the fluorescence signal collected at a fixed emitted energy depends linearly on the absorption coefficient of the material (μ). As expressed by:

$$I_f/I_0 \sim log(I_0/I_t) = \mu \tag{2.1}$$

where I_0, I_t, I_f are respectively the intensity of the incoming, transmitted and fluorescent beam. For larger numbers of absorbers equation 2.1 does not hold anymore and distortion effects, called self-absorption, appear in the recorded signal. This thesis studies exclusively thin samples, therefore the absorption spectra presented are always derived from the fluorescence signal emitted at a fixed energy, namely the energy corresponding to the 2p→1s transition (for Co it is 6930 eV), called K_α (Bergmann, 2009).

XANES

The lower energy part of the edge (usually a 50 eV region including the pre-edge) is referred to as X-ray Absorption Near-Edge Structure (XANES), see Fig. 2.1. The position and shape of the edge depend on the oxidation state and spin state of the absorber atom and on its ligand geometry. The interpretation of the XANES region requires solving a complex multi-electron problem, usually a more direct interpretation is obtained by comparison with known compounds.

An inverse dependence has been theoretically derived (Sheehy, 1989) and experimentally observed (Kasrai, 1991; Dau, 2003) between the resonant energy (i.e. the position of the edge)

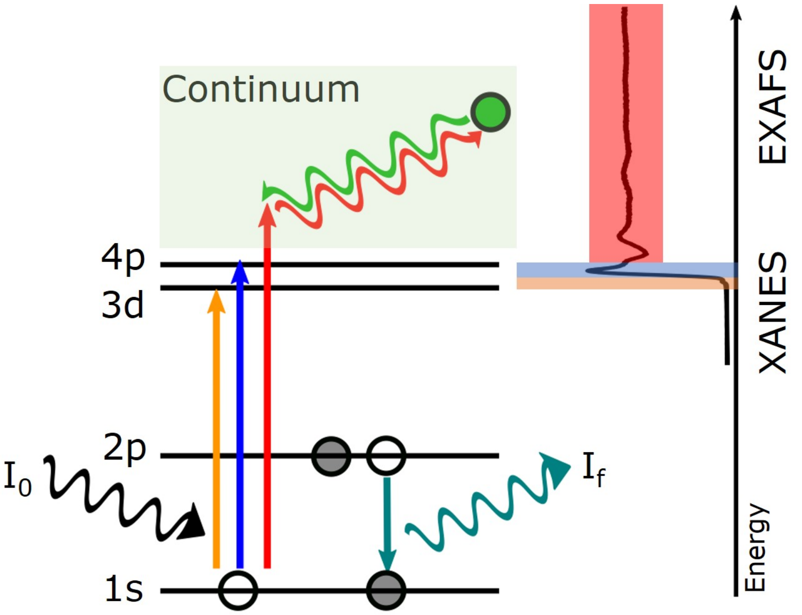

Figure 2.1: Schematic explanation of a typical X-ray absorption spectra for the Co K-edge. The incoming beam (I_0) excites a 1s core-electron to either the 3d level (dipole-forbidden transition, shown in orange), giving rise to the pre-edge, the 4p level (shown in blue), giving rise to the main absorption edge or to the continuum (shown in red). In the continuum the electron can be scattered by a neighboring atom (shown as a green dot), if the distance between the two atoms fits the electron wavelength, the emitted electron wave and the backscattered wave (shown as red and green waves) will interact constructively, enhancing the absorption coefficient at that wavelength. The modulation of the absorption coefficient due to scattering events in the continuum is visible in the EXAFS region of the spectra. The main absorption edge and the small pre-edge constitute the XANES region. A 2p electron decays to fill the hole in the 1s shell, emitting fluorescence (I_f), which can be detected.

and the distance between the absorber atom and its ligands:

$$E_{edge} = A + \frac{B}{R^2}. \tag{2.2}$$

For transition metals this dependence can be explained in two ways (Dau, 2003): first as the distance decreases, the position of the first scattering maximum increases in the k-space, moving to higher energies. At the same time, a decreased distance corresponds to a stronger bond and an increased splitting between bonding and anti-bonding molecular orbitals. Since the final state is an anti-bonding orbital, the increased splitting results in an increase in the resonant energy.

Similar explanations support the linear dependence of the edge position on the metal oxidation state, which was observed empirically, for example in the case of MnOx (Dau, 2003) and CoOx (Risch, 2015). By choosing a proper series of reference compounds, with the same type of ligands as the investigated sample, it is possible to construct a calibration line and to calculate the oxidation states from the position of the edge.

EXAFS

The higher energy region of the absorption spectra is called Extended X-Ray Absorption Fine Structure (EXAFS). It involves X-ray photons, which have enough energy to bring a core electron to the continuum (called photoelectron), where it can interact with neighboring atoms. EXAFS modeling is simpler than XANES and is routinely employed to derive information on the atomic environment surrounding the absorber atom.

Once the photoelectron is ejected from the atom it can be scattered by the neighboring atoms. The back-scattered electron wave interacts with the forward-propagating wave, in either a constructive or destructive manner. At certain values of the electronic momentum k there is a constructive interference and a standing wave is possible. The presence of an available electronic state (the standing wave case) with the appropriate energy and momentum increases the absorption probability, causing a small peak in the absorption spectrum. Therefore the presence of neighboring atoms determines a series of allowed and forbidden k, which appear as a modulation in the spectrum of the absorption coefficient.

This modulation can be extracted from the EXAFS and can be modeled as the addition of the contribution of different scatterers at certain distances. Each scattering distance is called coordination-shell. Depending on the level of order in the material, it is possible to detect shells up to 8-10 Å around the absorber atom. Each shell is characterized by its distance, the number of scatterers present at this distance, the identity of the scatterers and the Debye-Waller factor. The Debye-Waller factor represents the damping in the oscillations due to scatterers belonging to the same shell but distributed over slightly different distances, caused by defects or variations in the material and by atomic vibrations. To reduce the radiation damage to the sample, the noise level and the atomic vibrations contributions to the Debye-Waller factors, EXAFS spectra are usually acquired at low temperatures (20 K). This chapter will deal only with operando XANES measurements, examples of EXAFS spectra and their simulations can be found in chapters 6 and 7.

2.3 Results

2.3.1 Fixed-energy XAS: a time-resolved method

To obtain a XANES or EXAFS spectrum, the energy of the X-ray beam must be scanned over a defined energy range, the time needed to complete a scan determines the time resolution of the experiment (usually seconds to minutes). Conversely, during a fixed-energy XAS experiment, the X-ray-beam energy is fixed and the time resolution is limited by the electrochemical side of the experiment. In an operando experiment a change in the sample average oxidation state, caused by the electrochemical operation, is detected as a variation of the X-ray signal. For thin catalysts films, the metal X-ray fluorescence signal is recorded, which can be assumed proportional to the absorption coefficient (see Eq. 2.1).

For fixed-energy XAS, the energy of the X-ray beam is usually selected in the middle of the absorption edge rise, to assure the maximum variation of the X-ray fluorescence signal for changes in the sample oxidation state (see Fig. 2.2a). However, it can be chosen to reflect structural variations, e.g. at the top of the edge (González-Flores, 2018). An oxidation-state increase causes a shift to higher energies in the position of the edge and a consequent decrease in the fluorescence signal recorded, and vice versa for an oxidation-state decrease. In the following, the procedure to get a quantitative estimation of the oxidation state from the fluorescence signal is illustrated in detail. It is based on the construction of two calibration lines. The number obtained after the conversion procedure is the average oxidation state of Co atoms in the sample (e.g. 2.7 corresponds to 30% $\mathrm{Co^{II}}$ atoms and 70% $\mathrm{Co^{III}}$ atoms).

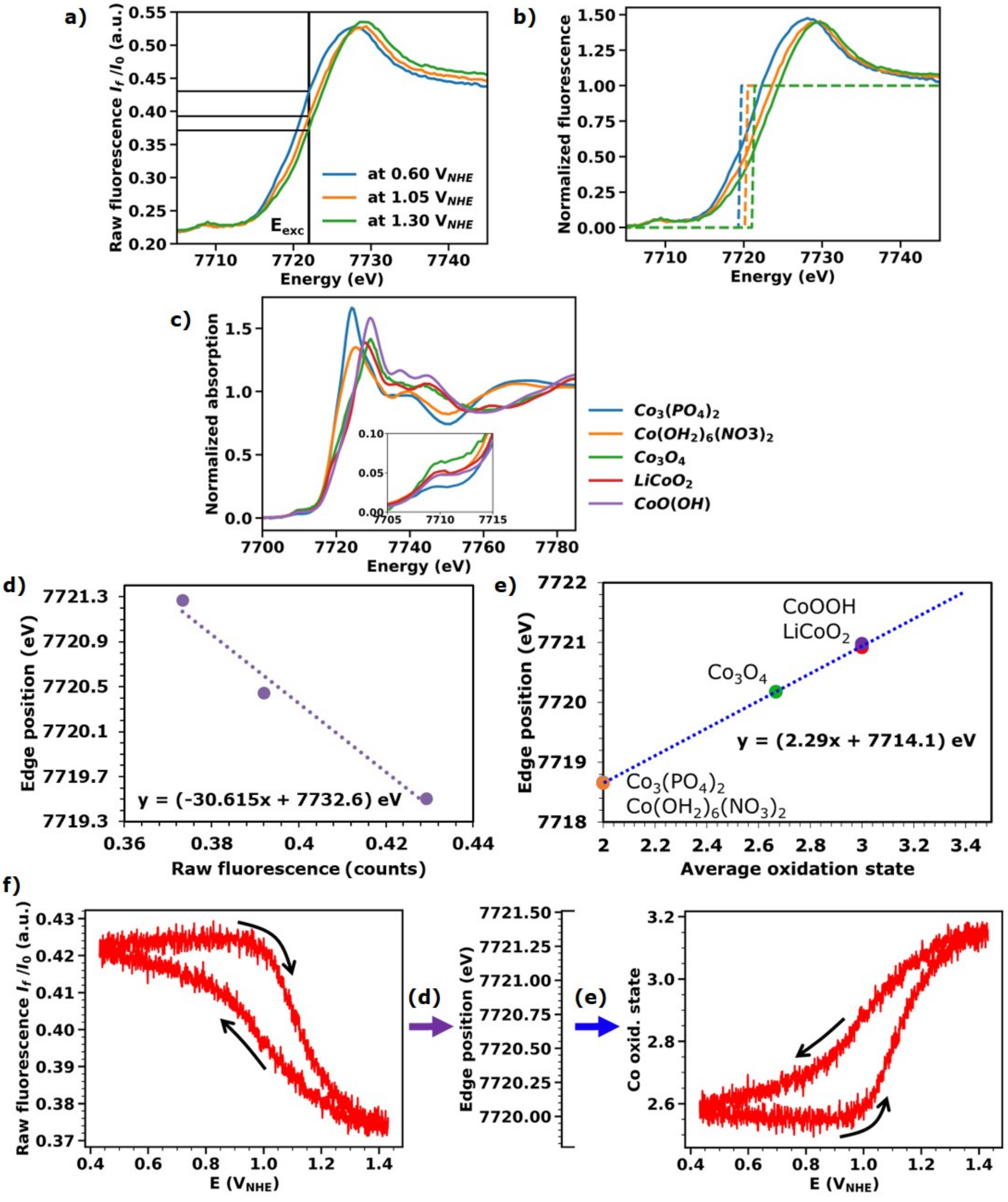
a)
Raw fluorescence I_f/I_0 (a.u.)
0.55
0.50
0.45
0.40
0.35
0.30
0.25
0.20
E_{exc}
at 0.60 V_{NHE}
at 1.05 V_{NHE}
at 1.30 V_{NHE}
7710
7720
7730
7740
Energy (eV)
b)
Normalized fluorescence
1.50
1.25
1.00
0.75
0.50
0.25
0.00
7710
7720
7730
7740
Energy (eV)
c)
Normalized absorption
1.5
1.0
0.5
0.0
0.10
0.05
0.00
7705
7710
7715
7700
7720
7740
7760
7780
Energy (eV)
$Co_3(PO_4)_2$
$Co(OH_2)_6(NO3)_2$
Co_3O_4
$LiCoO_2$
$CoO(OH)$
d)
Edge position (eV)
7721.3
7720.9
7720.5
7720.1
7719.7
7719.3
y = (-30.615x + 7732.6) eV
0.36
0.38
0.4
0.42
0.44
Raw fluorescence (counts)
e)
Edge position (eV)
7722
7721
7720
7719
7718
CoOOH
$LiCoO_2$
Co_3O_4
y = (2.29x + 7714.1) eV
$Co_3(PO_4)_2$
$Co(OH_2)_6(NO_3)_2$
2
2.2
2.4
2.6
2.8
3
3.2
3.4
Average oxidation state
f)
Raw fluorescence I_f/I_0 (a.u.)
0.43
0.42
0.41
0.40
0.39
0.38
0.37
0.4
0.6
0.8
1.0
1.2
1.4
E (V_{NHE})
(d)
Edge position (eV)
7721.50
7721.25
7721.00
7720.75
7720.50
7720.25
7720.00
(e)
Co oxid. state
3.2
3.0
2.8
2.6
0.4
0.6
0.8
1.0
1.2
1.4
E (V_{NHE})

Figure 2.2 *(previous page)*: Conversion of X-ray fluorescence values to a Co oxidation state for a CoCat film operated in 0.1 M KPi solution at pH 7. (a) Three calibration XANES spectra recorded at three different electric potentials. The intensities of the fluorescence signal at $E_{exc} = 7722$ eV in the spectra are indicated by black horizontal lines. (b) XANES spectra from panel a after processing, consisting in background subtraction, normalization and alignment. The edge positions obtained with the integral method (Dau, 2003) are indicated by the dotted lines. (c) XANES spectra of reference compounds of known oxidation state after processing. In the inset a magnification of the pre-edge region. The spectra were collected by Marcel Risch (Risch, 2015), but a new analysis was performed for this thesis work. (d) Calibration line relating raw fluorescence values to edge positions, obtained combining data from panels a and b. (e) Calibration line relating Co oxidation state to edge position, obtained from spectra in panel c. (f) Raw fluorescence signal obtained by keeping the energy fixed at $E_{exc} = 7722$ eV during a cyclic voltammetry experiment. The signal is divided by the incoming beam intensity. Calibration lines in panels d and e are used to convert the signal to an edge position and then to a Co oxidation state. Data from a single CV scan are smoothed with a moving average across 15 data points (1 data point corresponds to 10 ms).

1. Acquire two XANES spectra with the same applied potential one before and one after each time-resolved experiment. If they are not identical, secondary processes (e.g. film dissolution) may have affected the experiment, for details on possible solutions see section 2.3.4.

2. Perform the electrochemical experiment while illuminating the sample with an X-ray beam at a fixed energy. The energy of the X-ray beam is chosen approximately in the middle of the absorption edge (here $E_{exc} = 7722$ eV, vertical black line in Fig. 2.2a).

3. After the electrochemical experiment, collect at least two (three suggested) XANES spectra at the extremes of the potential range of interest, to serve as reference spectra. XANES spectra should extend over an energy range of several hundred eV to enable precise normalization of the edge jump to unity.

4. In the reference measurements, divide the fluorescence signal by the incoming beam intensity and note the fluorescence value corresponding to the selected energy (E_{exc}). In the following, this value is called “raw fluorescence signal” and will constitute the x-axis of the first calibration line (horizontal black lines in Fig. 2.2a).

5. Process the reference spectra by performing energy calibration for each of them (details in section 2.3.2); subtracting a linear background (usually obtained via linear fit in the low-energy region preceding the absorption edge) and normalizing to unity the fluorescence signal after the edge (via division of the spectrum by a polynomial fit or a spline calculated in the energy region above the absorption edge). Then, calculate the edge energy (dotted lines in Fig. 2.2b), preferably using the integral method described in Dau, 2003, which consists in the integration of the entire edge rise.

6. Build a calibration line relating the edge energy to the raw fluorescence signal (Fig. 2.2d). A new calibration line should be constructed for each change of experimental conditions, such as X-ray fluorescence detector position, detection settings or sample thickness.
7. Collect XANES spectra for a series of reference compounds with known oxidation state, which contain the same metal and the same type of ligand as the material of interest (in our case Co coordinated to oxygen, see Fig. 2.2c). Process the spectra as explained above, perform energy calibration and calculate their edge position.
8. Use the reference compounds data to construct a second calibration line linking the edge position to the metal oxidation state (Fig. 2.2e). For most metals, a linear dependence of the edge position on the metal oxidation state is expected (see section 2.2).
9. Use the two calibration lines to convert the raw fluorescence signal recorded during the electrochemical experiment first to an edge position and then to an average oxidation state (example in Fig. 2.2f).

In section 2.3.3 some examples of fixed-energy XAS experiments are presented. An estimation of the error on this method is found in section 2.3.6. The problem of secondary processes affecting operando experiments, especially film dissolution, and possible solutions are presented in sections 2.3.4 and 2.3.5.

2.3.2 Energy calibration

The energy of the X-rays at most synchrotron beamlines is calculated from the position of the monochromator, often with high relative precision, but typically with significant uncertainties regarding the absolute energy scale. The absolute energy scale may depend on experimental factors like positioning of mirrors and monochromator elements, slit widths and heat load to elements of the beamline optics. Thus, in typical X-ray absorption experiments, an energy calibration procedure is performed, ideally based on the simultaneous measurement of the sample of interest and of a stable reference compound. The reference compound must have a known position of the absorption edge and it is often a metal foil placed behind the sample.* However, this procedure introduces some constraints in the experimental setup. In the case of a large electrochemical cell that is not transparent for X-rays, like the one used in this work, the measurement of a reference compound placed behind the sample is technically impossible (see Fig. 2.14b).

Therefore, an alternative procedure for energy calibration was developed, which is based on the alignment of the pre-edge rise. The pre-edge is a feature of the XANES spectrum of cobalt ions, whose position, unlike the position of the main absorption edge, is not strongly influenced by the oxidation state of the sample (Koningsber, 1988). The spectra of reference compounds, used to build the calibration line, are also aligned following the same rationale. Since pre-edges are aligned, we are using the distance between the pre-edge rise and the edge rise for calibration.

The alignment here was facilitated by simulating the derivative of the pre-edge feature with Gaussian functions (Fig. 2.3), the center of the Gaussian function, corresponding to the middle of the pre-edge rise was set to 7708 eV. Since the pre-edge is not perfectly well described by

---

*For metal foils, edge positions have been determined on an absolute energy scale and are available as tabulated values (Thompson, 2001).

a Gaussian function, the range of the fit slightly affects the final alignment. The variation in oxidation state due to different fit ranges used for energy calibration is illustrated Fig. 2.4, showing an offset in the oxidation states of 0.06 and an overall conserved trend. This value represents the sensitivity of the absolute oxidation-state estimates towards uncertainty in the calibration of the energy axis.

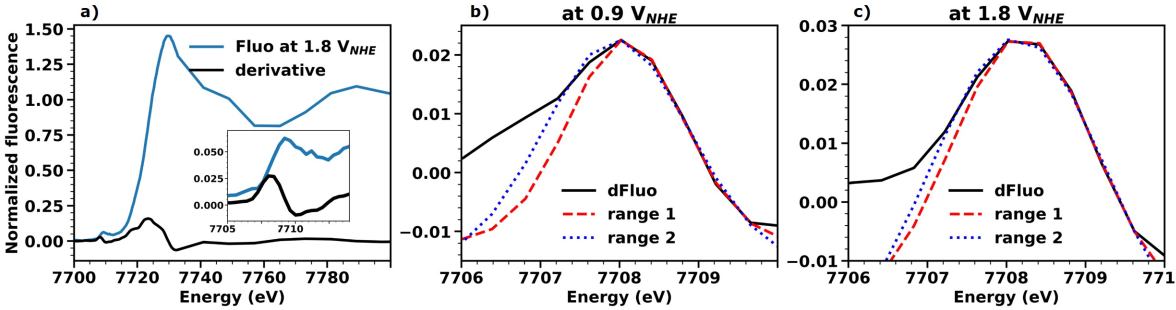

Figure 2.3: Details on the XANES alignment procedure, which consists in shifting the pre-edge rise to 7708 eV. First, the derivative of the edge is calculated (a), then the derivative peak corresponding to the rise of the pre-edge (shown in the in-set) is simulated with the sum of a Gaussian function and a linear slope (b-c). Finally, the XANES is shifted on the energy axis such that the center of the Gaussian (pre-edge rise) is at 7708 eV. Since the shape of the low-energy side of the derivative of the pre-edge is varying a lot between different spectra, sometimes being considerably wider and not symmetric, two fit approaches were considered. Range 1: only the maximum and the high energy side of the peak are simulated. Range 2: the entire peak is simulated. Range 1 was used, consistently, for alignment in this thesis work. The choice of the fit range has an effect on the estimated Co oxidation state, as shown in Fig. 2.4.

Other approaches are feasible, for example, the fine-tuning of the energy axis, aiming at the optimal alignment between the pre-edge rise of the measured spectrum and a reference spectrum. For X-ray data of sufficiently high quality, optimal alignment can be judged by mere visual inspection at high precision. We emphasize that, whatever method is used, the pre-edge alignment requires extreme care, because its precision is a major determinant of the precision of the final oxidation-state estimate.

2.3.3 Operando fixed-energy XAS applied to CoCat

To demonstrate the potentiality of fixed-energy XAS, time-resolved operando X-ray absorption experiments were performed on thin CoCat films (12 to 25 mC cm^{-2}) in 0.1 M KPi solutions at pH 7. Three types of experiments are illustrated, during each experiment the applied electrochemical potential varies between a low potential, at which oxygen evolution is not observed, and a high potential, at which oxygen evolution is observed, by either:

1. scanning at 10 mV/s, cyclic voltammetry experiment;

2. fast jumps between the two potentials, potential jumps experiment;

3. a series of small potential steps, potential stair experiment.

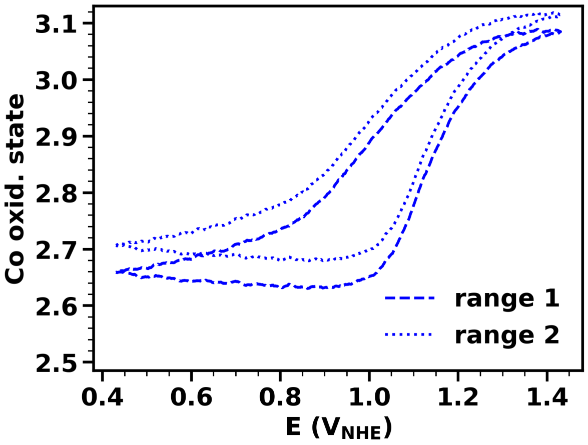

Figure 2.4: Impact of the edge alignment step on the accuracy of the fluorescence conversion to oxidation state. For a CV scan (at 10 mV s^{-1}) for a thin CoCat film (thickness 90 nm, corresponding to 25 mC cm^{-2}) in 0.1 M KPi solutions at pH 7. The two curves represent the result of using two different ranges for the Gaussian fit of the derivative of the pre-edge feature (simulations shown in Fig. 2.3). The use of a different fit range causes a variation of 0.06 oxidation state units. Data averaged from 9 CVs are shown after smoothing with a moving average over 15 points. The difference of 0.1 oxidation state units between the Co oxidation state reported in this figure versus the one observed in Fig. 2.5 relates to the different film thicknesses as well as experimental reproducibility.

Each experiment was preceded and followed by the collection of a series of XANES spectra, which were used to convert the recorded fluorescence into the oxidation state of Co. Other examples of fixed-energy XAS are presented in section 7.2.4.

Cyclic Voltammetry

Cyclic voltammetry (CV) consists in measuring the cell electric current, while the applied electric potential is scanned forward and backward. It is a tool capable of providing insights on both the kinetics and the thermodynamics of a chemical reaction (Marken, 2010). In a fixed-energy XAS experiment the oxidation state is recorded simultaneously with the current during a CV, revealing which metal species are involved for each specific applied potential and enabling the distinction between current linked to oxidation state changes and current stemming from other chemical reactions.

The X-ray fluorescence signal was recorded operando during a cyclic voltammetry experiment (at 10 mV s^{-1}). It was corrected for dissolution (see section 2.3.5) and converted into an average Co oxidation state following the procedure presented in section 2.3.1. The Co oxidation state is reported together with the simultaneously measured current density (Fig. 2.5a).

The rate of oxidation state changes is proportional to the rate of fluorescence changes, i.e. to the derivative of the fluorescence signal (shown in Fig. 2.5b). When the film thickness is known, the component of the current density which is responsible for oxidation state changes (I_{redox}) can be derived, according to:

$$I_{redox} = \frac{dQ}{dt} = \frac{d(ox.state)}{dt} * Q_{film} = \frac{d(ox.state)}{dV} * v_{scan} * Q_{film} \tag{2.3}$$

where $\frac{d(ox.state)}{dV}$ is the derivative of the fluorescence signal, after conversion to an oxidation state, v_{scan} is the CV scan rate and Q_{film} is the film deposition charge. Since the CoCat film undergoes dissolution when operated at neutral pH (see section 2.3.5), a dissolution factor had to be added to the calculation to obtain sensible results: $Q_{film} = Q_{dep} * diss$, for the data shown in Fig. 2.5b $diss = 0.7$ (corresponding to 30% film dissolution) was used. The value of the dissolution factor was chosen a posteriori, for optimal agreement between the measured current and the redox current calculated by Equation 2.3. In alternative, an experimental value for Q_{film} can be obtained by measuring the metal amount in the sample directly after the experiment. When the film is operated in alkaline electrolyte, dissolution is not observed ($diss = 1$, see section 7.2.4).

In this potential range, only two electron-accepting processes are expected to contribute to the measured current density, namely, Co oxidation state changes (linked to the redox current) and oxygen production (linked to the catalytic current). The difference between the measured current and the redox current (calculated from the derivative of the fluorescence using Eq. 2.3) is the catalytic current, i.e. the current responsible for oxygen production (shown in Fig. 2.5c).

At non-catalytic potential, full accordance between the redox current and the measured current is observed (Fig. 2.5b). If a second metal is present in the sample, the sum of the derivative of the two fluorescence signals, collected at the respective metal's edges, can be compared with the measured current. The accordance between fluorescence derivative and measured current implies that, in this potential range, the only process observed is the oxidation and reduction of the metal. On the contrary, the presence of a discrepancy would have provided an indication for either a charge transfer to other elements in the system (like in the case of catalytic activity) or an "unexpected" characteristic of the redox transition. Examples include a transient major structural change, a spin-state transition or a ligand-centered oxidation/reduction, which can be too fast to be observed by XANES or EXAFS on a minute scale. This has been previously observed for NiFe oxides using UV/vis absorption, where a discrepancy between the measured current and the derivative of the absorption signal was tentatively assigned to ligand oxidation Loos, 2019. The comparison of the X-ray signal and the current is a diagnostic tool for such unforeseen transitions.

The collected data for CoCat show that, at low potential, there is a mixture of $\mathrm{Co^{II}}$ and $\mathrm{Co^{III}}$ atoms. At ca. 0.95 $\mathrm{V_{NHE}}$ there is a small rise in current, which corresponds to a $\mathrm{Co^{II}} \rightarrow \mathrm{Co^{III}}$ oxidation. At 1.15 $\mathrm{V_{NHE}}$ $\mathrm{Co^{IV}}$ accumulates in the material and there is the onset of oxygen production. At higher current densities changes in the oxidation state are slowed down and tend towards saturation. During the backward scan, the oxidation state is higher than during the forward scan, suggesting the presence of a slow component in the Co reduction process.

Potential jumps

The "potential jumps" protocol consists in alternating a low (reducing) and a high (oxidizing) potential to study the kinetics of oxidation state changes. The process is repeated multiple times, so that the data can be averaged over different jumps to improve the signal-to-noise ratio without losing time resolution. The variations in the applied potential cause a change in the oxidation state that can be recorded via the fluorescence signal. The simulation of the fluorescence signal with a series of decaying exponential functions allows to study the different time components of oxidation state changes.

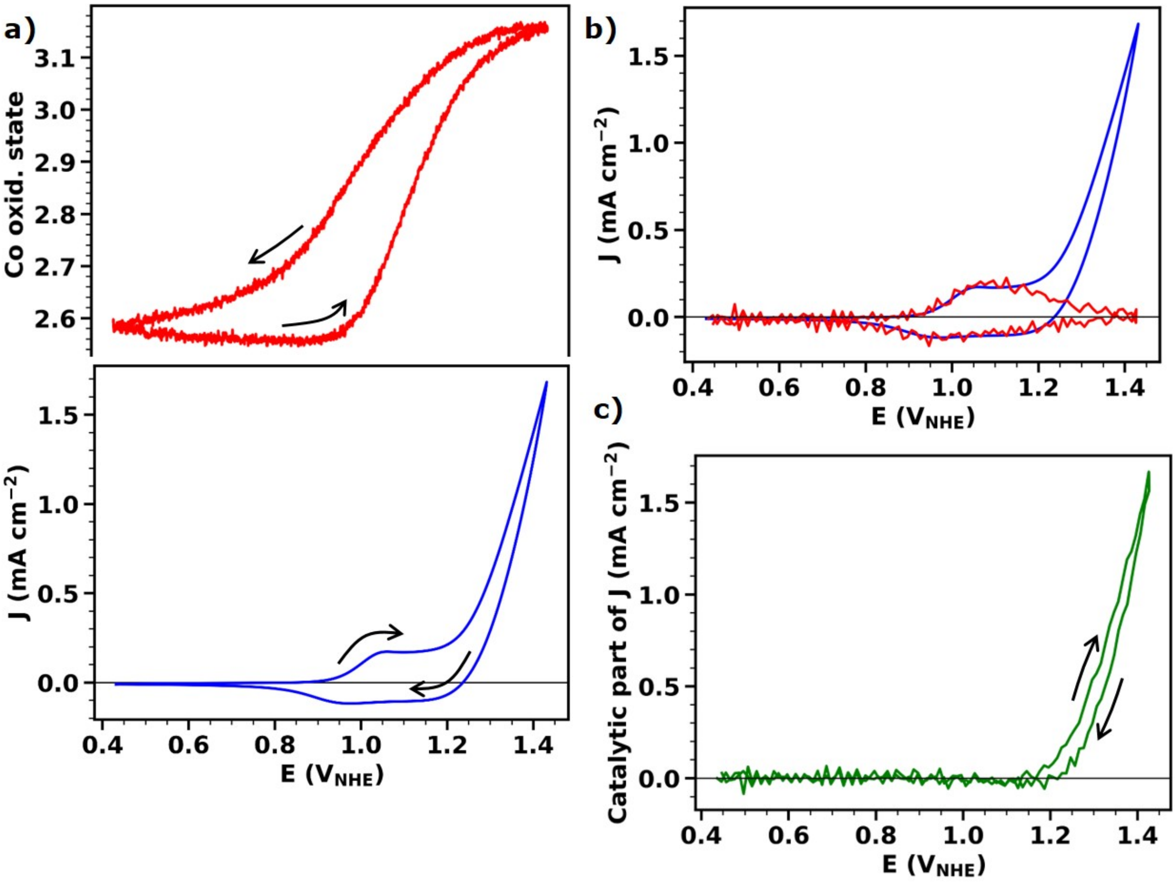

Figure 2.5: Cyclic voltammetry experiment (at 10 mV s^{-1}) for a thin CoCat film (thickness 90 nm, corresponding to 12.5 mC cm^{-2}) in 0.1 M KPi solutions at pH 7. Data averaged from 14 CVs are shown. (a) Simultaneously recorded current density (lower graph) and average oxidation state of the Co ions (upper graph). The X-ray fluorescence, recorded at an excitation energy of 7722 eV, was converted to an average Co oxidation state following the procedure described in section 2.3.1. (b) Current density (blue line) and redox current density (i.e. component of the current responsible for oxidation state changes, red line). The redox current was obtained from the derivative of the fluorescence signal according to Eq. 2.3. The dissolution factor was set to 0.7, resulting in excellent agreement between the redox current and the measured electric current in the redox-wave CV region. (c) Catalytic current density calculated as the difference between the total measured current density and the redox-current density. The black arrows indicate the scan direction.

The potential was alternated between 0.66 and 1.31 V_{NHE}. In this voltage range both the $Co^{II}\rightarrow Co^{III}$ and the $Co^{III}\rightarrow Co^{IV}$ oxidation state transitions are observed and excessively high currents are avoided. Each potential was kept constant for 20 s and data were recorded with a time resolution of 10 ms. Although, the first point after the reductive jump, is recorded with up to 80 ms delay, due to technical limitations. The fluorescence signal recorded was normalized and simulated with the sum of three decaying exponential functions (Fig. 2.6a).

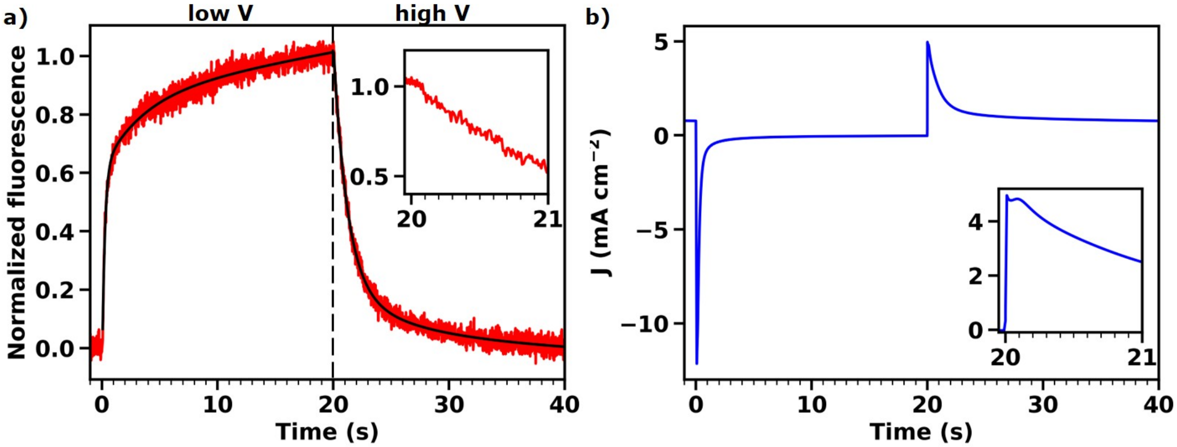

Figure 2.6: Potential jumps experiment for a thin CoCat film (thickness 180 nm, corresponding to 25 mC cm^{-2}) in 0.1 M KPi solutions at pH 7 with 0.1 M KNO_3 added to reduce the solution resistance. The potential was alternated between 0.66 and 1.31 V_{NHE} 30 times. The fluorescence signal was averaged over the different jumps and normalized. (a) Normalized fluorescence signal as a function of time, simulated with the sum of three decaying exponential functions (black line). (b) Current density as a function of time.

Three different kinetic components for the oxidation and the reduction processes were identified: one on the sub-second time-scale, one on the second time-scale and one at a considerably longer time scale. The last one is not exactly quantifiable due to it being longer than the time duration of the jumps in the experiment. The first component has a half-life of 0.1 s for the reduction process and 0.4 s for the oxidation process, while the second component has a half-life of 1.1 s for the reduction process and 1.7 s for the oxidation process. A more detailed interpretation of the presence of different kinetic components can be found in section 6.2.2.

For each kinetic component, the half-life for the oxidation process is longer than for the reduction process. A possible explanation is that the $Co^{II} \rightleftharpoons Co^{III}$ transition is slower than the $Co^{III} \rightleftharpoons Co^{IV}$ transition, due to the high concentration of Co^{II}. During reduction, the fast process is completed and, then, the slow begins. On the contrary, during oxidation, the slow process precedes and, thus, masks the fast one.

Potential stair

The "potential stair" protocol consists in increasing the potential through a series of small steps, for each step the potential is held constant until a stable state is achieved. A high time resolution is not required, but it is important to perform the experiment operando. This protocol allows to study the thermodynamics of a reaction and to acquire information on the stable state of the catalyst. It is possible to either acquire a full edge at each potential or continuously measure the fluorescence signal. This protocol is the same used, at high potentials, to measure the Tafel slope.

The potential was increased from 0.81 to 1.46 V_{NHE} in 30 mV steps, while continuously acquiring the fluorescence signal (Fig. 2.7a). At low potentials the fluorescence changes due to a combination of oxidation state changes and film dissolution (for more details on the effect of film dissolution, see section 2.3.5), while at high potentials oxidation state changes reach a saturation level.

The saturation begins at lower applied potential than during the CV. A possible reason is that the same oxidation state is reached at lower potential during the potential stairs than during the CV, likely because a component of oxidation state changes is slower than the CV scan rate. In the saturation process, contributions from mass transport limitations cannot be excluded (see section 4.2.3), these would also differ between potential stair and CV experiments.

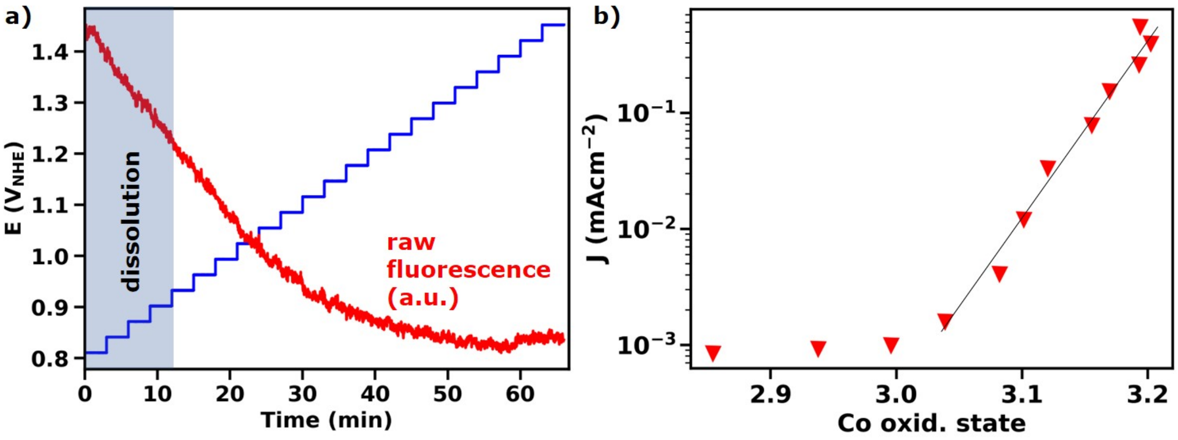

Figure 2.7: Potential stair experiment for a thin CoCat film (thickness 90 nm, corresponding to 12.5 mC cm^{-2}) in 0.1 M KPi solution at pH 7. The potential was increased from 0.81 to 1.46 V_{NHE} in 30 mV steps, each step lasted 3 min. (a) Raw fluorescence signal (red line) and applied potential (blue line). The blue area indicates the potential region strongly affected by dissolution. (b) Current density as a function of the oxidation state, shown for several different catalytic potentials. The black line was added to guide the eye.

At catalytic potentials, the stable value of the oxidation state and the current are recorded. The analysis of the catalytic current as a function of the oxidation state can lead to important mechanistic considerations on the factors controlling the catalytic activity. This method is often applied in the next chapters: it is combined with isotope effect measurements to exclude a direct potential-drive for oxygen production (Ch. 6) and is used as proof for different mechanistic behaviors in different pH regimes (Ch. 7). In Fig. 2.7b the current obtained at catalytic potentials is shown as a function of the oxidation state revealing an exponential dependence of the catalytic current on the number of Co^{IV} atoms in the sample (more details in Ch. 6).

2.3.4 Sources of experimental error

To assure the reliability of a fixed-energy XAS experiment, it is important to collect a XANES spectrum both before and after the experiment with the same electrochemical conditions.

Eventual differences between the two spectra, suggest the presence of undesired processes, which may affect the conversion of the signal to an oxidation state. There are different possibilities.

1. A change in the edge shape. An example in section 7.2.2. It indicates that the sample is being structurally modified during the experiment. The sample should be electrochemically treated until it reaches a stable state, to ensure that the structural changes are completed before the beginning of the operando experiment.

2. A change in the edge position. An example in Table 2.2. At parity of electrochemical conditions, the metal oxidation state and, thus, the edge position observed for a sample is expected to be repeatable. A difference in the edge positions suggests that the oxidation state changes are not fully reversible. This does not affect the reliability of the fixed-energy XAS method, but it should be discussed in data interpretation.

3. A decrease in the fluorescence level at X-ray energies far after the absorption edge. An example in Fig. 2.8a. It indicates that a part of the fluorescence-emitting sample has been lost during the experiment. It can have two origins.
    - The sample is detaching from the substrate, in this case the experiment cannot lead to reliable conclusions, different substrates should be tested.
    - The sample is gradually dissolving in solution. It is possible to correct the fluorescence signal to compensate for sample dissolution. Section 2.3.5 focuses on sample dissolution and the correction procedure is explained in detail.

Another important aspect is X-ray-induced damages to the sample, in form of X-ray photoreduction of high-valent metal sites, which is often observed when exposing a sample to strong X-rays for prolonged periods. This problem has been extensively discussed by (King, 2019). In the experiments reported in this thesis, photo-damage was avoided thanks to an out-of-focus geometry (11 x 2 mm beam spot size) and a low X-ray beam intensity (about 10^{11} photons s^{-1} Zizak, 2017).

2.3.5 Sample dissolution and how to compensate for it

The CoCat is not stable at pH 7 but slowly dissolves in the electrolyte (Surendranath, 2012). When a part of the sample is dissolved, there are fewer Co atoms that can emit X-ray fluorescence and the recorded signal decreases. Thus, during an operando experiment, a decrease in the detected fluorescence signal can not be exclusively assigned to oxidation state changes, because it can be partially caused by sample dissolution. It is possible to distinguish the two phenomena by exciting the X-ray fluorescence at high X-ray energies ($\sim$ 500 eV above the absorption edge). At these energies, the EXAFS modulations are reduced and the fluorescence intensity does not depend on the oxidation state, but only on the amount of Co in the sample.

To quantify the amount of sample dissolution, four operando XANES spectra were recorded at 0.5 V_{NHE}, interspersed with single CV measurements, on a 25 mC cm^{-2} thick CoCat sample in KPi at pH 7. During the CVs, the incoming X-ray beam was fixed at 7722 eV. This sequence was followed by 10 additional CVs and, lastly, two XANES spectra measured at 0.5 V_{NHE} and 1.4 V_{NHE} (Fig. 2.8). The list of performed XANES measurements is available in Table 2.2. The decrease in the intensity of the fluorescence signal for each subsequent XANES spectrum, well

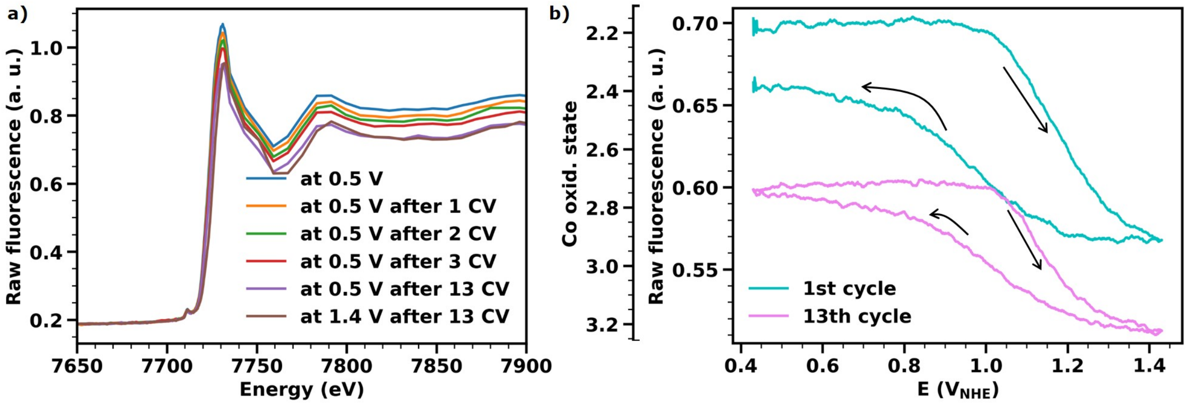

Figure 2.8: Effect of sample dissolution on edge measurements and CVs, for a CoCat sample (thickness 180 nm, corresponding to 25 mC cm^{-2}) operated in KPi at pH 7. (a) Unprocessed XANES spectra recorded at the beginning of the experiment, as well as after different numbers of CVs. The fluorescence signal was divided by incoming beam signal, but no background subtraction nor normalization were performed. The decrease in signal in the high-energy region indicates sample dissolution. (b) Fluorescence excited at 7722 eV recorded during the 1st and 13th CV, differences are due to film dissolution. The second axis represents the direct conversion of the fluorescence signal to a Co oxidation state, without compensation for sample dissolution.

Table 2.2: Quantification of sample dissolution and irreversible oxidation state changes during CVs by analysis of XANES spectra.[a, b]

	Dissolved film (%)	Edge position (eV)	Average ox. state
at 0.5 V	0	7720.09	2.62
at 0.5 V after 1 CV	3.0	7720.15	2.64
at 0.5 V after 2 CV	5.3	7720.22	2.67
at 0.5 V after 3 CV	7.6	7720.24	2.68
at 0.5 V after 13 CV	12.5	7720.33	2.72
at 1.4 V after 13 CV	13.8	7721.78	3.36

[a] The table refers to the absorption edges shown in Fig. 2.8a.

[b] The percentage of dissolution was obtained via a fit of the 7822 to 8000 eV region with a horizontal line, after background subtraction and division by the incoming beam intensity. The edge position was obtained via the integral method, after edge normalization and alignment. The oxidation state was obtained from the edge position using the calibration line shown in Fig. 2.2e.

visible at energies above 7800 eV, reflects the level of sample dissolution during each preceding CV (Fig. 2.8a).

The XANES spectra were processed by dividing each spectrum by the incoming beam intensity and subtracting a linear background, obtained by fitting a straight line in the region before the edge rise. Then the signal intensity for energies above 7822 eV was measured and the amount of the dissolved film was calculated, as a percentage of the initial fluorescence intensity (Table 2.2). During the first CV, 3% of the catalyst is dissolved, but after repeated cycling the dissolved amount decreases to 0.5% per CV. For this reason, in this thesis, the first CV cycle was always excluded from data analysis.

The shift in edge position between subsequent XANES measurements reveals that, in addition to dissolution, a fraction of Co atoms is irreversibly oxidized during the series of CVs, causing a change of about 0.1 oxidation-state units during the sequence of 13 CVs. The minor significance of this irreversible oxidation can be estimated, by comparing it to the amplitude of the total oxidation state change (0.64 units), which is observed in the potential range of a CV. The value of 0.64 oxidation state units was obtained as the difference in oxidation state between the XANES spectra recorded at 0.5 V_{NHE} and 1.4 V_{NHE} (last two spectra in Table 2.2).

The dissolution effect is also visible in the fluorescence signal recorded during the CVs and causes a mismatch of the start and end fluorescence values (Fig. 2.8b, blue trace). After 13 CVs the effect of dissolution is virtually absent (Fig. 2.8b, magenta trace). The second axis of Fig. 2.8b highlights the impact that the dissolution phenomenon can have on the estimation of the oxidation state. For the 13th CV a reliable estimate of the oxidation state is obtained because, since dissolution at the end of the experiment is minimal, the sample has the same thickness that it will have in the final XANES measurements, which are used as reference spectra. During the first CV instead, the sample is roughly 10% thicker than during the measurement of the reference spectra, resulting in an artificially low estimate of the oxidation state.

In the following, a simple procedure to correct the effect of sample dissolution is explained. The procedure is applied to the series of 10 subsequent CVs of the described experiment. If we exclude the first CV, the fluorescence and current values decrease linearly with cycle number (Fig. 2.9a, maximum values reached in each cycle is shown). Thus, it is assumed that, after a certain number of CV cycling, the rate of dissolution is linear over time. Furthermore, we decide to neglect the relatively small effect of the applied potential on the dissolution rate (see below) and not to distinguish the irreversible oxidation state change from dissolution, since in our case it is very small, i.e. less than 0.04 units per 10 CVs (see Table 2.2). In Fig. 2.9b, the fluorescence signal recorded during 9 CVs is plotted as a function of time (blue trace) and a straight line is drawn through the maximum fluorescence value of each CV (“maximum line”, $M(t)$). Since the XANES reference spectra are recorded after the measurement, the dissolution correction consists in scaling down the signal from all CVs to the level of the last CV (Fig. 2.9b, green trace). To achieve this, the fluorescence signal at each point in time, $fluo_{meas}(t)$, is divided by the “maximum line” value in that point, $M(t)$, and then multiplied by the fluorescence value recorded at the end of the CV series (last maximum in the fluorescence, $fluo_{last}$).

$$fluo_{cor}(t) = \frac{fluo_{meas}(t)}{M(t)} * fluo_{last} \tag{2.4}$$

It is also possible to study the dissolution phenomena with time-resolved operando measurements by fixing the incoming beam energy to values well above the absorption edge ($E_{exc} > 8000\ eV$). At these energies, the variation in the recorded fluorescence signal,

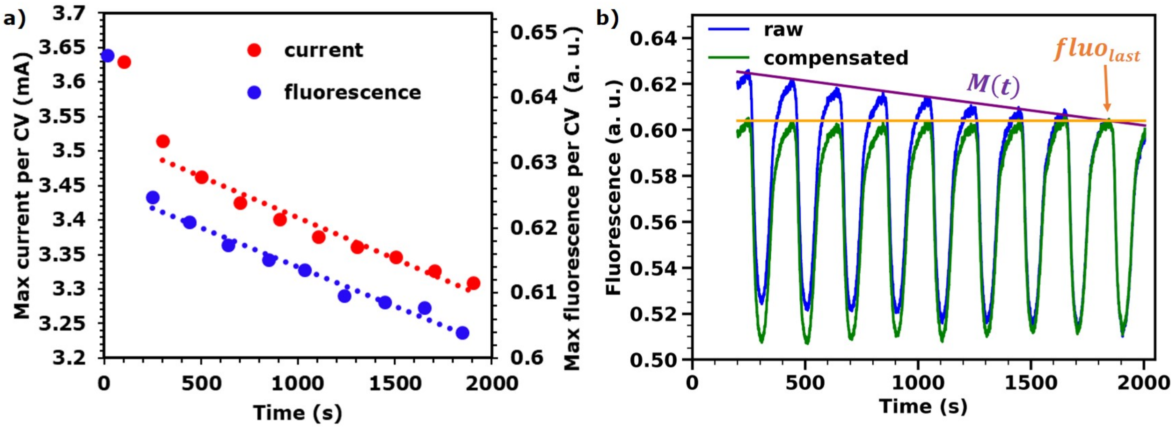

Figure 2.9: Correction for dissolution of the fluorescence signal recorded during 9 subsequent CVs. (a) A straight line is drawn through the maximum fluorescence value of each CV and used to scale the signal down to the level of the last CV. (b) Maximum values reached by the current and the fluorescence signal in each CV. When we exclude the first CV, the decrease in fluorescence and current due to film dissolution can be well approximated with a straight line (dotted lines).

will not depend on oxidation state changes but on the amount of metal in the sample. Two operando CV experiments were performed, in which the X-ray beam energy was set well above the Co absorption edge. In Fig.2.10a, the amount of sample dissolution over time during a CV is illustrated. The decrease due to dissolution (measured at $E_{exc} > 8000 eV$) is presented as a percentage of the total decrease due to oxidation state changes (measured at $E_{exc} = 7722\ eV$). It can be observed that the effect of sample dissolution is comparable in magnitude to the effect of oxidation state changes, but becomes less severe with increasing operation time. Large variations in the dynamic of film dissolution between different samples are possible and the difference between the two examples, showed in Fig. 2.10a, is most likely attributable to samples variability.

During the second experiment, the fluorescence recorded with $E_{exc} = 8000\ eV$ during a series of CVs was averaged over the applied potential (after excluding the first CV), to study the potential dependence of the dissolution phenomenon. At potentials below 1.1 V_{NHE} the fluorescence signal decrease, indicating sample dissolution, while above this potential the catalyst is stable (Fig. 2.10b). The potential dependence of the dissolution process is also visible as small oscillations in the blue curve of Fig. 2.10a.

In summary, for the here investigated CoCat films, sample dissolution can strongly affect the conversion of fluorescence signal to oxidation state, but the intensity of the dissolution process has a logarithmic decay with operation time. Repeated CV cycling before the start of the experiment reduces the impact of film dissolution on the X-ray fluorescence intensity to less than 10% of the changes resulting from potential-dependent oxidation state changes (see Fig. 2.10a). In this situation, the simple scaling procedure illustrated above is sufficient to correct for dissolution effects and obtain reliable metal oxidation-state values. Measurements at an excitation energy above the edge might be needed, at the beginning of each experiment, to assess when a sufficiently stable state of the catalyst is reached.

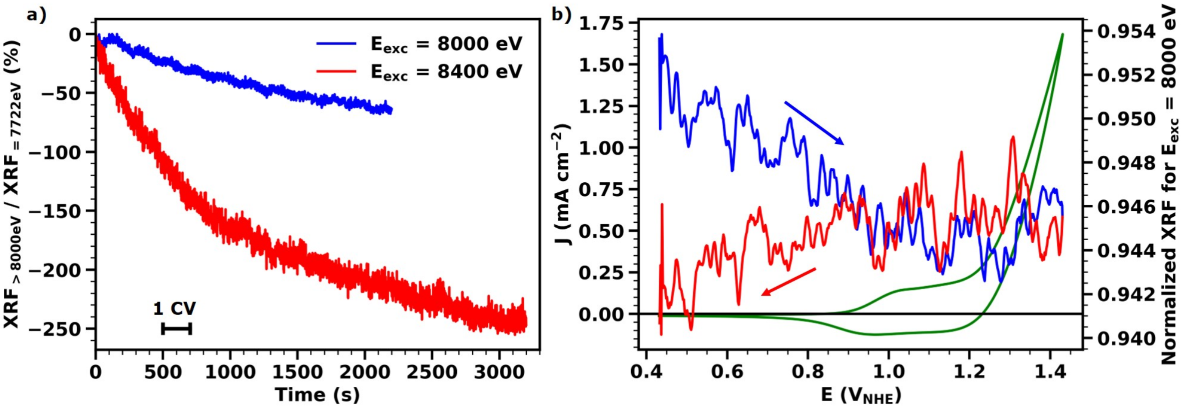

Figure 2.10: Time-resolved study of film dissolution for a CoCat sample CoCat sample (thickness 90 nm, corresponding to 12.5 mC cm^{-2}) operated in KPi at pH 7. The X-ray fluorescence is excited at energies above the Co absorption edge ($E_{exc} > 8000\ eV$) during a series of CVs. At these excitation energies the fluorescence signal is proportional to the quantity of material in the sample, i.e. is only sensitive to dissolution phenomena. (a) Fluorescence changes caused by film dissolution, measured at two different exemplary excitation energies recorded during a series of CVs as a function of time. The fluorescence excited at $E_{exc} > 8000\ eV$ is presented as a percentage of the total fluorescence change due to oxidation state changes, which was calculated from the fluorescence recorded during a CV with an excitation energy of $E_{exc} = 7722\ eV$. The black horizontal bar indicates the time scale of one CV. (b) Current density (green line, left axis) during the CV. Raw fluorescence signal (XRF) at $E_{exc} = 8000\ eV$ is mapped on the right axis and shown with blue color for the anodic scan and with red for the cathodic scan. The arrows indicate the scan direction. The fluorescence was first divided by the incoming beam intensity and then normalized by subtracting the background level and dividing it by the total edge jump. In this scale 1 represents the value of fluorescence at the beginning of the experiment, before dissolution, and 0 the value of fluorescence for a completely dissolved sample. The data represent the average of 9 CVs.

If the impact of film dissolution were more severe, it would be necessary to correct for dissolution in a more elaborate way, taking into account the potential dependence of the dissolution rate. Appropriate corrections could be obtained by an additional experiment on an identically prepared catalyst film, where the fluorescence intensity is recorded for energies of the incoming X-rays at least 300 eV above the absorption edge (like the experiment shown in Fig. 2.10b). The fluorescence signal recorded at these energies provides a good estimate of the amount of (non-dissolved) Co ions in the catalyst film and can be used for potential-dependent dissolution correction. This type of experiment revealed the presence of a dissolution threshold in the applied potential for CoCat in neutral electrolyte. Below 1.1 V_{NHE} the film gradually dissolves in the electrolyte, above the catalyst film is stable.

2.3.6 Error estimation for the conversion procedure

The analytical procedure proposed for the conversion of the X-ray fluorescence signal into an oxidation state requires a rather complex data analysis. In this section, I analyze the potential error that is added by the different steps of the procedure and estimate an uncertainty range for the results obtained in the CV proof-of-concept experiment (section 2.3.3).

The procedure is composed of two conversion steps: (1) the conversion of the fluorescence signal into an edge energy-position, based on the reference XANES measurements performed during each experiment (first calibration line) and (2) the conversion of the edge energy-position into an oxidation state, based on reference compounds (second calibration line). The absolute value of the oxidation state is affected by both conversions and therefore has a higher error, while the comparison between different experiments, using the same set of reference compounds (relative error), is more reliable.

For each calibration line, the reference data are simulated with a linear equation ($y = mx + q$), see Fig. 2.2 d and e, for the first and second calibration lines, respectively. The parameters obtained from this equation are then used for the conversion. From the simulation, the standard deviations (σ) on each of the fit parameters are obtained. Per each calibration line, two alternative equations were calculated using the standard deviation: $y = (m + \sigma_m)x + q - \sigma_q$ and $y = (m - \sigma_m)x + q + \sigma_q$. These two alternatives were employed as calibration lines for the conversion procedure on the operando CV experiment, obtaining different final values for the Co oxidation state (Fig. 2.11). Since the two parameters (m and q) are inversely correlated, we choose to assign opposite signs to the two standard deviations.

From the differences in the Co oxidation state values between the two variations, we can derive an uncertainty range of 0.11 and 0.01 oxidation state units for the first and second calibration lines, respectively. The uncertainty range for the second calibration line is very small, because the reference compounds used in this thesis were carefully chosen (as part of previous work) and nicely fit on a line, using a different set of reference compounds can lead to higher inaccuracies.

The uncertainty range for the first calibration line (0.11 oxidation state units) is an estimation of the relative error on the experiment, which includes the error due to noise in the raw fluorescence signal and the error on the edge position estimation with the integral method. Three factors contribute to the absolute error: (1) the relative error, (2) the uncertainty range for the second calibration line, and (3) the error made in the alignment of the energy axis, between the experimental XAS spectra and the reference compounds XAS spectra.

The error made in the alignment of the energy axis is discussed in section 2.3.2. A slightly alternative approach is used for alignment resulting in a different oxidation state value, the

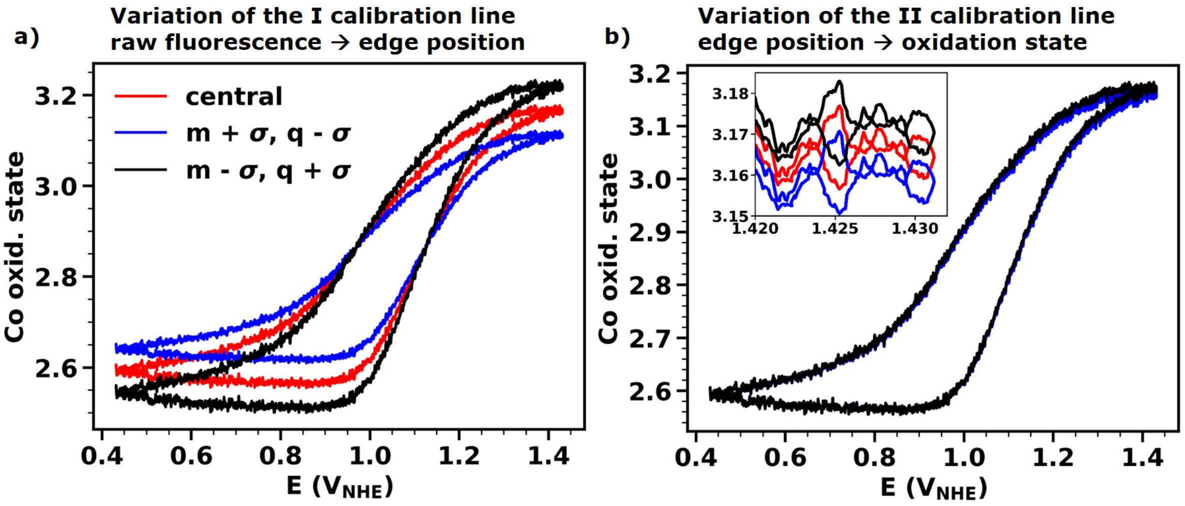

Figure 2.11: Estimation of the uncertainty range on the calculation of Co oxidation state during a CV scan (at 10 mV s^{-1}) for a thin CoCat film operated in 0.1 M KPi buffer at pH 7. The conversion of the raw X-ray fluorescence signal to a metal oxidation state requires the use of two calibration lines. The effect of a variation of each calibration line on the final Co oxidation state is presented. Per each calibration line, the m and q parameters ($y = mx + q$) obtained by simulation of the line were varied using one standard deviation (σ), obtaining two new calibration lines: $y = (m + \sigma m)x + q\check{}\sigma q$ and $y = (m - \sigma m)x + q + \sigma q$. (a) Effect of the variation of the first calibration line. (b) Effect of the variation of the second calibration line.

variation amounts to 0.06 oxidation state units. This value is assumed to be the error introduced by uncertainty in the calibration of the energy axis.

By summing all the different contributions, we obtain an estimate for the absolute error of 0.18 oxidation state units.

2.3.7 Operando UV-vis absorption spectroscopy, an alternative to XAS?

Visible absorption spectroscopy (UV/vis) has been reported to successfully track changes in the oxidation state of transition metals (Risch, 2015; Smith, 2017; Trotochaud, 2013; Polo da Fonseca, 1994). In comparison to X-ray absorption, UV/vis absorption is more sensitive to external factors that can be hardly addressed quantitatively (e.g. light scattering effects from bubbles due to hydrogen production) and does not offer a quantitative estimate of metal ion oxidation states, which complicates the comparison between electric current densities and absorption signals. However, it is technically less complicated and does not require a synchrotron facility. Thus, UV/vis absorption can help the preparation of an X-ray absorption experiment and, once the main results have been validated through X-ray absorption, UV/vis absorption can be employed to assess the impact of a wide range of parameters variations.

The CoCat has a wide absorption band between 400 and 700 nm, the molar extinction coefficient increases homogeneously over the 400 to 900 nm spectral range when a potential is applied (Fig. 2.12). The oxidation state obtained from quasi-in-situ XAS and the absorption value at 600 nm show the same potential dependence (Fig. 6.6b), proving that the absorption coefficient varies linearly with Co oxidation state. Some small discrepancy is only present at low potentials.

It is possible to perform an operando UV/vis electrochemical experiment following the same protocol used for fixed-energy XAS. During a CV the change in the absorption coefficient is proportional to the change in the oxidation state (Fig. 2.13). X-ray absorption experiments revealed that two oxidation state transitions, $Co^{II} \rightarrow Co^{III}$ and $Co^{III} \rightarrow Co^{IV}$, are embedded in the CV oxidation wave. An operando UV/vis electrochemical experiment can reveal the midpoint potential of the two transitions (indicated by stars in Fig. 2.13a, method shown in Fig. 2.13b). Furthermore, given the easy accessibility of UV/vis spectroscopy, it is possible to repeat the same experiment in a wide series of conditions (different pH, isotopes or buffer concentrations) to obtain further information on the mechanism of Co oxidation (an example in the inset of Fig. 2.13a, another example in Loos, 2019). This makes UV/vis spectroscopy a good complementary method to XAS for the in-situ study of oxidation state changes.

2.4 Summary

The potentiality of fixed-energy X-ray absorption spectroscopy as a tool to study the mechanism of the water oxidation reaction is unraveled. This technique consists in collecting the fluorescence signal operando at a fixed incident X-ray energy during a series of electrochemical experiments. An analytical method is established to obtain a time-resolved average value for the metal oxidation-state from the X-ray fluorescence signal, making use of two calibration lines. This method allows the calculation of the metal oxidation state with an absolute error of ±0.09 oxidation state units. The error on experiment repeatability is ±0.05 oxidation state units, when comparing two experiments performed with the same equipment and the same set of reference compounds (relative error). Possible sources of errors are discussed, including X-ray-induced

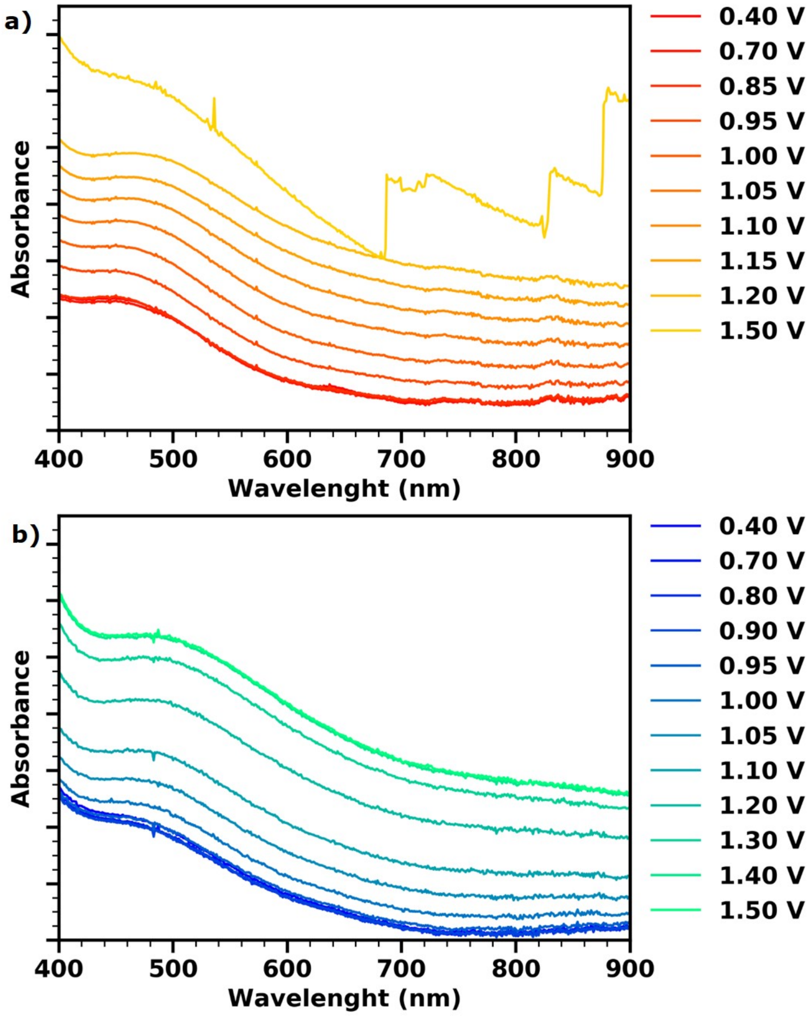

Figure 2.12: Visible absorption spectroscopy measured in-situ during steady-state chronopotentiometry for CoCat in 0.1 M KPi at pL 7 in (a) H_2O-containing buffer and (b) D_2O-containing buffer at different applied potentials (reported in NHE scale after correction for iR drop). Background of blank ITO was subtracted from the data. The values for absorbance extracted at 600 nm are shown in Fig. 6.2b. At the highest potential examined in H_2O-containing buffer bubbles accumulating in the electrolyte contribute to the increase in absorbance. Before extraction of the value at 600 nm the spectrum was corrected from bubbles contribution by subtracting a "bubble factor" to the steady-state value. The bubble factor was obtained as the difference in absorption before (electrolyte without bubbles) and after (electrolyte with bubbles) the measurement, obtained at low overpotentials (no direct bubble production).

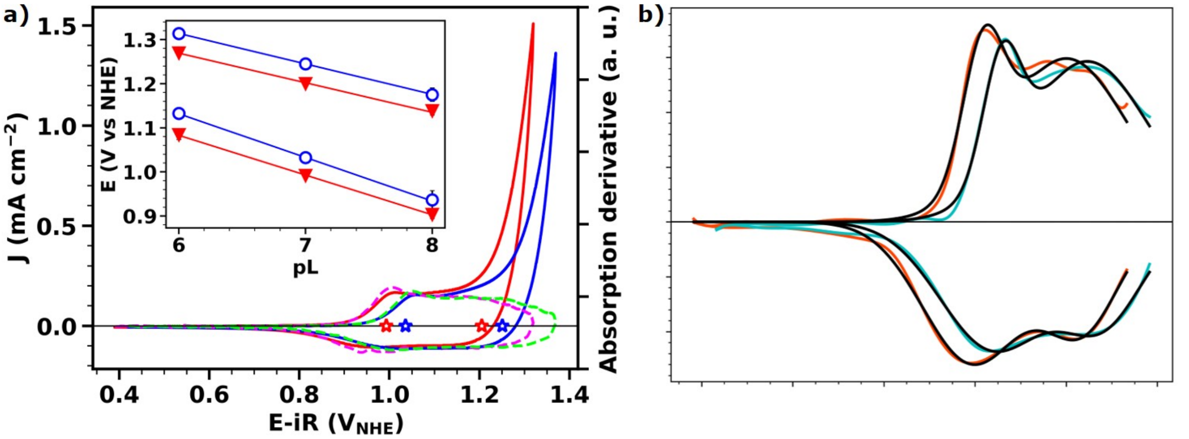

Figure 2.13: Operando time-resolved UV/vis absorption spectroscopy during a cyclic voltammetry experiment (at 20 mV s^{-1}) for a thin CoCat film (10 mC cm^{-2}) in 0.1 M KPi solutions at pH 7 at which was added 0.1 M KNO_3 to reduce the solution resistance. The buffer was prepared either with H_2O (red and pink lines) or D_2O (blue and green lines). (a) The current density (red and blue full lines, left axis) is shown together with the derivative of the absorption signal (pink and green dotted lines, right axis), redox potentials are indicated with stars. Compensation of the recorded potential for 85% of the iR drop was carried out during the experiment. (a-Inset) Values for the Co redox potentials at different pL in water (red triangles) and deuterated water (blue circles). Linear fits have a slope of -95±1 and -68±1 mV pH^{-1} for the first and second redox potentials respectively. (b) Procedure for the determination of redox peak positions. The derivative of the absorption (colored lines) was fitted using the sum of two Gaussian functions (one for each expected peak; black lines). Measurements were repeated three times per each pL on independent CoCat films.

radiation damage, sample structural instability, structural changes during operation and sample dissolution, for all of them tackling strategies are proposed. Catalyst dissolution is treated in detail and a data-correction protocol is proposed, moreover, it is shown that the rate of dissolution decreases with catalyst operation time and stops when the applied potential is higher than 1.1 V_{NHE}.

As proof-of-concept, operando measurements were performed on a thin CoCat electrodeposited catalyst in neutral-pH electrolyte and a time-resolved Co average oxidation state was derived using the proposed method. Three types of experiments are presented: (1) cyclic voltammetry, (2) fast jumps between two potentials and (3) a series of small potential steps. The operando experiments proved the suitability of this technique to:

- Detect metal-centered redox transitions with 10 ms time-resolution and study their kinetic.
- Measure the average oxidation state at which water oxidation begins.
- Distinguish the current responsible for redox transitions from the current linked to the catalytic reaction.
- Study the relation between oxidation state changes and catalytic current, thereby determining the factors controlling catalytic activity.
- Assess whether all redox transitions are metal-centered. In particular, comparing the derivative of the X-ray fluorescence with the measured current allows discerning more complex behaviors of a redox transition, such as transient major structural change, spin-states transition or ligand-centered oxidation/reduction.
- Investigate the stability of the catalyst in different electrochemical conditions.

UV/vis absorption spectroscopy is also able to track metal-centered oxidation state changes, using the same fixed-energy operando experiment. UV/vis absorption is more sensitive to spurious signals and lacks quantitative information, but is easier to access and is proposed as a complementary technique to XAS.

2.5 Experimental details

Materials

CoCat films were prepared by anodic electrodeposition following an established protocol (Kanan, 2008; Klingan, 2014), slightly modified: a potential of 1.05 V_{NHE} was applied in a 0.1 M phosphate buffer (KPi) at pH 7 containing 0.5 mM $Co(NO_3)_2$ solution. Sample preparation, as well as electrochemical experiments, were performed in a single-compartment three-electrode cell, using a Pt grid (2x2 cm^2, 90% purity) as a counter electrode and an Ag/AgCl(saturated) as a reference electrode. The working electrode was a 0.1 mm thick sheet made of glassy carbon, Hochtemperatur-Werkstoffe GmbH, 2 cm^2 working area. Before use, the glassy carbon substrate was sonicated in ethanol and water. The electrolyte solution was 0.1 M phosphate buffer (KPi) at pH 7 prepared using MilliQ water ($>$18 MΩ cm).

Operando X-ray Absorption Spectroscopy

X-ray absorption spectroscopy measurements were performed operando, during electrochemistry experiments, at the BESSY synchrotron (Berlin) at beamline KMC-3. Electrochemistry took place in a three-electrode self-made Teflon cell, where the working electrode is attached as a window to the wall (Fig. 2.14). The cell contains a standard volume of electrolyte (50 mL), to preserve appropriate electrochemical conditions. The X-ray excitation beam passes through the 100 µm thick conductive glassy-carbon substrate to reach the catalyst film, then the Co fluorescence is emitted at a 90°angle and crosses again the substrate before collection. The Co K_α-fluorescence is filtered by a Fe metal foil (10 µm thick, 99.99+% purity, Goodfellow) and then collected, at an angle of c.a. 90° from the incoming beam direction, by a scintillation detector (51BMI/2E1-YAPNeg, Scionix) using a photomultiplier operated at 0.9 kV. The outgoing current signal is converted to a voltage with a 1 MΩ resistor, amplified and then recorded by a potentiostat (BioLogic SP-300), which at the same time performs electrochemistry. An out-of-focus geometry assures a beam size at sample of 11 x 2 mm, the large area prevents radiation damage problems.

For details on the operando UV/vis absorption experiment refer to section 6.5.

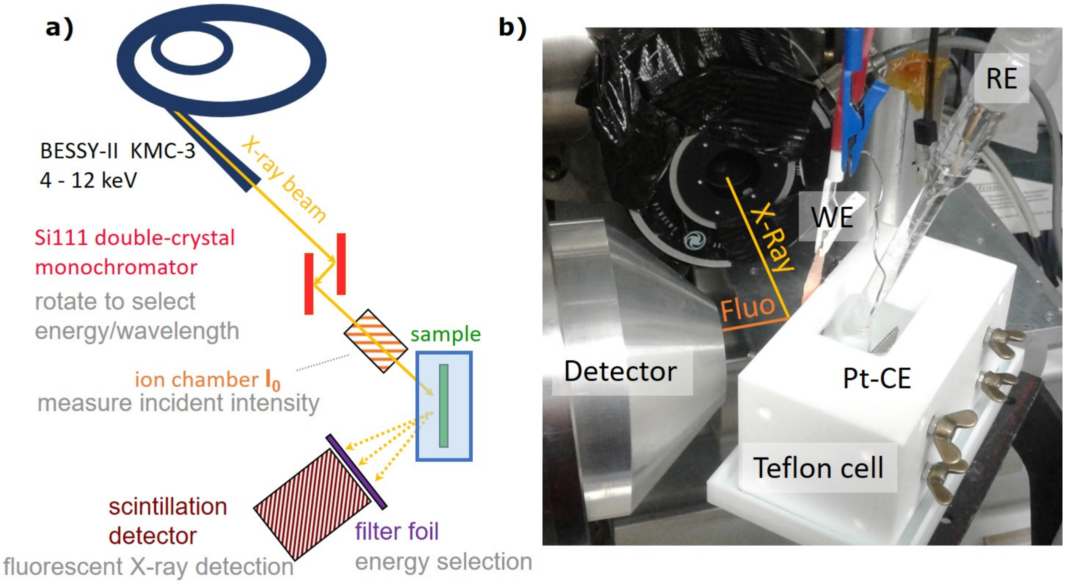

Figure 2.14: Operando setup used for operando time-resolved X-ray absorption measurements at KMC-3-Beamline at BESSY II synchrotron radiation facility, Helmholtz Zentrum Berlin. a) Scheme of the beamline setup. b) Picture of the homemade electrochemical cell.

3 Operando Raman spectroscopy tracks oxidation-state changes and reveals mechanistic insights in an amorphous Co-oxide material

Reproduced in part from

Pasquini, C.; D'Amario, L.; Zaharieva, I.; Dau, H., Operando Raman spectroscopy tracks oxidation-state changes in an amorphous Co oxide material for electrocatalysis of the oxygen evolution reaction. *J. Chem. Phys* **2020**, 152 (19), 194202.
DOI: 10.1063/5.0006306

with the permission of AIP Publishing.

Author Contributions: Data acquisition, data analysis, writing—original draft preparation, conceptualization C.P.; conceptualization, writing—review H.D.; writing—review and -introduction L.D.; support in synchrotron measurements and valuable discussions Z.I.

List of figures in the Appendix

3.1 Context and motivations

The investigation of electrochemical reactions involving multiple steps and of the catalyst's role in the reaction mechanism can be extremely challenging. Operando methods are an important tool to address this challenge, because they enable the study of reactions during their proceeding. For example, by coupling spectroscopic techniques with electrochemistry, valuable information on the state of the catalyst during the different reaction steps can be obtained. In the previous chapter, operando X-ray absorption spectroscopy (XAS) was used to study the metal-catalyst oxidation state at various applied potentials. XAS can provide accurate oxidation state values, however it is a challenging technique, which requires the use of a synchrotron facility and poses experimental constraints.

Raman spectroscopy is easier to couple with operando electrochemistry, since the Raman signal is not strongly dampened by water, and it does not require particularly advanced instrumentation, allowing more agile experiment planning. This method can provide information about the structure and the functional groups of a catalyst, about the presence of adsorbed molecules and about intermediates and active sites of a chemical reaction. It can be tuned on a specific element by exploiting resonance enhancement effects and, thus, be able to identify species with minority population (Ferraro, 2003).

Recently, operando Raman spectroscopy has been extensively used for the investigation of metal oxide catalysts for water oxidation and CO_2 reduction (Joya, 2015; Deng, 2017; Wang, 2016). An amorphous Co oxide, similar to CoCat, has been investigated at various potentials and for different thicknesses in alkaline electrolyte (Yeo, 2011). However, the spectra shown in this work were probably affected by laser heating damages, which lead to catalyst modifications.

This chapter is focused on the use of operando Raman spectroscopy to investigate amorphous transition-metal catalysts during the OER, CoCat serves as a model for this class of catalysts. The first section contains a brief introduction to Raman spectroscopy. Then, the experimental conditions needed to avoid laser heating artifacts and obtain reliable operando Raman spectra are illustrated. The interpretation of a CoCat Raman spectrum at various potentials, in the catalytic and near-catalytic range, is discussed. The assignment of the various observed bands to molecular groups is facilitated by variations in the deposition procedure and isotopic substitution (labeling of the catalyst material in D_2O or $H_2{}^{18}O$ water). Then, the unexpected decrease of the Raman bands at increasingly positive potentials is investigated. Lastly, a method to calculate Co oxidation state changes from Raman spectra is presented and results are compared with data obtained from XAS. In sections 4.2.2, 7.2.2 and 7.2.3, operando Raman spectroscopy is employed to study, respectively, mass transport limitations and the catalyst behavior at alkaline pH.

3.2 Theory of Raman spectroscopy

The monochromatic light used in Raman spectroscopy is visible light (1.65 to 3.10 eV), the same range as an electronic transition. However, the energy transferred to the sample, through an inelastic scattering process, is in the range of vibrational modes (0.5 to 0.005 eV). Thus, Raman spectroscopy allows the study of molecular vibrations and phonons, similarly to IR spectroscopy, but it can cross transparent materials, like bulk water, facilitating the performance of operando experiments (Siebert, 2007). Operando Raman spectroscopy is an important tool to probe the structural and chemical identity of the catalytic species and its intermediates and to identify surface-adsorbed molecules (Deng, 2017).

When a stream of photons with energy ν_0 and an associated electric field $\vec{E} = \vec{E}_0 \cos(2\pi\nu_0 t)$ hits a material, it can induce a dipole moment $\vec{p}_{ind} = \overline{\overline{\alpha}} \cdot \vec{E}$ depending on its polarisability ($\overline{\overline{\alpha}}(t)$):

$$\overline{\overline{\alpha}}(t) = \overline{\overline{\alpha}}_0 + \sum_j \left(\frac{\partial \overline{\overline{\alpha}}}{\partial Q_j}\right)_0 Q_j \cos(2\pi\nu_j t) \tag{3.1}$$

where the first order term is the polarisability at rest and the second order term includes all the variations in polarisability due to vibrational and rotational modes (j), with frequency (ν_j) and a small shift in the internal coordinates ($Q_j << 1$). Thus, the induced dipole moment is:

$$\vec{p}_{ind} = \vec{E}_0 \left\{ \overline{\overline{\alpha}}_0 \cos(2\pi\nu_0 t) + \frac{1}{2}\sum_j \left[\left(\frac{\partial \overline{\overline{\alpha}}}{\partial Q_j}\right)_0 Q_j \cos[2\pi(\nu_0+\nu_j)t] + \left(\frac{\partial \overline{\overline{\alpha}}}{\partial Q_j}\right)_0 Q_j \cos[2\pi(\nu_0-\nu_j)t] \right] \right\} \tag{3.2}$$

where the first term is referred to as elastic or Rayleigh scattering and the second and third terms refer to inelastic or Raman scattering. The scattered light has frequencies ($\nu_0 - \nu_j$) and ($\nu_0 + \nu_j$), corresponding to Stokes and anti-Stokes scattering, respectively. Since it corresponds to a second order term ($Q_j << 1$), the Raman signal has an intensity approximately 10^7 times lower than the elastically scattered signal. Furthermore, only the vibrations which cause a variation in the polarisability, $\left(\frac{\partial \overline{\overline{\alpha}}}{\partial Q_j}\right)_0 \neq 0$, are Raman active (Siebert, 2007).

More precisely the interaction between photons and phonons is mediated by an electron: the photon causes a transition to a "virtual" electronically excited state, which interacts with a phonon, and then decays in a vibrationally excited state (Stokes) or the opposite (anti-Stokes), see Fig. 3.1. The name "virtual" state means that Raman scattering does not require an electronic energy level at the appropriate energy. However, if ν_0 is close to an allowed electronic transition there is a strong enhancement factor of the Raman signal (up to 10^6 times), which is called Resonance Raman (Ferraro, 2003). Resonance Raman is also partially site-specific, because it enhances vibrations linked to a certain electronic transition. Surface-enhanced Raman spectroscopy is a surface-sensitive technique that exploits the enhancement effect (up to 10^{11} times) of localized surface plasmon resonances and arises when a roughened metal surface (Au, Ag, Cu) is used as a substrate (Joya, 2015; Schlücker, 2014).

The interpretation of Raman peaks is based mostly on comparison with spectroscopic "fingerprints" from known chemical groups and on symmetry considerations (Group Theory). It is also possible to use DFT to calculate the vibrational frequency for certain molecules or chemical groups. However, amorphous materials, like the one treated in this thesis, are more challenging because symmetry considerations do not hold and there is a lack of literature on the topic. In section 7.2.2, we follow the modifications in a Raman spectrum when the level of crystallinity in the material is varied. In section 3.3.3 the Raman spectrum of CoCat is interpreted using isotopic substitution, comparison with reference compounds and modification of the synthesis procedure.

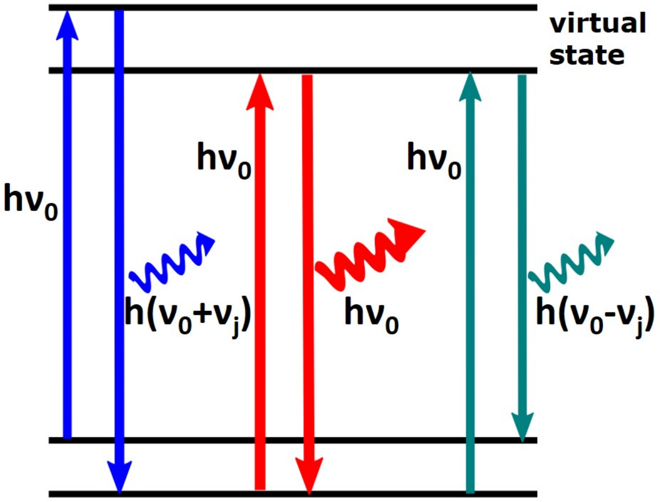

Figure 3.1: Schematic explanation of elastic Rayleigh scattering (red) and inelastic Stokes (green) and anti-Stokes (blue) Raman scattering. ν_0 and ν_j are the frequencies of the incident photons and the involved vibrational mode, respectively. Rayleigh scattering is approximately 10^7 times more intense than Raman scattering.

3.3 Results

3.3.1 Setting up the experiment

Electrochemistry cell

The implementation of an operando Raman spectroscopy experiment coupled with electrochemistry involved the design of an electrochemical cell. The Raman spectrometer used is equipped with a confocal microscope, to which is associated a water immersion objective. A water immersion objective eliminates air from the light path, drastically reducing the mismatch of the refractive indexes and resulting in improvement of detection sensitivity (Zeng, 2016). Furthermore, it allows the use of a thick electrolyte layer, which favors proper mass transport and makes the electrochemistry experiment more reliable.

The design of the cell envisages the presence of three electrodes and a fast system for sample exchange (a picture in Fig. 3.2). The Raman light hits the sample from the top and it is collected in backscattering geometry. The working electrode is connected via a Pt wire that is pressed on it and it is surrounded by a Pt ring, working as counter electrode. The focus on the sample had a line shape to reduce heating at the laser spot.

Choice of the working electrode substrate

The choice of the substrate for the working electrode required some investigation. A substrate with SERS effect would be desirable, but both Ag and Cu are not suitable because they oxidize at low potentials making electrodeposition of CoCat impossible. Thus, an Au substrate was chosen and roughened following an electrochemical protocol in KCl electrolyte. Raman spectra for the roughened Au electrode (after oxidation at a positive potential) and for a CoCat film

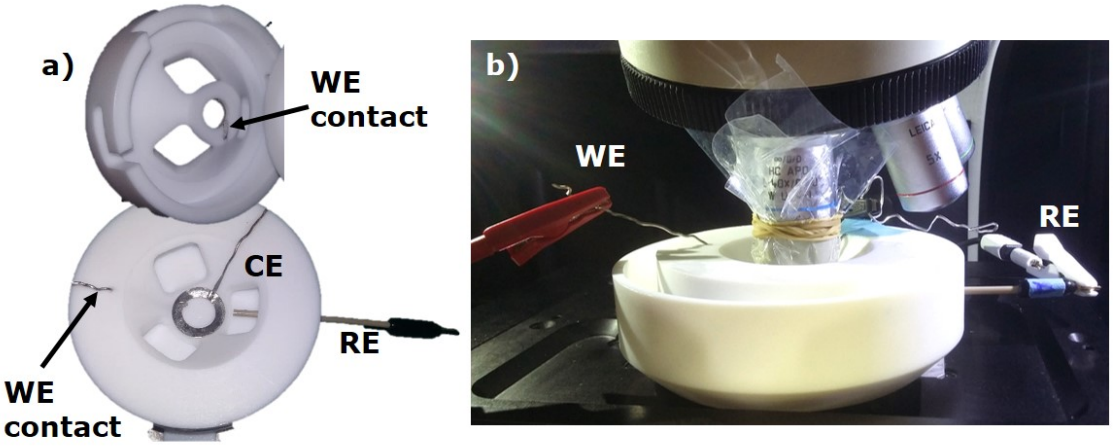

Figure 3.2: Picture of the home-built Raman cell. (a) The Pt ring counter electrode (CE), the reference electrode (RE) and the Pt wire which provides contact to the working electrode (WE) are visible, the WE itself is not mounted. (b) Raman cell during operation, in case of corrosive solutions a Teflon film is wrapped around the immersion objective to protect it, a drop of water between the Teflon film and the objective prevents abrupt changes in the refractive index.

deposited on Au are shown in Fig. 3.3. The position of the main band, corresponding to metal-oxo vibrations, is very similar for the two oxides and varies with applied potential. It is impossible to distinguish changes in the spectra due to CoCat operation from those due to film dissolution, which uncovers the underlying Au oxide. Thus, I decided not to use the Au substrate, meaning not to have any SERS effect.

The second substrate that I tested was glassy carbon, which performed well in neutral electrolytes. However, when the CoCat film deposited on glassy carbon was exposed to 1 M KOH in conjunction with Raman light, the spectrum changed with exposure time (Fig. 3.4a). The change in the spectrum appears to be dependent on the Raman light intensity and to lead to the appearance of the typical peaks reported for Co_3O_4 (Fig. 3.4b). Transformation of CoO to Co_3O_4 driven by Raman light has been previously reported by Rivas-Murias et al. (Rivas-Murias, 2017). Thus, the observed change can be attributed to heating damages caused by the laser light, due to the strong absorption bands of carbon in the region 1200-1700 cm^{-1}, which lead to an overheating in the sample. Previous spectra of amorphous Co oxide (Yeo, 2011), obtained operando, were probably affected by radiation damage and by overlap with vibration bands from the underlying Au substrate.

Eventually, Pt sheets were chosen, since the metallic substrate, with its high thermal conductivity, minimizes heating damages related to the laser beam. Furthermore, pure Pt does not present any Raman peak in the region of interest, independently from the applied potential (Fig. 3.5, compare with Fig. 3.9a).

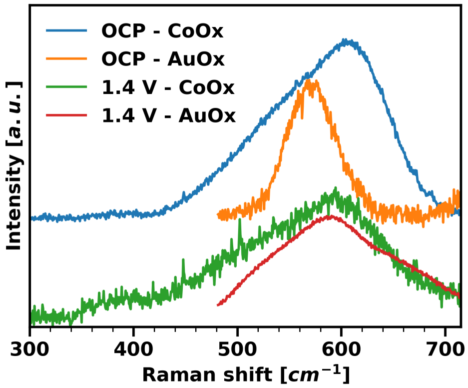

Figure 3.3: Raman spectra for CoCat deposited on a roughened Au electrode and for the bare Au electrode (after oxidation at a positive potential) in 0.1 M KPi solution. Spectra were collected both in open circuit potential conditions and with 1.4 V_{NHE} applied potential.

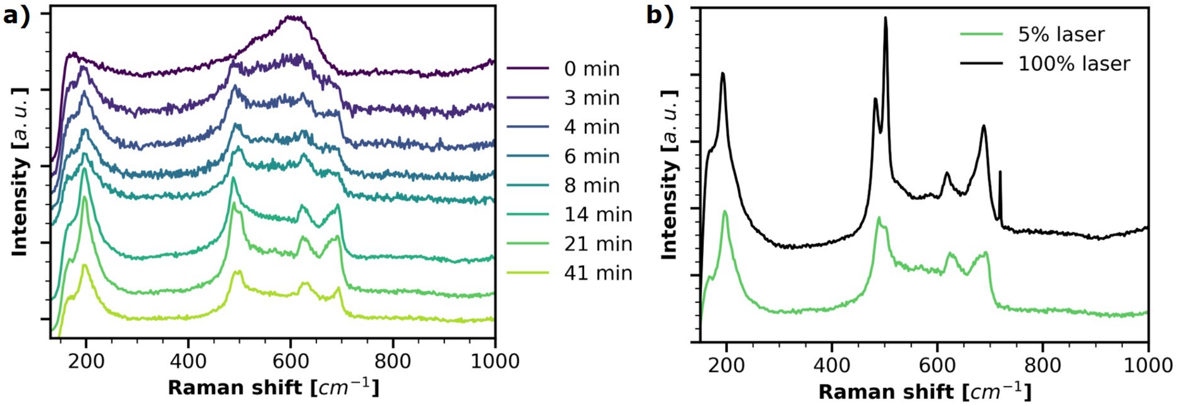

Figure 3.4: Raman spectra for CoCat deposited on glassy carbon and exposed to 1 M KOH (pH 13.8). (a) Changes in Raman spectrum and their dependence on exposure time to 1 M KOH and to Raman excitation laser combined. The spectrum at time 0 was recorded in 0.1 M KPi, the first 4 spectra in 1 M KOH had a collection time of 40 s per spectrum, the following spectra had a collection time of 3 min. (b) Changes in Raman spectrum and their dependence on laser power. An excitation laser wavelength of 633 nm was used.

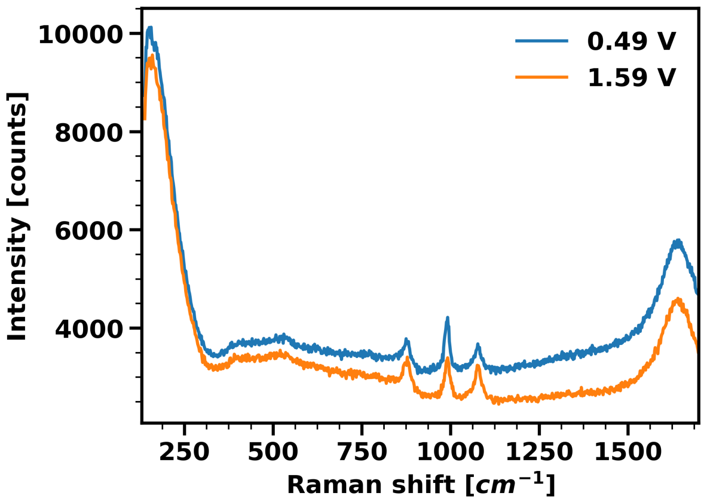

Figure 3.5: Raman spectra for a Pt substrate in 0.1 M KPi at two different applied potentials.

Wavelength dependence

The laser wavelength in a Raman experiment is usually chosen to correspond to an optical absorption band, to obtain enhancement effects (see Resonance Raman in section 3.2). CoCat has a very broad visible absorption band with an absorption coefficient that increases equally in the 450 to 800 nm spectral range, when an increasingly positive electric potential is applied (see Fig. 2.12). The presence of a resonance enhancement effect was investigated for CoCat by measuring the Raman spectrum for excitation with three different laser wavelengths (473 nm, 532 nm, and 633 nm). After rescaling the Raman signal by the laser power, no major differences were found in the intensity and shape of the three spectra (Fig. 3.6a). Given the very broad absorption bands of CoCat, it is conceivable that all spectral bands benefit almost equally from a resonance enhancement effect. Even when an electric potential is applied to the catalyst, no wavelength dependence is introduced (Fig. 3.6). For subsequent investigations, a 473 nm laser wavelength was used.

3.3.2 Searching for the active site

An analysis of the catalyst surface with the Raman microscope revealed that oxygen bubbles do not appear homogeneously but are always formed at certain "hot spots" (see section 5.2.1). A hypothesis would be that close to these "hot spots" there is a higher concentration of active sites, unfortunately, attempts to characterize the active sites with Raman spectroscopy were not successful.

Figure 3.7 reports the Raman spectra at different distances from a "hotspot", identified by the presence of a bubble, the spectra were collected while applying a catalytic potential. The only recognizable difference between the spectra is in the signal intensity, which strongly decreases in proximity of the bubble due to scattering effects (spectra in Fig. 3.7a are not rescaled).

In figure 3.7b an additional peak is present at 1057 cm^{-1}, in the spectrum collected at the bubble site. This peak was observed every time several bubbles were present in solution and also when the objective was strongly out of focus (Fig. 3.8). Therefore, it was classified as a

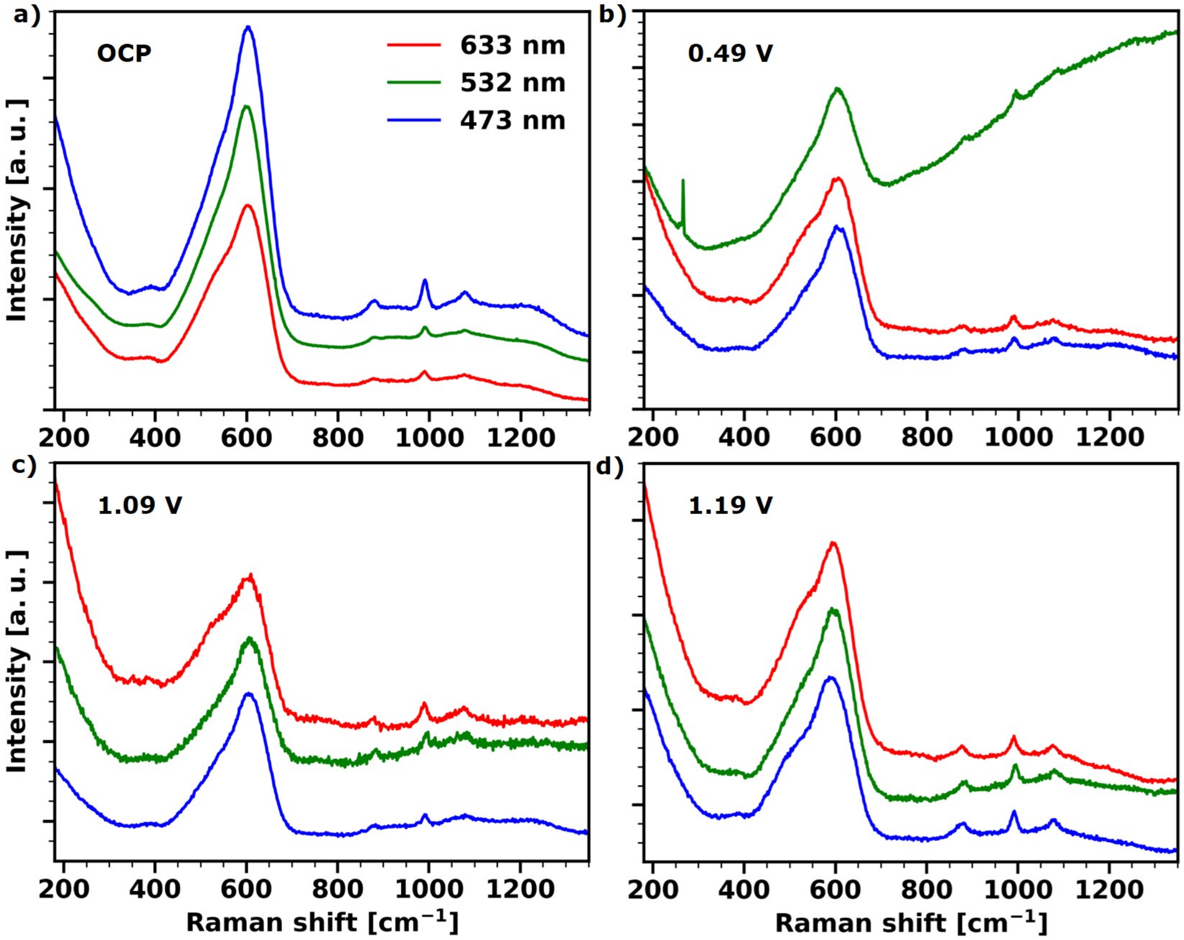

Figure 3.6: Raman spectra for CoCat, 300 mC cm^{-2} thick, deposited on Pt, in 0.1 M KPi. Spectra collected at open circuit potential and at 3 different applied potentials, with laser excitation at 473, 532 and 633 nm. In panel (a), the spectra were rescaled to compensate for the different laser powers. The rescaling factor was based on the number of counts obtained per each laser from a reference Si sample. In the other panels, spectra were rescaled and shifted for clarity purposes. Raman spectra acquisition was initiated after at least 3 min exposure at the indicated potential. Each spectrum was acquired for 3 min, in panel (a) the average of two different acquisition sites is shown.

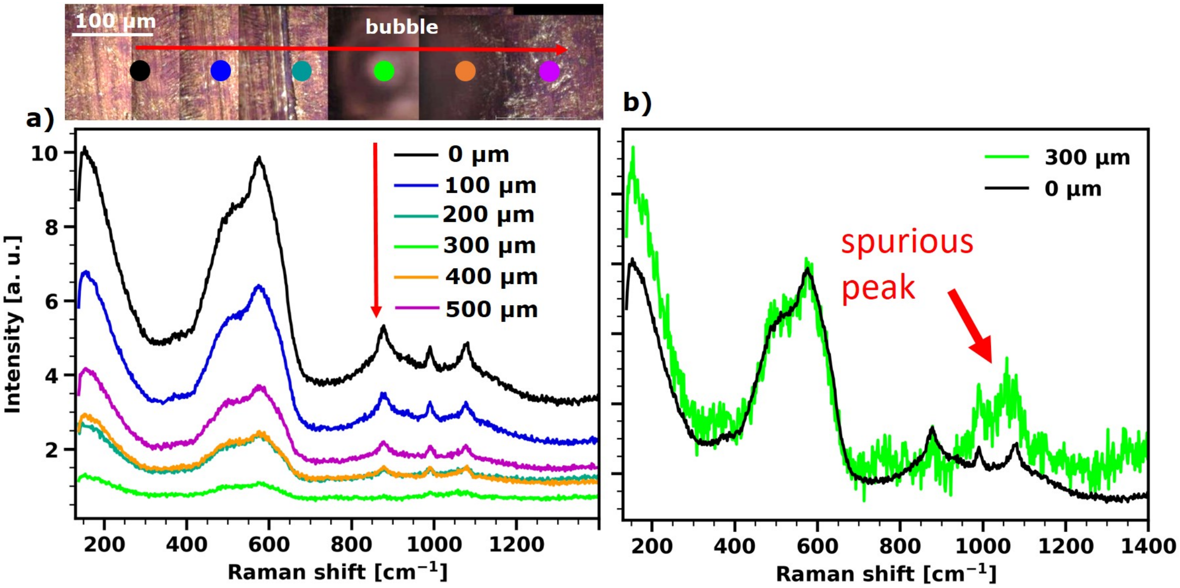

Figure 3.7: Raman spectra measured on consecutive areas, including close and far away from a bubble, for CoCat, 40 mC cm^{-2} thick, deposited on Pt, in 0.1 M KPi. Spectra were collected at 1.4 V_{NHE} with a 473 nm laser. (a) Raman spectra collected at different positions on the x-axis. Spectra are neither rescaled nor shifted in respect to each other. In the upper panel, overlapped microscope images of the catalyst surface are presented, in the center a bubble is visible. Every colored point represents a position at which a Raman spectrum was collected. The red arrow indicates the scan direction. (c) Rescaled spectra from (a), a spurious signal is visible at 1057 cm^{-1} at the bubble spot (see Fig. 3.8 for the peak identification), no other differences are visible between the spectra.

spurious peak, due to Raman light scattering. To collect proper Raman spectra, it is important to remove bubbles from the objective every time this spurious signal appears.

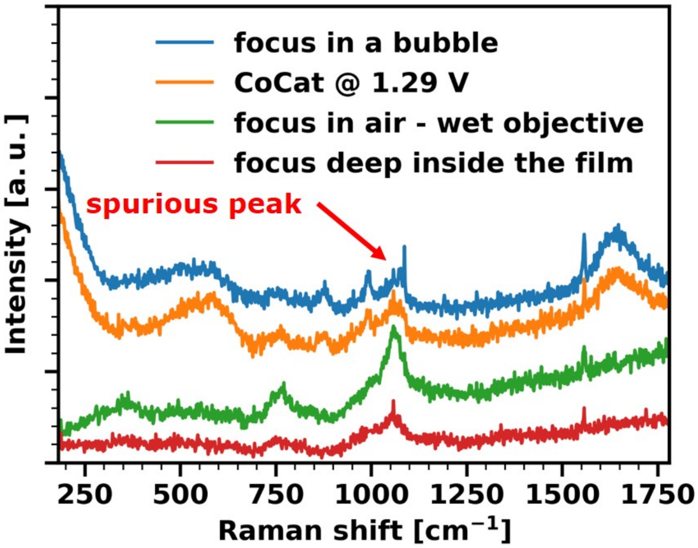

Figure 3.8: Raman spectra collected in different out of focus geometries, on an CoCat film under operating conditions and in correspondence of a bubble. The Raman peak visible at 1057 cm^{-1} in all the spectra is identified as a spurious signal due to light scattering.

3.3.3 Raman spectra of amorphous CoOx

A typical Raman spectrum of a CoCat film is composed of the sum of the electrolyte spectrum and the spectrum of a dry CoCat film (Fig. 3.9a), which is characterized by very broad bands. The presence of broad bands is typical for amorphous compounds, because the lack of order and the presence of defects broaden the distribution of bond strengths and angles, thus modulating the vibrational frequencies (Kwon, 2018). These broad bands are usually simulated using Gaussian functions, which represent the sum of Lorentzian functions with a broad distribution of vibrational frequencies.

In the spectral range shown in Fig. 3.9, the electrolyte (0.1 M KPi in water) exhibits a water band at 1641 cm^{-1} (H-O-H bending, Walrafen, 1964) and three comparably sharp bands stemming from the phosphate species in the aqueous solution (dotted lines in Fig. 3.9): 877 and 1077 cm^{-1} from $H_2PO_4^-$ and 990 cm^{-1} from HPO_4^{2-} (Heighton, 2012). During operando measurements, these bands can provide insight into the local pH close to the electrode surface (see section 4.2.1).

The spectra of the dry CoCat have three very broad bands (924, 1087 and 1225 cm^{-1}) in the same region as the vibration of phosphate species in solution. X-ray absorption measurements have previously proposed that phosphate can bind to terminal sites at the margins of Co oxide fragments (Villalobos, 2019). A possible hypothesis is that the 877 and 1077 cm^{-1} solution-peaks from $H_2PO_4^-$ (indicated by dotted red lines in Fig. 3.9) are broadened and shifted to 924 and 1087 cm^{-1} (solid red lines) when phosphate is trapped in between the Co-oxo clusters. A broadening and shifting in the same direction is observed when the phosphate concentration in solution is

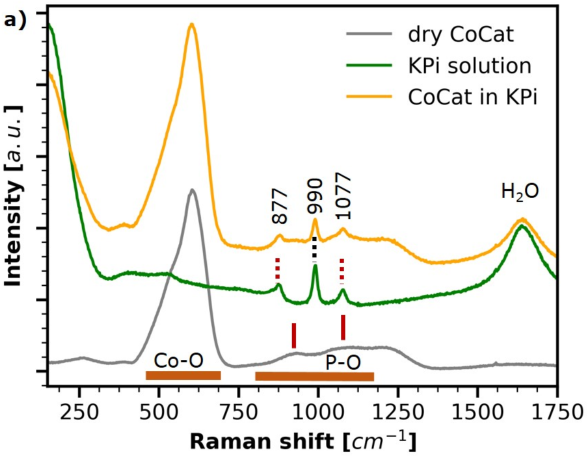

Figure 3.9: Raman spectra for CoCat, 300 mC cm^{-2} thick, deposited on Pt. (a) Dried CoCat sample, 0.1M KPi solution at pH 7 and CoCat in solution. (b) Dried CoCat sample deposited either in 0.1M KPi at pH 7 or in 0.1M KBi (potassium borate) at pH 9.2 and CoCat deposited in 0.1M KPi and then exposed to 0.1M KBi. Short vertical lines are used to indicate the peaks position, solid lines correspond to CoCat peaks, dotted lines to solution peaks, green color to Co-O vibrations, red color to $H_2PO_4^-$ vibrations and black color to HPO_4^{2-} vibrations.

increased (Preston, 1979). This change can be explained with the formation of phosphate dimers or polymers which share an oxygen atom, since phosphate polymerization is a reaction close to equilibrium (Rashchi, 2000). The polyphosphates, which likely surround the Co-oxo clusters, can form a hydrogen-bond network, which favors proton transport inside the catalyst material (Abe, 1994; Preston, 1979; Eom, 2019). On the contrary, the 990 cm^{-1} solution-peak (dotted black line) has no visible correspondence in the CoCat spectrum, suggesting that phosphate is present inside the CoCat film only in the $H_2PO_4^-$ form.

To test the assignment of these bands to phosphate, I changed the deposition solution from KPi to KBi buffer at pH 9.2. A more evident shoulder for the main CoOx peak and a large band at 1187 cm^{-1} with a left shoulder appeared in the Raman spectra (Fig. 3.9b). At the same time the 924 and 1087 cm^{-1} bands disappear, supporting their assignment to $H_2PO_4^-$. The 1187 cm^{-1} band is suggested to be the two-phonon scattering corresponding to the double frequency of the 599 cm^{-1} one-phonon scattering. Similarly, in KPi deposited CoCat, the 1225 cm^{-1} would be the two-phonon scattering corresponding to the 616 cm^{-1} one-phonon scattering, all Co-O vibrations are indicated by solid green lines in Fig. 3.9. A two-phonon scattering peak has been previously reported for CoO at 1060 cm^{-1} (Li, 2016).

When the sample deposited in KPi is exposed to KBi solution for 2.5 h, even while applying a potential, no change appears in the CoCat spectrum (Fig. 3.10). This result confirms that the exchange of phosphate in CoCat is very slow, as previously suggested (Ullman, 2016).

In the region typical for M-O vibrations, the CoCat has a peak at 615 cm^{-1} with a shoulder at 544 cm^{-1}, in agreement with spectra reported in literature (Yeo, 2011; Kwon, 2018). These two bands have been assigned respectively to symmetric Co-O stretching (A_{1g}, 595 cm^{-1}) and bridging Co-O-Co vibrations (E_g, 485 cm^{-1}) in a CoO_6 octahedra in the $LiCoO_2$ structure (Kwon, 2018; Rougier, 1997) and are present at similar frequencies in CoO(OH) (Koza, 2013). Therefore, in CoCat the broad main Co-O peak is likely dominated by Co-O stretching vibrations from both

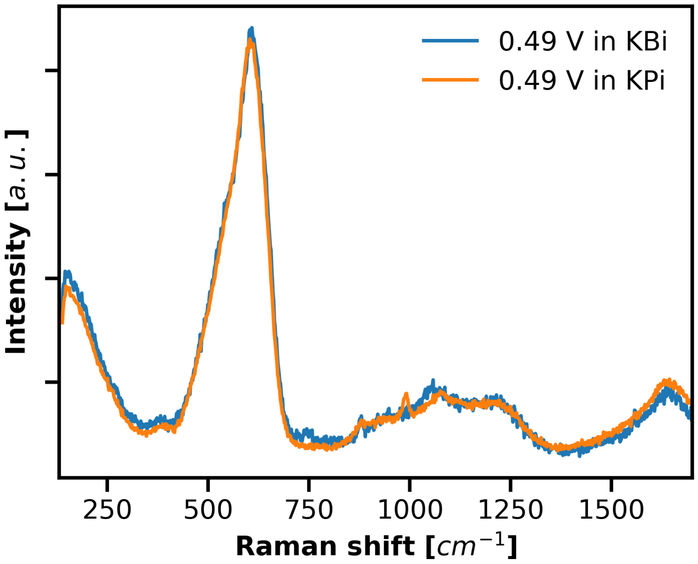

Figure 3.10: Raman spectra for CoCat, 300 mC cm^{-2} thick, deposited on Pt in 0.1 M KPi at pH 7 and operated either in 0.1 M KPi pH 7 or in 0.1 M KBi pH 9.2. Spectra were collected at 0.49 V_{NHE} after 3 min exposure to the potential. Peaks corresponding to CoCat-internal phosphate have similar relative intensities in the two spectra.

bridging and terminal oxygen atoms, whereas the shoulder at lower wavenumber is more closely related to Co-O-Co vibrations associated with µ-oxo bridging between Co ions. Consequently, the amplitude ratio could shift in favor of the long-wavelength shoulder upon increased µ-oxo bridging. The shoulder is more evident when CoCat is deposited in KBi (Fig. 3.9b), coherently with the presence of more Co-O-Co bond in the more ordered structure (Kwon, 2018).

The IR spectrum of CoCat was collected using an attenuated total reflection (ATR) mode and presents two main broad bands (Fig. 3.11). Each IR band corresponds to a Raman band: a Co-O band in the 450–500 cm^{-1} region and a P-O band in the 800–1200 cm^{-1} region. Unlike the Raman bands, these bands strongly depend on the thickness of the CoCat sample and are blue-shifted and broadened in thicker samples.

In summary, the study of the dry CoCat Raman spectrum revealed the presence of two Co-O vibrations peaks, with a corresponding two-phonon peak, and of two phosphate peaks. The presence of the corresponding bands in the IR spectrum suggests that these vibrations are both Raman and IR active. The broad main Co-O peak likely is dominated by Co-O stretching vibrations from both bridging and terminal oxygen atoms, whereas the shoulder at a lower wavenumber is more closely related to Co-O-Co vibrations associated with µ-oxo bridging between Co ions. Consequently, the amplitude ratio changes in favor of the long-wavelength shoulder upon increased µ-oxo bridging, as is observed, here, for a sample electrodeposited in KBi electrolyte. The phosphate bands can be assigned to phosphate trapped inside the material, mainly in the form of highly concentrated $H_2PO_4^-$ surrounding the Co-oxo clusters. At these concentrations, phosphate starts forming dimers or polymers constituting a hydrogen-bond network, which can be functional for proton transport (Abe, 1994; Preston, 1979; Eom, 2019).

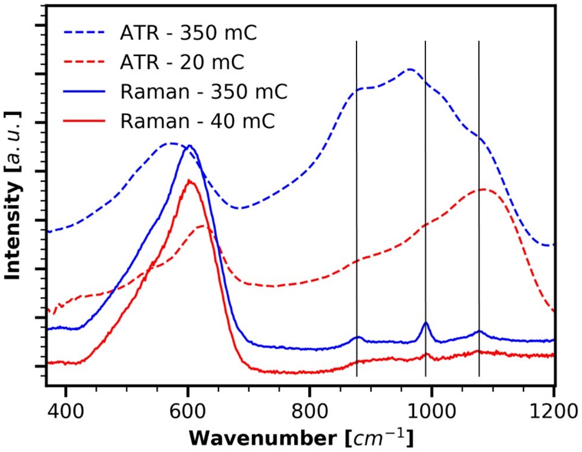

Figure 3.11: Raman (full lines) and IR-ATR (dotted lines) spectra for CoCat deposited on Pt, in 0.1 M KPi pH 7. The samples were either thin (20 or 40 mC cm^{-2}) or thick (350 mC cm^{-2}). The Raman spectra were acquired for CoCat immersed in electrolyte, while he IR-ATR specra were acquired in vacuum after sample operation.

3.3.4 Spectral changes with applied potential

The identification of catalytic intermediates in CoCat requires the use of operando Raman spectroscopy. The modifications of the Raman spectrum driven by the application of an electric potential were investigated. The potential was increased in small steps ("potential stair" protocol) and the Raman spectrum was measured at each potential after reaching a stable state (Fig. 3.12a and for thinner films Fig. 3.13). Peak positions and amplitudes are listed in Tab. 3.1, an example of the simulation in Fig. 3.15.

The above-mentioned modifications in the Raman spectrum are completely reversible (Fig. 3.12b) and consist in a shift to lower energies of the main Co-O peak and its shoulder, with the shoulder becoming more prominent and in the gradual disappearance of the 1225 cm^{-1} band (Fig. 3.12c). The relative increase in the shoulder intensity is likely due to the formation of additional μ-oxo bridges at higher potentials. Since the main 616 cm^{-1} band decreases with potential, the corresponding two-phonon process (at 1225 cm^{-1}), which involves a three-particle interaction, is expected to decrease even faster, as it is observed. The 924 cm^{-1} and 1087 cm^{-1} bands do not depend significantly on potential, confirming the assignment to $H_2PO_4^-$ vibrations of phosphate trapped in between the Co-oxo clusters.

At high potentials, no new bands appear in the 900 - 1200 cm^{-1} region. A series of O-O peaks were reported in this region when positive potentials were applied in alkaline electrolyte. For example, peaks from μ-OO peroxide in Co_3O_4 (Wang, 2016) and from NiO_x superoxide (Diaz-Morales, 2016) and peroxide (Smith, 2016), even though the Ni bands are also compatible with a two-phonons Raman band. The absence of such peaks in the spectra recorded for CoCat at neutral pH suggests that special oxygen species, e.g. terminal oxides (Co=O) or bound peroxides, are not long-lived intermediates in the OER reaction that accumulate at a detectable level. The absence of peroxide species is consistent with the mechanism proposed in chapter 6, where O-O bond formation is rate-limiting and thus it is not observable in a stable state.

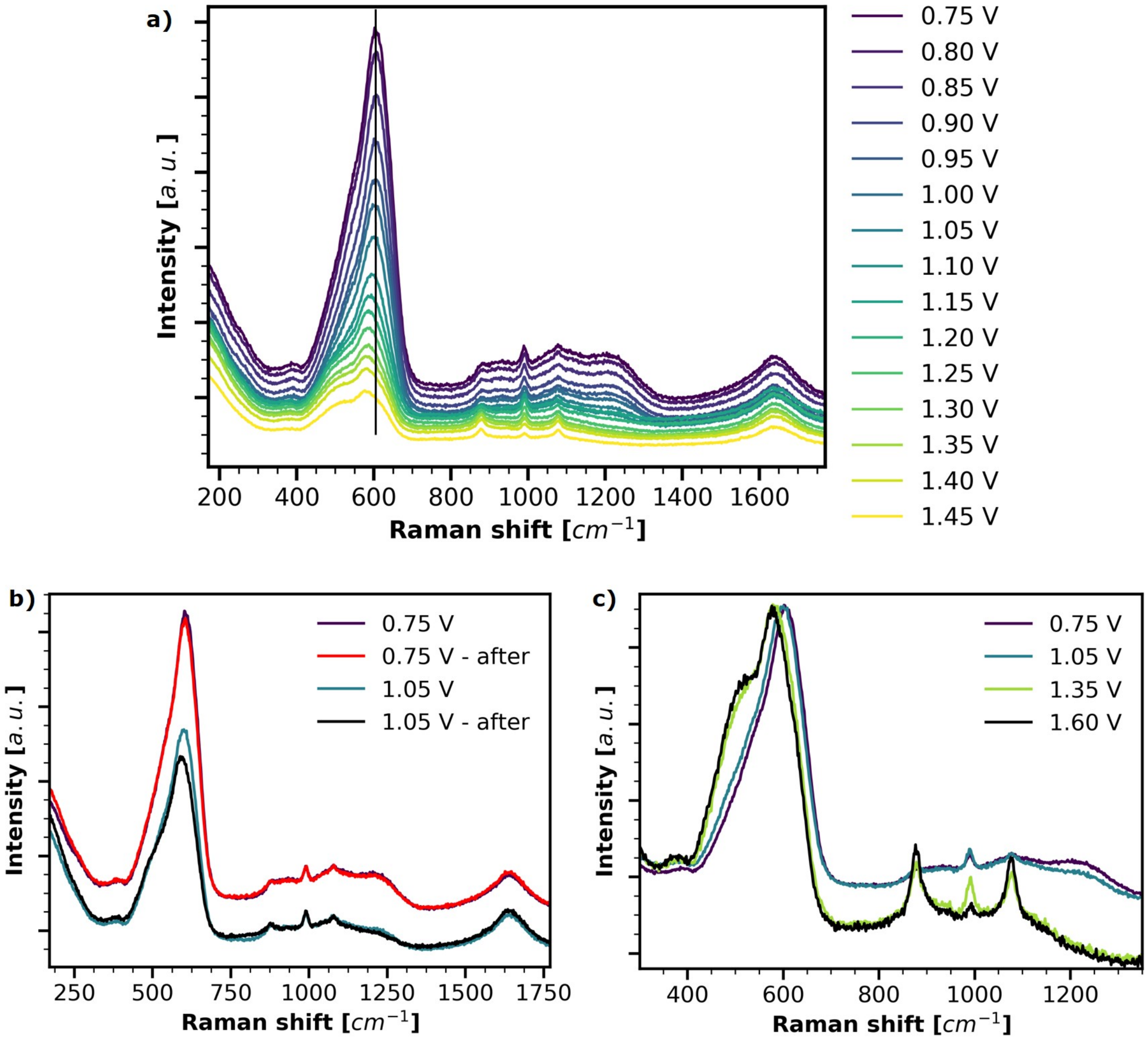

Figure 3.12: Raman spectra for CoCat, 40 mC cm^{-2} thick, deposited on Pt, in 0.1 M KPi. Spectra were collected at various potentials with laser excitation at 473 nm. (a) Raman spectra during a potential stair experiment. Some of the spectra were rescaled for clarity purposes, "raw" spectra without background subtraction and without rescaling factors are shown in Fig. 3.17. (b) Raman spectra collected at selected potentials during the “potential stair” experiment and directly after it, when the potential was lowered again (spectra denoted by “after”), to control the reversibility of the observed changes. (c) Selected spectra were rescaled to enhance differences in shape and position.

Table 3.1: Amplitudes and positions of the major Raman peaks (in counts and cm^{-1}, respectively) for CoCat operated at different potentials.[a, b, c, d, e]

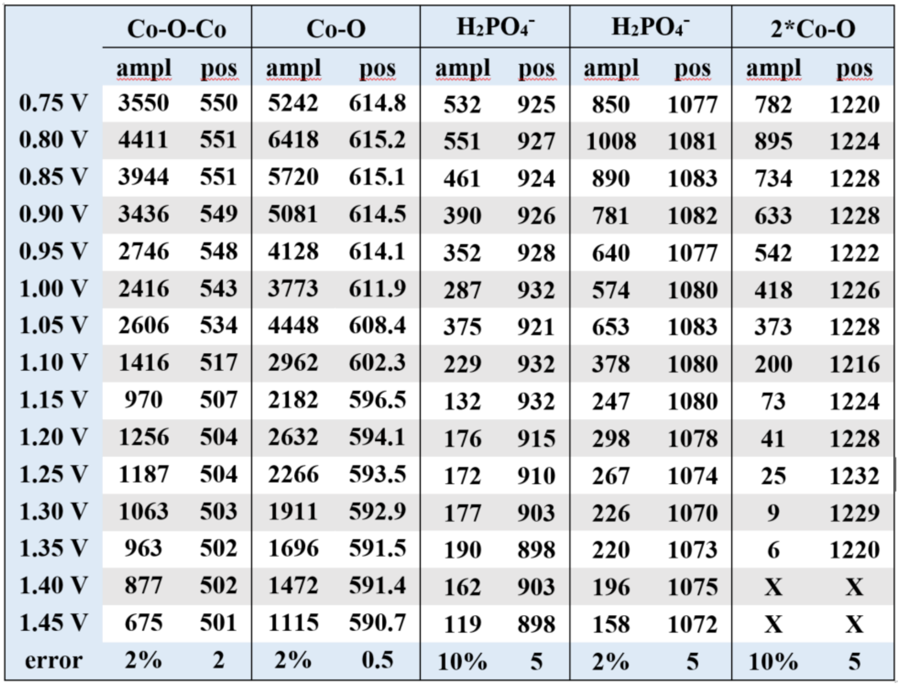

	Co-O-Co		Co-O		$H_2PO_4^-$		$H_2PO_4^-$		2*Co-O	
	ampl	pos	ampl	pos	ampl	pos	ampl	pos	ampl	pos
0.75 V	3550	550	5242	614.8	532	925	850	1077	782	1220
0.80 V	4411	551	6418	615.2	551	927	1008	1081	895	1224
0.85 V	3944	551	5720	615.1	461	924	890	1083	734	1228
0.90 V	3436	549	5081	614.5	390	926	781	1082	633	1228
0.95 V	2746	548	4128	614.1	352	928	640	1077	542	1222
1.00 V	2416	543	3773	611.9	287	932	574	1080	418	1226
1.05 V	2606	534	4448	608.4	375	921	653	1083	373	1228
1.10 V	1416	517	2962	602.3	229	932	378	1080	200	1216
1.15 V	970	507	2182	596.5	132	932	247	1080	73	1224
1.20 V	1256	504	2632	594.1	176	915	298	1078	41	1228
1.25 V	1187	504	2266	593.5	172	910	267	1074	25	1232
1.30 V	1063	503	1911	592.9	177	903	226	1070	9	1229
1.35 V	963	502	1696	591.5	190	898	220	1073	6	1220
1.40 V	877	502	1472	591.4	162	903	196	1075	X	X
1.45 V	675	501	1115	590.7	119	898	158	1072	X	X
error	2%	2	2%	0.5	10%	5	2%	5	10%	5

[a] Each peak was simulated with a Gaussian function.
[b] In the simulation four solution peaks were included at fixed positions.
[c] Typical errors (confidence intervals) are reported in the last row (in percent of the peak-amplitude values and in cm^{-1} for the peak positions).
[d] X indicates peaks with near-zero amplitude, which were not included in the simulation.
[e] All simulation parameters are shown in Appendix Tab. 9.1 and an example of the simulation in Fig. 3.15.

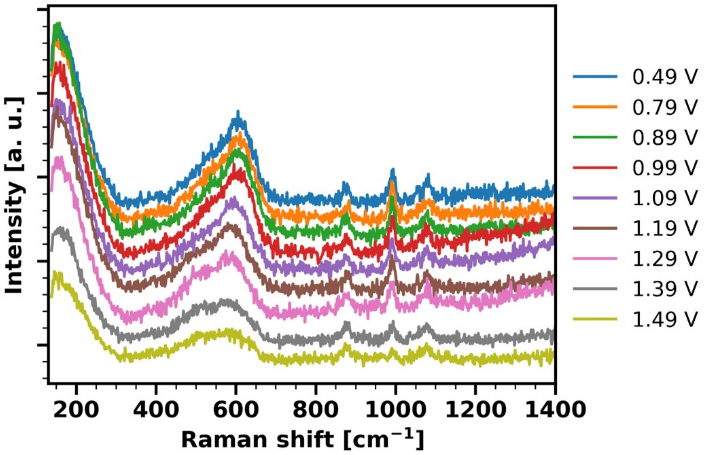

Figure 3.13: Raman spectra for CoCat, 10 mC cm^{-2} thick, deposited on Pt, in 0.1 M KPi, spectra collected at various potential. Raman spectra acquisition was initiated after 3 min exposure at the indicated potential. Each spectra was acquired in 1 min. Spectra are not rescaled but an offset is added for clarity purposes, spectra without offset addition in Fig. 3.18a.

The behavior of the Co-O Raman peaks following application of potential is in line with the proposed peak assignment and excludes the formation of a major fraction of a long-lived peroxide intermediate. The change in signal intensity and the red-shift of the two main Co-O peaks with potential are further investigated in sections 3.3.6 and 3.3.7, while section 3.3.5 is dedicated to isotopic substitution.

3.3.5 H/D and $^{16}O/^{18}O$ isotope effect

Isotopic substitution is often used in vibrational spectroscopy for band assignment and, when coupled with applied potential, can provide insights into the reaction mechanism. In this section, the modification of the Raman spectrum caused by deuterated water ($^{2}H_2{}^{16}O$ isotope) and normalized water ($^{1}H_2{}^{18}O$) electrolytes are investigated using the same potential stair protocol used in the previous section.

In deuterated water, shifts for the water and phosphate peaks are visible (Fig. 3.16a,c), these peaks move to 1207, 862, 988 and 1085 cm^{-1}, respectively and so are the peaks in the 3000-3500 cm^{-1} region (Fig. 3.14). The shift of the Co-O is comparatively minor (Fig. 3.16e). Bands positions were determined by simulation with Gaussian functions and are presented in table 3.2, the simulation parameters are shown in Appendix Tab. 9.1 and an example of the simulation in Fig. 3.15.

The first two peaks, corresponding to Co-O vibrations, are both red-shifted in D_2O by ca. 5 cm^{-1} and the shift is less pronounced at high potentials. The isotope shift suggests the catalyst film (i) harbors a significant number of protonated oxygen, both as bridging (Co-OH-Co) and terminal (Co-OH and Co-OH_2) ligands at low potentials and (ii) deprotonation happens when the potential is increased. Deprotonation of bridging or terminal oxygen atoms accompanies Co oxidation (proton-coupled electron transfer) and avoids charge buildup (Weinberg, 2012; Mattioli, 2011; Dau, 2010). The deprotonation of µ-oxo bridges at high potentials has been

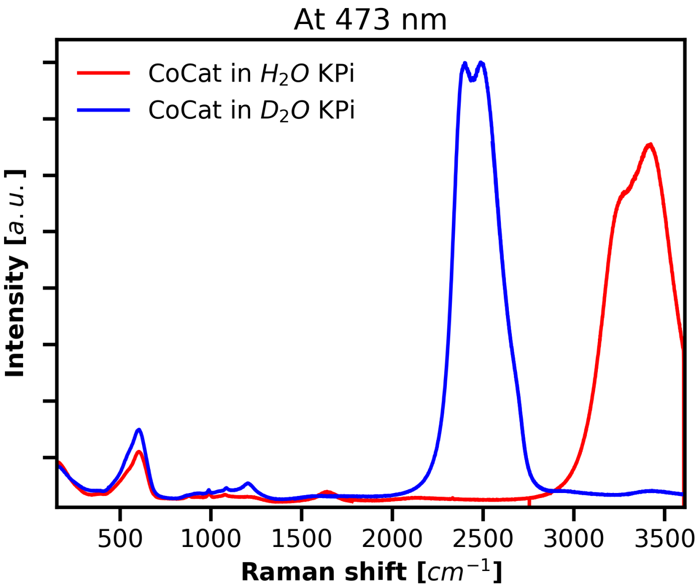

Figure 3.14: Raman spectra for CoCat, 40 mC cm^{-2} thick, deposited on Pt, in 0.1 M KPi made by water (red) or deuterated water (blue).

proposed before, based on XAS data (Risch, 2015), but we provide the first direct experimental evidence here.

The other vibrational bands do not show isotopic dependence, in the limit of our sensitivity, although this cannot be excluded for the 1225 cm^{-1} band because of the overlaying deuterated water bending vibration, which prevents a good quality simulation of this band.

For measurements in ^{18}O water, the sample was conditioned by exposure of the CoCat to ^{18}O water electrolyte for 30 min at OCP followed by a slow CV (0.8 – 1.3 V_{NHE} with a scan rate of 1 mV s^{-1}). This procedure has been shown to promote the exchange of all ^{16}O atoms that are directly involved in O-O bond formation, resulting in release of only $^{18}O_2$ (Ullman, 2016). Spectra obtained in ^{18}O electrolyte show no major differences from those obtained in ^{16}O electrolyte (Fig. 3.16b,d). The simulation of the bands' positions reveals that the main Co-O peak is red-shifted by ca. 2-3 cm^{-1} in ^{18}O electrolyte (Fig. 3.16f and Tab. 3.2), while the shoulder corresponding to Co-O-Co vibrations is not shifted.

For an isolated Co-O bond, at this wavelength, an ^{18}O isotopic shift of around 7 cm^{-1} is expected and experimental observation of Ir=O revealed a 59 cm^{-1} isotopic shift (Pavlovic, 2017). The small shift observed suggests that the majority of oxygen atoms is not exchangeable (no ^{18}O incorporation), not even via catalyst operation at catalytic potentials. The CoCat has been proposed to consist of comparably small fragments of a layered oxide (less than 20 Co ions) with internal oxygen atoms bridging between three Co ions (μ_3-O) and peripheral oxygen atoms found in the form of μ_2-O bridges and terminally coordinated oxygen atoms (Co-OH$_2$, Co-OH, Co=O; Risch, 2009; Kanan, 2010; Du, 2012). The minority fraction of exchangeable Co-bound O most likely can be found as terminally coordinated oxygen at the periphery of the oxide sheets, as the exchange of bridging oxygen atoms is expected to be especially slow. Previously, participation of bridging oxygen atoms, denoted as "lattice oxygen", to OER has been reported, e.g., for perovskites with high covalency of the metal-oxygen bonds (Grimaud,

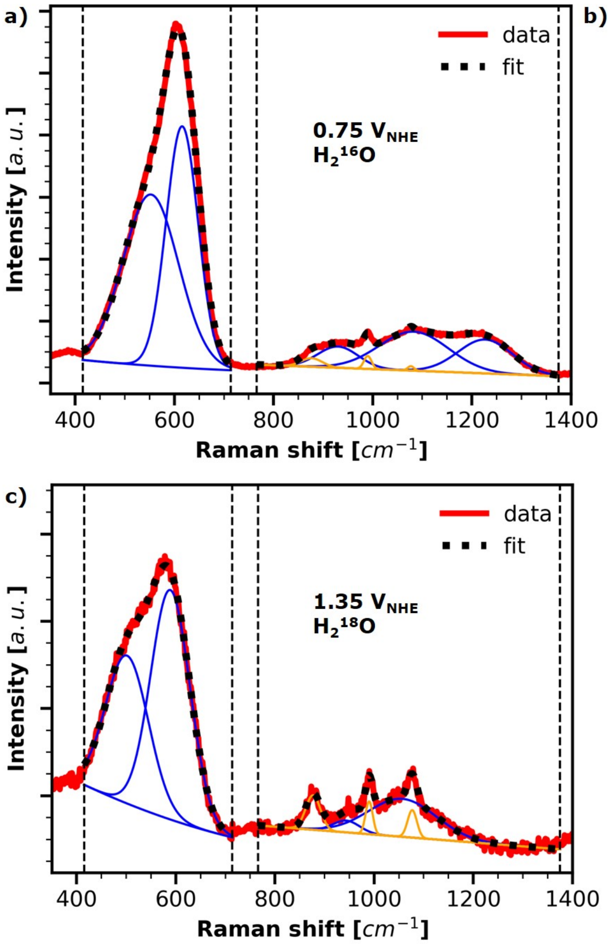

Figure 3.15: Simulation of the operando Raman spectra of CoCat, examples from different potentials and in different electrolytes are shown. The raw data (red line) are simulated using a series of Gaussian functions. The fit is shown as a dotted black line, the baseline and the Gaussian functions referring to CoCat peaks as blue lines and the Gaussian functions referring to solution peaks as orange lines. The fit was performed separately in two regions 415 to 714 cm^{-1} and 766 to 1375 cm^{-1} (indicated by vertical dashed lines). All fit parameters and details on the fit procedure are reported in Appendix Tab. 9.1.

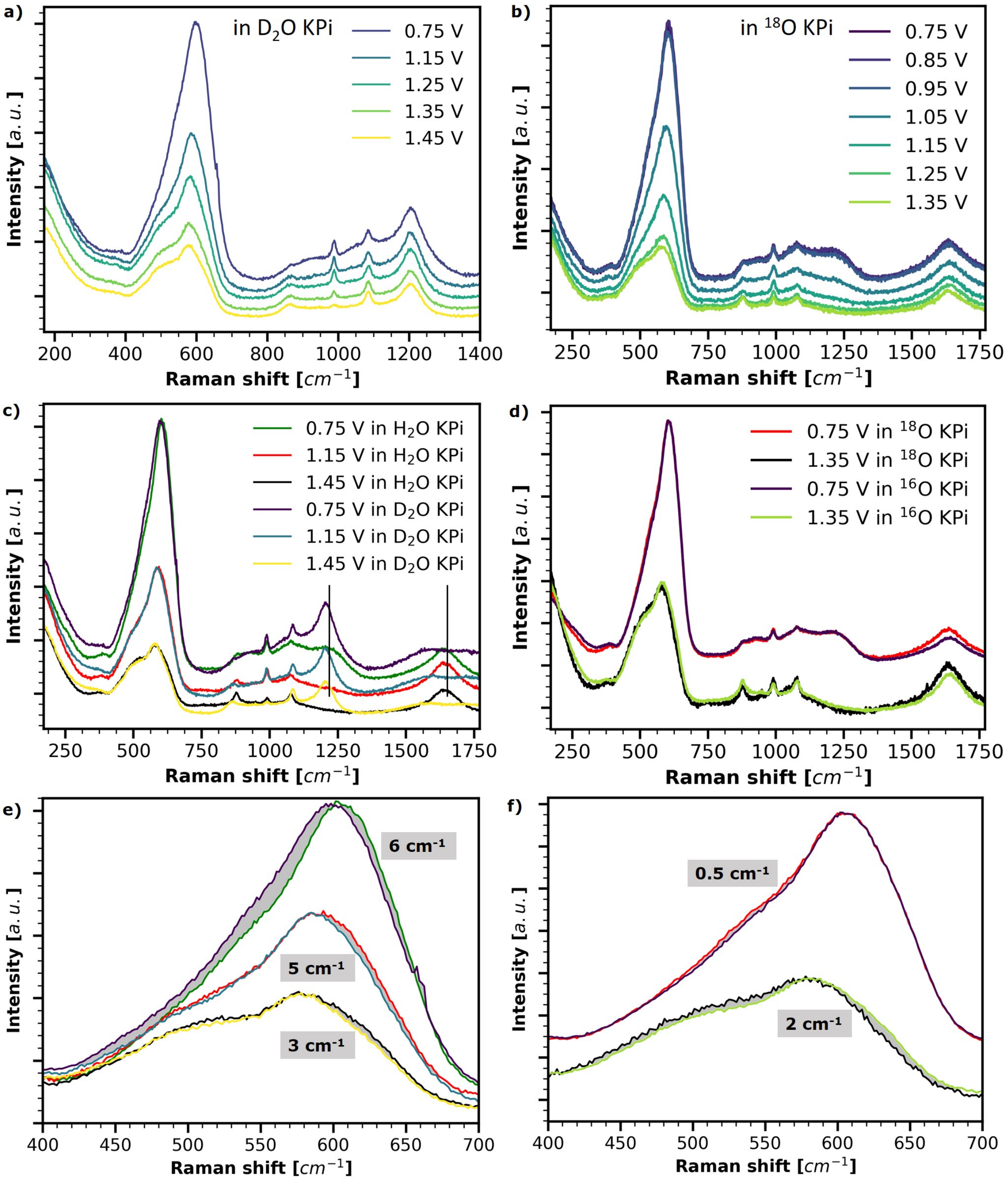

Figure 3.16: Raman spectra for CoCat, 40 mC cm^{-2} thick, deposited on Pt, in 0.1 M KPi made from deuterated (with the ^{2}H isotope) or normalized (with the ^{18}O isotope) water. Spectra were collected during operation at the indicated potentials with laser excitation at 473 nm. Raman spectra acquisition was initiated after 2-3 min exposure at the indicated potential. Peaks position are reported in Tab. 3.2. (a) Spectra in deuterated water and (c) spectra in deuterated water and in water rescaled for comparison. (b) Spectra in normalized water and (d) spectra in normalized water and in water rescaled for comparison. (e-f) The spectral region corresponding to Co-O vibrations is expanded to emphasize the differences (gray area) between the deuterated water and water spectra in (e) and between the normalized water and water spectra in (f).

Table 3.2: Positions of the major Raman peaks (in cm^{-1}) for CoCat operated at different potentials in electrolytes made by water, deuterated water or normalized water.[a, b, c, d]

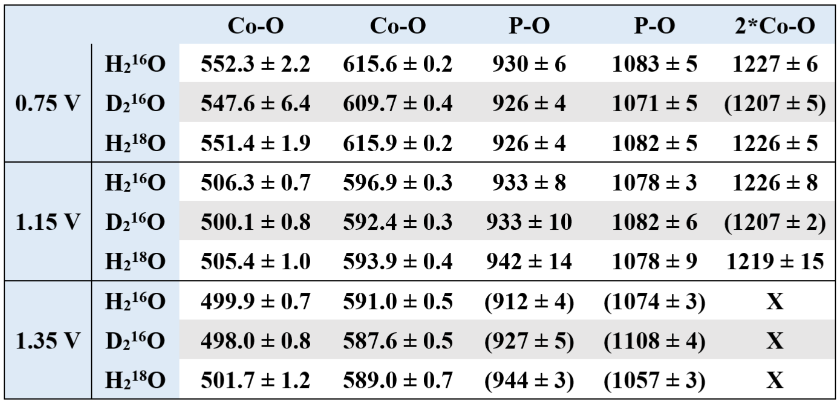

		Co-O	Co-O	P-O	P-O	2*Co-O
0.75 V	**$H_2{}^{16}O$**	**552.3 ± 2.2**	**615.6 ± 0.2**	**930 ± 6**	**1083 ± 5**	**1227 ± 6**
	$D_2{}^{16}O$	**547.6 ± 6.4**	**609.7 ± 0.4**	**926 ± 4**	**1071 ± 5**	**(1207 ± 5)**
	$H_2{}^{18}O$	**551.4 ± 1.9**	**615.9 ± 0.2**	**926 ± 4**	**1082 ± 5**	**1226 ± 5**
1.15 V	**$H_2{}^{16}O$**	**506.3 ± 0.7**	**596.9 ± 0.3**	**933 ± 8**	**1078 ± 3**	**1226 ± 8**
	$D_2{}^{16}O$	**500.1 ± 0.8**	**592.4 ± 0.3**	**933 ± 10**	**1082 ± 6**	**(1207 ± 2)**
	$H_2{}^{18}O$	**505.4 ± 1.0**	**593.9 ± 0.4**	**942 ± 14**	**1078 ± 9**	**1219 ± 15**
1.35 V	**$H_2{}^{16}O$**	**499.9 ± 0.7**	**591.0 ± 0.5**	**(912 ± 4)**	**(1074 ± 3)**	**X**
	$D_2{}^{16}O$	**498.0 ± 0.8**	**587.6 ± 0.5**	**(927 ± 5)**	**(1108 ± 4)**	**X**
	$H_2{}^{18}O$	**501.7 ± 1.2**	**589.0 ± 0.7**	**(944 ± 3)**	**(1057 ± 3)**	**X**

[a] Each peak was simulated with a Gaussian function.
[b] In the simulation four solution peaks were included at fixed positions.
[c] Parenthesis indicates peaks that are uncertain due to significant spectral overlap with other Raman bands; X indicates peaks with near-zero amplitude, which were not included in the simulation.
[d] All simulation parameters are shown in Appendix Tab. 9.1 and an example of the simulation in Fig. 3.15.

2017). The case of CoCat is different because, even though oxygen atoms from the bulk of the material are involved in OER (Ullman, 2016), these are most likely not "lattice oxygen", but rather may be classified as "surface species" (i.e. terminally coordinated oxygen) that are present in the volume of the material, thanks to its specific amorphous structure.

In summary, the isotopic H/D substitution suggests that, likely, (i) a major fraction of both terminal and bridging oxygen atoms are protonated at low potentials and (ii) the number of protonated oxygen atoms is significantly reduced at higher potentials, in line with proton-coupled electron transfer in oxidation/reduction of Co ions. Furthermore, the majority of oxygen atoms are non-exchangeable and they either do not take part in the catalytic reaction or they contribute only indirectly, meaning that they do not leave the catalyst in the form of molecular oxygen. This suggests that oxygen molecules produced in the reaction are only made of terminally bound oxygen atoms.

3.3.6 Raman intensity dependence on Co oxidation state

In Fig. 3.17a Raman spectra of the CoCat film at various potentials are shown without rescaling or background subtraction. Both the level of the Raman background and the intensity of the CoCat peaks continuously decrease with an increase in the potentials, similarly to what was observed in Co-based battery materials (Inaba, 1997; Matsuda, 2019). However, part of the trend, at potentials higher than 1.25 V_{NHE}, may be due to the presence of bubbles in the solution, which decrease the Raman signal intensity.

The observed decrease in the magnitude of the Raman bands for increasingly positive potential (Fig. 3.17c, Appendix Tab. 9.1) is unexpected because CoCat, like many others transition metal oxides, is an electrochromic material. Electrochromic materials change their absorption spectrum with the applied potential (Trotochaud, 2013; Smith, 2017; Pasquini, 2019; Polo da Fonseca,

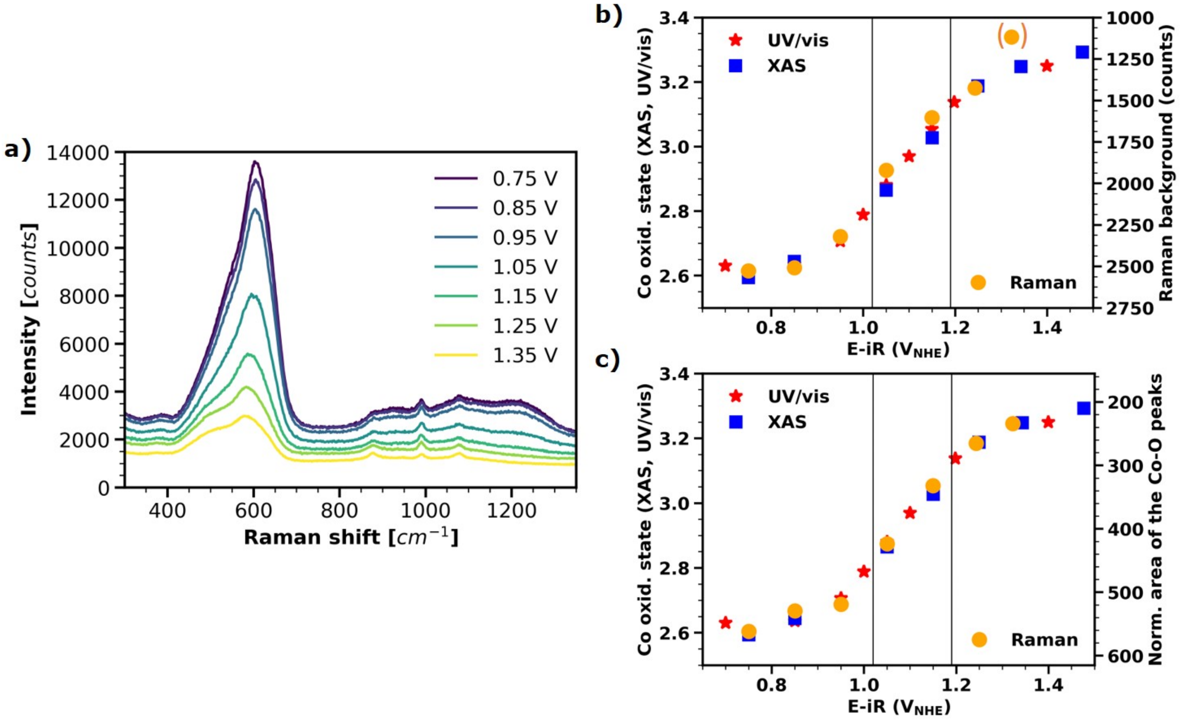

Figure 3.17: Dependency of the Raman signal intensity of CoCat on the applied potential (deposition charge of 40 mC cm^{-2}, Pt substrate, 0.1M KPi at pH 7 electrolyte). (a) Raw (not rescaled) Raman spectra at different applied potentials. (b) Raman-spectra background intensity (right axis, notice the inverted axis) and (c) normalized area of the Co-O Raman peaks (right axis, notice the inverted axis) compared with the Co oxidation state obtained from x-ray and UV/Vis absorption measurements (left axis). The background intensity refers to the average of the Raman counts measured between 735 cm^{-1} and 805 cm^{-1}. The peak area was calculated from a fit of the Co-O peak in the 415–712 cm^{-1} range (details are given in Appendix Tab. 9.1 and Fig. 3.15), after subtraction of a linear background, and was normalized by the background intensity. The parentheses in (b) indicate the data point possibly affected by the presence of bubbles in the solution. The UV/Vis absorption data were rescaled to match the x-ray data. Details on the x-ray and UV/Vis data in section 6.2.3.

1994). In the case of CoCat, the absorption increases with an increase in potential (see Fig. 2.12), thus an increase of the Raman resonance enhancement factor is expected at higher potentials. This increase is, indeed, observed for Ni oxides (Diaz-Morales, 2016), whereas we observe a decrease for the CoCat here. An increase in the Raman background for increasingly positive potential was reported for Cu surface oxides (Jiang, 2019), which presumably relates to specific surface plasmon effects (Mahajan, 2009), that are likely irrelevant for the CoCat Raman signal.

The level of the broad background of the Raman signal is shown on the right axis of Fig. 3.17b, in comparison with the change in the Co oxidation state with potential (left axis). The change in the Co oxidation state was obtained by x-ray absorption measurements. The UV/Vis absorption at 600 nm also increases with potential (as expected for electrochromic materials) and perfectly follows the increase in the oxidation state (see section 6.2.3 for details on XAS and UV/Vis data). From the comparison of the different datasets emerges that the Raman background intensity has an inverse (notice the inverted axis) dependence on the Co oxidation state and on the Co absorption coefficient.

A possible explanation for the observed behavior is that the Pt background (Fig. 3.5) decreases with the increase in the Co oxidation state because Co absorption quenches the background signal due to the increase in its absorption coefficient. The same rationale and a self-absorption phenomenon can explain the decrease in the Co-O band. This explanation is supported by the analysis of a thin CoCat film (deposition charge of 10 mC instead of 40 mC cm^{-2}), which shows a strongly reduced dependence on the applied potential (Fig. 3.18).

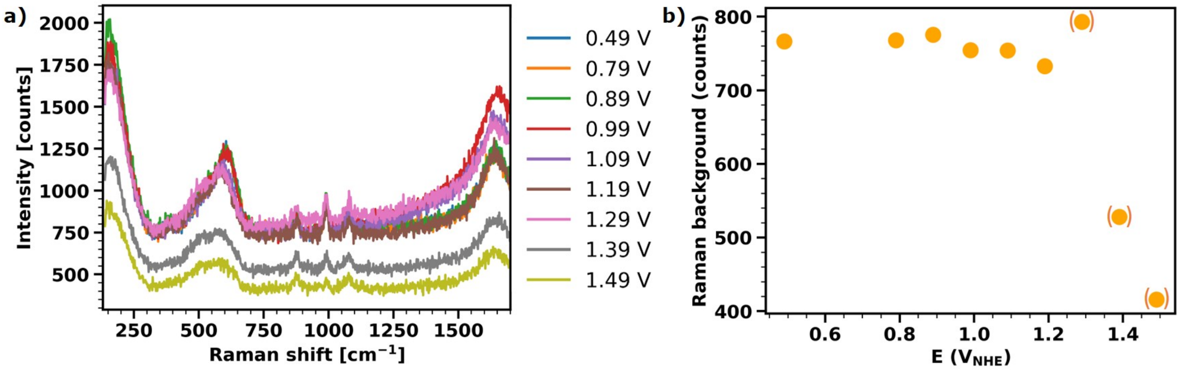

Figure 3.18: Dependency of the Raman signal background and intensity of CoCat peaks on the applied potential for a thin film (deposition charge of 10 mC cm^{-2}, Pt substrate, 0.1M KPi at pH 7 electrolyte). (a) Raw (not rescaled) Raman spectra at different applied potentials. (b) Background intensity calculated as the average of the Raman counts measured between 735 and 805 cm^{-1}. The data points in parenthesis are detected in the catalytic regime, where a diminished signal resulting from shading by O_2 bubbles in the optical path is likely.

CoOx represents an anomaly among electrochromic materials because both the level of the Raman background and the intensity of the Co-O band have an inverse dependence on the Co oxidation state and absorption coefficient. Like the background intensity, potential-dependent Raman band intensities could also be related to a self-absorption phenomenon, arising from the very broad visible absorption band of Co, which has an increased absorption coefficient at high potentials. In any event, the observed dependence provides a method to qualitatively trace changes in the Co oxidation state by Raman spectroscopy.

3.3.7 Tracking oxidation state changes with Raman spectroscopy

In section 3.3.4, a red-shift of the Co-O peaks with potential was observed, suggesting that this peak reflects the oxidation state of Co. In this section, this hypothesis will be tested by comparing the shift in the Raman peak with the oxidation state of Co obtained by XAS measurements.

When an increasingly positive potential is applied and Co ions are increasingly oxidized, the Co-O bond gets stronger and a pure stretching vibration would be expected to exhibit a blue shift. Therefore, the observed red-shift suggests that the Co-O vibration is linked to bending modes and not pure stretching vibration. Also, in battery materials ($LiCoO_2$), a red-shift of the Co-O peaks has been observed upon Li deintercalation (Matsuda, 2019; Inaba, 1997), which is linked to a structural change and to Co oxidation.

As a first attempt to study the potential dependency of the Co-O peaks, the 415 to 727 cm^{-1} region in the Raman spectra (corresponding to Co-O vibrations) was simulated with two Gaussian functions, obtaining the peak positions at different potentials. The Co-O peak positions were compared with the oxidation state of Co at different potentials, obtained from freeze-quench X-ray absorption data (Appendix Fig. 9.1, for details on X-ray measurements see section 6.2.3). The shift of the peak is restricted in a smaller potential region than the oxidation state change, resulting in a poor match, even though the Raman data reflect well the midpoint potential of the Co oxidation transition. Therefore, a more complicated approach was attempted.

At each potential, the Raman spectrum is well represented by the sum of 4 Gaussian functions, whose relative intensities change with potential, while their position and full-width-at-half-maximum (FWHM) stay fixed (globally fitted set of spectra with 4 identical peak positions, 4 identical FWHM and varying intensities). An example of the spectral simulation is presented in Fig. 3.19. The percentage of the total peak area belonging to each Gaussian varies with potential (Fig. 3.20a). Note that an assignment of the 4 Raman peaks to specific Raman modes or Co oxidation states is not possible. Inter alia because of µ-O(H) bridging between Co^{II}, Co^{III}, and Co^{IV} ions, each of the oxidation state species present in the CoCat could contribute to each of the 4 Gaussian-shaped Raman peaks, which were employed merely to describe the spectra by a limited set of parameters.

Even though there are 4 peaks, there are only two independent spectral components of the potential-controlled changes. The reduction from 4 to 2 is due to the fact that areas of the 620 and 539 cm^{-1} peaks have exactly the same potential dependence (Fig. 3.21) and the 584 cm^{-1} potential dependence can be obtained as a difference of the other three, due to normalization of the total peak area at each potential. The normalization of the total peak area was necessary due to the strong dependence of the signal intensity on the applied potential (see section 3.3.6).

In the investigated potential range, three different Co species have been detected for CoCat: Co^{II}, Co^{III} and Co^{IV} (Risch, 2015; Gerken, 2011; McAlpin, 2010). For Co ions in the different oxidation states, different Co-O bond lengths and possibly different protonation states of the oxygen ligands (O, OH^{-1}, or H_2O) are expected, suggesting that the three Co species exhibit different spectral fingerprints. The normalization of the total peak area, needed here, impedes the identification of specific spectra for each Co species. However, the two independent components of potential-controlled area changes can represent, through a linear combination, the two Co oxidation transitions occurring in this potential range (Co^{II}$\rightarrow$Co^{III} and Co^{III}$\rightarrow$Co^{IV}).

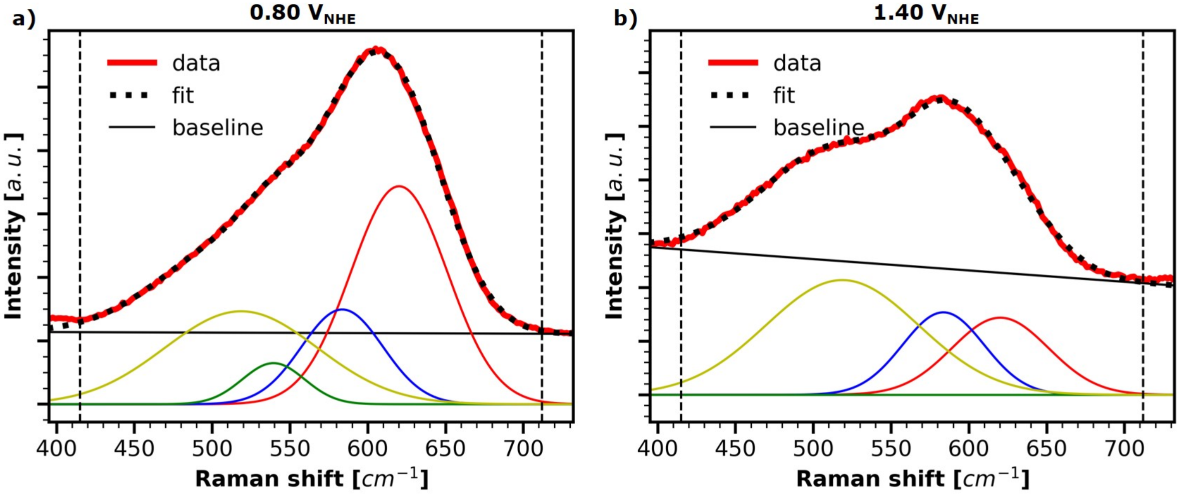

Figure 3.19: Simulation of the operando Raman spectra of CoCat in the region of Co-O vibrations. Samples conditioned at (a) 0.80 V_{NHE} and (b) 1.40 V_{NHE} are shown as examples. Each spectrum was simulated in the region 415 to 712 cm^{-1} (indicated by vertical dashed lines) with a linear baseline (black line) and 4 Gaussian functions (colored lines). The Gaussian functions have globally fitted positions (620, 584, 539 and 519 cm^{-1}), globally fitted FWHMs (63, 72, 47 and 116 cm^{-1}, respectively) and varying amplitudes.

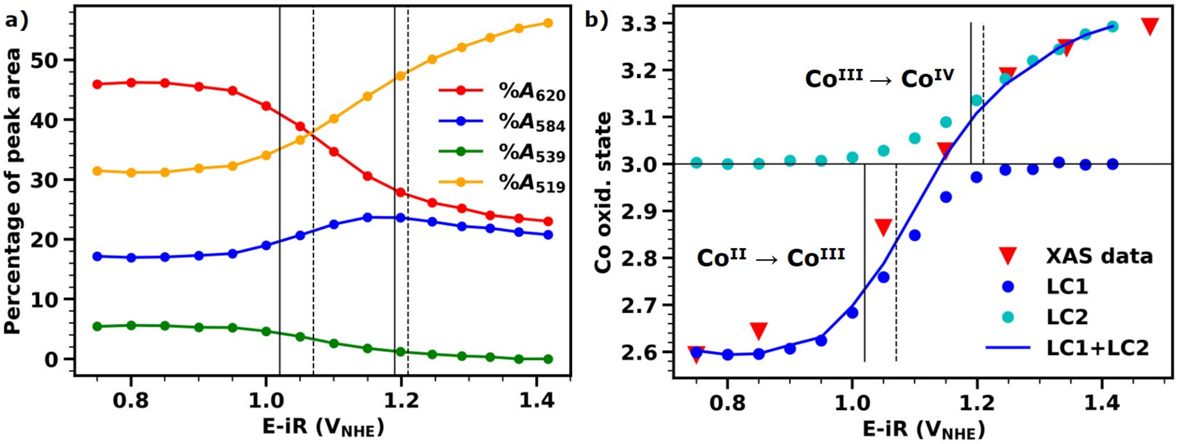

Figure 3.20: Analysis of the Raman spectra for CoCat (spectra in Fig. 3.12). Each Raman spectrum was simulated with 4 Gaussian functions with fixed positions and varying amplitudes, simulation details in Fig. 3.19. (a) Percentage of the total area belonging to each Gaussian as a function of potential. (b) Comparison between the change in Co oxidation state with potential and a linear combination of the Raman peaks area (LC1 and LC2). The percentage of peak area for the 519 and 620 cm^{-1} peaks were combined to represents the two individual Co oxidation state transitions, i.e. for $Co^{II} \rightarrow Co^{III}$: $LC1 = -(0.45 \cdot \%A_{519} + \%A_{620})$ and for $Co^{III} \rightarrow Co^{IV}$: $LC2 = \%A_{519} + 0.6 \cdot \%A_{620}$. Co oxidation state is obtained by freeze-quench X-ray measurements. The vertical full lines indicate the midpoint potentials for the two Co oxidation state transitions (details in section 6.2.3). The vertical dotted lines indicate the potential at half-height for LC1 and LC2. The Raman data are shifted and rescaled to match the lowest and highest oxidation state reached by the XAS data.

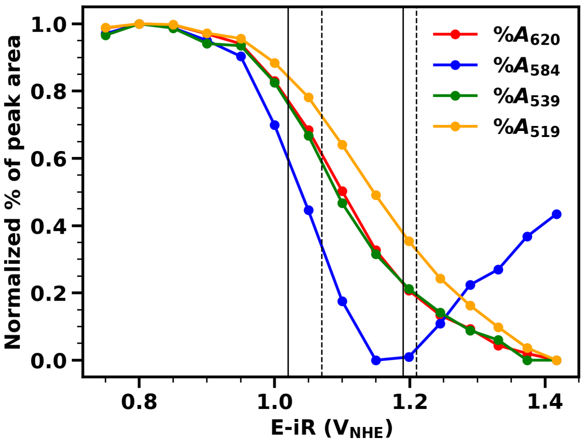

Figure 3.21: The Raman spectra of CoCat collected at various potentials (spectra in Fig. 3.12) were simulated in the 415 to 712 cm^{-1} region with 4 Gaussian functions (at 620, 584, 539 and 519 cm^{-1}). Here is shown the normalized percentage of the total area belonging to each Gaussian as a function of potential. The not normalized data are shown in Fig. 3.19 and simulation details in Fig. 3.20.

In Fig. 3.20b, the XAS data representing the change in Co oxidation state is compared with the two linear combination of potential-controlled area changes that plausibly reflect the two oxidation state transitions, i.e. $LC1 = -(0.45 \cdot \%A_{519} + \%A_{620})$ for Co^{II}→Co^{III} and $LC2 = \%A_{519} + 0.6 \cdot \%A_{620}$ for Co^{III}→Co^{IV}. The linear combination coefficients are almost unique, because significantly different combinations do not result in curves that could plausibly reflect the potential dependence of the Co oxidation states. The obtained curves were shifted and rescaled to match the lowest and highest oxidation state of each transition previously detected by XAS. The midpoint potentials of the two Co oxidation transitions obtained from the XAS data (vertical full lines in Fig. 3.20, see section 6.2.3 for details) are similar to the potential at half-height for LC1 and LC2 (vertical dotted lines). The difference could result from a comparably minor shift of midpoint potentials occurring during CoCat operation (see Fig. 3.22).

In summary, the CoCat Raman spectra in the Co-O region are well simulated by four Gaussian functions, whose areas change with the applied potential. The spectral changes reflect exactly two linearly independent components, which can be assigned to two Co redox transitions (Co^{II}→Co^{III} and Co^{III}→Co^{IV}). Thus, Raman spectroscopy facilitates the monitoring of the redox transitions of the material. While XAS analysis typically results in the determination of an average oxidation state only, Raman spectroscopy provides access to the individual redox transitions. This approach likely can be generalized to the study of other metal-oxide-based OER catalysts, where typically M$^{II/III}$ and M$^{III/IV}$ redox transitions are involved, as well as battery materials.

3.4 Summary

An investigation and analysis approach applied to electrochemical operando Raman spectroscopy is presented, establishing a promising method for the mechanistic investigations of OER catalysts,

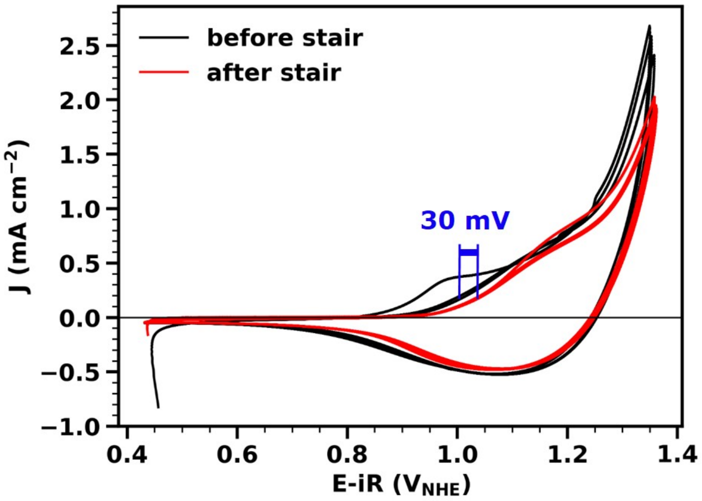

Figure 3.22: Cyclic voltammetry (CV) experiment (at 20 mV s^{-1}) for CoCat, 40 mC cm^{-2} thick, deposited on Pt, in 0.1 M KPi at pH 7. Three CVs (black line) were collected before the potential stair experiment (reported in Fig. 3.12) and 3 CVs (red line) just after the potential stair experiment.

including tracking of oxidation-state changes. First, an introduction to the experimental set-up is given, including the reasons for the choice of a Pt substrate: Au substrate peaks overlap with the CoCat spectrum and carbon-based substrates increase laser-heating damages to the sample. Then, the Raman spectra of the Co catalyst in different electrochemical conditions are analyzed, addressing changes in the electronic and atomic structure of the catalyst material that are of likely relevance for mechanistic insight in OER catalysis, as summarized in the following.

- Two broad bands (around 877 cm^{-1} and 1077 cm^{-1}) in the CoCat Raman spectrum are assignable to concentrated $H_xPO_{4^-}$ ions (likely x = 2), possibly forming dimers or polyphosphates, which can favor proton transport via formation of hydrogen-bonds networks.

- In response to changes in the electric potential, an unexpected behavior was observed in both the Raman background intensity and the magnitude of Raman bands, both decreasing with increasingly positive electrode potentials. The unexpected behavior presumably does not represent a novel type of potential-dependent Raman enhancement, but rather variable re-absorption of the Raman light by the electrochromic CoCat material. The decrease in signal magnitude was shown to properly track the increase in the Co absorption coefficient and, thus, the increase in the average Co oxidation state (and consequently can be employed to track oxidation state changes).

- At sub-catalytic and catalytic potentials, no evidence was found for accumulation of special, potentially reactive, oxygen species (no evidence for Co=O, Co-O$^\bullet$, Co-O-OH). Experimental results neither can exclude a minor population with Raman intensities below the detection limit, nor conflict with reactive oxygen species that are transiently formed during O_2-formation. Raman bands in the spectra that might be related to such species

(800–1200 cm^{-1}) are assigned to two-phonon Raman scattering (twice the vibrational frequency of the main Co-O bands).

- Isotopic ^{1}H/^{2}H labeling enabled the detection of protonated/deprotonated oxygen species, presumably present as both, bridging (Co-OH-Co) and terminal (Co-OH and Co-OH$_2$), ligands. The Co-O stretching from these bands appears in the 415 to 727 cm^{-1} region. At increasingly positive potentials, deprotonation of these species occurs, supporting proton-coupled electron transfer in the Co redox transitions.

- Exposure of a ^{16}O-CoCat to ^{18}O-water showed that, also at catalytic potentials, only a minority fraction of the oxygen sites of the CoCat harbors exchangeable oxygen atoms. The majority fraction of non-exchangeable oxygen atoms most likely corresponds to bridging oxygen, which, consequently, are not the oxygen atoms that leave the catalyst in the form of dioxygen. The minority fraction of exchangeable ^{16}O likely corresponds to terminal Co ligands at the periphery of Co oxide fragments, suggesting that terminally coordinated water species are oxidized in OER by the CoCat material. Oxidation of non-coordinated water species also would not conflict with the herein reported results. This finding provides relevant support to recent mechanistic proposals based on mass spectroscopy experiments (Ullman, 2016; Koroidov, 2015) and computational chemistry (Mattioli, 2013).

- The normalized Raman spectra of CoCat in the 415 cm^{-1} to 712 cm^{-1} region, corresponding to Co-O vibrations, are accurately described by four Gaussian peaks with potential dependent areas, but only two independent components of potential-controlled area changes. In the potential range studied, two Co oxidation processes have been reported, i.e., $\mathrm{Co^{II}}\rightarrow\mathrm{Co^{III}}$ and $\mathrm{Co^{III}}\rightarrow\mathrm{Co^{IV}}$. Each of the Co oxidation reactions can be represented by a linear combination of the recorded spectral changes. Thus, Raman spectroscopy, unlike the published XAS studies, can distinguish the $\mathrm{Co^{II}}\rightarrow\mathrm{Co^{III}}$ from the $\mathrm{Co^{III}}\rightarrow\mathrm{Co^{IV}}$ oxidation.

3.5 Experimental details

Materials

CoCat films were prepared by anodic electrodeposition following an established protocol (Kanan, 2008; Klingan, 2014), slightly modified: a potential of 1.05 V_{NHE} was applied in a 0.1 M phosphate buffer (KPi) at pH 7 or 0.1 M borate buffer (KBi) at pH 9.2 containing 0.5 mM $Co(NO_3)_2$ solution. The potential was applied until the accumulation of a predefined charge, the value of the charge is reported in each figure, 1 mC corresponds to ca. 10 nmol of Co atoms. Sample preparation was performed in a single-compartment three-electrode cell, using a Pt grid (2x2 cm^2, 90% purity) as a counter electrode and an Ag/AgCl(saturated) as a reference electrode. The working electrode was a 0.1 mm thick sheet of Pt with 99.95% purity (Labor-Platina Kft.). Before use Pt substrates were sonicated in ethanol and water, no polishing was used for Pt substrates because it reduces the adherence of the CoCat film. The electrolyte solution for all experiments was 0.1 M phosphate buffer (KPi) at pL 7, made using either MilliQ water (>18 MΩ cm), deuterated water (isotope purity of 99.8%, Roth) or ^{18}O water (isotope purity of 97%, Eurisotop).

Raman spectroscopy

Raman spectra were collected in-situ using a confocal geometry and a self-made Teflon cell, with the incident laser hitting the catalyst from the top (Fig. 3.2, more details in section 3.3.1). The Renishaw inVia Raman spectrometer was coupled with a Leica microscope equipped with a water immersion objective (N.A. 0.8). A grating of 2400 lines/mm and a slit size of 20 µm were used. The spectral position was calibrated on a Si wafer. The laser power was adjusted to a value of ca. 1 mW using optical (neutral density) filters.

Raman-spectra acquisition was initiated after 2 min application of the indicated potential. Depending on the noise level, a minimum of 3 and a maximum of 6 spectra were collected at each potential (1 min per spectrum), the averaged data is presented. At least two different sample positions were used at each potential. If not stated otherwise in all the presented figures Raman spectra were rescaled and shifted for clarity purposes, no background subtraction was performed. Simulations of the Raman spectra were performed by the software "peak-o-mat" and the in-house software “gloFit”. Applied potentials are reported in the NHE scale. Compensation of the recorded potential for iR drop was done during data analysis.

ATR spectroscopy

A Bruker VERTEX-80v FTIR vacuum spectrometer with KBr beamsplitter, DTGS detector and an ATR unit with a diamond crystal was employed to collect ATR spectra. After conditioning in an electrochemical cell, samples were dried for few seconds under a N_2 gas flux, transferred to the ATR spectrometer and measured under vacuum. Before the measurement of each new sample, a background spectrum was collected in vacuum and later used for background subtraction, according to the formula $log_{10}\left(\frac{T_0}{T}\right) A(\omega)$, where T and T_0 are the transmitted intensities for sample and background, respectively, and A is a factor proportional to the wavelength.

For details on the freeze-quench X-ray absorption experiments and on the operando UV/vis absorption experiment refer to section 6.5.

4 Operando Raman spectroscopy reveals local pH changes affecting catalytic performances

4.1 Context and motivations

During the water oxidation reaction, four protons are produced on the anode side per each water molecule (Eq. 1.1) and are combined in two hydrogen molecules on the cathode side. When the OER is performed at neutral pH, a buffer solution is used to transfer the protons to the cathode side. The efficiency of the transport process is important for catalytic activity: proton-transport limitations are reported to prevent the development of efficient devices (Jin, 2014; McKone, 2014) and constitute one of the most important challenges in the scaling up of devices size (Ahmet, 2019).

When the solution is not stirred (preventing convection processes) and a supporting electrolyte is used (only minor migration processes), near the electrode the mass transport of an electroactive species is dominated by diffusion processes (Bard, 2000a). In the presence of a buffer, proton transport is mostly mediated by the transport of the protonated buffer species, whose contribution depends on buffer concentration and pK_a (Engasser, 1974; Engasser, 1980).

At sufficiently high current densities, the buffer capacity will be overrun. For CoCat it was shown that, in this regime, the catalytic activity is controlled by the availability of proton-accepting base for a variety of tested buffer electrolytes (Klingan, 2014). The same behavior has been observed for a Mn-based catalyst in phosphate buffer (Bergmann, 2013). Other studies suggest that the catalytic activity is controlled by the diffusion of buffer molecules (Costentin, 2016) or protons (Brodsky, 2018) between the catalyst inner layers. Shinagawa et al (Shinagawa, 2017b; Shinagawa, 2017c) proposed that, at mild-pH and high current densities, the transport of protonated buffer species controls catalytic activity. Thus, the buffer concentration should be chosen to maximize both the activity of the deprotonated buffer species and the diffusion coefficient of the electrolyte.

The study of the factors controlling the catalytic activity at lower current densities is more complicated and most mechanistic interpretations are based on Tafel slope analysis. The Tafel slope is the overpotential needed to increase the current ten times and is a key parameter to assess catalysts efficiencies. The standard interpretation is based on the Butler–Volmer equation (Bard, 2000b; Fletcher, 2008). The expected values of the Tafel slope for different oxygen evolution mechanisms (Bockris, 1983) and for different rate-limiting steps (Shinagawa, 2015; Dunwell, 2018b) can be theoretically derived. However, the experimental values cannot be always related to theoretical values (Shinagawa, 2015). The influence of mass transport limitations is often underestimated for Tafel slope interpretation and, in the past, this repeatedly led to incorrect mechanistic interpretations (Dunwell, 2018b).

Bediako et al. developed a model for bulk active catalysts at neutral pH which takes into account different rate-controlling phenomena, including those related to mass transport limitations, e.g., diffusion of protons or buffer components inside the film or at the film–solution interface (Bediako, 2013). Experiments on CoCat were in accordance with model predictions, providing a Tafel slope of 59 mV dec^{-1} for high buffer concentrations and 118 mV dec^{-1} for buffer-free solutions. In the intermediate cases, a transition between the two behaviors is predicted. We proposed a model to study the effects of proton transport limitations on the Tafel slope (Dau, 2019). At intermediate current densities, the model predicts Tafel slope values which smoothly variate with the electrolyte buffer capacity, due to the formation of local pH gradient close to the catalyst surface.

Local pH gradients due to mass transport limitations have an even higher impact on the CO_2 reduction reaction, in which carbon dioxide is converted to a fuel. The product's composition for this reaction is affected by local pHs (Wang, 2018; Hashiba, 2018; Klingan, 2018). This sparked the interest in models to study pH gradients formations (Gupta, 2005; Hashiba, 2018; Yang, 2019; Burdyny, 2017; Auinger, 2011), including their dependence on the catalyst surface morphology (Suter, 2018), and on methods to experimentally measure the local pH at the catalyst surface. Experimental methods included the use of a pH-sensitive fluorescence probe (Obata, 2020), of a concurrent, pH-dependent, non-faradaic reaction (Ryu, 2018) and of attenuated total reflectance infrared absorption spectroscopy (ATR) (Dunwell, 2018a; Yang, 2019). Another possibility is operando Raman spectroscopy, which was used in my working group to detect local alkalinization on CuCat surfaces (Klingan, 2018). For CuCat local alkalinization can improve CO and C_2H_4 Faradaic efficiency.

In this chapter, operando Raman spectroscopy is established as a method to study local pH changes at the catalyst surface during OER. It is proven to have spatial sensitivity and better resolution of the relevant peaks in comparison with ATR. Evidence is provided of local pH gradients forming at catalytic potentials in 0.1 M KPi buffer. Then, the effects of proton transport limitations on the catalytic activity are investigated, both in the mass transport limited region and in the linear Tafel region. The main predictions of the proton transport model (Dau, 2019) are verified experimentally. In particular, I study the dependence of the high current densities and of the Tafel slope on the pH and, thus, on the buffer capacity of the electrolyte.

4.2 Results

4.2.1 How Raman spectroscopy can measure pH values

Buffer solutions are composed of a weak acid (protonated species) and its conjugated base (deprotonated species), which are in equilibrium and convert into each other to stabilize the pH of the solution. If the pH of a solution is changed, i.e. by the addition of a large number of protons, the ratio between the weak acid and the base will change as well. Usually, these two species have different Raman active vibrations, thus it is possible to record pH changes, also at the local level, by observing variations in the Raman spectra.

The most common buffer used at neutral pH in OER is KPi buffer, which is made by a mixture of $H_2PO_4^-$ (weak acid) and HPO_4^{2-} (its conjugate base). Its Raman spectra has two peaks at 877 and 1077 cm^{-1} due to $H_2PO_4^-$ and one at 990 cm^{-1} due to HPO_4^{2-} (Heighton, 2012). Previously, ATR spectroscopy was employed, to measure pH changes in KPi buffer (Yang, 2019). An advantage of Raman spectroscopy is that the relevant peaks are better separated between each other than in IR spectra (compare Fig. 4.2a with ref (Yang, 2019).).

A series of reference spectra were recorded in 0.1 M KPi solution at different pHs (Fig. 4.2a). As the pH is scanned from 5.0 to 8.5, the intensity of the peaks corresponding to $H_2PO_4^-$ decreases, while the one corresponding to HPO_4^{2-} increases. Details on the calculation of the peak intensities are in the Method section and an example in Fig. 4.1. The intensity of the $H_2PO_4^-$ peak relative to the total intensity of the three peaks has a sigmoidal dependence on pH (Fig. 4.2c) and it was simulated with a sigmoidal function (simulation parameters in Fig. 4.2d). By inverting the function we obtain:

$$pH = 6.97 - \log_{10}\left(\frac{0.81}{A_{fr}} - 1\right) \tag{4.1}$$

where $A_{fr} = A_{HPO_4^{2-}}/(A_{HPO_4^{2-}} + A_{H_2PO_4^-})$.

Quantitative measurement of the local pH from the Raman spectrum can be obtained by calculating the area of the phosphate peaks and using equation 4.1. If the measurement is repeated at the catalyst-electrolyte interface, the presence of wide Raman bands belonging to the catalyst spectra slightly modifies the peak areas and therefore the parameters of the sigmoidal function (Fig. 4.2b-d).

4.2.2 Local acidification during OER

During the oxygen evolution reaction, a great number of protons are released at the film-electrolyte interface and in the bulk of the film. If the proton transport rate is lower than the rate of proton production, the capacity of the buffer can be overrun causing the formation of a local pH gradient at the film surface, which can be investigated using Raman spectroscopy.

Raman spectra were collected at different distances from the film-electrolyte interface at open circuit potential (OCP) and at catalytic potentials (Fig. 4.3a-b) in a 0.1 M KPi buffer at pH 7. In OCP conditions the ratio between the $H_2PO_4^-$ (lateral peaks) and HPO_4^{2-} (central peak) is not changing with the distance from the surface. On the contrary, at catalytic potentials, the ratio between central and lateral peaks changes, depending on the distance from the catalyst surface. At the catalyst surface, a local acidic pH is observed.

The local pH was calculated for each Raman spectrum using Eq. 4.1, then the pH gradient caused by OER was estimated as the difference between the pH at catalytic potentials (applied for 30 min) and in OCP (Fig. 4.3c). At 15 µm from the film surface, we have an increase in pH of 0.28 pH units, which decreases only slightly up to 100 µm distance and disappears at 500 µm. The presence of the underlying CoCat bands, which are changing with potential, makes the pH estimation unreliable at distances shorter than 15 µm. The depletion of the pH gradient was also investigated by collecting spectra at the film surface in OCP after applying 1.5 V_{NHE} for several minutes (Fig. 4.4). It takes around 5 min for the electrolyte at the film surface to reequilibrate. However, this result could be affected by the presence of the water immersion objective (see Fig. 3.2), which can partially hinder electrolyte movement inside the cell.

Local acidification is observed in the standard CoCat electrolyte (0.1 M KPi at pH 7), under relatively low catalytic potentials (1.3 V_{NHE}). A small pH gradient (a quarter of a pH unit) is formed at the film surface, it extends over 100 µm and takes around 5 min to be depleted. Stronger pH gradients are expected if the buffer is operated at different pHs (in the 5 to 9 pH range), where the buffer capacity is lower.

4.2.3 Proton transport limitations effects on catalytic activity

The Tafel slope represents the increase in overpotential needed to increase the current ten times, it is a key parameter to determine catalyst efficiency. A Tafel plot for CoCat is reported in Fig. 4.5a, the value of the current density is recorded at each potential after reaching a steady state. We can recognize two main regions: the first is the linear Tafel region, where the logarithm of the current varies linearly with potential. The slope depends on the rate-limiting step and is called Tafel slope (Bard, 2000b; Fletcher, 2008; Bockris, 1983; Shinagawa, 2015; Dunwell, 2018b). In the second region, the current is reaching a plateau, due to mass transport limitations. The dependence of the current from pH will be examined for the first region in the next section and for the second region in this section.

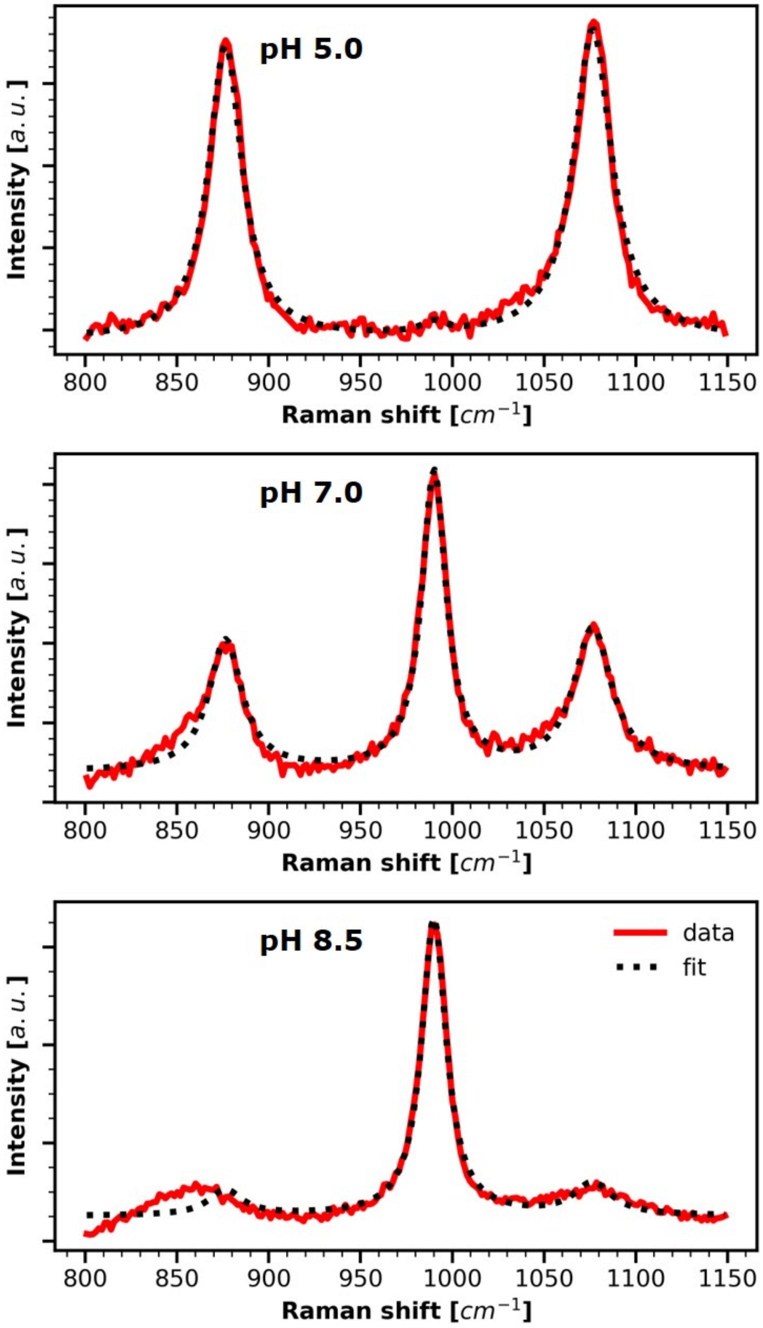

Figure 4.1: Raman spectra of 0.1 M KPi electrolyte and its simulation, examples for different pHs are shown. The raw data (red line) are fit with three Lorentzian functions and a second-order polynomial baseline. The fit is shown as a dotted black line. The positions and FWHMs of the Lorentzian functions were obtained through a global fit considering the data collected at all the investigated pHs. Their values for the three peaks are respectively: 876, 990 and 1077 cm^{-1} (positions) and 22, 16 and 25 cm^{-1} (FWHMs). The areas of the peaks are reported in Fig. 4.2.

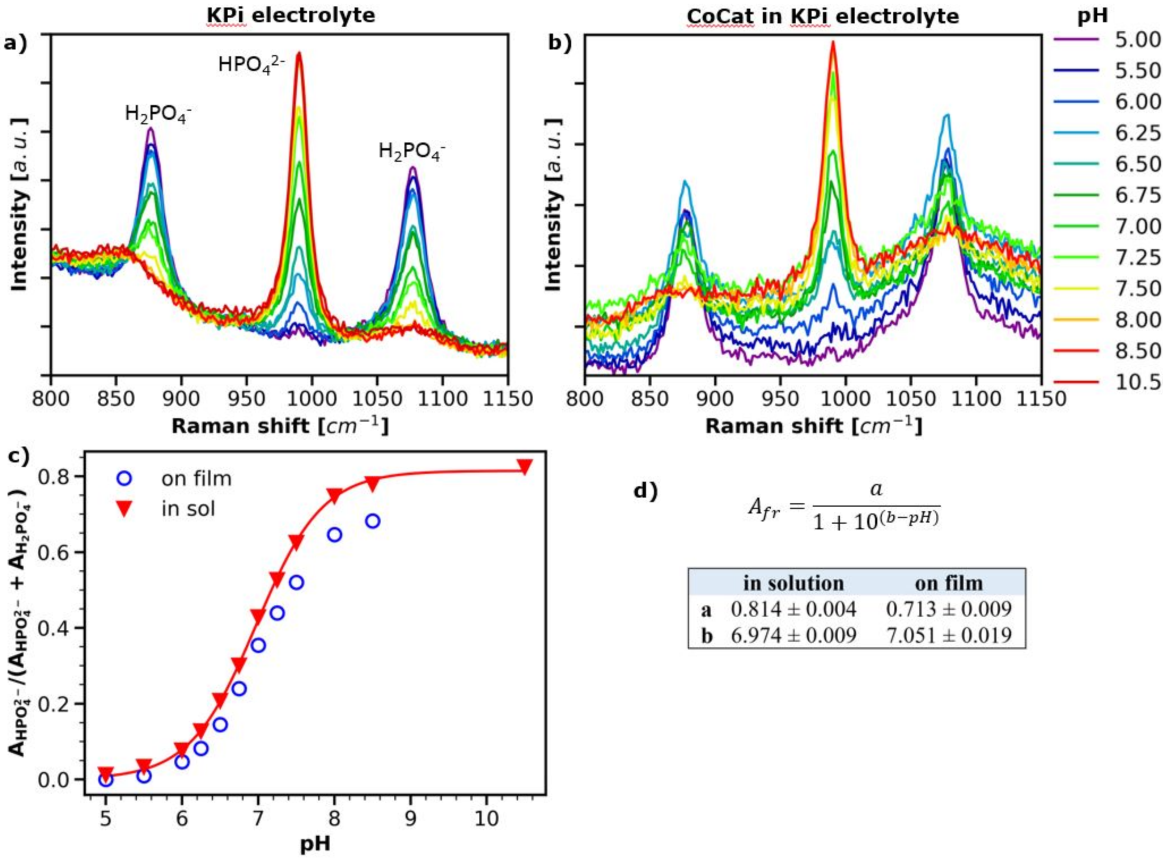

$$A_{fr} = \frac{a}{1 + 10^{(b-pH)}}$$

	in solution	on film
a	0.814 ± 0.004	0.713 ± 0.009
b	6.974 ± 0.009	7.051 ± 0.019

Figure 4.2: Estimation of the solution pH from the Raman spectrum. Raman spectra were collected in 0.1 M KPi solution at different pHs: (a) in the electrolyte (at a distance of several millimeters from the film surface) and (b) at the catalyst-electrolyte interface. (c) The relative peak area ($A_{fr} = A_{HPO_4^{2-}}/(A_{HPO_4^{2-}} + A_{H_2PO_4^-})$) has a sigmoidal dependence on pH, with parameters reported in (d). The presence of an underlying catalyst spectrum changes slightly the parameters. The solution pH can be obtained from a Raman spectrum using Eq. 4.1.

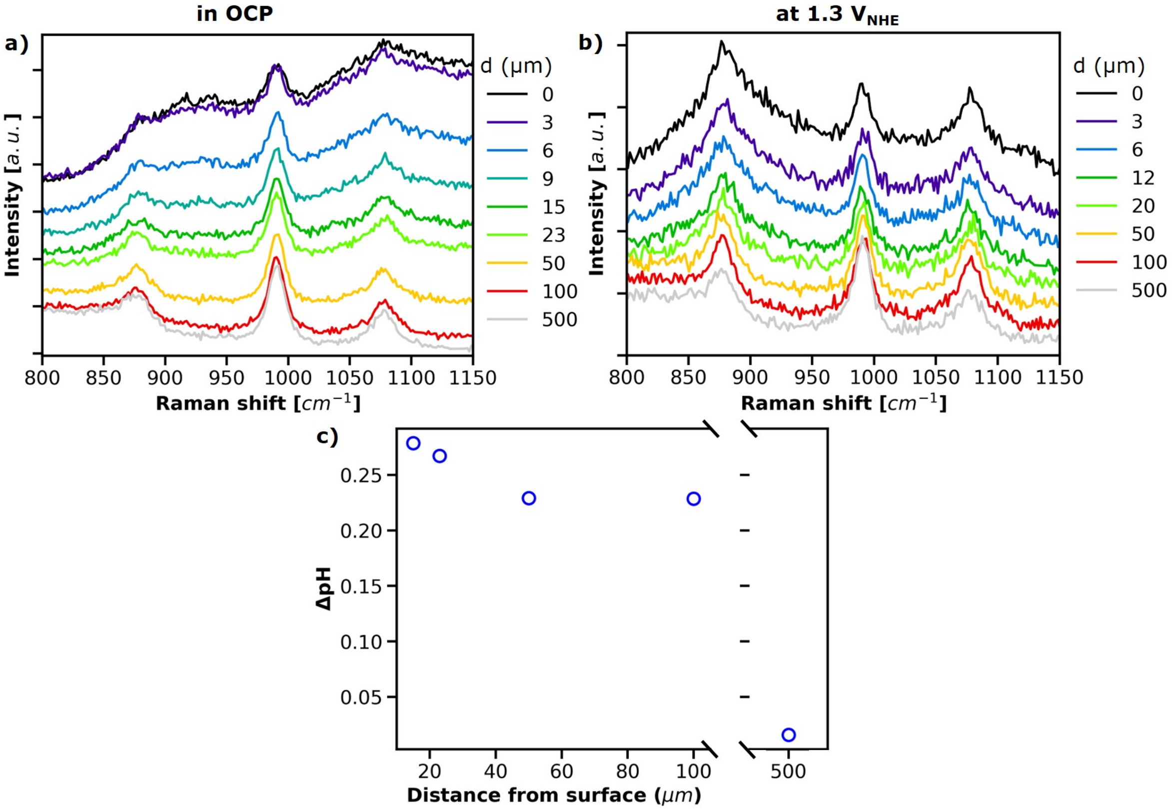

Figure 4.3: Raman spectra for CoCat collected in 0.1 M KPi solution at different distances from the film-electrolyte interface: (a) at open circuit potential and (b) at catalytic potentials. Raman spectra were neither rescaled nor shifted and no background subtraction was performed. (c) Local pH changes caused by catalytic operation calculated as the difference between the pH at catalytic potentials (applied for 30 min, data in panel b) and in OCP (data in panel a). The solution pH is obtained from Raman spectra using Eq. 4.1.

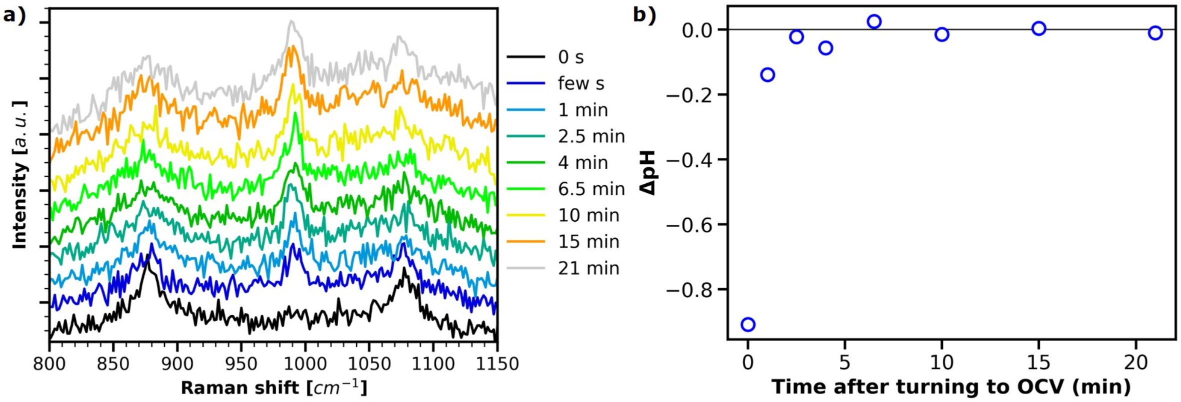

Figure 4.4: (a) Raman spectra for CoCat collected in 0.1 M KPi solution in OCP at different times after applying 1.5 V_{NHE} for several minutes. Raman spectra were measured in the proximity of the catalyst surface, they were shifted for better visualization but not rescaled. (b) Time dependence of local pH, showing how the local acidity created by the catalytic potential is depleted with time. The steady-state value was calculated as the average of the last 4 points and taken as the zero value. The solution pH reported is obtained from Raman spectra in panel (a) using Eq. 4.1.

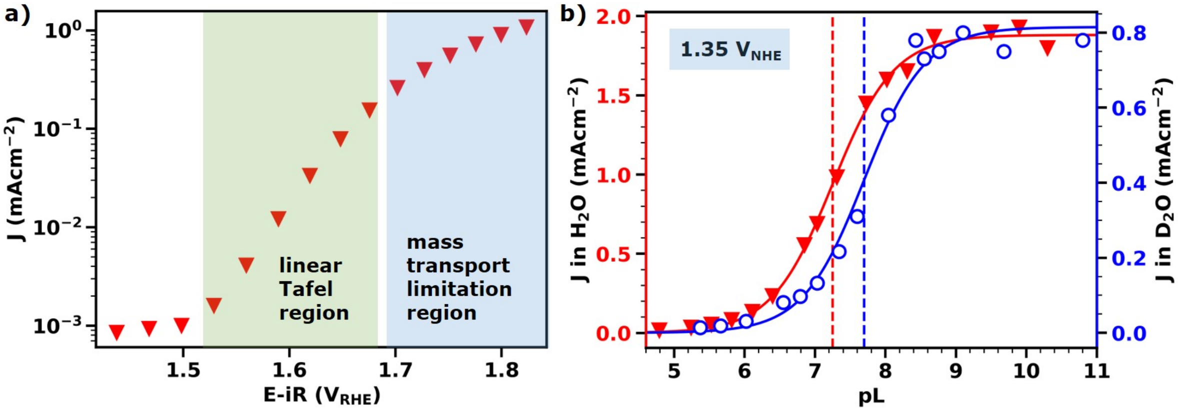

Figure 4.5: (a) Tafel plot from steady state (values taken after 3 min) chronopotentiometry measurements for a 12.5 mC cm^{-2} thick CoCat film in 0.1 M KPi solution. The Tafel linear region and the mass transport limited region are indicated. (b) pH titration of the catalytic current (at 1.35 V_{NHE}) in the mass transport limitation region in water (red, left axis) and deuterated water (blue, right axis) electrolyte. The titration was executed from low to high pL by adding 1 M KOH/KOD, while applying a constant potential and measuring the current. The solution was stirred during measurements. The data were fitted (solid lines) with Eq. 4.3, derived from the Henderson-Hasselbalch equation, to determine the pK_a values (dotted vertical lines, parameters in Tab. 4.1).

A pH titration of the catalytic current (at 1.35 V_{NHE}) was performed in the mass transport limitation region in phosphate buffer (KPi) made by water or deuterated water (Fig. 4.5b). The titration consisted in varying the pL from low to high by adding 1 M KOH/KOD to 0.1 M KH_2PO_4, while applying a constant potential and measuring the current. Since protons are a product of OER and we are in the mass transport limited region, we can expect an exponential rise in catalytic current with pH increase, because a linear pH increase exponentially decreases the number of protons in the electrolyte. The titration curves for the current, instead, follow a sigmoidal function which resembles the titration curve of a base. Similar behavior was already observed for Mn (Bergmann, 2013) and Co (Klingan, 2014) oxides for a series of buffer solutions. In deuterated water the curve is shifted at higher pH, in accordance with the shift expected for the pK_a of most bases.

An hypothesis is that the current (J) is controlled by proton transport and therefore is proportional to the concentration of unprotonated buffer species ($[A^-]$): $J = c[A^-]$, where c is a constant. According to the Henderson-Hasselbalch equation:

$$pH = pK_a + \log_{10}\left(\frac{[A^-]}{[HA]}\right) \tag{4.2}$$

Since we are in the pH region were only one buffer equilibrium reaction is relevant, namely $H_2PO_4^- \rightleftharpoons HPO_4^{2-} + H^+$, we can use $[HA] = B_0 - [A^-]$, where B_0 is the total buffer concentration and solve the equation for $[A^-]$, thus we obtain:

$$J(pH) = c[A^-](pH) = \frac{cB_0}{1 + 10^{pK - pH}} \tag{4.3}$$

Equation 4.3 was used to simulate the titration data (with c and pK as parameters) and returned values for pK (both in water and deuterated water) very similar to the pK_a of the phosphoric acid second deprotonation step (Tab. 4.1), confirming our hypothesis. The experiment was performed on thin samples (21 nm thickness). For a thicker sample lower pK_a values were obtained, probably due to the concurrent influence of proton transport inside the bulk of the film.

Table 4.1: Parameters obtained from the simulation (with Eq. 4.3) of the titration-experiment data (see Fig. 4.5b) and literature values for the pK_a of phosphoric acid second deprotonation step.[a]

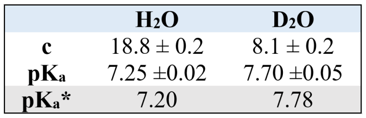

	H_2O	D_2O
c	18.8 ± 0.2	8.1 ± 0.2
pK_a	7.25 ±0.02	7.70 ±0.05
pK_a*	7.20	7.78

* Experimental values reported in ref (Robinson, 1969).

[a] The measurement units of c are mA cm mol^{-1}.

Using a pH titration experiment we found evidence that in the mass transport limitations region, at fixed overpotential, the catalytic current is controlled by the transport of proton away from the film-electrolyte interface and therefore is proportional to the concentration of unprotonated buffer species. For thick films, the influence of proton transport through the film can also play a role, which was not analyzed in the present work.

4.2.4 Tafel slope dependence on local pH

In this section, we will focus on the linear Tafel region (Fig. 4.5a), where a linear dependence between the overpotential and the logarithm of the current is observed. We observe that the Tafel slope is influenced by the solution pH, due to proton transport limitations which cause local pH changes.

A Tafel plot for CoCat was obtained from steady-state chronopotentiometry measurements performed at a series of potentials. The experiment was repeated for the entire neutral-pH range in 0.1 M KPi made by water or deuterated water (Fig. 4.6a,b), each time using a fresh sample. The Tafel slopes were calculated in the linear region and show a pH dependence.

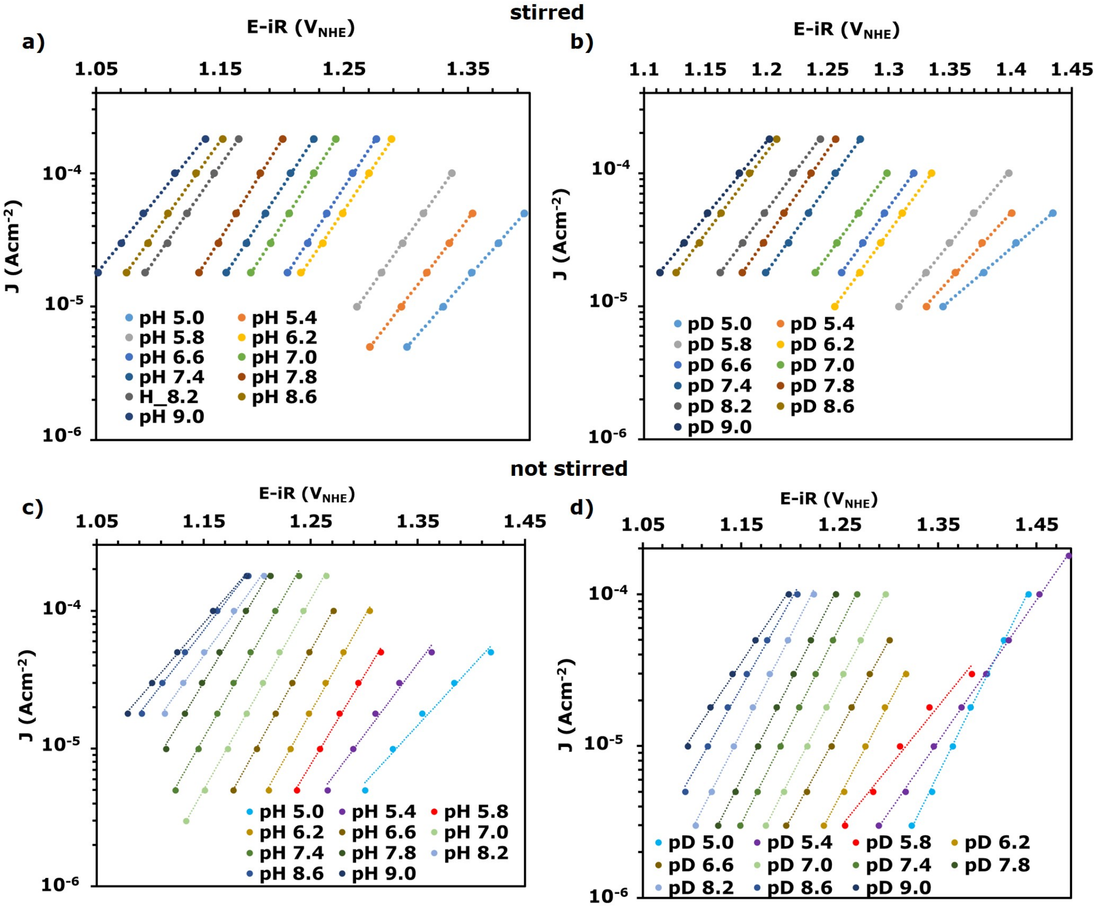

Figure 4.6: Tafel plots from steady state (values taken after 3 min) chronopotentiometry measurements of CoCat in the neutral pH regime ($6 \leq pL \leq 9$) in 0.1 M KPi made of (a,c) water and (b,d) deuterated water. The pL values are reported in the legend. Solutions were either (a,b) stirred or (c,d) not stirred during measurements. Data were corrected for iR drop. The linear fits used to calculate the Tafel slope are displayed as dotted lines.

The Tafel slopes obtained in water vary from 69 mV/decade at pH 7 up to 93 at pH 5 (Fig. 4.7). In D_2O made solutions the values appear slightly larger, varying in a range from 76 to 119 mV/decade depending on pH. The Tafel plot values follow a parabolic behavior. When the experiment is repeated in not stirred solutions (Tafel plots in Fig. 4.6c,d), the pH dependence is stronger and the parabola is three times steeper, suggesting an influence from mass transport limitations in the electrolyte.

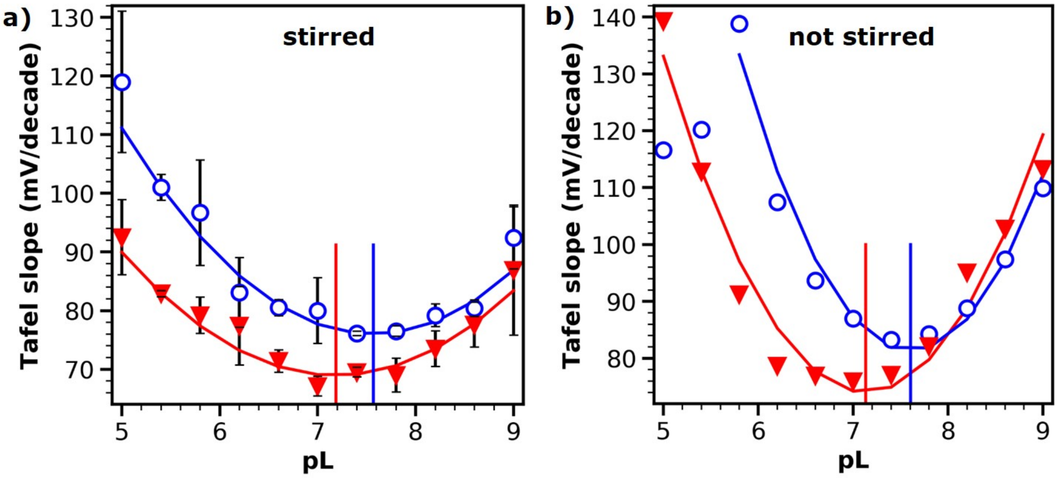

Figure 4.7: Tafel slope values as a function of pL for 10 mC cm^{-2} thick CoCat films in 0.1 M KPi solution made by water (blue circles) or deuterated water (red triangles). The solutions were either (a) stirred during measurements or (b) not stirred. Solid lines are parabolic fits (fit parameters are listed in Tab. 4.2) and vertical lines indicate the minimum of the parabola. Error bars represent the standard deviation of three independent measurements, in the case of not-stirred solutions the experiment was repeated only twice and no standard deviation was calculated.

For the stirred solutions the minimum of the parabola is at pH 7.19 ± 0.07 and pD 7.57 ± 0.04, for H_2O and D_2O made solutions respectively (all fit parameters in Tab. 4.2). These values are in great accordance with the reported pK_a values for the phosphoric acid second deprotonation step: pK_aH 7.20, pK_aD 7.78 (Robinson, 1969).

Table 4.2: Parabolic fit parameters for the Tafel slope values as a function of pH referring to data in Fig. 4.7.[a, b]

	stirred		not stirred	
	H_2O	D_2O	H_2O	D_2O
pK_a	7.19 ± 0.07	7.57 ± 0.04	7.13 ± 0.05	7.6 ± 0.04
Vertex y (V_y)	68.9 ± 0.4	76.0 ± 0.2	74 ± 2	81 ± 2
Steepness (a)	4.4 ± 0.4	5.3 ± 0.3	13.0 ± 1.1	16.0 ± 1.4

[a] The fitting equation is $f(pH) = V_y + a(pH - pK_a)^2$.

[b] In the case of the stirred data a weighted fit is performed. The weighting factors are the standard deviations obtained from three repetition of the experiment.

The buffering capacity (β) measures the resistance of a buffer to pH changes due to the addition of a strong acid or base, in our case the ability to neutralize the protons produced during the oxygen evolution reaction. The buffering capacity varies with pH and has a maximum when the pH is equal to the pK_a of the buffering species, see $\beta(pH)$ for KPi in Fig. 4.8a. The Tafel slope values can also be simulated with the inverse of the buffer capacity (4.8b). Thus, a lower value of the Tafel slope corresponds to a higher value of the buffer capacity of the solution, because a buffer with a higher buffer capacity can better neutralize the protons released during OER. The same behavior was also found for CoCat in borate buffer (KBi) in a bachelor thesis that I helped to supervise (Schwendke, 2018).

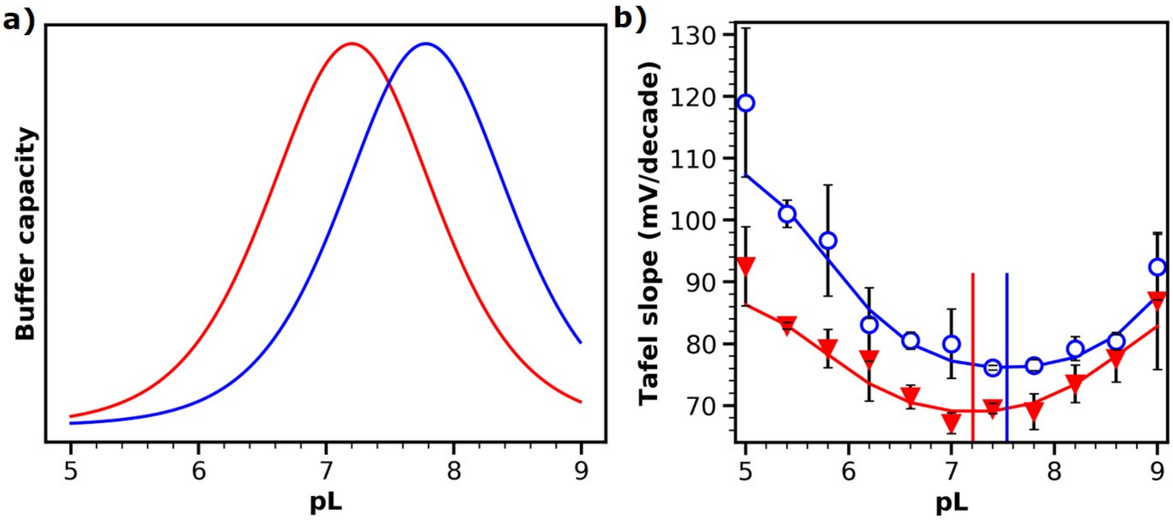

Figure 4.8: (a) Theoretical buffer capacity (β) for 0.1 M KPi made by water (red) or deuterated water (blue). The buffer capacity was calculated using $\beta(pH) = 2.303\frac{C_B K_a [H^+]}{(K_a+[H^+])^2}$, where C_B is the buffer concentration, K_a is the acid dissociation constant and $[H^+]$ is the proton concentration. (b) Tafel slope values as a function of pL for 10 mC cm^{-2} thick CoCat films in 0.1 M KPi stirred solution made by water (blue circles) or deuterated water (red triangles). The solid lines are a fit of the inverse of the buffer capacitance $\frac{A}{\beta(pH,pK_a)+C} + B$. The obtained pK$_a$ values are indicated with vertical lines and correspond to 7.21 ± 0.09 and 7.54 ± 0.03, for water and deuterated water solutions respectively.

In the linear region of a Tafel plot, the slope was proven to have a parabolic dependence on pH, with a minimum at the pK$_a$ of the used buffer. From there, an inverse dependence of the Tafel slope from the buffer capacity of the solution is derived, meaning that the Tafel slope is lower (better catalytic performances), when the solution can efficiently remove the protons released during OER. The observed behavior suggests that proton transport limitations are strongly influencing the catalytic current, also at relatively low overpotential, and may lead to higher Tafel slope values and incorrect interpretation of the reaction mechanism.

4.3 Discussion

In ref Dau, 2019, we proposed a simple model to study the effect of proton transport limitations on the catalytic activity. The model main characteristics are:

- protons are produced at the catalyst surface, no proton transport inside the catalyst is considered (infinitely thin catalyst);
- the catalytic current dependence on applied potential and pH follow the Buttler-Vollmer and the Nernstian equations, respectively;

- the proton diffusion in the electrolyte is mediate by the diffusion of buffer molecules which follow Fick's law.

In this chapter, the three predictions made by the model were verified employing electrochemical experiments performed at different pHs and by Raman spectroscopy.

1. At high current densities (mass transport limited region in Fig. 4.5a), the catalytic activity is controlled by the transport of protons. A maximum current density (J_{max}) can be defined, which is proportional to the concentration of unprotonated buffer molecules ($[A^-]$), according to $J_{max} = k_D[A^-]$. k_D is an effective diffusion constant, defined as $k_D = FD/(d_{el}/2)$, where F is the Faraday constant, D is the diffusion coefficient and d_{el} is the distance between the two electrode. In section 4.2.3, a pH titration experiment in the high current density region was performed. A linear dependence of the catalytic current with the concentration of unprotonated buffer molecules was found (see Eq. 4.3) and k_D was determined in both water and deuterated water (reported as c in Tab 4.1).

2. The Tafel slope is composed of a term, equal to the intrinsic Tafel slope of the electrocatalyst material, which dominates at low current densities, and a term affected by the pH at the electrolyte catalyst interface, which dominates at higher current densities or for insufficient buffering capacities. At intermediate current densities, both terms count and the Tafel slope have an inverse dependence on the buffer capacity of the electrolyte. An example of the Tafel slope values predicted by the model is shown in Fig. 4.9. In section 4.2.4, Tafel slope values were measured for a series of pH, revealing the same pH dependence predicted by the model but slightly higher Tafel slope values (compare Fig. 4.9 and Fig. 4.7). The data confirmed the inverse dependence of the Tafel slope on the buffer capacity of the electrolyte (Fig. 4.8).

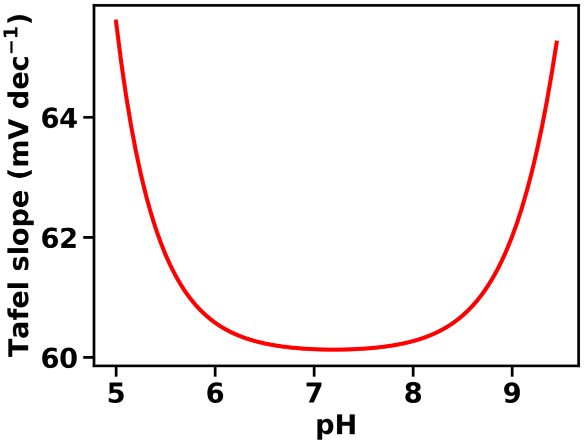

Figure 4.9: Tafel slopes at various pH extrapolated at 1 µA cm^{-2}, calculated according to the derivative of Equation (20) in ref (Dau, 2019). The following parameters were used in the simulation: $\alpha_{ET} = 1$, $k_D = 18.8$ mA cm mol^{-1}, $B_0 = 0.1$ M, $pK_{aB} = 7.20$.

3. The limitations of proton transport are assigned to proton transport in the electrolyte phase. If this is the case, acidification of the electrolyte near the electrode surface is expected. In section 4.2.2, operando Raman spectroscopy revealed local acidification

(extending over 100 µm) of the electrolyte in the proximity of the OER catalyst under operating conditions.

4.4 Summary

Operando Raman spectroscopy is able to measure the pH of a buffer solution with a spatial resolution of tens of micrometers. For CoCat operated at catalytic potentials in standard KPi buffer (0.1 M, pH 7), the acidification of the electrolyte is observed, up to around 100 µm distance from the catalyst and with 5 min depletion time. The local pH changes prove that the oxygen evolution reaction at neutral pH is affected by proton transport limitations in the electrolyte, even in the presence of a buffer and at intermediate current densities.

As predicted by our model (Dau, 2019), here is shown that the local acidification affects the catalyst efficiency causing a change in the Tafel slope of the reaction. Ignoring the effect of local pH changes on the Tafel slope can lead to incorrect mechanistic interpretations. When the pH of the solution does not correspond to the pK_a of the buffer, the buffer capacity of the electrolyte is decreased and an increase of the Tafel slope values, due to local pH changes, is observed. As predicted by our model, at intermediate current densities the Tafel slope values are inversely proportional to the buffer capacity. This means that Tafel slope values have a parabolic dependence on the solution pH, with a minimum at the buffer pK_a.

At current densities higher than the linear Tafel region, there is a region dominated by proton transport limitations. Here, the current densities are directly proportional to the concentration of deprotonated buffer molecules, in accordance with our model. In this region, the effective diffusion constant of buffer molecules was calculated: the value in water is roughly double that in deuterated water.

4.5 Experimental details

Electrochemical deposition and analysis

CoCat thin films were prepared by anodic electrodeposition following an established protocol (Kanan, 2008; Klingan, 2014), slightly modified: a potential of 1.05 V_{NHE} was applied in a 0.1 M phosphate buffer (KPi) at pH 7 containing 0.5 mM $Co(NO_3)_2$ solution, until the accumulation of a fixed charge on the working electrode (1 cm^2 exposed area). The conversion from deposited charge to sample thickness is 1 mC = 7 nm, as calculated in ref (Klingan, 2014). Sample preparation, as well as electrochemical analysis, were performed in a single-compartment three-electrode cell, using a Pt grid (2x2 cm^2, 90% purity) as a counter electrode and an Ag/AgCl(saturated) as a reference electrode. The working electrode was either an indium tin oxide (ITO) coated glass slide (VisionTek Systems Ltd, 1 cm^2 working area) or, in the case of Raman spectroscopy, a 0.1 mm thick sheet made of Pt with 99.95% purity (Labor-Platina Kft.). For the parallel deposition of 10 films and the Tafel slope measurements, 10 units of potentiostat Interface 1000 (Gamry Instruments) were used, while the other experiments were performed with a SP-200 potentiostat (BioLogic). Films were dried for at least 24 h in air before performing the experiments, to improve sample stability. The testing solution for all experiments was 0.1 M phosphate buffer (KPi) at different pHs, made using either MilliQ water (>18 MΩ cm) or deuterated water (purity 99.8%, Roth) and mixing the appropriate amount of KH_2PO_4 and

K_2HPO_4 to obtain the desired pH. The pL in D_2O electrolytes were calculated by adding 0.4 pH units to the pH-meter reading obtained with a H_2O-calibrated pH-meter (Covington, 1968). A fresh-deposited film was used for each different pH and hydrogen isotope. The potential drop due to resistance (R≈50 Ω) was compensated during data analysis.

For the titration experiment, the resistance was calculated at the beginning (at the lowest pH investigated) and then used for an 80% iR compensation. The solution was stirred during measurements and the current value was noted after ca. 60 s equilibration time.

Operando Raman spectroscopy and video recording

Raman spectra were collected operando using a confocal geometry and a self-made Teflon cell, with the incident laser hitting the catalyst from the top (Fig. 3.2). The Renishaw inVia Raman spectrometer was coupled with a Leica microscope equipped with a water immersion objective (N.A. 0.8). A grating of 2400 lines/mm and a slit size of 20 µm were used. The spectral position was calibrated on a Si wafer and a laser excitation at 473 nm was used. Raman spectra were neither rescaled nor shifted and no background subtraction was performed. Applied potentials are reported in the NHE scale. The area of the Raman peaks was calculated with the in-house software "gloFit" by first subtracting a polynomial background and then simulating the spectra with three Lorentzian functions. The positions and the FWHMs of the Lorentzian functions were obtained by a global fit (examples and parameters in Fig. 4.1).

5 O_2-bubble formation and catalyst destruction traced by video microscopy and Raman spectroscopy

5.1 Context and motivations

Research on water oxidation usually focuses on the reaction mechanism at the atomic level. However, the optimization of macro-factors (e.g. electrochemical cell design, mass transport, catalyst stability) is as important as catalyst efficiency for the construction of an efficient and functional electrolyzer prototype (McKone, 2014; Xu, 2019; Zeng, 2010). In chapter 4, the negative effects of proton transport limitations on the catalytic activity are investigated. In this chapter, we focus on the other OER product: molecular oxygen. The release of molecular oxygen from the catalyst, in the form of bubbles, influences catalyst activity, mass transport in the electrolyte and especially catalyst stability.

The presence of bubbles or nanobubbles with high residence time on the catalyst surface (Seddon, 2011) can isolate part of the catalyst from the electrolyte, reducing the catalytic activity (Vogt, 2012; Zeng, 2010). However, bubbles are also beneficial to catalysis, the bubble flow can have a stirring effect on the electrolyte and improve mass transport (Singh, 2015). The dominating effect depends on the behavior of the bubbles (Janssen, 1978), which is influenced by many factors, including the nature of the gas, the electrolyte, the catalytic surface and the rate of catalysis (Fernández, 2014; Janssen, 1970; Janssen, 1973). The optimization of these factors led to the development of nano-porous architectures, where the bubbles have low contact areas and therefore low adhesive force to the surface (Lu, 2014; Zeradjanin, 2014). In the case of CO_2 reduction, it has been shown that spiked catalyst structures favor smaller and more frequent bubbles, improving mass transport and increasing by 4-fold the current density (Burdyny, 2017).

Molecular oxygen release has also a strong impact on catalyst stability, the mechanical stress caused by bubble formation and detachment on the catalyst surface can damage the catalyst (Spoeri, 2017). For certain perovskite catalysts, structural oscillations due to the formation of oxygen nanobubbles in the first layers of the material were observed by environmental transmission electron microscopy (TEM) (Han, 2016; Ronge, 2021). In the case of an amorphous catalyst like CoCat, where molecular oxygen is formed in the bulk of the catalyst (Surendranath, 2010; Klingan, 2014), the impact could be even more disruptive.

This chapter employs operando microscopy to observe and characterize bubbles formation on CoCat and its dependence on the substrate material and on the applied potential in a qualitative fashion. The effects of bubble-type on catalytic activity are discussed. It is proven that, for a sufficiently thick catalyst film, microbubbles can form inside the catalyst bulk and damage it during their release. Bubbles release can cause abrupt stops of catalytic activities and macroscopically visible and irreversible sample damage. The choice of the substrate material and of the film thickness becomes essential to enable operation at high current densities without catalyst destruction and improve the lifetime of amorphous water-splitting catalysts. Redeposition of a thin catalyst layer on the damaged areas is observed using Raman spectroscopy.

5.2 Results

5.2.1 Phenomenology of oxygen-bubbles formation

Molecular oxygen leaves the catalyst surface in the form of bubbles, in this section, operando microscopy is employed to investigate the phenomenology of bubbles formation. A thin layer of CoCat is deposited on a glass coated with ITO and on a Pt substrate, both commonly used in electrochemistry. The ITO shows a very smooth surface on a micrometer scale, while the Pt sheets are rough with a series of small scratches and cracks. The overlaying catalysts reproduce the irregularities of the substrates, resulting in two very different catalyst-solution interfaces (Fig. 5.1).

At catalytic potentials, bubbles form on the catalyst surface and are released. Using a microscope equipped with an immersion objective, it is possible to observe a large variety of bubbles, with radius (r) varying from few µm to hundreds of µm. On the ITO surface big bubbles ($r > 200$ µm) dominates and there are relatively few bubbles, while on the Pt surface a large number of bubbles are visible, mostly of smaller size ($10 < r < 200$ µm), see an example in Fig. 5.1 and Video 1.

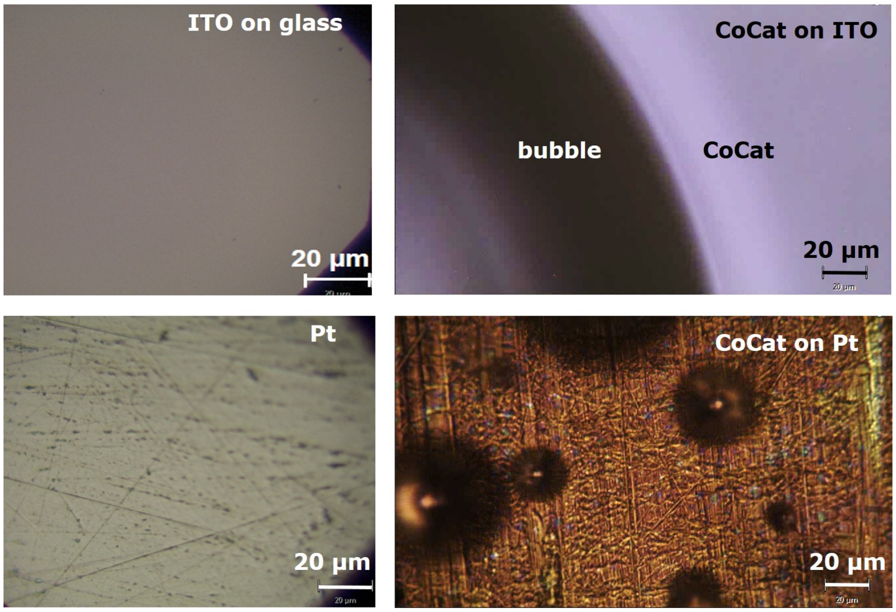

Figure 5.1: Left: microscope images of a bare substrate before catalyst deposition, ITO on glass (top picture) and Pt substrate (bottom picture). Right: microscope images of bubbles on the surface of a CoCat film deposited on an ITO layer on glass substrate (175 nm thick film, top picture) or a Pt substrate (280 nm thick film, bottom picture). The images were recorded operando, under exposure to catalytic potentials. The theoretical optical resolution of the immersion objective with a numerical aperture of 0.8 is around 400 nm, a figure which is confirmed by visual inspection of microscope images, e.g. for the scratches in the Pt surface.

Video 1. `https://vimeo.com/584088524`

> CoCat film deposited on a Pt substrate (280 nm film thickness) and operated at 1.4 V_{NHE}. The video shows the growth of a bubble on the catalyst surface, starting in the millisecond time domain with a diameter well below 5 μm. Eventually, the bubble detaches and disappears. With a delay of 20 s seconds, a second bubble starts to form at the same site.

The irregular Pt surface favors smaller oxygen bubbles, because the rough surface:

1. reduces adhesion limiting bubbles residence times on the surface and therefore bubbles size;

2. offers various nucleation sites for bubbles formation.

Bubbles usually repeatedly appear at the same spot, with an interval of some seconds between a bubble and the subsequent, suggesting that the formation of an optically visible microbubble follows the presence of a certain concentration of molecular oxygen or of smaller nanobubbles on the catalyst surface.

An example of a bubble growth with time on a Pt substrate is shown in Fig. 5.2 for two different catalytic potentials. At the higher potential shown, the catalytic current is ca. three times higher than at the lower, meaning that three times more oxygen is produced. This can give rise to faster bubble production (like in the case shown in the figure) or to more bubble spots. The time between bubble release and formation of a new bubble can variate from several seconds to less than a second, depending on the bubble release site, but, in the observed case, it does not depend on the applied potential.

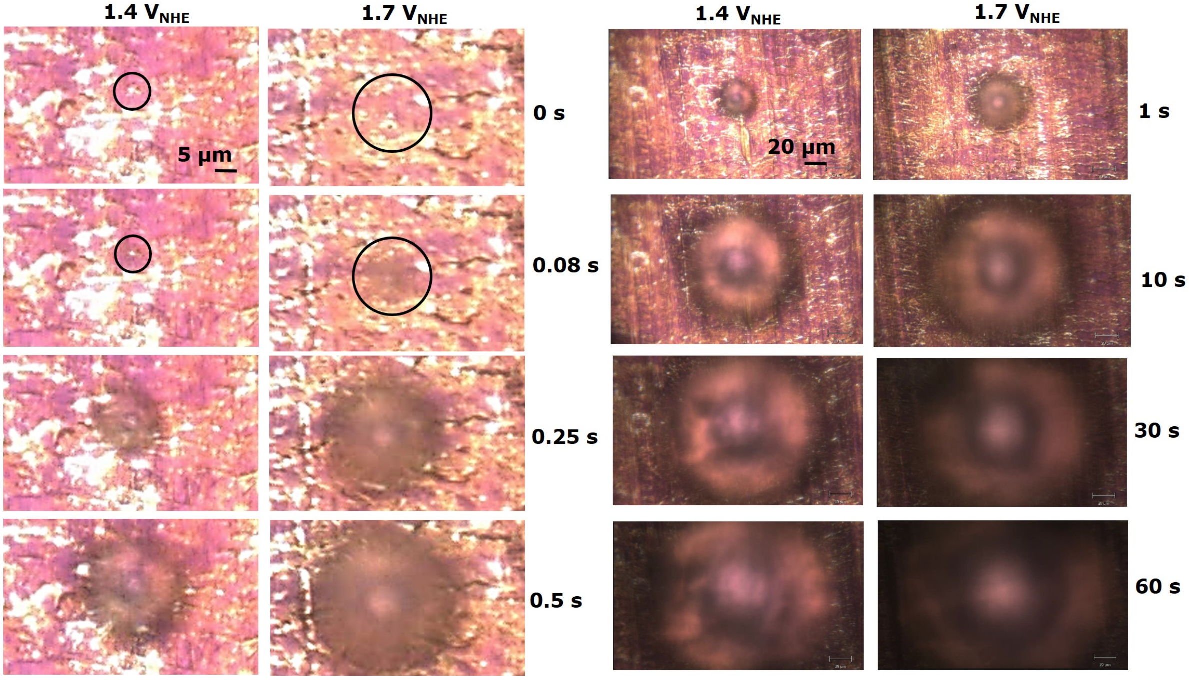

Figure 5.2: Microscope images reporting the growth of one bubble in time, for a 280 nm thick CoCat film on a Pt substrate. Two different catalytic potentials were applied: 1.4 V_{NHE} resulting in 0.7 mA catalytic current (upper panels) and 1.7 V_{NHE} resulting in 2.2 mA catalytic current. The left panels show the short time growth and have a smaller spatial scale than the right panels. Video 1 contains the complete video on bubble formation at 1.4 V_{NHE}.

The formation of optically visible bubbles on the catalyst surface was investigated using operando microscopy. Bubbles can repeatedly form in specific bubble sites, but there is a large variety of bubbles sizes and bubbles residence times between different sites and even within bubbles formed on the same site. The nature of bubble sites is extremely flexible and they can also be inactivated after releasing a certain number of bubbles. The size and number of bubbles are influenced by the substrate used, namely, the irregular Pt surface favors smaller and more numerous bubbles in respect to the smooth ITO surface. Small bubbles in large numbers can help catalytic activity by improving mass transport in the electrolyte (Janssen, 1978; Burdyny, 2017; Singh, 2015). On the other hand, large bubbles with high residence time on the surface can suppress OER by covering some Co-active sites and separating them from the electrolyte (Zeradjanin, 2014).

5.2.2 Calculation of bubble feeding area

In the following, the area of the film responsible for producing the oxygen that feeds an average bubble during its growth on the film surface is calculated. The calculation is performed for the bubble growth on a 280 nm thick CoCat film on a Pt substrate, with an applied potential of 1.5 V_{NHE}.

The calculation requires two assumptions: equal activity on all the film surfaces and equal distribution of bubble sites. The bubble leaves the film surface after $\Delta = 30.68$ s with a final diameter of d = 152.5 µm, the average current during the experiment is I = 1.2 mA.

The number of moles contained in the bubble when it leaves the film surface (mol_b) can be obtained from the diameter.

$$mol_b = \frac{V_b}{V_{mol}} = \frac{4}{3}\pi\left(\frac{d}{2}\right)^3 \frac{1}{V_{mol}} = 8.29 \cdot 10^{-11} mol \tag{5.1}$$

Where V_b is the bubble volume and V_{mol} is the volume of 1 mol of gas at standard pressure and temperature. For each molecule of oxygen produced, 4 electrons are transferred from the film to the oxygen atoms, thus the charge necessary to produce the bubble (Q_b) is:

$$Q_b = 4N_{b,O_2} q_{e^-} = 4 mol_b N_A q_{e^-} = 32\mu C \tag{5.2}$$

Where N_{b,O_2} is the number of oxygen molecules in a bubble, N_A is the Avogadro number and q_{e^-} is the electron charge. The ratio between the area responsible for feeding the bubble (A_b) and the total electrode area ($A_T = 0.7cm^2$) is equal to the ratio between the charge fed to the bubble (Q_b) and the total charge (Q_T).

$$A_b = \frac{Q_b}{Q_T} A_T = \frac{Q_b}{I\Delta t} A_T = 6.1 \cdot 10^4 \mu m^2 \tag{5.3}$$

The area of the film responsible for feeding a bubble corresponds to a circle with a diameter of 278 µm. A repetition of the calculation for another bubble at the same site returned a similar value ($A_b = 5.6 \cdot 10^4 \mu m^2$). However, it is important to note that on the same electrode and under the same conditions there is a large variety of bubble sizes and bubbles residence times and the one examined here is only exemplary.

5.2.3 Oxygen bubbles can damage the catalyst

In the previous sections, bubbles formation on a catalyst surface for a 240 nm thick catalyst film was investigated. The behavior is very different for a thicker catalyst (2.1 µm thickness), where large quantities of oxygen are formed in the bulk of the catalyst, separated by many layers from the catalyst-electrolyte interface. This section reveals that oxygen can nucleate into microbubbles already inside the catalyst, causing major damage and catalyst degradation during microbubbles release.

The CoCat catalyst is known to be a bulk active material (Surendranath, 2010; Klingan, 2014), producing molecular oxygen not only at the catalyst-electrolyte interface but also in the inner layers (catalyst bulk). Molecular oxygen can percolate to the catalyst-electrolyte interface or nucleate into microbubbles and break the catalyst surface to be released. By observing the surface of a thick catalyst film during operation, evidence for the second phenomenon is found. Namely, a semicircular cut is formed on the catalyst surface, a flap rises and lets a microbubble escape, several examples of this phenomenon were observed, examples are shown in Fig. 5.3a and Video 2. The bubble continues to grow once reached the catalyst surface. Semicircular cuts or openings are often visible on the surface of a thick catalyst film after operation (Fig. 5.3b).

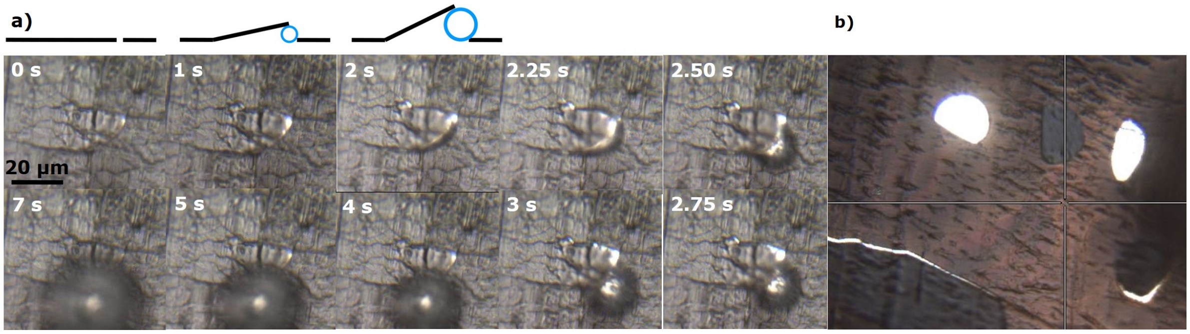

Figure 5.3: Bubble release and related film damage for a 2.1 µm thick CoCat film on a Pt substrate. (a) Microscope images reporting the release of an oxygen microbubble formed in the bulk of the catalyst. In the upper part of the figure, a scheme with the side view of the bubble release process is shown. Video 2 contains the complete video. (b) Example of a catalyst film damaged by bubbles formation.

Video 2. `https://vimeo.com/584088355`

> CoCat film deposited on a Pt substrate (2 μm film thickness) and operated at 1.4 V_{NHE}. The video illustrates the destruction of the catalyst film due to bubble formation causing the detachment of the film from the substrate. The CoCat film is visible as a grey area with a structure determined by the underlying Pt substrate. The bright areas correspond to areas of the Pt metal surface that are not covered by any CoCat film and consequently reflect the light strongly. In the center, the video features the release of bubbles from a semicircular flap. On the upper-left side, a defect caused by bubbles is visible, where a part of the CoCat film, already detached from the underlying substrate, is moved away from the surface by bubbles formation.

To study the damages suffered by the catalyst, due to bubble formation, I performed a cyclic voltammetry experiment and observed operando the catalyst surface (Fig. 5.4 and Video 3). It is possible to notice that:

- The second CV has a lower catalytic current and smaller redox area than the first CV.
- During the first forward scan the catalyst becomes darker with increasing potentials as previously revealed by UV/vis experiments (see section 2.3.7).
- During the backward scan and the second CV cycle only small part of the film, likely in an area where the film is thinner, change their color.

- During the last backward scan there is a semicircular cut on the catalyst surface.

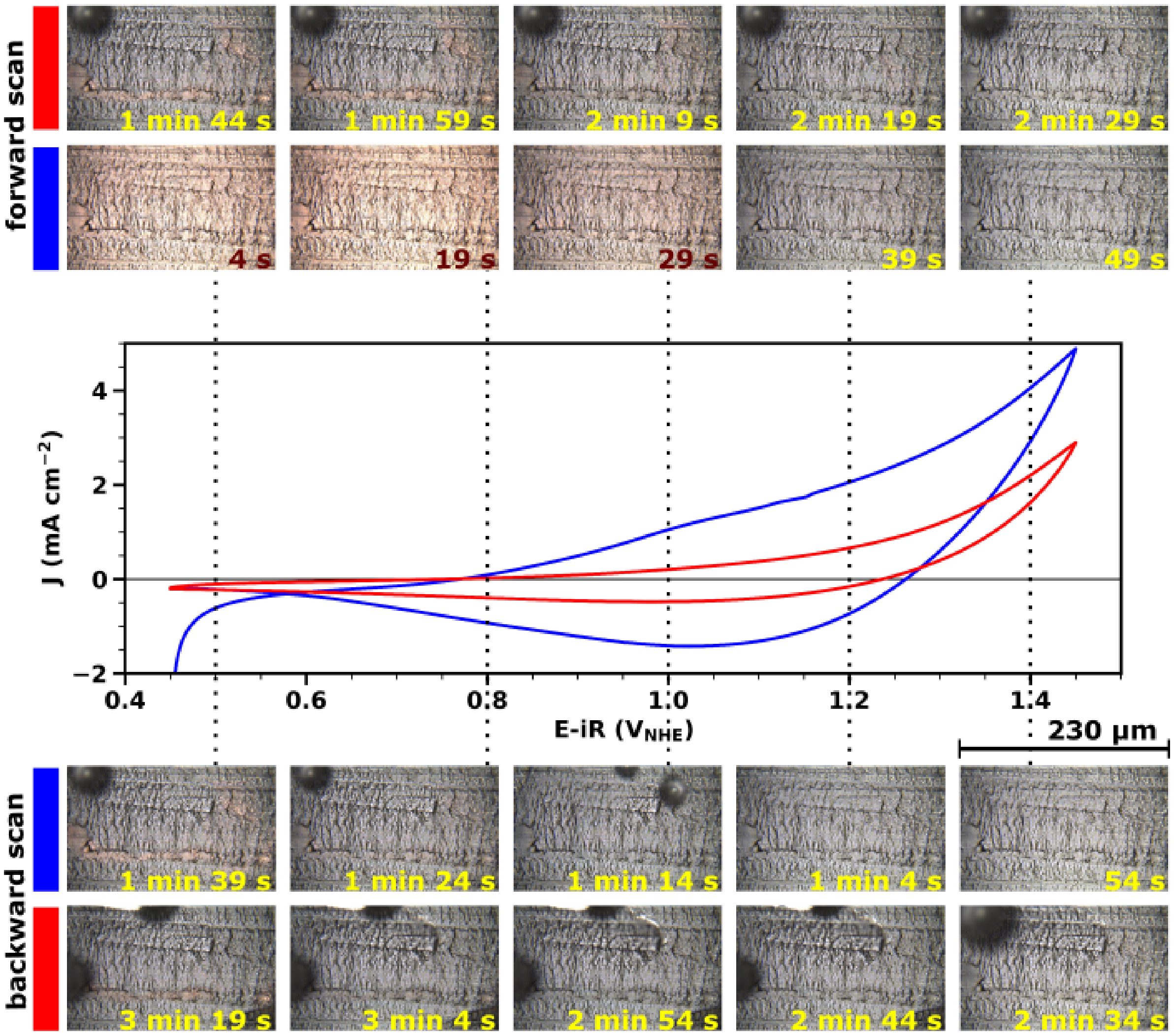

Figure 5.4: Microscope images obtained operando during a cyclic voltammetry experiment (at 20 mV s^{-1}, one CV takes 100 s) for a 2.1 µm thick CoCat film on a Pt substrate. The first cycle is shown in blue, the second in red, the third cycle was equal to the second and is not shown, the same color code is used for the images. The vertical dotted lines indicate the potential at which each image was collected. The corresponding video is Video 3.

Video 3. `https://vimeo.com/584088392`

Two cyclic voltammetry cycles (at 20 mV s^{-1}) for a CoCat film deposited on a Pt substrate (2.1 μm film thickness). The panel on the left side shows the recorded current, while the panel on the right side features the film surface, the two panels were recorded at the same time. The video illustrates the change in color of the Pt surface due to the applied potential, the delayed formation of bubbles and catalyst damage, caused by bubbles.

These observations point towards microbubbles forming in the bulk of the catalyst and breaking it or disconnecting it from the substrate. During the CV is also possible to see the surface inflating for the underlying bubbles. Only the portion of the catalyst which can still maintain a connection to the substrate can change its oxidation state, resulting in reduced color change and reduced catalytic activity during the second scan.

Furthermore, the first bubbles appear on the catalyst surface only during the backward scan, suggesting a delay between oxygen production and the nucleation of a microbubble. This was supported by a second experiment, where we applied a catalytic potential and then switched to OCP. Bubbles kept forming on the catalyst surface up to 5.8 s after turning off the potential.

When a thick film is operated for a long time at catalytic potentials, most of the film is removed from the substrate. A visual analysis of the surface reveals the presence of brownish areas on the Pt substrate, together with fragments of the catalyst film (visible as black areas), see Fig. 5.5 and 5.6a. During operation, bubbles are produced mostly by the catalyst fragments (Fig. 5.6b).

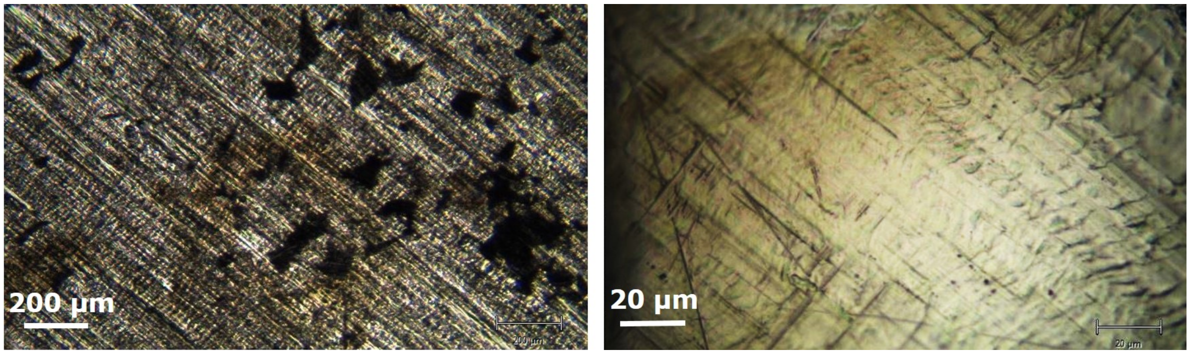

Figure 5.5: Microscope images of a dry 2.1 µm thick CoCat film on a Pt substrate after prolonged operation at 1.38 V_{NHE}. The bubbles produced during catalytic operation damaged the film. The sample was cleaned with MilliQ water and dried before examination. Left panel has 5 times magnification, right panel 50 times. Black areas are remaining fragments of the CoCat film, brownish areas are most likely Co atoms redeposited from solution during operation.

Raman spectroscopy confirmed that the brownish areas are made of Co (Fig. 5.6a), which has a peak at 600 cm^{-1} (see section 3.3). Two hypotheses for their formation were considered: (1) the brownish areas are made by Co atoms which dissolved from the catalyst and were later redeposited or (2) a thin layer of CoCat is left on the Pt surface, when the upper layer peels off. The redeposition hypothesis is supported by the fact that these layers are very thin and they cover only portions of the Pt substrate. The redeposition hypothesis would suggest that, in the case of Pt substrates, microbubbles are formed between the substrate and the catalyst, rather than in the catalyst bulk, and cause the peel off of the entire catalyst film.

For thinner catalyst films the presence of bubbles is less disruptive, because the density of molecular oxygen in the bulk of the film is lower and bubbles usually form at the catalyst-electrolyte interface. However, even for 70 nm thick CoCat films degradation was observed during prolonged operation at catalytic potentials (above 1.3 V_{NHE}), when the film is operated at 1.5 V_{NHE}, catalytic activity is reduced by ca. 90% in the course of 15 h (Mohammadi, 2020). This degradation can also likely be assigned to bubbles.

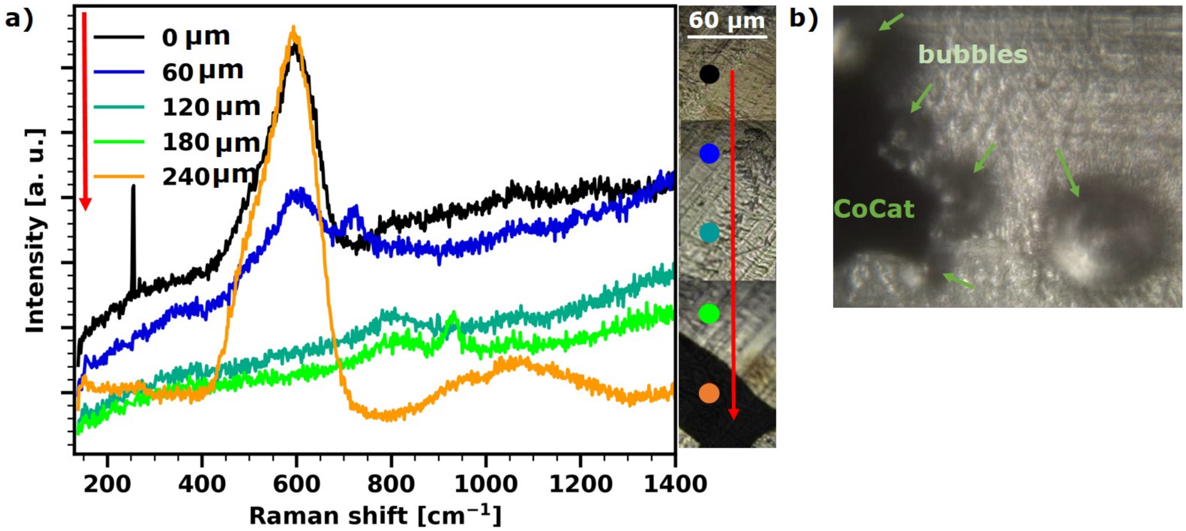

Figure 5.6: (a) Raman spectra of a CoCat film on a Pt substrate (film thickness of 2.1 µm), the catalyst film was damaged by oxygen bubbles produced during operation at 1.38 V_{NHE} for several minutes. The right panel shows five consecutively acquired microscope images of the catalyst surface, the colored points indicate the five positions at which Raman spectra were collected (sequence of data collection indicates by red arrow). The measurements were performed on the dry sample after washing it with MilliQ water. Spectra are neither rescaled nor shifted. (b) An operando microscope image of the damaged catalyst under operation at catalytic potentials. Bubbles in the process of forming are visible, as well as a remaining part of the damaged catalyst film.

In a thick CoCat film, the oxygen produced during OER forms microbubbles inside the bulk of the film. The presence and release of microbubbles damage the catalyst, by breaking it and detaching it from the substrate. Catalyst destruction can strongly affect industrial applications, where thick catalyst films, high current densities and long operation times are needed. The use of metal foam substrates in flow cell arrangements may alleviate the problem of bubbles damages, by supporting higher catalyst loading without increasing the film thickness.

For research purposes, it is important to avoid high current densities and thick catalyst films (film thicknesses lower than 200 nm are suggested) to prevent extensive damage caused by bubbles. As observed during a CV on a thick film (Fig. 5.4), partial catalyst damage or detachment of the catalyst from the substrate can be hard to detect optically, but still produces unreliable experimental results. Thus, it is suggested to control the connection between the catalyst and the substrate at the end of each experiment (e.g. with an impedance measurement).

5.3 Summary

Molecular oxygen is a product of the oxygen evolution reaction, which is normally released from the catalyst surface in the form of optically-visible bubbles. Operando microscopy measurements show a rather large variability in bubble size and time passed between subsequent bubble releases and the presence of preferred bubble-release sites. The roughness of the catalyst surface, which replicates the roughness of the underlying substrate, has a strong influence on the size of the bubbles and on the frequency of their release. A rough surface (e.g. CoCat on unpolished Pt substrate) produces smaller and more frequent bubbles, frequent bubbles release stirs the solution and can improve proton transport. On the contrary, a flat surface (e.g. CoCat on ITO substrate) presents more than 10 times larger bubbles with higher residency time, which can isolate part of the catalyst decreasing catalytic activity. The catalyst area that feeds a single average bubble (with a final diameter of 150 µm) was estimated as a circle with a diameter of 278 µm. A lag phase between potential application and bubble formation suggests that microbubbles form from a microscope-invisible precursor, i.e. dissolved molecular oxygen or nanobubbles.

When the catalyst film is sufficiently thick (already observed over 2 µm thickness), oxygen molecules nucleate in the bulk of the catalyst, forming microbubbles that break the film or detach it from the substrate. Even for thin films (70 nm thickness) the strong decrease in catalytic activity observed for prolonged operation at catalytic potentials (Mohammadi, 2020) can likely be assigned to bubble damage. Redeposition of thin CoCat films was observed in some of the areas where the catalyst film has been peeled off from the substrate. The damage caused by bubbles release to thick films is permanent and strongly reduces their catalytic activity and lifetime. The use of foam substrates is proposed as a possible solution to enable the high current densities needed in industrial applications. For mechanistic investigations short operation times and the use of thin catalyst films (suggested below 200 nm) are mandatory to obtain reliable results.

5.4 Experimental details

Electrochemical deposition and analysis

CoCat thin films were prepared by anodic electrodeposition following an established protocol (Kanan, 2008; Klingan, 2014), slightly modified: a potential of 1.05 V_{NHE} was applied in a 0.1 M phosphate buffer (KPi) at pH 7 containing 0.5 mM $Co(NO_3)_2$ solution, until the accumulation of a fixed charge on the working electrode (1 cm^2 exposed area). The conversion from deposited charge to sample thickness is 1 mC = 7 nm, as calculated in ref (Klingan, 2014). Sample preparation, as well as electrochemical analysis, were performed in a single-compartment three-electrode cell, using a Pt grid (2x2 cm^2, 90% purity) as a counter electrode and an Ag/AgCl(saturated) as a reference electrode. The working electrode was either an indium tin oxide (ITO) coated glass slide (VisionTek Systems Ltd, 1 cm^2 working area) or a 0.1 mm thick sheet made of Pt with 99.95% purity (Labor-Platina Kft.). Experiments were performed with a SP-200 potentiostat (BioLogic). Films were dried for at least 24 h in air before performing the experiments, to improve sample stability. MilliQ water ($>$18 MΩ cm) was employed to prepare the 0.1 M phosphate buffer (KPi) electrolyte.

Operando Raman spectroscopy and video recording

Raman spectroscopy and microscopy experiments were performed operando using a confocal geometry and a self-made Teflon cell, where the catalyst lays horizontally and the objective is positioned above the catalyst (Fig. 3.2). The Renishaw inVia Raman spectrometer was coupled with a Leica microscope equipped with a water immersion objective (N.A. 0.8) and the built-in video camera of the Renishaw was used for video recording. For Raman measurements, a grating of 2400 lines/mm and a slit size of 20 µm were used. The spectral position was calibrated on a Si wafer and a laser excitation at 473 nm was used.

6 H/D isotope effects reveal factors controlling catalytic activity in Co-based oxides leading to a mechanistic hypothesis

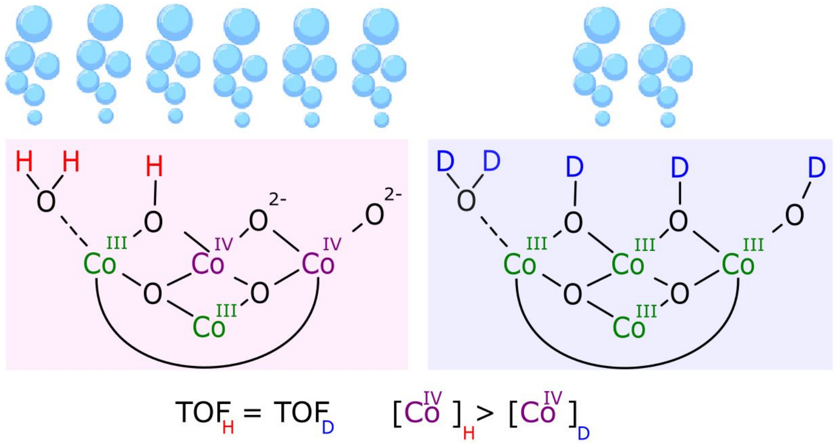

Reproduced in part with permission from

Pasquini, C.; Zaharieva, I.; González-Flores, D.; Chernev, P.; Mohammadi, M. R.; Guidoni, L.; Smith, R. D. L.; Dau, H., H/D Isotope Effects Reveal Factors Controlling Catalytic Activity in Co-Based Oxides for Water Oxidation. *J. Am. Chem. Soc.* **2019**, 141 (7), 2938-2948.
DOI: 10.1021/jacs.8b10002

Author Contributions: Data acquisition, data analysis, writing—original draft preparation, conceptualization C.P.; conceptualization, writing—review H.D. and R.S.; supervision for DFT calculations L.G.; support in synchrotron measurements and valuable discussions Z.I., D.G.-F., P.C., M.R.M.

6.1 Context and motivations

Understanding the mechanistic details of the water oxidation reaction is important for the development of more efficient catalysts. For each oxygen molecule produced, 4 protons and 4 electrons need to be released (see equation 1.1). The timing of their transfer and the factors controlling it are still debated and can contain the key to understand the factors controlling the catalytic activity.

The release of an electron is usually associate with the release of a proton, which enables accumulation of oxidizing equivalents without buildup of a charge, which would increase the required overpotential (Weinberg, 2012; Dau, 2010). Such proton-coupled electron transfer (PCET) reactions can follow a two-step pathway, where either the electron transfer or the proton transfer can be rate-limiting, or a concerted pathway (CPET) (Weinberg, 2012; Costentin, 2009; Costentin, 2007; Huynh, 2007). Isotopic substitution is a fundamental tool to investigate reactions mechanisms: the exchange of hydrogen for deuterium affects both the thermodynamics and the kinetics of proton-coupled electron transfer reactions (Krishtalik, 2000). In this chapter, the two effects are separated and, in the following, I will refer to them as equilibrium isotope effect (EIE) and kinetic isotope effect (KIE), respectively (Parkin, 2009).

An EIE implies a change in the reaction thermodynamics (Parkin, 2009; Zhang, 2012; Wolfsberg, 1972) due to an increase in the vibrational zero-point energy of a bond involving hydrogen by a factor proportional to the bond strength. Isotope exchange alters the protonation-deprotonation equilibrium if the bond strength of the proton donor differs from that of the proton acceptor, thereby shifting the standard reduction potential for the PCET reaction. On the other hand, the observation of a KIE implies a change in the kinetics of the reaction (Krishtalik, 2000; Bigeleisen, 1958) and provides proof for proton transfer being involved in the rate-determining step.

CoCat has already been used as a model to study the role of protons in amorphous oxide catalysts. Bediako et al. studied the dependence of current on overpotential (Tafel plots) with different buffer concentrations and conditions, decoupling the catalytic reaction from the proton-electron hopping inside the film (Bediako, 2013). Subsequent work focused on CV analysis to estimate a lower limit for the catalytic rate and proposed that catalysis is limited by the diffusion of the proton accepting base (Costentin, 2016). Previous works evidenced the dependence of catalytic activity on the protonation state and the nature of the buffer electrolyte, which works as a proton acceptor (Klingan, 2014; Risch, 2012; Aiso, 2017; Hunter, 2016a). An isotope effect study appears to be the missing information to enable clear distinction of the factors controlling the catalytic rate (Bediako, 2013).

Hydrogen-to-deuterium exchange has been previously applied to a molecular model compound made by Co_4O_4 units that resemble the structure of CoCat (Symes, 2011). Two cases were observed: proton and electron are transferred to the same chemical species with a CPET, or they are transferred each to a distinct chemical species with a PT-ET. The transferability of this result to the extended oxide has yet to be proven. The isotope effect on the electron conductivity inside the CoCat catalyst was investigated, in deuterated electrolytes a higher potential was needed for the film to become conductive (Brodsky, 2018). The isotope effect on similar catalysts have been examined in alkaline conditions as well, but a clear distinction between the thermodynamic and kinetic isotope effects was not reported (Aiso, 2017; Tse, 2016).

Here, the effects of hydrogen-to-deuterium and ^{16}O-to-^{18}O exchange on the water oxidation reaction by CoCat are investigated. Lower catalytic activities in deuterated buffers are consistently observed across a range of solution pH values. Analysis by visible (in-situ) and X-ray (quasi-in-situ) absorption spectroelectrochemistry enable us to identify an EIE and the absence of a KIE in the precatalytic redox transitions and to formulate a hypothesis on the factors controlling catalytic activity. The correlated behavior between the precatalytic and catalytic processes lead us to exclude deprotonation as a component of the rate-determining step. Based on these results a mechanism for water oxidation at neutral pHs is proposed.

6.2 Results

6.2.1 Isotope Effect on the Catalytic Activity

The influence of the deprotonation steps on the catalytic activity was investigated for CoCat in 0.1 M potassium phosphate (KPi) solutions in the close-to-neutral pH range ($6 \leq \text{pL} \leq 9$) using different hydrogen isotopes. Tafel plot data from galvanostatic measurements show an anodic shift in potential on the Normal Hydrogen Electrode (NHE) scale with pH decrease. The Nernst equation states that the equilibrium potential for a reaction involving the transfer of protons and electrons in equal numbers will vary by 59 mV per pH unit at room temperature. The potential needed to obtain a fixed catalytic current exhibits near-ideal Nernstian behavior (Fig. 6.1), indicating that the catalytic activity involves the coupled release of one proton per one electron transferred. Preparing electrolyte solutions with D_2O leads to further anodic shifts (Fig. 6.1a and 4.6) and to a decrease in the current at parity of potential. This effect is observed in two ways: (i) the current at 1.25 V_{NHE} and pL 7 is decreased by 87% in D_2O solutions relative to H_2O solutions, or (ii) the potential required to obtain a given current density is shifted by 58 ± 4 mV and 68 ± 8 mV for 30 and 300 µA cm^{-2} catalytic current, respectively.

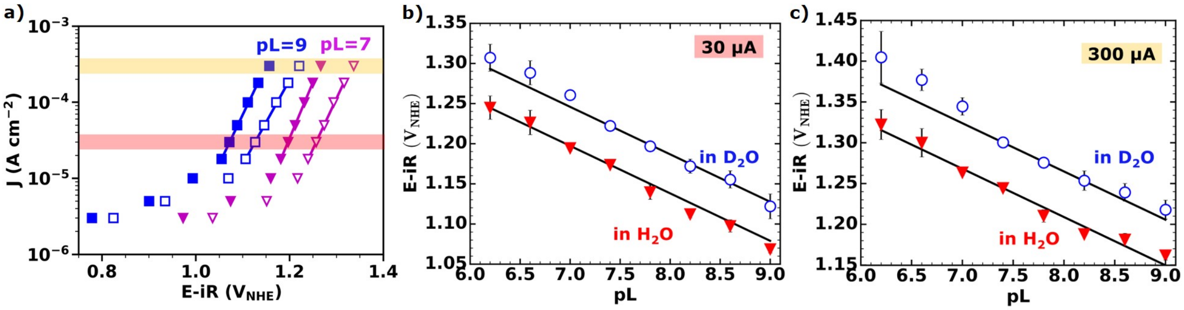

Figure 6.1: Steady state chronopotentiometry measurements (values taken after 3 min) of CoCat at different pL in 0.1 M KPi buffer prepared with H_2O or D_2O. (a) Tafel plot for selected pL (full series in Fig. 4.6) in water (closed symbol) and deuterated water (open symbols) solutions. (b) Potential needed to obtain 30 µA cm^{-2} and (c) 300 µA cm^{-2}, these current values are highlighted with colored bands in panel a. Black lines represents Nernstian behavior (59 mV pH^{-1}). The H-D shift for $6 \leq \text{pL} \leq 9$ corresponds to 58 ± 4 mV (at 30 µA cm^{-2}) and 68 ± 8 mV (at 300 µA cm^{-2}). All solutions were stirred during measurement.

6.2.2 Analysis of Kinetic Isotope Effect on Co Redox Transitions

Time-resolved in-situ visible absorption spectroscopy during “potential-jump” experiments, where the potential is stepped between a reducing and an oxidizing one, showed no evidence of a

KIE for Co redox transitions. CoCat has a wide absorption band between 400 and 700 nm (Fig. 2.12) with a molar extinction coefficient that increases linearly with Co oxidation state, as previously proven by comparison with X-ray absorption experiments (Risch, 2015) and again in this thesis (see section 2.3.7). UV-vis absorption spectroscopy thus enables the tracking of changes in the oxidation state of transition metals during electrochemical experiments (Risch, 2015; Trotochaud, 2013; Polo da Fonseca, 1994; Smith, 2017). Here, the absorption time traces recorded with 10 ms temporal resolution during potential jumps show no significant differences in kinetics when hydrogen is substituted with deuterium (Fig. 6.2a).

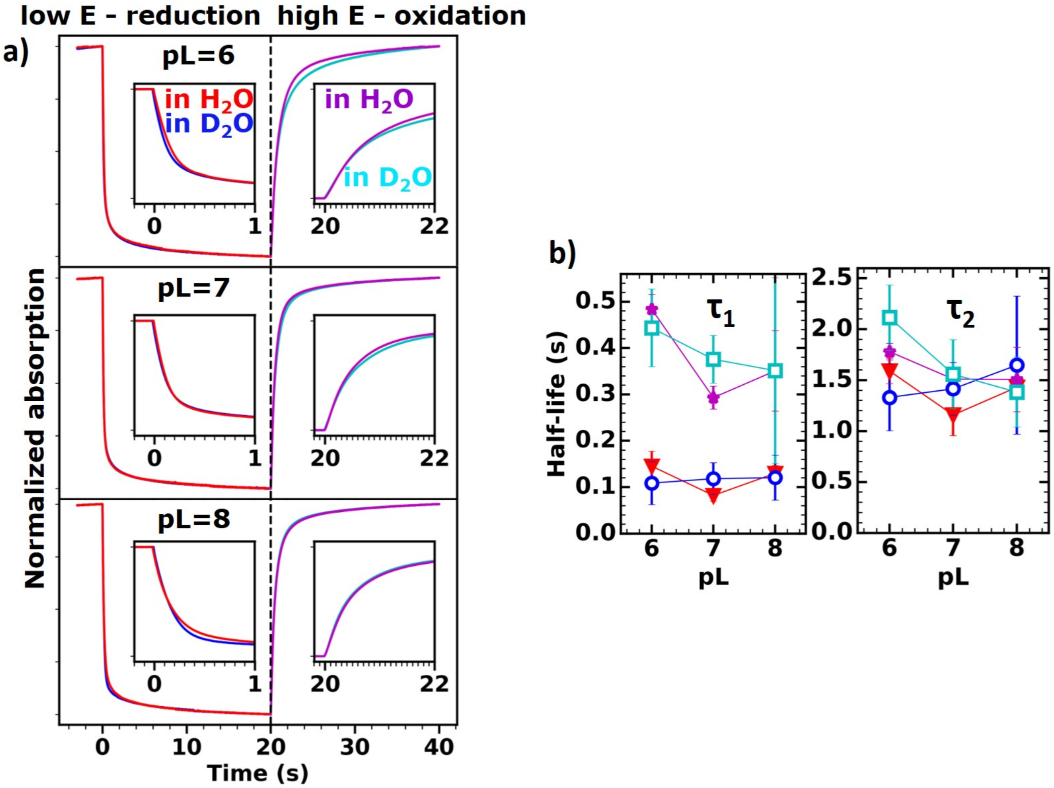

Figure 6.2: (a) Time-resolved in-situ visible absorption spectroscopy during step-wise changes between reducing and oxidizing potential, for CoCat in 0.1 M KPi H_2O electrolyte (red and violet lines) or D_2O electrolyte (blue and cyan lines) with pL 6, 7, 8. The potential jumps were repeated 30 times with a time resolution of 10 ms, the recorded absorption signals were averaged and simulated using a sum of three exponential functions. (b) Half-lives of the first two exponentials. All simulation parameters are provided in Table 6.1.

Three different time components are clearly distinguished when the absorbance is mathematically fitted (Table 6.1) or plotted on a logarithmic time scale (Fig. 6.3). The fastest phase exhibits half-lives of 0.15 s for reduction and 0.4 s for oxidation and accounts for the major changes in oxidation state. An intermediate phase with a half-life of about 1.5 s and a slow phase with a half-life in the minute regime are observed (Fig. 6.4a). During the Co-oxidation process, the oxidation of neighboring atoms and the structural rearrangements change the environment, the local pH and the effective potential inside the catalyst film. These changes likely result in a different kinetic for the oxidation of further Co atoms. The presence of multiple time constants for Co oxidation state changes is therefore believed to arise from a stretched exponential decay, here modeled as three time-phases. Half-life values for the first two phases are presented in Fig. 6.2b and show no dependence on the isotope used or on the pL. Values for the third phase are reported in Table 6.1, the third exponential was approximated to a linear decay due to the very long process studied (several minutes) as compared to the experiment time scale (40 s per jump).

Table 6.1: Parameters for the simulation of in-situ visible absorption data measured during step-wise changes between reducing and oxidizing potential.[a, b, c, d]

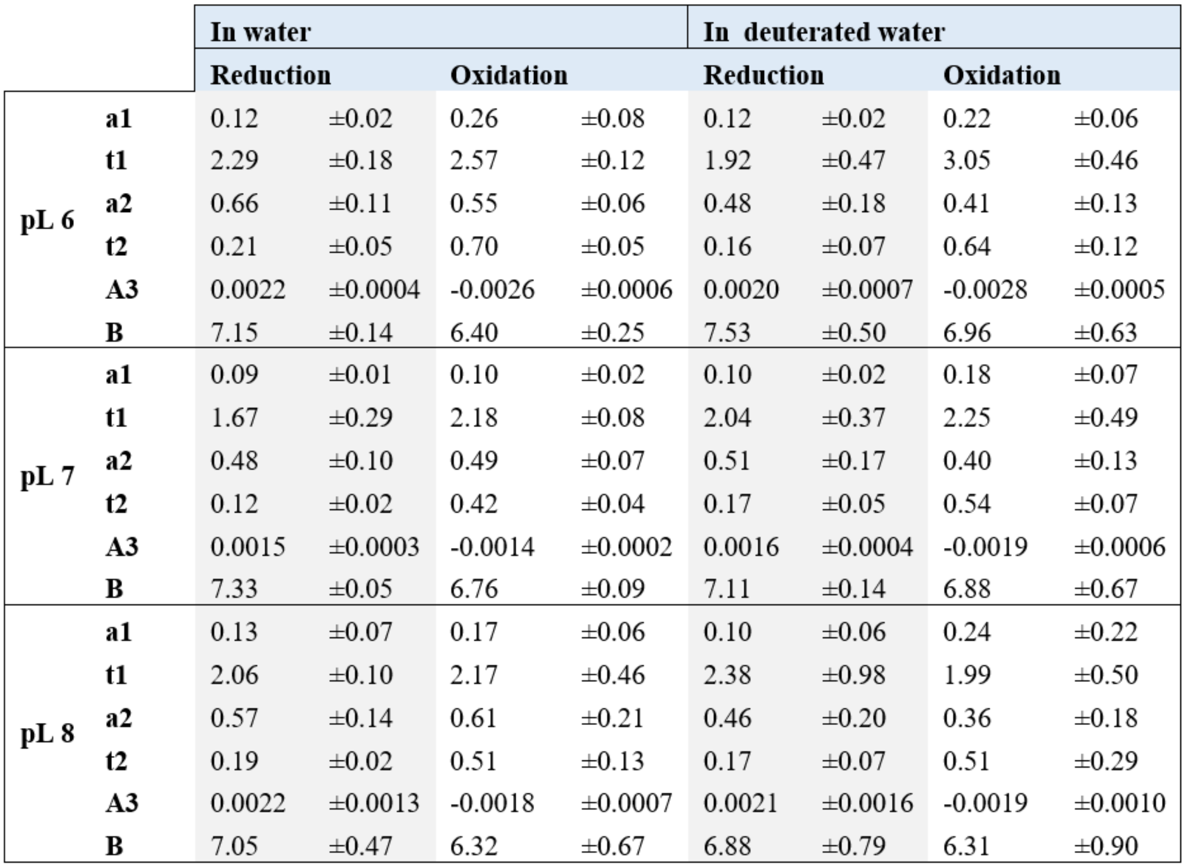

		In water				**In deuterated water**			
		Reduction		**Oxidation**		**Reduction**		**Oxidation**	
pL 6	**a1**	0.12	±0.02	0.26	±0.08	0.12	±0.02	0.22	±0.06
	t1	2.29	±0.18	2.57	±0.12	1.92	±0.47	3.05	±0.46
	a2	0.66	±0.11	0.55	±0.06	0.48	±0.18	0.41	±0.13
	t2	0.21	±0.05	0.70	±0.05	0.16	±0.07	0.64	±0.12
	A3	0.0022	±0.0004	-0.0026	±0.0006	0.0020	±0.0007	-0.0028	±0.0005
	B	7.15	±0.14	6.40	±0.25	7.53	±0.50	6.96	±0.63
pL 7	**a1**	0.09	±0.01	0.10	±0.02	0.10	±0.02	0.18	±0.07
	t1	1.67	±0.29	2.18	±0.08	2.04	±0.37	2.25	±0.49
	a2	0.48	±0.10	0.49	±0.07	0.51	±0.17	0.40	±0.13
	t2	0.12	±0.02	0.42	±0.04	0.17	±0.05	0.54	±0.07
	A3	0.0015	±0.0003	-0.0014	±0.0002	0.0016	±0.0004	-0.0019	±0.0006
	B	7.33	±0.05	6.76	±0.09	7.11	±0.14	6.88	±0.67
pL 8	**a1**	0.13	±0.07	0.17	±0.06	0.10	±0.06	0.24	±0.22
	t1	2.06	±0.10	2.17	±0.46	2.38	±0.98	1.99	±0.50
	a2	0.57	±0.14	0.61	±0.21	0.46	±0.20	0.36	±0.18
	t2	0.19	±0.02	0.51	±0.13	0.17	±0.07	0.51	±0.29
	A3	0.0022	±0.0013	-0.0018	±0.0007	0.0021	±0.0016	-0.0019	±0.0010
	B	7.05	±0.47	6.32	±0.67	6.88	±0.79	6.31	±0.90

[a] The "potential jumps" were repeated 30 times and averaged. The time resolution was 10 ms.

[b] Data were simulated as a sum of three exponential plus a constant: $a1\ \exp(-x/t1) + a2\ \exp(-x/t2) + a3\ \exp(-x/t3) + b$.

[c] Due to the slow process represented by the third exponential ($x << t3$), we report in the table values for a linear approximation of the third exponential: $a1\ \exp(-x/t1) + a2\ \exp(-x/t2) + A3\ x + B$, obtained from $A3 = -a3/t3$ and $B = b + a3$.

[d] Reported errors are the standard error (95% confidence interval) from three independent measurements.

Potential jump measurements conducted in KPi buffered H_2O and D_2O at three different pLs and repeated using different electrode materials establish confidence in the accuracy of these results. For H_2O solutions the reducing potential was chosen on the Reversible Hydrogen Electrode scale (V_{RHE}) to lie well below the first oxidation wave (1.03 V_{RHE}) while the oxidizing

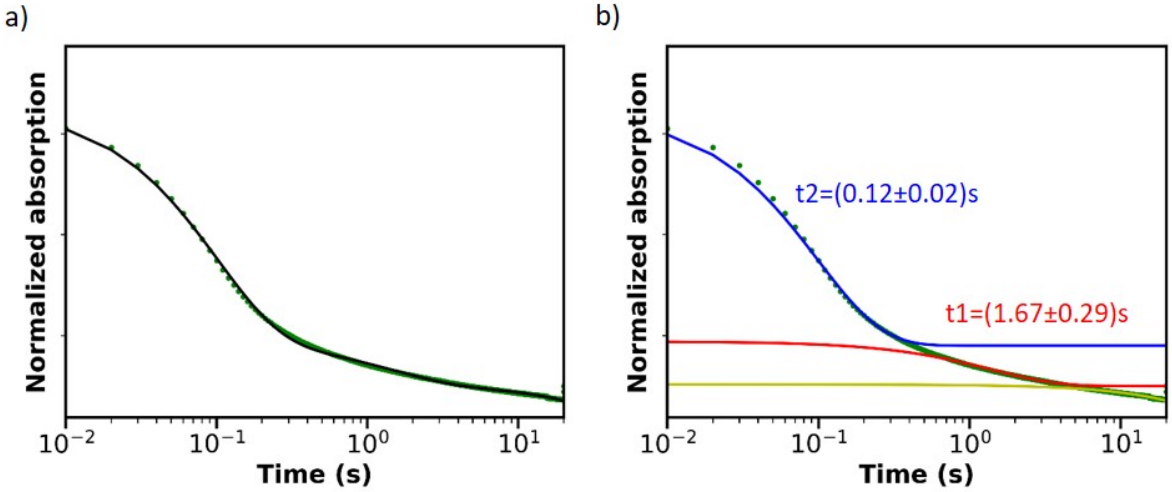

Figure 6.3: Data for explanatory purposes from time-resolved in-situ visible absorption spectroscopy measured during the reduction step in potential-jumps experiments. The purpose of this figure is to justify the use of three exponentials in the simulation of the time behavior. The data shown in a logarithmic scale highlights the three phases that compose the signal and are represented by three exponential functions with very different half-times. (a) The simulated curve superimposed on the experimental data. (b) Individual components are plotted together with the experimental curve.

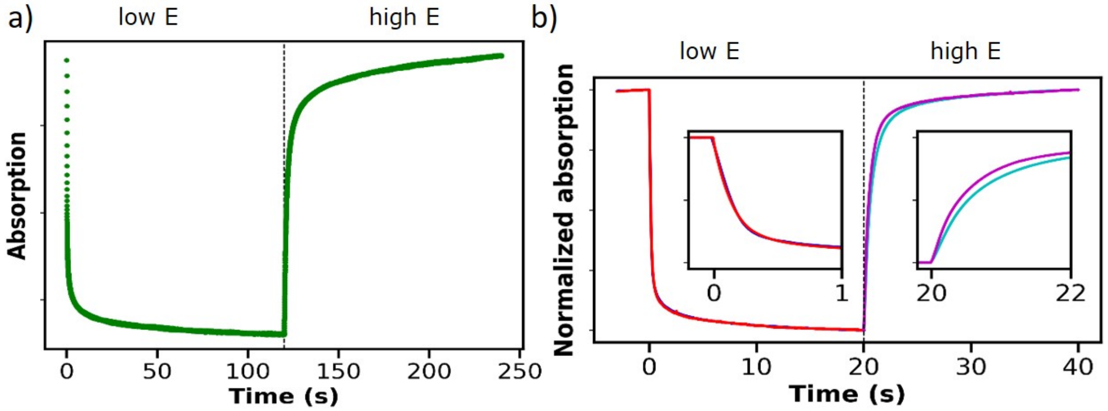

Figure 6.4: Longer time-resolved in-situ visible absorption data measured during potential jumps between reducing and oxidizing potentials, for CoCat in 0.1 M KPi at pH 7 (H_2O buffer). The signal has not reached a stable level after potential application for 2 min.

potential was in the catalytic region (1.68 V_{RHE}). An additional 50 mV was added when measuring in D_2O electrolyte to compensate for the isotopic shift and to ensure consistency of the analyzed processes (Giordano, 2016).

Control measurements with identical potentials for H_2O and D_2O buffers (i.e. no 50 mV shift considered; Fig. 6.4b), and on a substrate with lower resistance (glassy carbon; Fig. 6.5a), showed no further differences between the recorded time traces. The substrate capacitance was estimated to be 24.8 µF (Fig. 6.5b), it yields a cell time constant of ca. 0.5 ms. The electrochemical double layer is therefore fully charged in 1.5 ms and does not interfere with the process observed in the chronoamperometric experiments (Fig. 6.2b), which are 2-3 orders of magnitude slower (fastest half-life measured is 100 ms).

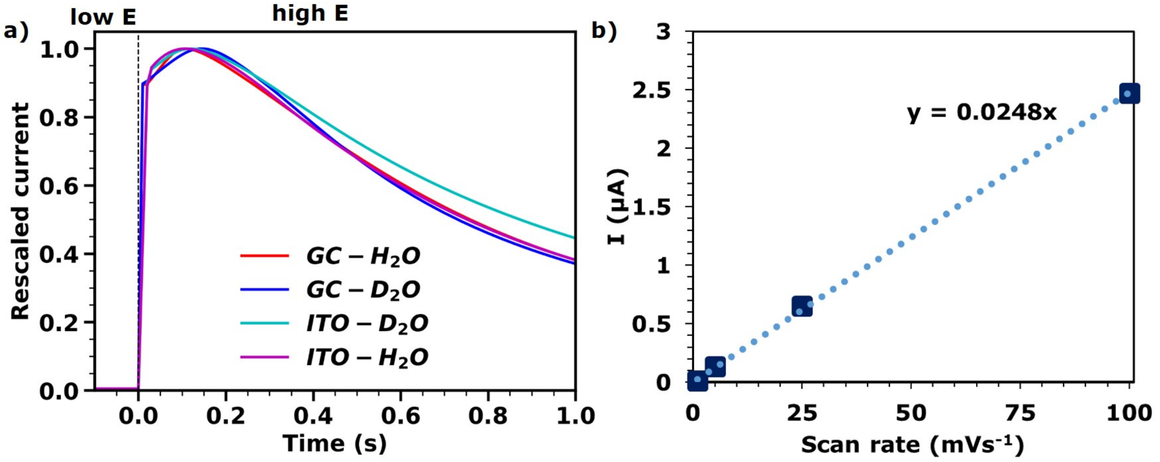

Figure 6.5: (a) Time-resolved current signal measured during potential jumps between a reducing and an oxidizing potential, for CoCat in 0.1 M KPi H_2O-containing buffer (red and violet lines) or D_2O-containing buffer (blue and cyan lines) at pL 7. Data were collected on two different substrates: glassy carbon (GC) that has a lower resistance and ITO that has a higher resistance. ITO is transparent and therefore is necessary for the in-situ collection of visible absorption signals. The higher resistance influences the current at times lower than 20 ms, therefore not affecting the detected half-lives (lower one at 118 ms). The current was rescaled to achieve a better comparison of the different time courses. (b) Estimation of the time constant to charge the electrochemical double layer during "potential jumps" experiments. A series of CV measurements with different scan rates in the range 0.5 to 1.0 V_{NHE} were performed on blank ITO. The set-up used was the same as in the time-resolved visible absorption spectroelectrochemical experiments, the solution was 0.1 M KPi at pH 7 with added 1 M KNO_3. From the dependence of the capacitive current on the scan rate I extracted a capacitance value of 24.8 µF, the cell resistance is 21.1 Ω, thus the cell time constant is ca. 0.5 ms. The electrochemical double layer is therefore fully charged in 1.5 ms. The time constants extracted from the chronoamperometric experiments (Figure, 6.2b) are 2-3 orders of magnitude larger than this (i.e. slower).

The comparison of half-lives reveals that the kinetics of Co oxidation state changes are unaffected by pL (in the range $6 \leq pL \leq 8$) or hydrogen isotope used. Therefore, proton transfer is not rate-limiting in the precatalytic Co redox reactions, at least for the major phases with a half-life larger than 0.10 s.

6.2.3 Analysis of Equilibrium Isotope Effect on Co Redox Transitions

X-ray absorption spectroscopy was used to investigate the EIE that occurs upon H-D exchange on the equilibrium potential of Co redox transitions. This method provides direct information on the average Co oxidation state through the analysis of the X-ray absorption near-edge structure (XANES), as well as information on the average atomic environment surrounding Co atoms from the extended X-ray absorption fine structure (EXAFS) (Newville, 2004; van Oversteeg, 2017; Penner-Hahn, 1999; Dau, 2003). A typical Co K-edge absorption spectrum (Fig. 6.6a) has a symmetry forbidden pre-edge peak that is formally assigned to the 1s→3d and a main absorption edge corresponding to the 1s→4p transition. The location of the absorption edge depends on Co oxidation state, spin and metal-ligand coordination symmetry; with appropriate considerations, a linear correlation between oxidation state and edge location is observed (van Oversteeg, 2017; Penner-Hahn, 1999; Dau, 2003). We found that the edge position is shifted to lower energy for samples conditioned in D_2O electrolytes as compared to samples conditioned in H_2O electrolytes at the same potential (Fig. 6.6a), indicating that samples conditioned in D_2O electrolytes attain lower oxidation states. The conditioning method consisted in freezing samples during steady-state electrochemistry to obtain quasi-in-situ X-ray absorption spectra.

A direct comparison between X-ray and UV-vis absorption spectroscopy confirms that visible absorption data closely follow the X-ray data, except for low oxidation states where a small discrepancy is observed (Fig. 6.6b, full UV-vis spectra in Fig. 2.12). This provides further confirmation that the molar extinction coefficient increases linearly with Co oxidation state and UV-vis absorption spectroscopy is a valid tool for detecting changes in oxidation state. Both X-ray and UV-vis absorption data show a sigmoidal increase in Co oxidation state with applied potential. Repeating the experiment in deuterated water causes a shift of the curve to higher potentials by ca. 58 mV. To identify the isotopic shift for both the redox transitions embedded in the oxidation state rise ($Co^{II} \rightarrow Co^{III}$ and $Co^{III} \rightarrow Co^{IV}$), I simulated the data with the modified Nernst equation proposed in a previous work: (Risch, 2015; Julien, 2003)

$$E = E_{m,j} + (k_B T + E_I) \ln\left(\frac{Y - Y_{min,j}}{Y_{max,j} - Y}\right) \tag{6.1}$$

where E is the applied potential, j indicates the redox transition, E_m is the transition midpoint potential, k_B is the Boltzmann constant, T the temperature, E_I is a term describing the interaction between Co sites and Y is the average Co oxidation state, with $Y_{max/min}$ representing the maximum and minimum achieved oxidation state respectively. $Y_{max/min}$ were fixed at the saturation value for each measurement type and E_m and E_I were freely varied during the simulation. The simulation results are presented in Tables 6.2. The simulation details and the two redox transition components plotted separately are in Fig. 6.7.

The interaction term (E_I) represents the reciprocal influence between Co atoms, a positive value implies that the oxidation of a fraction of Co atoms will hinder the oxidation of the others. The value obtained by fitting the X-ray absorption data, $E_I = (47 \pm 10)$ mV, indicates that the interaction between Co atoms increases the potential, that is needed to obtain a certain oxidation state. Electronic coupling between metal atoms is generally observed in multinuclear metal complexes. The broad redox transitions (Fig. 6.6b) require an interaction energy to be properly simulated and provide evidence that the electronic coupling is having a strong influence in CoCat. The midpoint potentials for the two transitions (E_{m1} and E_{m2} reported in Table 6.2) are in line with literature values (Risch, 2015). The isotope shift for the $Co^{II} \rightleftharpoons Co^{III}$ transition

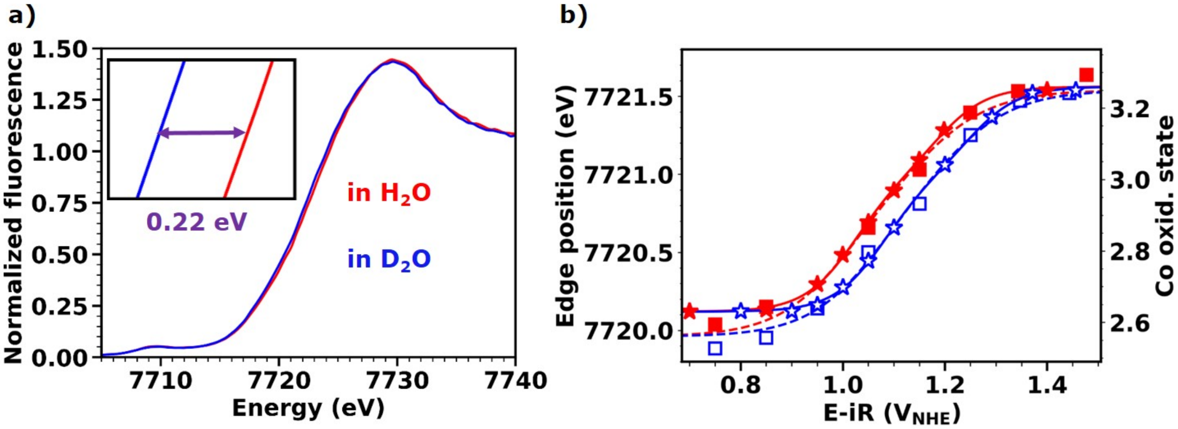

Figure 6.6: X-ray absorption measurements at the Co K-edge for CoCat samples frozen during the application of an oxidizing potential (freeze-quench method) in 0.1 M KPi buffer at pL 7 containing H_2O (red) or D_2O (blue). (a) XANES data recorded for samples frozen with 1.15 V_{NHE} applied. (b) Changes in Co oxidation state for different applied potential, obtained from XANES (squares) and in-situ UV-vis absorption measurements (stars). The XANES data were analyzed to extract the edge positions (left axis), which were then converted to Co average oxidation state values (right axis) using Eq. 6.4. The UV-vis absorption data cannot be directly converted to an absolute oxidation state value and were rescaled to match with the X-ray data, the absorption values were taken at 600 nm illumination. The data were simulated with a sigmoidal curve (Eq. 6.2 derived from Eq. 6.1, solid line for UV-vis and dotted line for X-ray absorption), parameters and results from the simulation are reported in Table 6.2.

Table 6.2: Midpoint potential for $Co^{II} \rightleftharpoons Co^{III}$ and $Co^{III} \rightleftharpoons Co^{IV}$ transitions and other parameters from simulation of Co oxidation state at different applied potential with a modified Nernst equation (Eq. 6.2).[a, b, c]

XAS				UV/vis			
	H_2O V_{NHE}	D_2O V_{NHE}	Δ(D-H) mV		H_2O V_{NHE}	D_2O V_{NHE}	Δ(D-H) mV
E_{m1}	1.01±0.02	1.07±0.02	58	E_{m1}	1.020±0.002	1.078±0.002	58
E_{m2}	1.17±0.02	1.22±0.04	47	E_{m2}	1.189±0.003	1.250±0.004	62
E_I	47±10 mV			E_I	24±2 mV		
Y_{min1}	2.56			Y_{min1}	2.63		
Y_{max2}	3.25			Y_{max2}	3.26		

[a] Freeze-quench X-ray absorption measurements and in-situ UV-vis absorption measurements were used for simulation (data are shown in Fig. 6.6b).
[b] In the simulation $E_{m1,2}$ were free to vary, E_I was constrained to have the same value for each data type, $Y_{min1,max2}$ were fixed at the saturation value for each measurement type and $Y_{max1,min2}$ were fixed to 3.
[c] Errors represent one standard deviation obtained with the Bootstrap method.

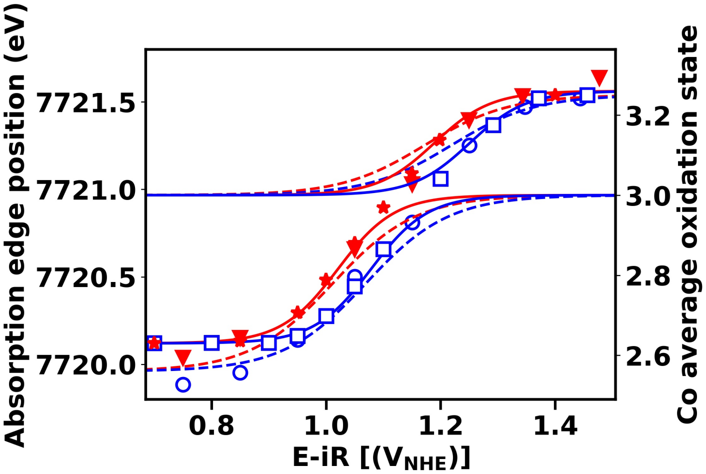

Figure 6.7: Highlight of the two components derived from Eq. 6.1, corresponding to the $Co^{II}\rightleftharpoons Co^{III}$ and the $Co^{III}\rightleftharpoons Co^{IV}$ transitions. The exact equation used for simulation was:

$$Y = \frac{Y_{max,1}e^{f(E,1)} + Y_{min,1}}{e^{f(E,1)} + 1} + \frac{(Y_{max,2} - Y_{max,1})e^{f(E,2)} + Y_{min,2} - Y_{max,1}}{e^{f(E,2)} + 1} \tag{6.2}$$

with $f(E,j) = \frac{E-E_{m}j}{K_BT+E_I}$ and $Y_{max,1} = Y_{min,2} = 3$. Changes in Co oxidation state for different applied potential, obtained from freeze-quench X-ray absorption measurements (triangles and circles) and in-situ visible absorption measurements (stars and squares), on CoCat samples in 0.1 M KPi buffer at pL 7 containing H_2O (red) or D_2O (blue). The data were simulated with a sigmoidal curve (solid line for visible and dotted line for X-ray absorption), parameters for and results from the simulation are reported in Table 6.2. The sigmoidal curves representing the sum of the two components are shown in Fig. 6.6b.

is 58 mV for both methods while for the $Co^{III} \rightleftharpoons Co^{IV}$ transition we obtain two different values with higher uncertainty, due to the limited number of points available for the fit. When taking the error range into account both transitions present the same isotopic shift, which coincides with the isotopic shift in the overpotential needed to obtain 30 µA cm^{-2} steady-state catalytic current (58 ± 4 mV). We conclude that the lower current observed in deuterated water is due to a decrease in the average Co oxidation state, linked to an EIE.

Further evidence of an active EIE on redox transitions arises from the observation of open circuit potential (OCP). The OCP reflects the equilibrium potential of a reaction (Corrigan, 1987; Roberts, 2013) and in CoCat it has been linked to the $Co^{II} \rightleftharpoons Co^{III}$ reaction (Surendranath, 2012). Tracking of the OCP in H_2O and D_2O buffers reveals a lower OCP in H_2O electrolytes, suggesting a lower $Co^{II} \rightleftharpoons Co^{III}$ equilibrium potential (Fig. 6.8). After exchanging the H_2O electrolyte solution for D_2O the oxidation state will not change, because in OCP there is no electron transfer, but the corresponding equilibrium potential will increase, which yields a shift comparable to that measured with X-ray absorption spectroscopy. After solution exchange a period of ca. 10 minutes is required to reestablish equilibrium. The calculated EIE explains as well the shift in the potential at which the film becomes conductive, which was observed by Brodsky et al. in deuterated electrolyte (Brodsky, 2018).

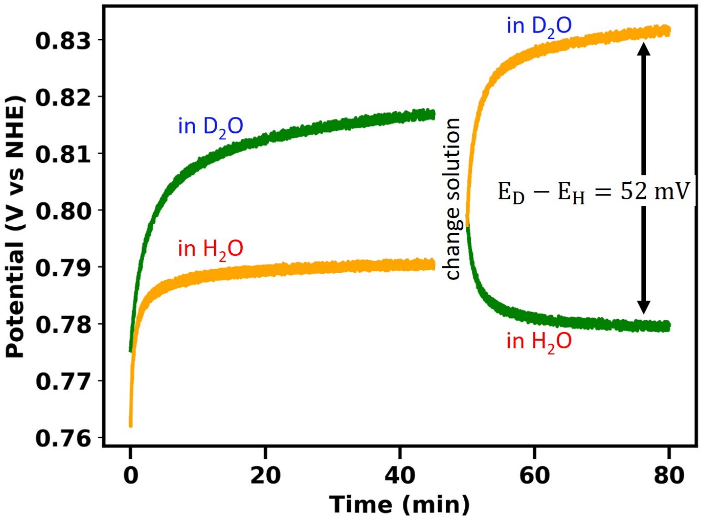

Figure 6.8: Time traces of open circuit potential (OCP) for CoCat in 0.1 M KPi prepared with H_2O (lower lines) or D_2O (upper lines). A dried CoCat film (yellow traces) was exposed first to a KPi-H_2O buffer and then to a KPi-D_2O buffer. Another film (green traces) was exposed first to a KPi-D_2O buffer and then to a KPi-H_2O buffer.

At high applied overpotentials the oxidation state saturates at a value of ca. 3.3, which is the same for samples operated in H_2O and D_2O. The concurrency of the potential region where saturation is observed with the region of mass transport limitation (Fig. 6.9) suggests a correlation between the two phenomena. Cyclic voltammetry experiments (Fig. 6.10) with and without stirring confirm the presence of mass transfer limitations in this potential region.

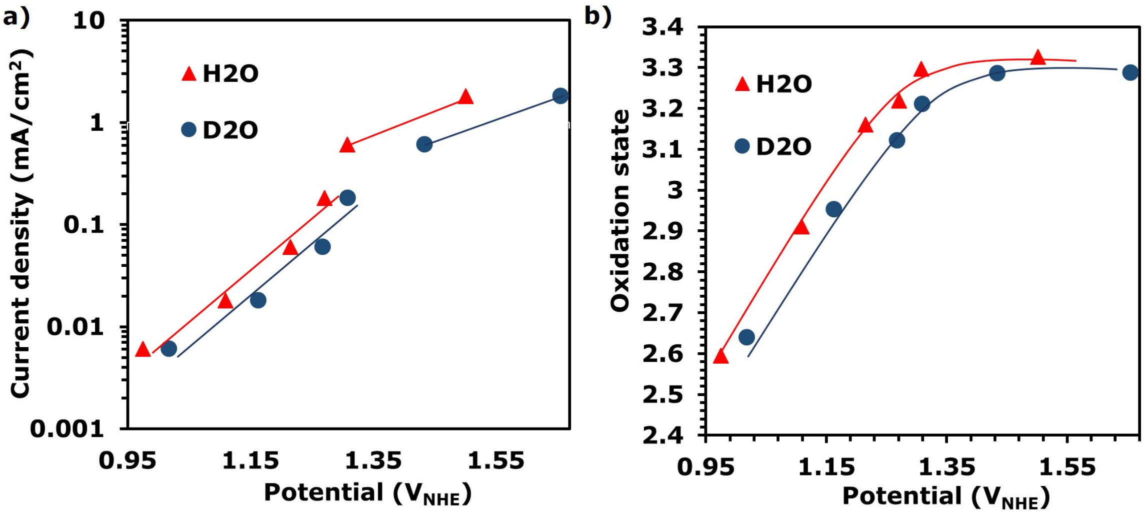

Figure 6.9: (a) Current density and (b) Co average oxidation state as a function of the applied potential for CoCat in 0.1 M KPi at pL 7 prepared with H_2O (red triangles) or with D_2O (blue circles). Lines were added to guide the eye. Samples were prepared with the freeze-quench method, a fixed current was applied before freezing. The reported potential was measured 1 min before freezing.

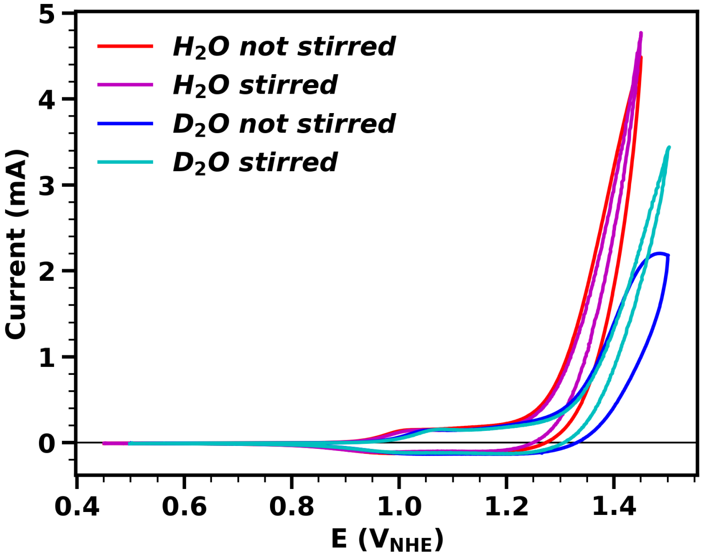

Figure 6.10: Cyclic voltammetry (20 mVs^{-1}) for CoCat in 0.1 M KPi at pL 7 prepared with H_2O (red and violet lines) or with D_2O (blue and cyan lines), for stirred and not stirred solutions. The effect of stirring is visible at high potentials where mass transport limitations start to influence the catalytic rate. The CV's potential-range was shifted anodically by 50 mV in D_2O, in order to perform the measurements in the same current range.

6.2.4 Analysis of Structural Features

The extended X-ray absorption fine structure provides insight into the structural changes that accompany the oxidation reactions. The Fourier transform of the EXAFS data contains two peaks that can be distinguished from the noise, corresponding to the Co-O and the Co-Co distance (Fig. 6.11a). A direct comparison between films frozen at the same potential in H_2O and D_2O show the peaks at the same distance but with slightly different heights. While the differences in height are small, their consistency across all measured spectra builds confidence in their presence.

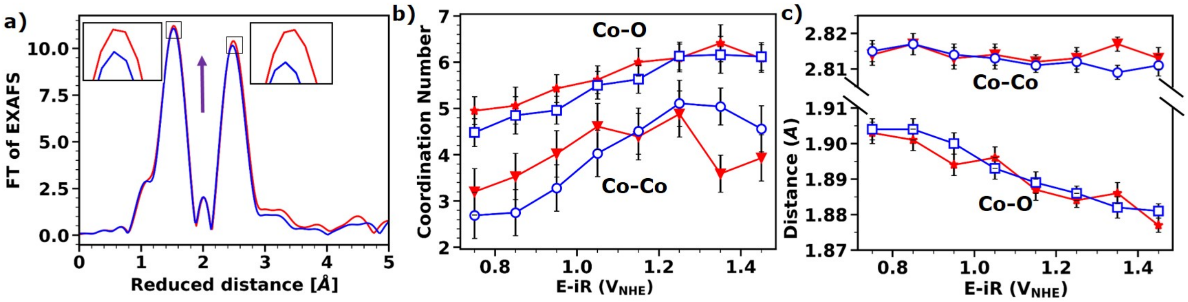

Figure 6.11: X-ray absorption measurements at the Co K-edge for CoCat samples frozen during the application of an oxidizing potential (freeze-quench method) in 0.1 M KPi buffer at pL 7 containing H_2O (red) or D_2O (blue). (a) EXAFS data recorded for samples frozen with 1.15 V_{NHE} applied. In the insets, the differences between data collected in H_2O and D_2O are highlighted. The k^3-weighted EXAFS were simulated using a two shells approach (accounting for Co-O and Co-Co distances), the least-square fitting provided parameters for (b) the coordination numbers, (c) the distances and (Fig. 6.13) the Debye-Waller parameters.

Quantitative analysis involved the simulation of k^3-weighted EXAFS spectra (Fig. 6.12, Table 6.3) using two coordination shells, with three free parameters each: coordination number (N), distance (R) and Debye-Waller parameter (σ). The average number of Co-O bonds increases with applied potential from 5 to 6 and then stays constant (Fig. 6.11b), while the distance decreases continuously from 1.90 to 1.88 Å (Fig. 6.11c). The Debye-Waller parameter oscillates around 0.057 Å (Fig. 6.13), suggesting convolution of two slightly different distances. The same behavior was observed in previous measurements (Risch, 2015) and interpreted as a mixture of 4 or 5-coordinated Co^{II} ($R_{Co\text{-}O}$=2.043 Å) and 6-coordinated Co^{III} (RCo-O=1.895 Å) (Wood, 1998) that is oxidized to an all Co^{III} compound before being partially oxidized to Co^{IV}. The Co-Co bond distance stays constant at 2.81 Å, a value typical for di-µ-oxo bridged Co ions. The Co-Co coordination number increases with potential, indicating further formation of di-µ-oxo bridges as 4/5-coordinated Co^{II} gets oxidized to 6-coordinated Co^{III}. At potentials where Co^{IV} is observed the coordination number stays constant.

Identical structural rearrangements occur in both H_2O and D_2O electrolytes upon oxidation state changes. The measured interaction term (E_I) suggests that the oxidation of a Co atom hinders the oxidation of its neighbors, this effect could be attenuated by the structural rearrangements.

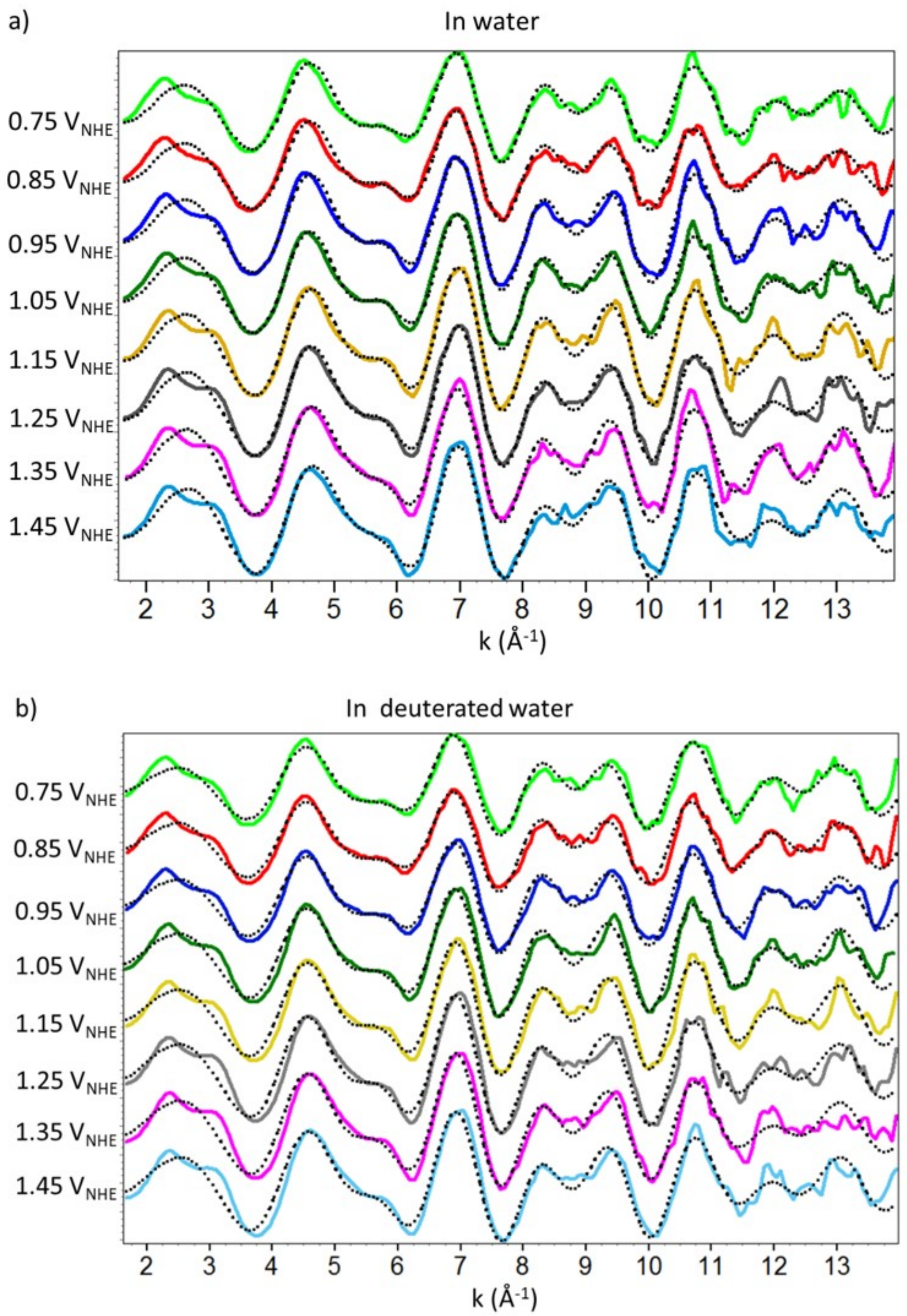

Figure 6.12: k^3-weighted EXAFS (solid line) and their simulation (dotted line) at the Co K-edge for CoCat in 0.1 M KPi at pL 7 made with (a) H_2O or (b) D_2O. Samples were prepared with the freeze-quench method, the potential applied before freezing are reported on the vertical axis. Simulation results are shown in Fig. 6.13, Fig. 6.11 and listed in Table 6.3.

Table 6.3: EXAFS fit results at the Co K-edge for CoCat frozen in-situ in 0.1 M KPi at pL 7 made with H_2O (upper table) or D_2O (lower table). [a, b]

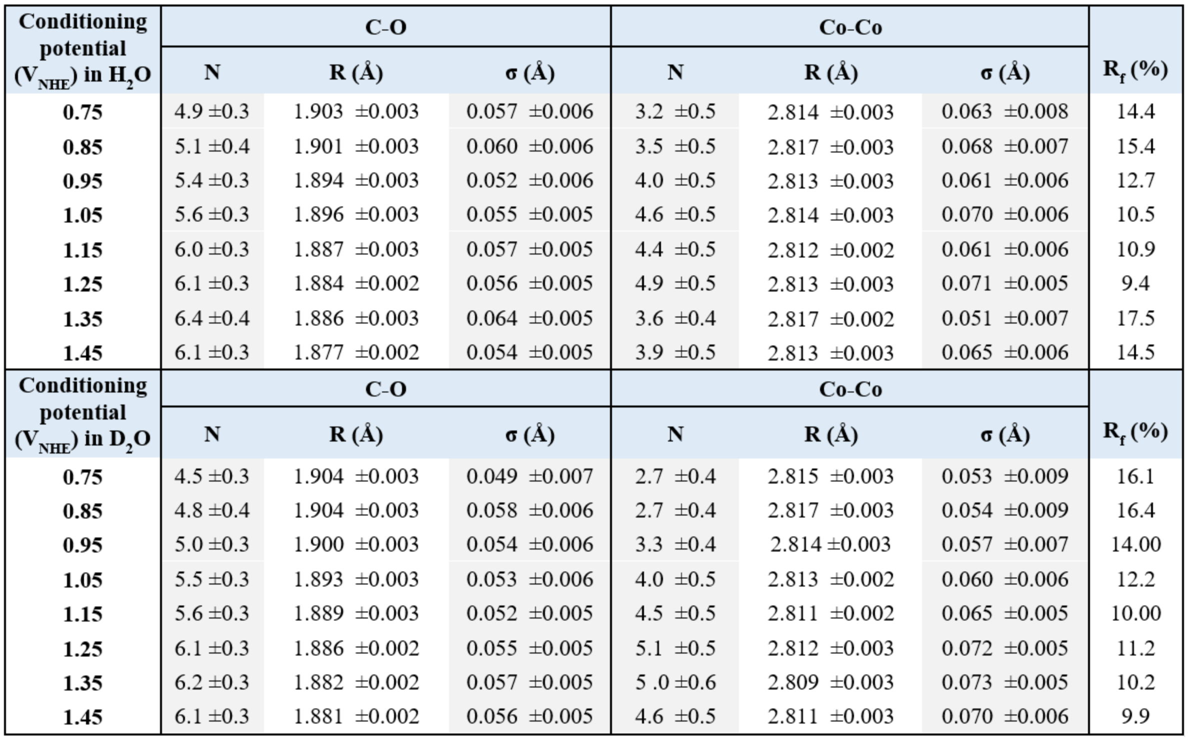

Conditioning potential (V_{NHE}) in H_2O	**C-O**			**Co-Co**			
	N	**R (Å)**	**σ (Å)**	**N**	**R (Å)**	**σ (Å)**	**R_f (%)**
0.75	4.9 ±0.3	1.903 ±0.003	0.057 ±0.006	3.2 ±0.5	2.814 ±0.003	0.063 ±0.008	14.4
0.85	5.1 ±0.4	1.901 ±0.003	0.060 ±0.006	3.5 ±0.5	2.817 ±0.003	0.068 ±0.007	15.4
0.95	5.4 ±0.3	1.894 ±0.003	0.052 ±0.006	4.0 ±0.5	2.813 ±0.003	0.061 ±0.006	12.7
1.05	5.6 ±0.3	1.896 ±0.003	0.055 ±0.005	4.6 ±0.5	2.814 ±0.003	0.070 ±0.006	10.5
1.15	6.0 ±0.3	1.887 ±0.003	0.057 ±0.005	4.4 ±0.5	2.812 ±0.002	0.061 ±0.006	10.9
1.25	6.1 ±0.3	1.884 ±0.002	0.056 ±0.005	4.9 ±0.5	2.813 ±0.003	0.071 ±0.005	9.4
1.35	6.4 ±0.4	1.886 ±0.003	0.064 ±0.005	3.6 ±0.4	2.817 ±0.002	0.051 ±0.007	17.5
1.45	6.1 ±0.3	1.877 ±0.002	0.054 ±0.005	3.9 ±0.5	2.813 ±0.003	0.065 ±0.006	14.5
Conditioning potential (V_{NHE}) in D_2O	**C-O**			**Co-Co**			
	N	**R (Å)**	**σ (Å)**	**N**	**R (Å)**	**σ (Å)**	**R_f (%)**
0.75	4.5 ±0.3	1.904 ±0.003	0.049 ±0.007	2.7 ±0.4	2.815 ±0.003	0.053 ±0.009	16.1
0.85	4.8 ±0.4	1.904 ±0.003	0.058 ±0.006	2.7 ±0.4	2.817 ±0.003	0.054 ±0.009	16.4
0.95	5.0 ±0.3	1.900 ±0.003	0.054 ±0.006	3.3 ±0.4	2.814 ±0.003	0.057 ±0.007	14.00
1.05	5.5 ±0.3	1.893 ±0.003	0.053 ±0.006	4.0 ±0.5	2.813 ±0.002	0.060 ±0.006	12.2
1.15	5.6 ±0.3	1.889 ±0.003	0.052 ±0.005	4.5 ±0.5	2.811 ±0.002	0.065 ±0.005	10.00
1.25	6.1 ±0.3	1.886 ±0.002	0.055 ±0.005	5.1 ±0.5	2.812 ±0.003	0.072 ±0.005	11.2
1.35	6.2 ±0.3	1.882 ±0.002	0.057 ±0.005	5 .0 ±0.6	2.809 ±0.003	0.073 ±0.005	10.2
1.45	6.1 ±0.3	1.881 ±0.002	0.056 ±0.005	4.6 ±0.5	2.811 ±0.003	0.070 ±0.006	9.9

[a] Two coordination shells were used with three free parameters each: coordination number (N), distance (R) and Debye-Waller parameter (σ).

[b] The amplitude reduction factor ($S_0{}^2$) was 0.7.

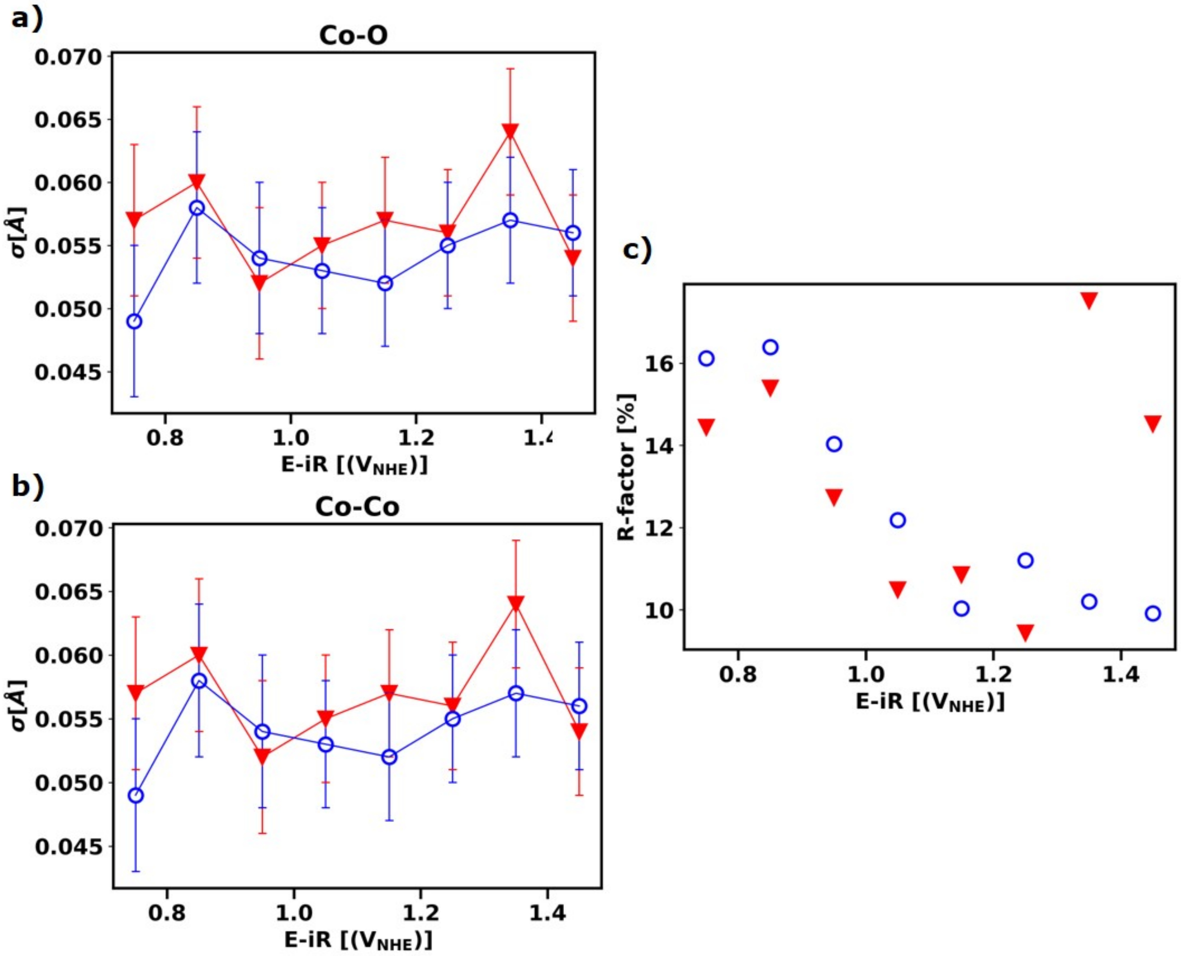

Figure 6.13: Debye-Waller parameter for (a) Co-O and (b) Co-Co shells simulated on the k^3-weighted EXAFS. (c) R-factor for the reported simulations. Data from X-ray absorption measurements at the Co K-edge for CoCat samples frozen during the application of an oxidizing potential (freeze-quench method) in 0.1 M KPi H_2O buffer (red triangles) or D_2O buffer (blue circles) at pL 7. The other simulation parameters are reported in Fig. 6.11. The R-factor is obtained from the sum of the residuals.

6.2.5 Direct dependence of current from oxidation state

Quasi in-situ X-ray absorption spectroscopy opens the possibility to directly relate the Co oxidation state with the rate of catalysis and gain insight on the factors determining the catalytic activity. I conditioned a new series of samples in the catalytically active region by enforcing the same catalytic rate in H_2O and D_2O, i.e. samples were frozen during galvanostatic measurements. The Co oxidation states required to drive any given current density in H_2O and D_2O overlap within their standard error range (Fig. 6.14). The current, and thus the catalytic activity, therefore depends on the oxidation state and is not directly influenced by the applied potential, which is different between H_2O and D_2O samples, but only related to it through the change in oxidation state. The need for an additional 50 mV of overpotential in D_2O, compared to H_2O, to obtain a given steady-state current (Figs. 6.1 and 6.9) can thus be understood as the thermodynamic requirement to attain the same oxidation state (Fig. 6.6b). In the catalytically active region the current increases exponentially with the Co oxidation state (Fig. 6.14), which mainly represents the percentage of Co^{IV} atoms in the structure.

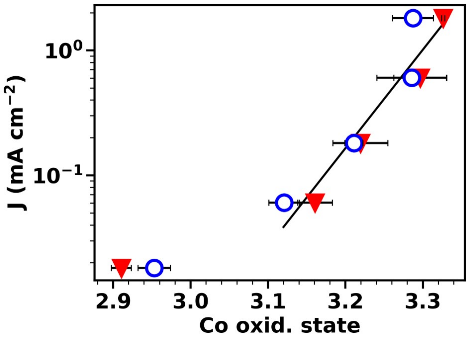

Figure 6.14: Current density shown as a function of Co oxidation state, as determined from freeze-quench X-ray absorption measurements at the Co K-edge, for CoCat samples in 0.1 M KPi at pL 7 prepared with H_2O (closed symbols) or with D_2O (open symbols). The samples were frozen during galvanostatic measurements. Error bars represent the standard error with 95% confidence interval, calculated from at least three spectra acquired on the same sample. The black line is a linear regression, highlighting the exponential dependence of current on Co oxidation state.

6.2.6 DFT Model of the EIE

The origin of the isotopic shift for the redox transitions is illustrated in Fig. 6.15: the zero-point vibrational energy depends on the hydrogen atom mass by a factor proportional to the bond strength, according to $\omega = \sqrt{\frac{k}{\mu}}$, where ω is the vibrational energy, k the bond strength and μ the reduced mass. Since the bond strength is higher in the initial state, when the proton is bonded to CoOx than in the final state with the proton solved in solution, the Gibbs energy difference between the initial and final state will be higher for deuteron than for proton (see Fig. 6.15). For the same reason upon proton-to-deuteron exchange, the pK_a of proton donors change differently from the pK_a of proton acceptors. The consequence is a change in the reaction thermodynamics, called EIE (Parkin, 2009; Zhang, 2012; Wolfsberg, 1972). The EIE affects the protonation-deprotonation equilibrium and therefore shifts the midpoint potential of the two redox transitions.

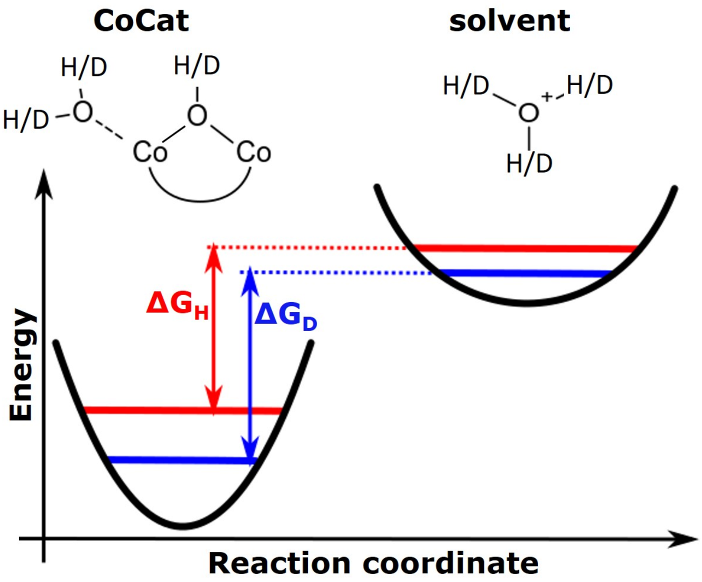

Figure 6.15: Variations in zero-point vibrational energy with hydrogen isotope (red for hydrogen and blue for deuterium) and with bond strength (left initial state and strong bond, right final state and weak bond). The difference in bond strength between initial and final states causes an increase in the transition Gibbs energy when substituting H_2O with D_2O.

To estimate the theoretical effect of the EIE on the CoCat deprotonation I simulated a model complex of two Co-atoms (Fig. 6.16) using Density Functional Theory (DFT, details in Methods section). The theoretical EIE was calculated as the change in zero-point energy when a hydrogen atom linked to the Co complex is substituted with a deuterium atom, at which is subtracted the difference in zero-point energy for a proton/deuteron solved in water. This calculation has proven to be effective for the isotopic pK_a shift in sixteen different organic acids (Mora-diez, 2015), where ΔpK_a values were very similar to each other with an average value of 0.57. I repeated the calculation for various hydrogen atoms in the Co complex and obtained ΔpK_a isotopic shifts ranging from 0.45 to 0.68, corresponding to an EIE of 26.5-40.4 mV (average 33.3 mV, results in Table 6.4). The EIE values obtained for the Co complex are very similar to the ones obtained for the organic acids (Mora-diez, 2015) and are in the same order of magnitude as the experimental EIE (about 60 mV). The similarity suggests that the observed isotope effect can be explained as an EIE changing the zero-point energies.

6.2.7 $^{16}O/^{18}O$ Isotope Effect

Isotopic labeling experiments using ^{18}O labeled water show a decrease in catalytic currents (Fig. 6.17), suggesting that O-O bond formation is involved in the rate-limiting step for catalytic OER. Chronoamperometric experiments in the linear region of Tafel plots were continuously repeated with fresh aliquots of electrolyte solution, consisting of 0.1 M KPi pH 7 prepared with either $H_2{}^{16}O$ or $H_2{}^{18}O$, inserted into the cell for each cycle (Fig. 6.17a). The catalyst

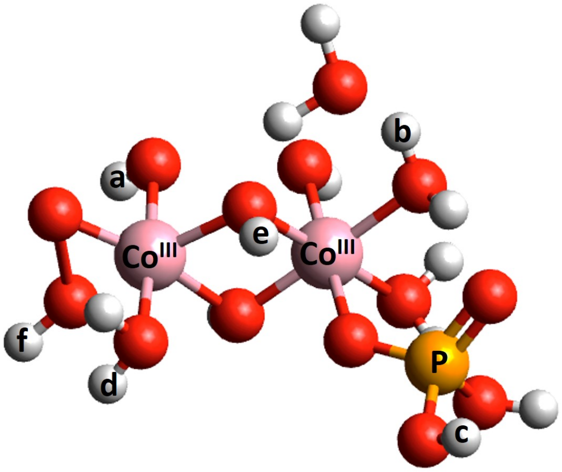

Figure 6.16: Example of a structure used for DFT calculations. Letters refer to the features explained in Table 6.4. The mixed structure is only for exemplification purposes: features f, c and b where each part of separately optimized structures.

Table 6.4: Values for EIE obtained from DFT calculations for differently coordinated protons (details in Method Section and Fig. 6.16).

Species	Fig. S12	ΔE_{fin}-ΔE_{in} (mV)	ΔpK_a
Co^{II}-OH		26.5	0.45
Co^{III}-OH		29.7	0.50
Co^{III}-Co^{III}-OH	(a)	30.3	0.51
Co^{II}-OH$_2$		31.6	0.53
Co^{III}-OH		32.6	0.55
Co^{III}-Co^{III}···P-OH	(c)	32.8	0.56
Co^{III}-OH$_2$		33.5	0.57
Co^{III}-Co^{III}-OH$_2$	(d)	33.7	0.57
Co^{III}-Co^{III}-OH$_2$	(d)	33.8	0.57
Co^{III}-OH$_2$		33.8	0.57
Co^{III}–OH$_2$···OH$_2$	(b)	34.3	0.58
Co^{III}-OH···OH$_2$		34.8	0.59
Co^{III}-OH-Co^{III}	(e)	35.4	0.60
Co^{III}-OH-Co^{III}	(e)	36.6	0.62
Co^{III}-OOH	(f)	40.4	0.68

film degrades upon solution exchange and this protocol was adopted to deconvolute current losses due to catalyst degradation from those due to an isotope effect. A kinetic isotope effect (KIE) of 1.11±0.03 was estimated from the ratio of two parallel trend lines, where the linear slope is due to catalyst degradation (Fig. 6.17b). An alternative experimental protocol yielded a KIE of 1.10±0.01 (see Fig. 6.18). These values are larger than those typically reported in literature, which range from 1.01 to 1.04 depending on the considered mechanism (Roth, 2009; Ashley, 2010; Angeles-Boza, 2014). The measured decrease in catalytic rate upon ^{16}O to ^{18}O substitution provides evidence that O-O bond formation is rate-limiting, but the instability of the films during the testing protocol limits quantitative interpretations.

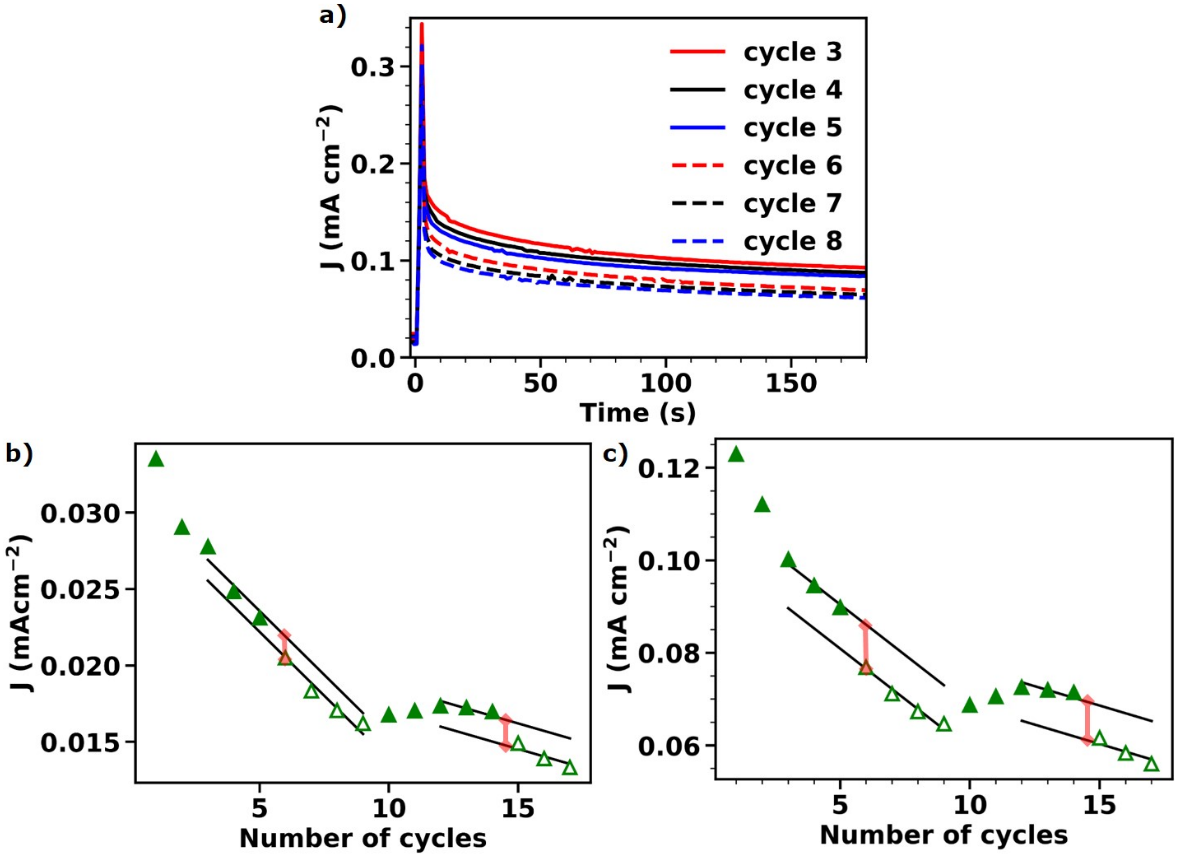

Figure 6.17: Potential steps (3 min each) in 0.1 M KPi at pH 7 made of either $H_2{}^{16}O$ (continuous lines, closed triangles) or $H_2{}^{18}O$ (dashed lines, open triangles). The solution was exchanged after each protocol repetition consisting in 2 potential steps (1.20 and 1.25 V_{NHE}, corrected for iR drop, 6 min in total). (a) Example of potential steps at 1.25 V_{NHE}. (b, c) Each point represents the average of the current during the last 2 min of a potential step either at 1.20 V_{NHE} (b) or at 1.25 V_{NHE} (c). Black lines represent the activity decrease due to catalyst degradation linked mostly to solution exchange and are forced to be parallel between $H_2{}^{16}O$ and $H_2{}^{18}O$ solutions. Red lines indicate the points used to estimate the KIE.

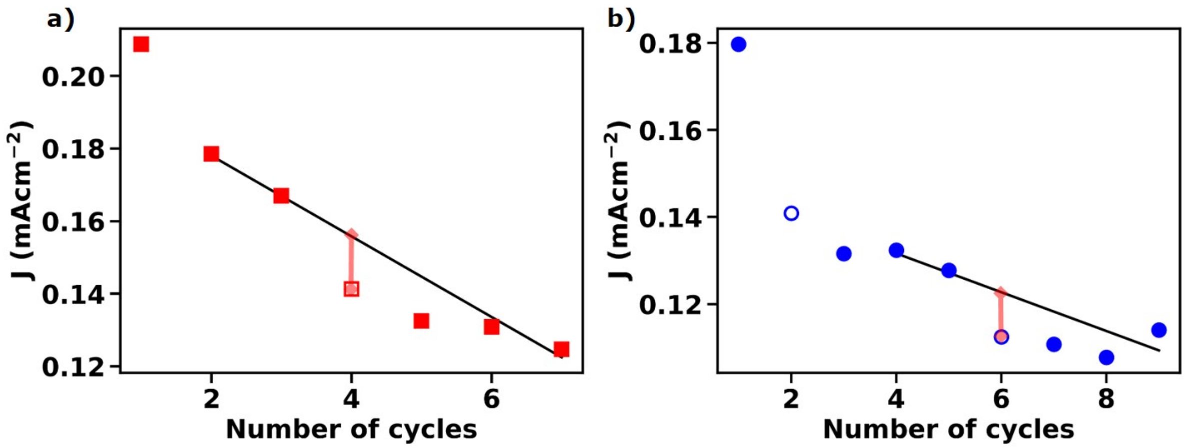

Figure 6.18: Alternative ways to calculated the $^{16}O/^{18}O$ KIE. Each point represents a potential step (3 min each) in 0.1 M KPi at pH 7 made of either $H_2{}^{16}O$ (closed symbols) or $H_2{}^{18}O$ (open symbols). The solution was exchanged after each protocol repetition consisting of 3 potential steps (1.25, 1.30 and 1.35 V_{NHE}, corrected for resistance drop, 9 min in total). Data are presented only for 1.25 V_{NHE}, because at higher potential mass-transport limitations influence the behavior. (a) and (b) represent two independent repetitions, black lines are a linear regression of points acquired in $H_2{}^{16}O$ (excluded the one directly after $H_2{}^{18}O$ exposure) and represent normal catalyst degradation linked to solution exchange between each point. Red lines connect the point in $H_2{}^{18}O$ with the value it would have had in $H_2{}^{16}O$ and were used to estimate the KIE, a KIE = 1.10, 1.09 was obtained for (a) and (b) respectively. Another value for KIE estimation was obtained from the ratio between the first two points in (b): decrease caused by both KIE and catalyst corrosion, after correction by the percentual decrease between the first two points in (a): decrease caused only by catalyst corrosion, a KIE = 1.10 was obtained. All alternative methods furnished KIE values compatible with the KIE = 1.11±0.03 found with the main method (Fig. 6.17).

6.3 Discussion

The catalytic current decreases by 87% upon proton-to-deuteron substitution (at 1.25 V_{NHE} and pL 7). Previous studies for Ni and Co electrodeposited catalysts in alkaline pH revealed an inverse isotope effect appearing at low current density (Tse, 2016) that was tentatively assigned to OH^- binding to the metal. In the neutral pH range, where the concentration of OH^- is considerably lower, we observe a normal isotope effect. The decrease in current is best interpreted as a shift in the potential needed to obtain a fixed current. The similarity between the isotopic potential shift observed for catalytic current (58 ± 4 mV, Fig. 6.1b) and the shift observed for redox potentials (shifts of 58 mV and 47 to 62 mV for the two transitions, respectively, Table 6.2) suggests that the factors controlling the Co oxidation reaction are the same ones regulating the catalytic activity. Therefore, we infer that the isotope effect observed as a decrease in oxygen production is due to a potential increase in one of the two redox transitions. Since Co^{IV} was proven to be necessary for catalytic activity (McAlpin, 2010), the EIE causing a potential shift in the

$$Co^{III}O_xH_y \rightarrow Co^{IV}O_xH_{y-1} + H^+ + e^- \tag{6.3}$$

electron-proton transfer is responsible for the decrease in catalytic current in D_2O containing electrolyte. The $Co^{III}\rightleftharpoons Co^{IV}$ equilibrium potential will determine the number of active sites at a certain overpotential and thus the catalytic activity (Fig. 6.14). The above effect fully explains the reduced catalytic current density in deuterated water, suggesting that there is no KIE affecting catalysis. Thus, the rate-determining O-O bond formation step is not directly coupled to proton release nor oxo-hydroxo proton transfer. The absence of proton release during the rate-determining step was previously suggested based on electrochemical studies at different buffers concentration (Surendranath, 2010). Furthermore, the energetic barrier for O-O bond formation was found to be lower when two terminal oxo species ($Co^{IV}=O$) are involved in respect to a hydroxo species (Co^{IV}-OH) with a terminal oxo species (Wang, 2011). However, the isotope effect studies reported here are the first experimental evidence that excludes turnover-limiting oxo-hydroxo proton transfer.

The absence of any detectable KIE or pH dependence for the Co-oxidation time traces suggest that the kinetics of all detected phases does not depend on the proton transfer time (Fig. 6.2). The proton transfer is not rate-limiting, indicating for both $Co^{II}\rightleftharpoons Co^{III}$ and $Co^{III}\rightleftharpoons Co^{IV}$ reactions a proton transfer followed by a rate-limiting electron transfer (PT-ET). A parallelism between the mechanism for amorphous Co oxides and that for molecular Co_4O_4 (Symes, 2011) is thus found, with the PT-ET identified in amorphous Co oxides being observed in molecular Co_4O_4 in case of transfer of proton and electron to distinct chemical species. The major phase of oxidation state changes has a half-life larger than 0.10 s (Fig. 6.2b), suggesting not a simple PT-ET mechanism but a slow rate-determining process possibly involving structural rearrangements, for example the formation of new μ-oxo bridges, observed in the EXAFS data (Fig. 6.11). The presence of a positive interaction term (E_I) indicates that the oxidation of a fraction of Co atoms will hinder the oxidation of the others, the structural rearrangements may lower the effect of the interaction. The positive effect of structural rearrangements on Co oxidation could explain the frequent observation that more disordered material, able to rearrange more easily, are more active for OER (Risch, 2012; González-Flores, 2015; González-Flores, 2016).

The equality between catalytic current in H_2O and D_2O at parity of Co oxidation state (Fig. 6.14) suggests that the catalytic current is exclusively dependent on Co oxidation state with no further influence from the applied potential. The lack of direct influence of the applied potential on the catalytic rate suggests that electron transfer is not involved in the catalytic rate-determining step. In other words, the rate is limited by a reaction that is chemical in nature. Previous work on similar catalysts suggest oxygen-oxygen bond formation as the rate-limiting step (Surendranath, 2010; Risch, 2015; Mattioli, 2013; Costentin, 2017), and our finding of a KIE for $^{16}O/^{18}O$ substitution but not for H/D substitution provides strong support for such an assignment.

The exponential relationship between catalytic current density and cobalt oxidation state (Figure 6.14) is unlikely to be related to Faradaic processes of unrelated "bulk" sites as this relationship is specific to steady-state catalytic currents and spans the linear Tafel region. This relationship does not follow a simple first order or second order dependence, thereby indicating a situation that is more complicated than assumed in conventional electron transfer theories or binuclear reactions. Our analysis explains the exponential relationship by taking into account the electronic coupling between nearby Co^{IV} sites. The interaction term (E_I) extracted from the dependence of the average cobalt oxidation state on the applied potential indicates that the oxidation of a Co^{III} ion hinders the oxidation of its neighbors. This implies that the redox potential for generation of Co^{IV} ions inside a Co fragment increases as this high oxidation state accumulates, continuously reducing the energy difference towards the transition-state energy of the O-O bond formation step. In the framework of transition state theory, the reaction rate constant depends exponentially on the height of the energy barrier. Therefore, I propose that the exponential dependence of the catalytic rate on the number of Co^{IV} ions in the structure is evidence that the accumulation of these highly oxidized states is a critical feature in catalytic OER on cobalt oxides.

After the publication of the work described in this thesis, a very similar mechanism was reported in *Nature* for an IrOx electrocatalyst (Nong, 2020). There, operando XAS provided evidence that the applied potential does not affect the reaction rate directly, but rather it promotes charge accumulation in the material, which increases the reaction rate.

6.3.1 Proposed mechanism for water oxidation at neutral pH

A mechanistic proposal that captures the results obtained here is presented in Fig. 6.19a. The structural model represents the periphery of a CoCat fragment where catalysis takes place (Kwon, 2018; Farrow, 2013; Risch, 2012; Bediako, 2015; Fester, 2017) and is based on the structural evolution suggested by X-ray absorption spectroscopy (Fig. 6.11) and by computational work (Mattioli, 2013). The redox behavior begins with a film containing some 4- or 5-coordinated Co^{II} atoms that undergo a proton-coupled electron transfer that induces the formation of an additional μ-oxo bridge, resulting in a precatalytic state in which all cobalt ions have a coordination number of 6. This precatalytic state is further oxidized by a proton-coupled electron transfer to yield Co^{IV} ions; the accumulation of Co^{IV} atoms depends on the applied potential and on the interaction energy (E_I) between neighboring Co atoms. The probability of forming the active-state depends exponentially on the number of Co^{IV} atoms in the CoOx fragments, yielding the observed exponential relationship between cobalt oxidation state and catalytic current. The rate-limiting step is proposed to be oxygen-oxygen bond formation by the coupling of terminal oxygen atoms of two adjacent Co^{IV} ions.

For the oxygen-oxygen bond formation mechanism, a bulk water nucleophilic attack is excluded based on the results obtained by Koroidov et al (Koroidov, 2015). The other possible mechanism

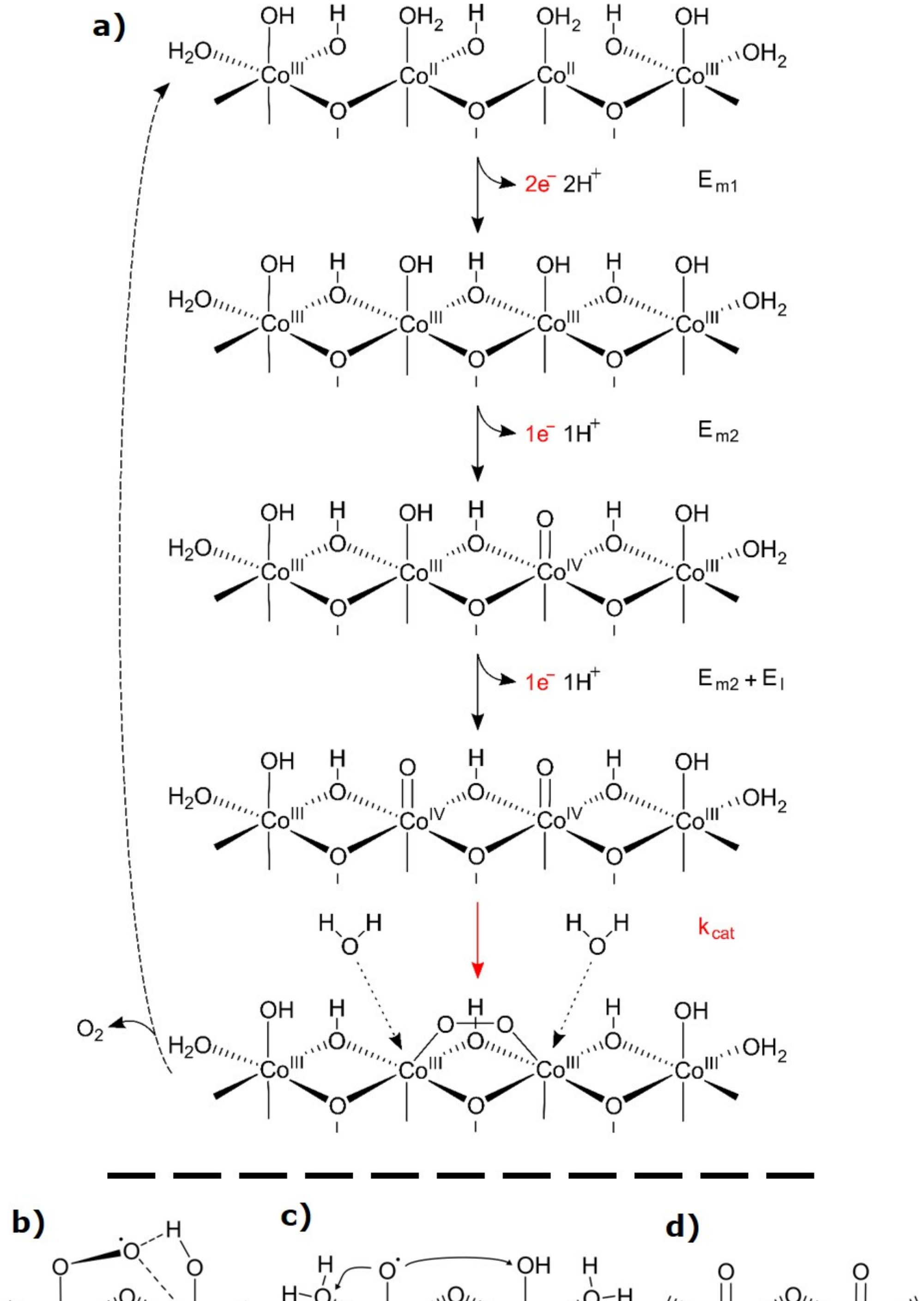

Figure 6.19: (a) Proposed mechanism for water oxidation on CoCat in neutral pH. Steps occurring after the proposed rate-limiting step are not drawn. The catalyst state preceding the rate-determining step in mechanistic proposals by (b) the Frei group (Zhang, 2014), (c) the Messinger group (Koroidov, 2015) and (d) the Nocera and Costentin groups (Costentin, 2017).

is intramolecular oxygen coupling (IMOC) (Betley, 2008), which could involve the coupling of a terminal oxygen both with a hydroxyl linked to the same Co or with a terminal oxygen linked to a neighboring Co. The involvement of bridging oxygen is excluded by their low exchange rate (Koroidov, 2015; Ullman, 2016; Nguyen, 2015, see also section 3.3.5). The presence of two neighboring Co^{IV} atoms in the active site and the absence of KIE for H/D substitutions favors oxygen-oxygen bond formation between the two terminal oxygen atoms linked to neighboring Co atoms, DFT calculations provided a low energy barrier for this pathway (Wang, 2011).

Previous mechanistic analyzes agree on the presence of a precatalytic state containing Co^{IV} (Surendranath, 2010; Risch, 2015; Gerken, 2011; McAlpin, 2010; Kanan, 2010), and on the necessity of further oxidation to obtain a catalytically active state (Mattioli, 2013; Costentin, 2016; Koroidov, 2015; Li, 2013). The proposed oxidation states and nature of the species preceding the O-O bond formation, however, varies. Rapid-scan infrared spectroscopy and isotopic substitution on Co_3O_4 nanoparticles identified production of a superoxo species bridging two cobalt ions (Fig. 6.19b) (Zhang, 2014). Further oxidation of cobalt sites has also been proposed (i.e. $Co^{IV} \rightarrow Co^{V}$) to precede O-O bond formation (Fig. 6.19c) (Koroidov, 2015), a proposal that has been supported by DFT calculations (Mattioli, 2013; Li, 2013). While such a reaction cannot be excluded by our data, studies on a Co_4O_4-cubane model system (Brodsky, 2017), the absence of rate-limiting oxo-hydroxo proton transfer in our results, and the increasing redox potential of concentrated Co^{IV} atoms all lead us to favor the pairing of adjacent Co^{IV}. The pairing of adjacent Co^{IV} ions with terminally coordinated oxygen ions has been proposed for cobalt oxide films, with indications of an increased redox potential for the formation of Co^{IV} pair (Fig. 6.19d) (Costentin, 2017). Our model refines the view of this past work by revealing an exponential relationship between the average Co oxidation state and the catalytic current – a feature that we assign to an energy level continuously increasing with the number of Co^{IV} atoms in the fragment, which means a continuous decrease in the energy barrier for water oxidation.

6.4 Summary

The coupling of isotopic studies with the measurement of the oxidation state of transition metals enabled the distinction between kinetic isotope effects and equilibrium isotope effects on Co oxidation state changes and revealed the dependence of the catalytic current on the metal oxidation state. The influence of Co redox potential on the catalytic rate is made evident by the decrease in catalytic current in deuterated electrolyte, due to an energetic isotope effect acting on the precatalytic $Co^{III/IV}$ oxidation. We detected neither a KIE nor a pH dependence for precatalytic Co redox transitions, suggesting that proton transfer is not rate limiting and the oxidation kinetics are controlled by electron transfer. The isotope-induced changes in electrocatalytic OER behavior mirror those of the precatalytic redox transitions, leading us to conclude that the decrease in catalytic current in D_2O is fully explained by an EIE that increases the energy needed for CoOx deprotonation when deuterium is involved. Therefore, neither proton release nor oxo-hydroxo proton transfer is rate-limiting. In addition, electron transfer is not rate-limiting as evidenced by the lack of direct influence of the applied potential on the catalytic current. An observed $^{16}O/^{18}O$ KIE suggests that O-O bond formation is rate-limiting for CoCat under neutral conditions. An exponential relationship is observed between catalytic currents and the cobalt average oxidation state. This feature cannot be described by conventional electron transfer theories and is proposed to arise due to an electronic coupling of cobalt sites, that increases the redox potential for $Co^{III/IV}$ oxidation as Co^{IV} accumulates within the catalyst material and gives rise to higher energy states with a lower energy barrier for water oxidation. We propose a mechanism wherein O-O bonds are formed by the coupling of terminal oxygen atoms on adjacent Co^{IV} sites. The methodology employed here is expected to be adaptable and could apply broadly to transition-metal-based catalysts that undergo oxidation state changes during catalysis.

6.5 Experimental details

Electrochemical deposition and analyzes

CoCat thin films were prepared by anodic electrodeposition following an established protocol (Kanan, 2008; Klingan, 2014), slightly modified: a potential of 1.05 V_{NHE} was applied in a 0.1 M phosphate buffer (KPi) at pH 7 containing 0.5 mM $Co(NO_3)_2$ solution, until the accumulation of a 10 mC charge on the working electrode (1 cm^2 exposed area). Sample preparation, as well as electrochemical analysis, were performed in a single-compartment three-electrode cell, using a Pt grid (2x2 cm^2, 90% purity) as a counter electrode and an Ag/AgCl(saturated) as a reference electrode. The working electrode was either an indium tin oxide (ITO) coated glass slide (VisionTek Systems Ltd, 1 cm^2 working area) or, in the case of X-ray absorption measurements, a 0.1 mm thick glassy carbon sheet (Hochtemperatur-Werkstoffe GmbH, 2 cm^2 working area). For the parallel deposition of 10 films, 10 units of potentiostat Interface 1000 (Gamry Instruments) were used, while electrochemical analysis was performed with SP-200 potentiostat (BioLogic). The testing solution for all experiments was 0.1 M phosphate buffer (KPi) at pL 7, made using either MilliQ water (>18 MΩ cm), deuterated water (purity 99.8%, Roth) or O^{18} water (purity 97%, Eurisotop). The pL in D_2O electrolytes were calculated by adding 0.4 pH units to the pH-meter reading obtained with a H_2O-calibrated pH-meter (Covington, 1968). A fresh-deposited film was used for each different pH and hydrogen isotope. The potential drop due to resistance was compensated operando ($R \approx 50$ Ω, 85% compensation), except in the case of X-ray absorption measurements, where the compensation was done during data analysis. Every electrochemical experiment was repeated three times, average and standard deviation are reported.

UV-vis absorption spectroscopy

Electrochemical in-situ analysis was performed in a quartz cuvette (2.5 cm x 2.5 cm x 4 cm height) with a coiled Pt wire as counter electrode and a Hg/Hg_2SO_4 (saturated) reference electrode. The cuvette was placed in the beam path, with the beam crossing the working electrode perpendicularly. The change in transmitted light in the UV-vis range was tested for steady-state measurements in a commercial spectrophotometer (Cary 50, Varian). The UV-vis data acquisition at each fixed potential started after 1 min equilibration and lasted 90 sec. The data at high potentials were corrected for bubbles formation, by subtracting the absorption contribution due to bubble scattering. For time-resolved measurements (10 ms resolution) at a fixed wavelength (633 nm) a home-built setup was used (Zaharieva, 2016). This consisted of a pulse-driven light-emitting diode (Avago Technologies, 50 kHz pulses, light-on and light-off periods of equal length) and a silicon photodiode (1 cm^2) connected to a lock-in amplifier (Princeton Applied Research, model 5209). 1 M KNO_3 was added to increase the conductivity of the electrolyte and thus avoid diffusion-controlled delays. ITO films showed a capacitance of ca. 20 µF in the electrolyte solutions used here, yielding a cell time constant of ca. 1 ms. A good signal-to-noise ratio was obtained by averaging 30 absorption traces.

X-ray absorption spectroscopy, freeze-quench method

CoCat films were mounted in single-time use sample holders (Fig. 6.20) that worked as electrochemical cells, containing 400 µL of 0.1 M KPi solution at pL 7 prepared with H_2O or D_2O. A thin Pt wire served as a counter electrode and was positioned at a distance of 1 mm from the working electrode, minimizing the risk of mass transport limitations. The desired potential was applied for 3 min versus a Hg/Hg_2SO_4 (saturated) reference electrode. Then the reference electrode was removed resulting in a two-electrode cell and the potential was adjusted accordingly. After an additional 1 min, liquid nitrogen was cast on the sample holder, with the double purpose of removing the solution and freezing the cobalt film. The frozen sample was stored in liquid nitrogen and measured at 20 K (in Oxford He-flow cryostat) at the BESSY synchrotron (Berlin) at beamline KMC-1 and KMC-3 (Schaefers, 2007). The X-ray excitation energy was selected by a Silicon (111) double-crystal monochromator and the Co K_α fluorescence, emitted after sample illumination, was collected with a 13-channel energy-resolving Ge detector (Canberra). X-ray absorption fine structure data were collected until k-14 and simulated in k-space.

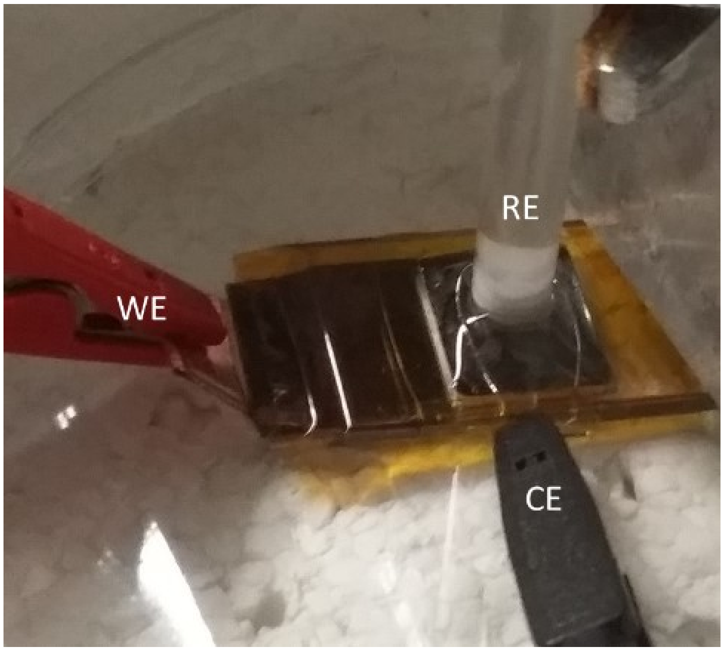

Figure 6.20: Single-time use electrochemical cell for freeze-quench sample preparation, prior to X-ray absorption measurements. The counter electrode is a Pt wire positioned at a distance of 1 mm from the working electrode (X-ray transparent GC). The reference electrode is a Hg/Hg_2SO_4 (saturated), that is removed before freezing the sample.

To convert the edge position in an oxidation state, I used an equation obtained in a previous work (Risch, 2015). There, a series of crystalline Co-oxide compounds was measured, revealing that the energy distance between the position of the pre-edge and the position of the edge half-rise increases linearly with oxidation state following:

$$ox.state = \frac{1}{2.29}(edgepos - 7714.1eV) \tag{6.4}$$

Accordingly, I carefully aligned the pre-edge feature of the different spectra to the reference compounds, extracted the edge position using the integral method (Dau, 2003) and converted it in oxidation state scale using Eq. 6.4. For the direct comparison of samples in H_2O and D_2O solutions at the same current density (galvanostatic measurements), no pre-edge alignment was required, instead, I used a reference compound for energy calibration.

Error estimation

Reported errors and error bars on collected data represent the standard error with a 95% confidence interval, they were obtained from at least three measurements. Errors on simulation parameters represent one standard deviation (68% confidence interval) and were obtained from the covariance matrix. A more complex error estimation using the Bootstrap method was used for data of Co oxidation state as a function of potential simulated with a sigmoidal curve (results in Table 6.2).

Computational Methods

The energetic isotope shift was obtained through DFT calculations as the difference in Gibbs free energy (G) between the deprotonation reaction ($AH + H_2O \rightleftharpoons A^- + H_3O^+$) performed in water and in deuterated water:

$$\Delta G_{D-H} = (\boldsymbol{G_{D_3O^+}} - G_{SD} - \boldsymbol{G_{D_2O}}) - (\boldsymbol{G_{H_3O^+}} - G_{SH} - \boldsymbol{G_{H_2O}}) = G_{SH} - G_{SD} - \mathbf{5.2615}\ \boldsymbol{kJ/mol} \tag{6.5}$$

Gibbs free energies were calculated in harmonic approximation (Wilson, 1955). Computations were performed on a series of systems modeling the CoOx catalyst, containing either one or two Co atoms. The atoms were octahedrally (Co^{III}) or tetrahedrally (Co^{II}) coordinated with oxygen and fully protonated. The spin multiplicity was fixed to be M=4 for Co^{II} and M = 1 for Co^{III} to reflect the spin state reported in literature (McAlpin, 2010) for these species. Geometry optimizations and the calculations of the harmonic frequencies were carried out with ORCA program (Neese, 2012) using spin unrestricted B3LYP functional with RIJCOSX algorithm (Neese, 2009). All atoms were described with TZVP basis sets. The surrounding solvent was modeled with the COnductor-like Screening MOdel (Klamt, 1993) (COSMO) with a dielectric constant of 80.4.

7 Water oxidation in alkaline versus neutral electrolyte: structural ordering leads to a mechanistic change

7.1 Context and motivations

Alkaline electrolyzers based on transition metals (David, 2019) are commercially available and contend the market to PEM electrolyzers,* while this is not the case for electrolyzers operated at neutral pH. Some of the reasons favoring electrolyzers operating at alkaline over neutral pH are: better mass transport in the electrolyte (Jin, 2014; Shinagawa, 2017b), inherent stability of the catalyst material, which can dissolve at neutral pH (Surendranath, 2012; Görlin, 2016; Mohammadi, 2020), and higher efficiency of the OER catalysts, with consistently (up to 500 times) higher catalytic currents reported for a vast range of catalyst materials (Görlin, 2016; Grimaud, 2017; Gerken, 2011; Trześniewski, 2015; Takashima, 2012; Huynh, 2014; González-Flores, 2016).

On the other hand, the coupling of OER with CO_2 reduction requires catalysts active in neutral electrolyte, because CO_2 would react with any base to form bicarbonate (Garg, 2020). Moreover, neutral electrolytes are not corrosive, which simplifies coupling with photoabsorber materials for direct photoelectrolysis (McKone, 2014; Nocera, 2012) and decentralized usage. Understanding the differences in the catalysts behavior and reaction mechanism between neutral and alkaline pH is, thus, of fundamental importance, for the knowledge-guided development of efficient OER catalysts operating at neutral pH.

In 2011, a comprehensive study (Gerken, 2011) of CoOx in the 0-14 pH range build a Pourbaix diagram containing the various protonation and oxidation state of Co at different pHs and potentials. Smith et al (Trześniewski, 2015). studied Fe-containing Ni oxides and assigned the better catalytic performances observed in alkaline electrolyte (pH 13), in respect to borate buffer (pH 9.2), to a deprotonation process which leads to the formation of an "active oxygen" species. In Mn oxides, the overpotential needed for catalysis decreases at pH > 9, this is explained with a comproportionation mechanism forming Mn^{III}, which is believed to be the precursor for OER (Takashima, 2012).

A common point between these studies is the importance of different protonation and oxidation states of the metal. Thus, we employed quasi-in-situ and time-resolved operando XAS to investigate differences in the energetic and kinetic of oxidation state changes and in the reaction mechanism for CoCat in neutral and alkaline electrolytes. We observed three main differences in alkaline electrolyte: a lower onset of OER, caused by a down-shift in the equilibrium potential of the $Co^{III} \rightleftharpoons Co^{IV}$ reaction; faster redox kinetics, linked to better proton and electron transfer; a different mechanism, with a rate-determining step possibly involving electron transfer. One of the topics of this chapter is the experimental evidence and mechanistic reason behind these three differences. The second topic relates to the structural transformation of the catalyst in alkaline electrolyte.

Recent works highlighted the importance for catalytic activity and stability of often disregarded factors, such as Fe impurities (Trotochaud, 2014), CO_2 dissolved in solution (Hunter, 2016a), electrolyte cations (Zaffran, 2017; Kang, 2017; Risch, 2012) and substrate employed (Gorlin, 2017; Yeo, 2011; Chakthranont, 2017; Zou, 2015). Here, I focus on the time accorded for equilibration after exposing the catalyst to alkaline electrolyte. The presence or absence of a resting time, at the beginning of an experiment, in which the catalyst is exposed to the electrolyte without any applied potential (here referred to as “equilibration”), is usually not even

---

*Companies selling alkaline electrolyzers include Hydrogenics, McPhy, Nel and Green Hydrogen systems.

reported in scientific works. In this chapter, we show that it has a strong influence on catalyst activity, redox properties and degree of crystallinity.

Modifications of the structure of the catalyst by exposure to the electrolyte or during catalytic operation were reported previously. During OER, some crystalline materials, including perovskites (May, 2012), $LiCoPO_4$ (Lee, 2012) and pakhomovskyite (González-Flores, 2015) are becoming amorphous. Formation of crystalline areas was reported for Ni-Fe (Görlin, 2016) and Ni-Fe-Co (Sayeed, 2017) oxides operated at pH 13. For Co crystalline compounds, amorphization to CoO(OH) is thought to be beneficial for catalytic activity (Favaro, 2017; Yang, 2016). During OER both $Co(OH)_2$ and the near-surface layer in Co_3O_4 amorphize to CoO(OH), the amorphization is reversible in the case of Co_3O_4 (Huang, 2016; Bergmann, 2015; Yeo, 2011). Co selenite converts in an amorphous bulk active phase when exposure to alkaline electrolyte is directly followed by catalytic operation, otherwise a more-ordered less-active phase is formed (Hausmann, 2020).

For Ni oxide, two phases for the oxidized material exist as the limiting form of a large variety of structures, with differences arising from material preparation and history: a largely anhydrous phase and a hydrated phase, respectively referred to as β-NiOOH and γ-NiOOH. A conversion between phases is possible: upon overcharging the material β-NiOOH converts to γ-NiOOH, via cation intercalation, while, upon aging in alkaline electrolyte, the reduced form of γ-NiOOH converts to the reduced form of β-NiOOH, as shown in the Bode scheme (Bode, 1966; Doyle, 2013; Oliva, 1982; Klaus, 2015). For Co materials the existence of two distinct phases is less clear and less investigated, however, the formation of a hydrous phase was reported upon anodic polarization, while a largely anhydrous phase forms upon aging in alkaline solutions (Benson, 1964; Doyle, 2013; Hausmann, 2020).

Nocera et al (Bediako, 2012) assigned the activation of amorphous Ni oxides in borate buffer (pH 9.2), which is required to obtain appreciable catalytic activity, to conversion from a β-NiOOH to a γ-NiOOH phase. The γ-NiOOH phase was characterized by its local structure, which lacks Jahn-Teller distortion, and by the ability to reach higher oxidation states upon application of a potential, while Takanabe et al (Shinagawa, 2017a) highlighted its ability to accommodate water and K^+ ions in its structure. On the contrary, amorphous Co oxides, electrodeposited and operated in phosphate buffer (pH 7), neither require activation nor show substantial structural modification during operation (Mohammadi, 2020). Their as-deposited state is already a hydrous phase, as revealed by its bulk activity (Surendranath, 2010; Klingan, 2014), and it presents extensive redox changes (see section 2.3.3).

However, when amorphous Co oxides are operated in alkaline electrolyte, a spontaneous phase transformation occurs, which may be analogous to the transition from γ to β phase in NiOOH. The transformation was studied for three differently prepared Co-oxide catalysts and was consistently coupled with crystallization and a major change in Co oxidation state. Raman spectroscopy and analysis of EXAFS data were employed to follow the structural changes, which resulted in a structure with bigger CoOx clusters, fewer defects and strong similarities to CoO(OH). The loss of amorphicity most likely improved electron transfer but reduced the number of Co active sites, resulting in poorer catalytic performances. We propose a technique to stop the crystallization process, by applying a strong oxidative potential immediately after exposing the catalyst to alkaline solution.

7.2 Results

7.2.1 Increased electrochemical performances in alkaline electrolyte

The electrocatalytic properties of CoCat as an OER catalyst were tested in alkaline pH electrolyte (1 M KOH, pH 13.8) revealing better performances than in neutral pH electrolyte (0.1 M KPi, pH 7.0), see Fig. 7.1. In both cases, the catalyst was electrodeposited at neutral pH following an established protocol (Kanan, 2008), dried in air to improve stability and, then, operated. Potentials were reported on the Reversible Hydrogen Electrode scale (V_{RHE}) to factor out the 59 mV/pH shift in the OER equilibrium potential: in the RHE scale the OER equilibrium potential is 1.23 V at every pH (see scheme in Fig. 7.2).

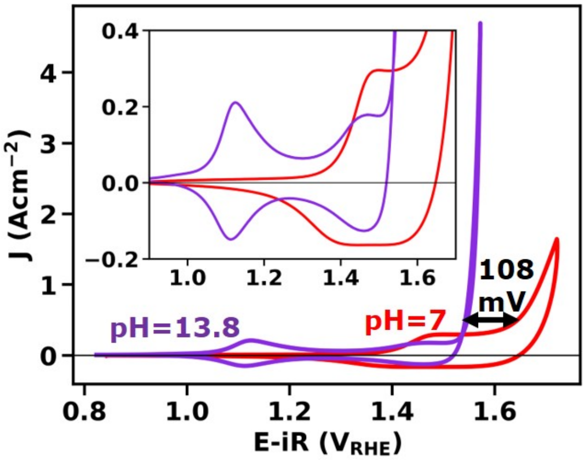

Figure 7.1: Cyclic voltammetry (10 mV/s scan rate) for a 25 mC cm^{-2} CoCat film electrodeposited on GC in 0.1 M KPi pH 7 and tested either in the same solution (red) or in 1 M KOH pH 13.8 (violet). Samples were equilibrated with the electrolyte without potential (OCP) or at low potentials (0.96 V_{RHE}) for at least 15 min before being exposed to catalytic potentials.

The established reaction mechanism at neutral pH entails two proton-coupled electron transfers linked to $Co^{II} \rightarrow Co^{III} \rightarrow Co^{IV}$ oxidations, prior to the rate limiting O-O bond formation (see also chapter 6) (Surendranath, 2010; Risch, 2015; Mattioli, 2013). The shoulder visible during the CV (Fig. 7.1) corresponds to $Co^{II} \rightarrow Co^{III}$ oxidation (Risch, 2015; Gerken, 2011) while $Co^{III} \rightarrow Co^{IV}$ is indistinguishable from the catalytic activity since the presence of Co^{IV} enables O_2 production (see also section 2.3.3) (Surendranath, 2010; Gerken, 2011; Kanan, 2010).

In alkaline electrolyte the two redox waves are both shifted to lower potentials (the first redox wave by ca. 300 mV) and appear to be completely separated between each other, indicating two different pH dependences. A down shift is also visible in the onset potential for oxygen evolution, which decreases by 108 mV in alkaline electrolyte (value at 0.5 mA cm^{-2}).

7.2.2 Exposure to alkaline electrolyte drives oxidation and structural ordering

Although the same catalyst preparation method is used, the catalyst film operated in alkaline electrolyte is structurally different from the one operated in neutral electrolyte. In fact, the "as-deposited" catalyst is not stable in alkaline electrolyte and undergoes structural modifications,

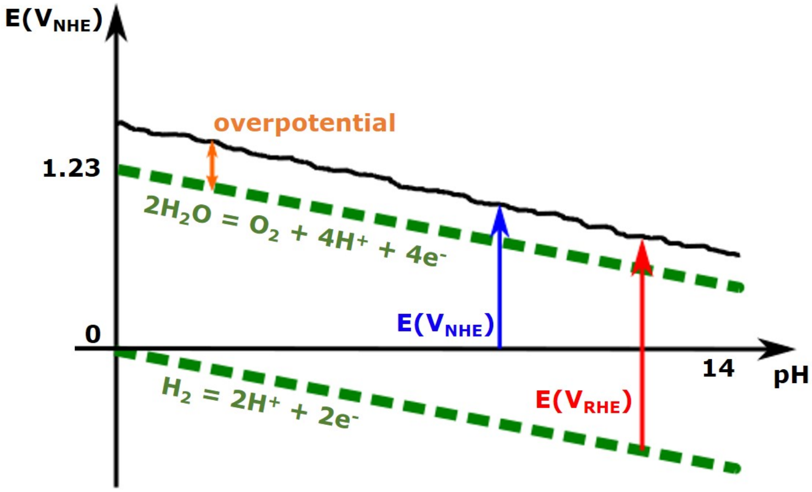

Figure 7.2: Scheme illustrating the different potential scales used in this thesis. The potential for the water oxidation and hydrogen formation reactions are shown as a function of pH (green lines). Their difference is the standard potential for water electrolysis, 1.23 V. In experimental conditions, an additional voltage is required to drive the reaction (black line, the line does not represent experimentally measured values). The potential can be expressed according to a variety of possible scales or as overpotential. The overpotential is the difference between the standard potential and the potential required in experimental conditions (orange arrow). In the Normal Hydrogen Electrode scale (NHE, blue arrow) the potential needed to drive the water oxidation reaction varies with pH, while in the Reversible Hydrogen Electrode scale (RHE, red arrow) it is independent of pH, because the RHE scale is based on the hydrogen formation reaction.

which we refer to as equilibration process. We use Raman and X-ray absorption spectroscopy operando to follow the equilibration process and study the resulting structure.

Raman spectra were collected immediately after sample exposure to 1 M KOH at OCP, using an immersion objective in back-scattering geometry and recording a spectrum every minute (selected spectra in Fig. 7.3a). The broad Raman features are reshaped, over the course of 20 minutes, to a series of sharper peaks and more definite features. To exclude that the change in structure was driven by the laser heating power, the measurement was repeated recording only three spectra and showed the same behavior over time (Fig. 7.3b).

The same experiment was performed using operando X-ray absorption spectroscopy and recording Co-K edges in rapid succession during the equilibration process. The edge position shifted with time, revealing progressive oxidation accompanied by a structural change (indicated by the change in edge shape), which took ca. 40 minutes to complete (Fig. 7.3d, each edge lasts 3 min). During this time the average Co oxidation state changed from 2.4 (dry film) to 3.1 (equilibrated film).

The Raman spectrum of an equilibrated film is shown in Fig. 7.3c, together with an "as-deposited" sample. Table 7.1 reports the respective peak positions. The as-deposited sample has a very broad peak at 544 cm^{-1} with a shoulder at 615 cm^{-1}, similar to spectra reported in literature for CoCat (Kwon, 2018; Yeo, 2011). Broad bands are typical for amorphous compounds and their position reflects LiCoO$_2$ vibrations (Kwon, 2018; Rougier, 1997), see also section 3.3.3. The spectra recorded after exposure to alkaline electrolyte have the same broad band (indicated by a red line in Fig. 7.3c), but a series of sharp peaks are superimposed to it (black lines), which corresponds to the reported Raman spectrum for CoO(OH) (in lit. peaks are reported at 503, 572, 641, 705, 1023 and 1149 cm^{-1}; Yang, 2010; Aiso, 2017).

Table 7.1: Parameters obtained from the simulation of CoCat Raman spectra. The samples are: (1) a dry film measured directly after deposition (pH 7 as-deposited) and (2) a dry film measured after exposure at OCP to 1 M KOH (pH 14 equilibrated).[a]

pH 7 as deposited				pH 14 equilibrated			
pos	**fwhm**	**area**	**assignment**	**pos**	**fwhm**	**area**	**assignment**
544	122	1513	Co-O-Co	497	24	48	CoO(OH)
615	79	1607	Co-O	585	120	268	Co-O
924	135	235	P-O	631	31	69	CoO(OH)
1087	163	476	P-O	708	75	49	CoO(OH)
1225	128	328	2*Co-O	1006	48	8	2*CoO(OH)
				1057	179	83	2*Co-O
				1150	64	40	2*CoO(OH)
				1213	104	69	2*CoO(OH)

[a] Each peak was simulated with a Gaussian function. For each Gaussian are reported the values of the position (in cm^{-1}), the FWHM (in cm^{-1}), the area (in cm^{-1} · counts) and the feature to which it is assigned.

In the 1000-1250 cm^{-1} region the as-deposited sample has 3 very broad bands (924, 1087, 1225 cm^{-1}): the first two can be assigned to phosphate incorporated in the catalyst structure and the third to a two-phonon vibration (see section 3.3.3). After exposure to alkaline, new bands appear (dotted lines in Fig. 7.3c) corresponding to the two-phonon vibrations of the new peaks in the 400-800 cm^{-1} region. In addition, the phosphate bands disappear, indicating that during equilibration the phosphate atoms are leaving the CoCat structure.

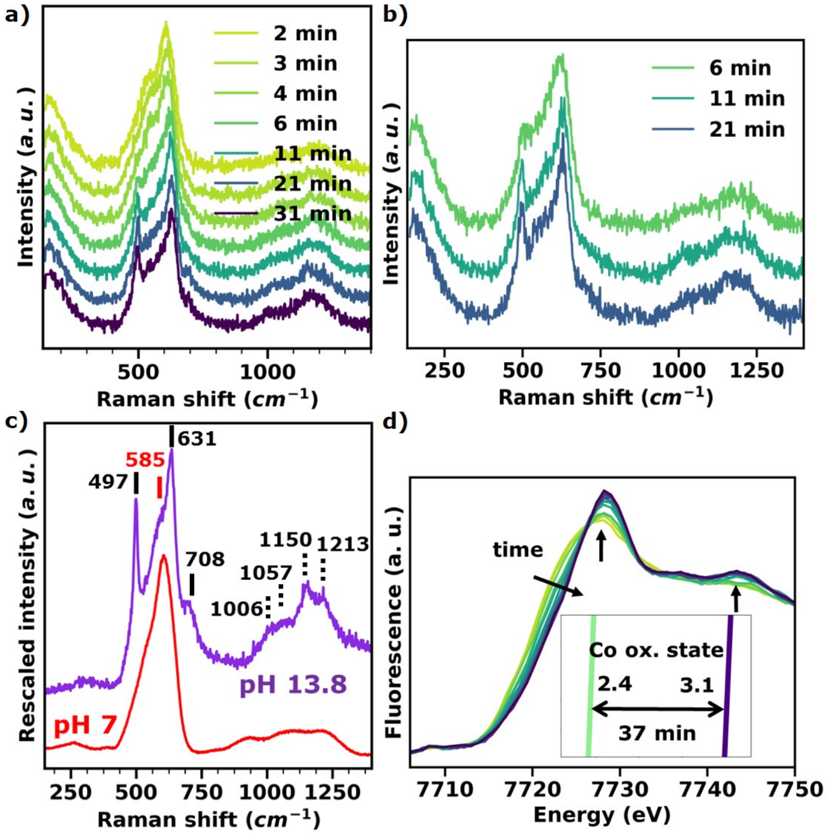

Figure 7.3: Structural and compositional changes during equilibration in 1 M KOH for a CoCat film deposited in 0.1 M KPi pH 7. (a) Operando Raman spectra were collected in OCP starting directly after film exposure to the electrolyte. A Raman spectrum was taken every minute, for a total of 26 spectra, selected spectra are shown. (b) Only three Raman spectra were recorded during the equilibration process, to assess the role of laser light in the equilibration process. In (a) and (b), spectra were not rescaled but shifted on the y-axis for better visualization. (c) Raman spectra for a dry film measured directly after deposition in neutral electrolyte (red) and a dry film measured after exposure to 1 M KOH at OCP (violet). The intensity of the spectra collected after 1 M KOH exposure was multiplied by a factor 4 for better visualization. Peak positions are reported and corresponds to peak typical for CoCat (red tick), CoO(OH) (black ticks) and double frequency peaks (dotted ticks). (d) Co K-edges measured by operando XAS. The first edge was recorded 2 s after exposure of a CoCat film to 1 M KOH, the last one 40 min after exposure, the substrate used was CFP and the deposition charge was 12.5 mC cm^{-2}.

To prove it, samples at different stages of the equilibration process were analyzed with total reflection X-ray fluorescence (TXRF) spectroscopy (Fig. 7.4), revealing that phosphate content diminishes constantly during equilibration. This is a specificity of alkaline electrolyte, because phosphate is still present in large amounts after several hours of exposure to borate buffer (see section 3.3.3). Two additional samples were prepared as a control, one equilibrated in 1 M NaOH and one in 1 M KOH with added 0.1 M KPi (0.1 M KPi is the buffer used for deposition). Their equilibration was performed at 0.96 V_{RHE} for 15 min and followed by 3 CVs. The current profiles during the CV and the equilibration process (Fig. 7.5) reproduce the ones recorded in 1 M KOH (Figures 7.6 and 7.1), suggesting that neither the presence of K atoms nor the absence of P atoms in the electrolyte is necessary for the equilibration process.

The equilibrated samples registered consistently a decrease in phosphate amount by ca. 6 times in respect to the as-deposited sample (Fig. 7.4), which indicates that phosphate depletion is not driven by the lower phosphate concentration in solution. Potassium content measured in the sample strongly increases with exposure time to alkaline electrolytes, unfortunately, the glassy carbon (GC) substrate can absorb potassium (see the blank sample) and can have affected this result. The Co content is stable during equilibration. After the equilibration process, there was an increase (from less than a second to ca. 45 minutes) in the time required to digest the sample in acid. Probably this is due to some kind of stronger bond, which is formed during equilibration between catalyst and carbon substrate.

Raman spectroscopy and X-ray absorption edges indicate an increase in structural order during the equilibration process. A more quantitative estimation can be obtained by the extended range of the X-ray absorption spectra (EXAFS), which gives information on the local environment surrounding the Co atom (Newville, 2004; Bokhoven, 2016). A very low potential (0.96 V_{RHE}) was chosen to drive the slow equilibration and a series of samples were prepared at different stages of the equilibration process (Fig. 7.6), using the freeze-quench method. The sample exposed for 10 min at low potentials has the same structure as the one equilibrated for 1h in OCP and then conditioned at the same low potential (Fig. 7.7). The two modes of equilibration appear equivalent and the conditioning is only necessary to attain the same oxidation state in the two samples. The EXAFS data before FT are presented in Fig. 7.8, the spectral features become more definite with increasing time in alkaline electrolyte. The FT of the EXAFS presents two major peaks at 1.9 Å and 2.8 Å for all the samples, corresponding to the first oxygen and cobalt coordination spheres, respectively (Fig. 7.9a) (Kanan, 2010; Risch, 2009). A third major peak is visible only at the end of the equilibration process and corresponds to the second Co coordination sphere at the double distance 5.6 Å (Co-O-Co-O-Co).

An increase in the height of all three peaks, meaning an increase in structural order, accompanies the equilibration process (Fig. 7.9a), with a resulting structure very similar to CoO(OH) (Huang, 2016). In Fig. 7.9b, the height of the third major peak (corresponding to Co-Co-Co distance) is reported as a function of time in alkaline electrolyte (green series) and potential applied (orange series). The third major peak, whose presence indicates higher structural order, is visible only when a low potential is applied and is absent at neutral pH (red series).

The increase in the height of the peaks can be interpreted as two combined factors: an increase in the number of atoms in the coordination sphere and a decrease in the variation between bonding distances for that coordination sphere, visualized as a decrease in the Debye-Waller factor. The FT-EXAFS spectra were simulated with a model containing the 5 coordination spheres indicated in Fig. 7.9a, to extract these parameters (all parameters are reported in Table 7.2). The Debye-Waller factor for the Co-O distances decreases 2-times when going from the

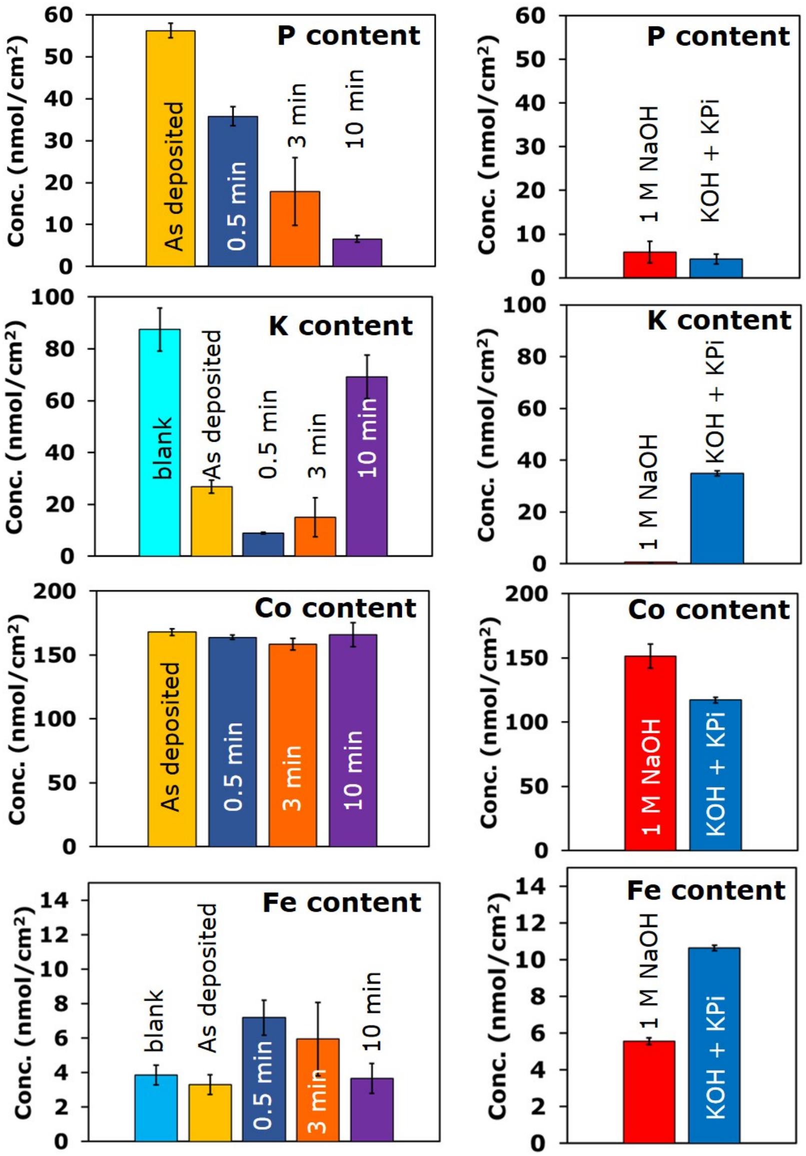

Figure 7.4: Element composition measured with TXRF directly after deposition in neutral electrolyte (as-deposited) or after operation at low potential (0.96 V_{RHE}) in 1 M KOH for different times or after operation at low potential (0.96 V_{RHE}) for 15 min in either 1 M NaOH or 1 M KOH with added 0.1 M KPi. The films were prepared with a deposition charge of 15 mC cm^{-2}, corresponding to ca. 150 nmol cm^{-2} of Co atoms.

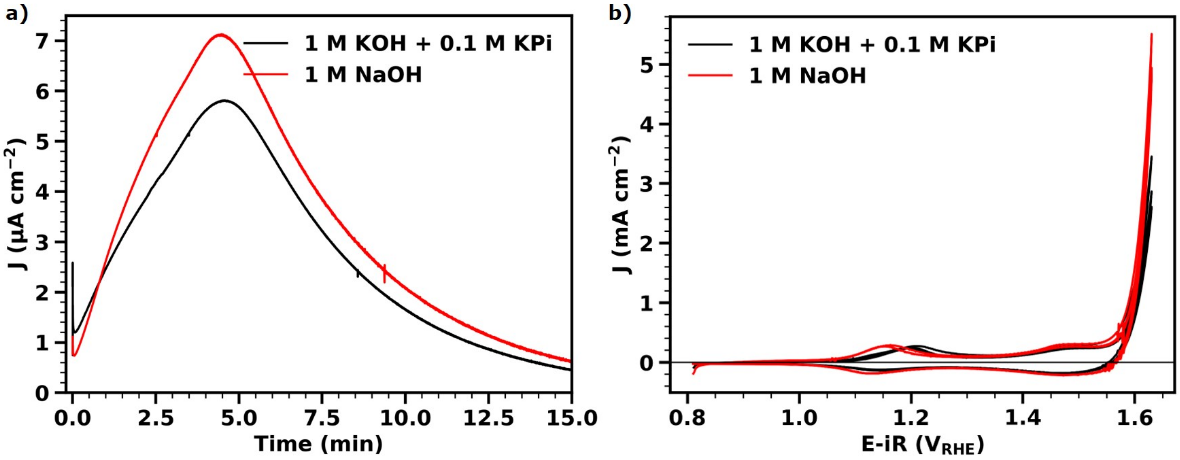

Figure 7.5: Equilibration process for a CoCat film. The film was exposed at 0.96 V_{RHE} for 15 min to an alkaline electrolyte made by 1 M KOH with added 0.1 M KPi (red lines) or by 1 M NaOH (black lines). (a) Current density recorded during the equilibration process. (b) CV at 20 mV s^{-1} performed after the equilibration process was completed.

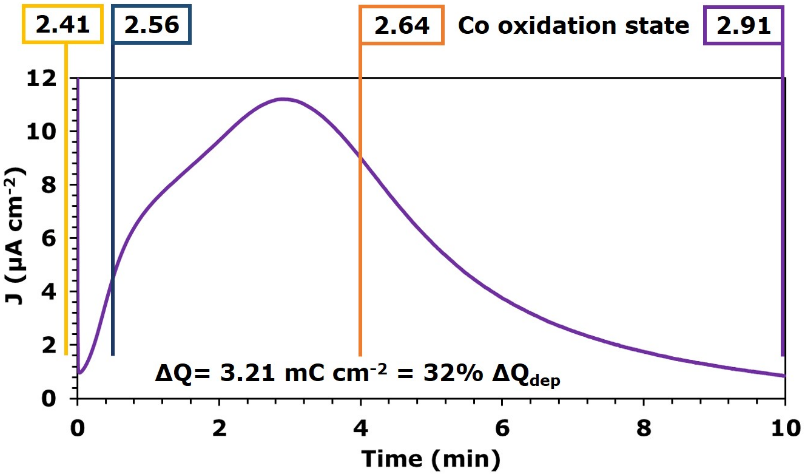

Figure 7.6: Current density recorded during the equilibration process, which consisted in the exposure of a CoCat sample to 1 M KOH with 0.96 V_{RHE} applied potential. The sample was 10 mC cm^{-2} thick, deposited at pH 7 on a GC substrate. Each of the vertical lines represents a different sample which was conditioned for the amount of time indicated by the line position, frozen with liquid nitrogen and, then, measured with XAS. The number on top of the line indicates the oxidation state calculated for that sample. The value reported on the graph is the integration of the curve area, indicating the charge passed during the experiment and the percentage of Co sites that can be oxidized with that charge (based on sample thickness).

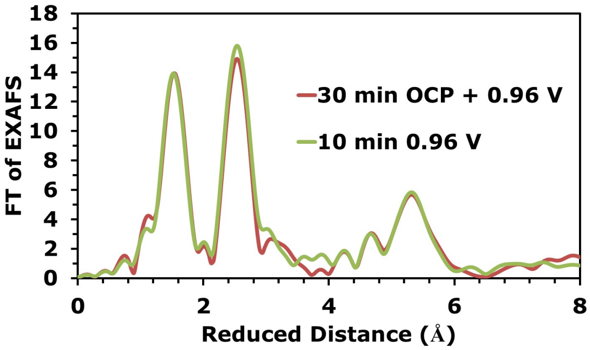

Figure 7.7: FT of the EXAFS for CoCat films prepared with the freeze-quench method after the equilibration process in alkaline electrolyte. Two modes of equilibration are compared: either the sample is exposed for 30 min to OCP, then dried, then exposed for 1 min to 1.56 V_{RHE} and finally conditioned for 3 min to 0.96 V_{RHE} or it is directly exposed for 10 min to 0.96 V_{RHE}.

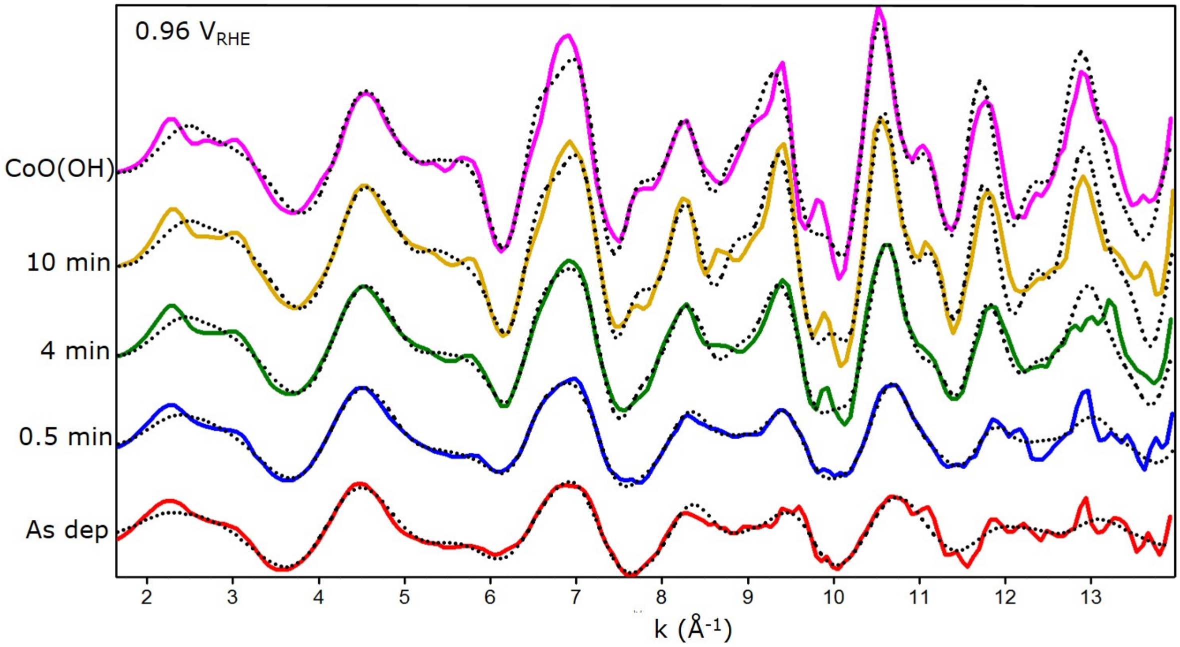

Figure 7.8: k^3-weighted EXAFS (solid line) and their simulation (dotted line) at the Co K-edge for CoCat after deposition in neutral electrolyte (As dep) or after operation at a low potential (0.96 V_{RHE}) in 1 M KOH for different times. Samples were frozen during chronoamperometry. The spectra of CoO(OH) (measured by Marcel Risch, Risch, 2011) is reported for comparison. Simulation results are shown in Fig. 7.9 and listed in Table 7.2.

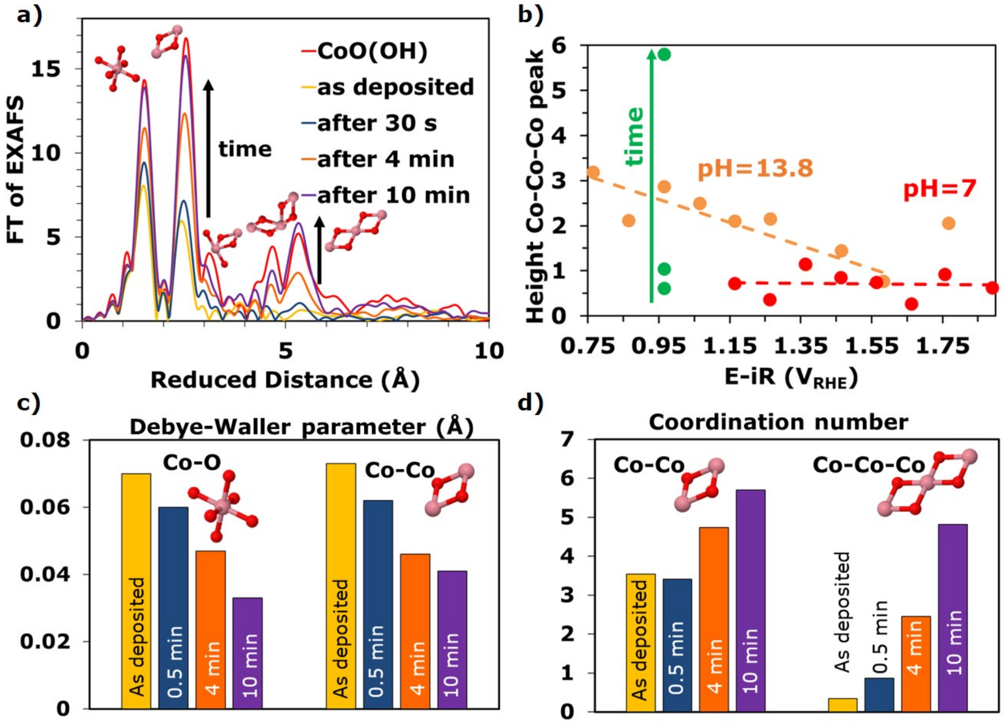

Figure 7.9: EXAFS for CoCat films frozen during chronoamperometry. (a) FT of EXAFS recorded directly after deposition in neutral electrolyte (as-deposited) or after operation at low potential (0.96 V_{RHE}) in 1 M KOH for different times. The spectra of CoO(OH) (measured by Marcel Risch, Risch, 2011) is reported for comparison. The typical atomic features responsible for each peak are indicated in the figure. (b) Height of the third major peak in the FT of EXAFS, which corresponds to the second Co coordination sphere (at 5.3 Å). Comparison between samples operated in 0.1 M KPi or 1 M KOH for 4 min and sample operated in 1 M KOH at a low potential (0.96 V_{RHE}) for different amounts of time. (c) and (d) Parameters from the simulation of the EXAFS, which was performed using the five coordination shells indicated in (a). The samples were measured after different exposure times to 1 M KOH at low potential (0.96 V_{RHE}). The optimized parameters are: the Debye-Waller factor, shown in (c); the distance between the two atoms and the coordination number, shown in (d). EXAFS spectra, details on EXAFS simulation and results for all parameters and shells are presented in Fig. 7.8 and Tab. 7.2.

as-deposited to the fully equilibrated sample (Fig. 7.9c). In the first Co coordination sphere, the number of atoms increases from 3.5 to 5.7, while the Debye-Waller factor is almost halved (Fig. 7.9c-d). At the same time, an average of 4.8 second-coordinated Co-atoms organizes around each Co adsorber atom (Fig. 7.9d), suggesting major ordering of the local structure and increase in the size of Co clusters.

Table 7.2: Parameters from the simulation of EXAFS measured at the Co K-edge for CoCat after deposition in neutral electrolyte (As dep) or frozen in-situ after operation at low potential (0.96 V_{RHE}) in 1 M KOH for different times.$^{a, b, c, d, e}$

Exposed to 1 M KOH at 0.96 V_{RHE}	**C-O**			**Co-Co**		
	N	**R (Å)**	**σ (Å)^{d}**	**N**	**R (Å)**	**σ (Å)^{d}**
As dep	5.4 ±0.6	1.893 ±0.007	0.070 ±0.008	3.5 ±0.8	2.794 ±0.007	0.073 ±0.011
0.5 min	5.6 ±0.5	1.902 ±0.005	0.060 ±0.008	3.4 ±0.7	2.815 ±0.005	0.062 ±0.011
3 min	6.0±0.5	1.903 ±0.004	0.047 ±0.008	4.7 ±0.6	2.838 ±0.003	0.046 ±0.009
10 min	6.4 ±0.4	1.895 ±0.003	0.033 ±0.009	5.7 ±0.5	2.850 ±0.002	0.041 ±0.007
CO(OH)^{c}	6.3 ±0.4	1.899 ±0.003	0.034 ±0.008	6.1 ±0.6	2.859 ±0.003	0.044 ±0.007

	C-O		**Co-Co**		**Co-Co-Co^{e}**	
	N	**R (Å)**	**N**	**R (Å)**	**N**	**R_f (%)**
As dep	2.6 ±1.6	3.41 ±0.05	1.2 ±1.6	5.021 ±0.076	0.3 ±0.5	14.5
0.5 min	3.5 ±1.4	3.40 ±0.03	0.8 ±1.1	4.912 ±0.082	0.9 ±0.4	7.7
3 min	4.2 ±1.2	3.41 ±0.02	2.5 ±0.9	4.961 ±0.019	2.5 ±0.5	9.0
10 min	5.0 ±1.1	3.43 ±0.01	3.5 ±0.9	4.990 ±0.013	4.8 ±0.6	11.2
CO(OH)^{c}	6.4 ±1.1	3.40 ±0.01	6.8 ±1.1	5.012 ±0.008	4.6 ±0.7	12.7

[a] Five coordination shells were used with three parameters each: coordination number (N), distance (R) and Debye-Waller parameter (σ).

[b] The amplitude reduction factor ($S_0{}^2$) was 0.7. The R-factor (R_f) was calculated between 0.5 ≤ R (Å) ≤ 6.0.

[c] The simulation of the CoO(OH) spectrum, measured by Marcel Risch, Risch, 2011, is reported for comparison.

[d] For each sample two Debye-Waller factors were computed: one by a collective simulation of the Co-O coordination shells and the other by a collective simulation of the Co-Co coordination shells.

[e] The distance for the second Co-Co coordination shell was fixed at the double of the first-coordination-shell distance, which is 5.7 Å. A multiscattering shell was added for this distance.

XAS and Raman spectra reveal a spontaneous equilibration process, observed upon exposure of a CoCat film to alkaline electrolyte, which is coupled with Co oxidation (oxidizing as far as 40-70% of the Co sites) and a structural change, in the direction of the CoO(OH) structure. This process does not happen if the catalyst is operated at neutral pH. The structural change leads to an ordering of the sample local structure, with less variety in the bond distances and bigger Co clusters, that can support vibrations typical of the crystalline CoO(OH). A possible reason is that phosphate, which is considered responsible for limiting the size of Co clusters (Kwon, 2018; Risch, 2012; King, 2017; Farrow, 2013), is extruded from the catalyst bulk, as observed by TXRF measurements. In the following sections, a CoCat sample equilibrated and operated in alkaline electrolyte is compared with one operated in neutral electrolyte.

7.2.3 pH effect on the midpoint potential of oxidation state changes

In section 7.2.1, a higher catalytic activity and a down-shift of the oxidation wave were observed during CVs in alkaline electrolyte in respect to neutral electrolyte. The down-shift in oxidation waves suggests a lowering of the midpoint-potential for the Co oxidation reactions. Since Co^{IV} formation is proposed to be the pre-equilibrium step for OER (see chapter 6) (Surendranath, 2010; Gerken, 2011; Kanan, 2010), reducing the overpotential for the formation of these species would result in an overall improvement of the reaction energetic. XANES recorded quasi-in-situ at different potentials were used to study Co oxidation state changes and their relation to pH.

As explained in sections 2.3.1 and 6.2.3, in a XANES spectrum the distance between the pre-edge peak and the main absorption edge is proportional to the catalyst oxidation state. A series of samples were conditioned at different potentials using the freeze-quench method during steady-state chronoamperometry (same sample series presented in Fig. 7.9). Their edge positions indicate that the Co oxidation state, at parity of potentials, is higher in alkaline electrolyte in respect to neutral (Fig. 7.10). In particular, the equilibrium potentials for the Co redox transitions are shifted by 390 mV for the $Co^{II} \rightleftharpoons Co^{III}$ and by 135 mV for the $Co^{III} \rightleftharpoons Co^{IV}$, suggesting two different pH dependencies for the two transitions, simulation parameters in Table 7.3 and simulations details in section 6.2.3.

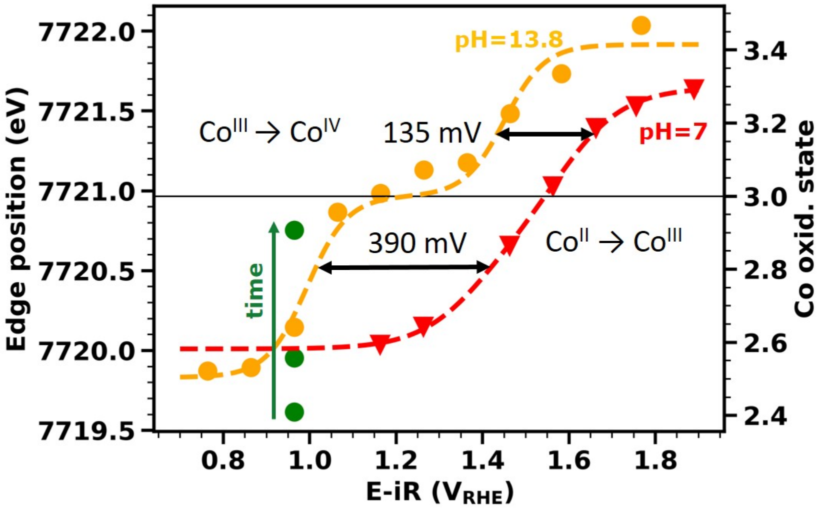

Figure 7.10: Co K-edge position determined with XAS and derived Co average oxidation state at different potentials are shown. CoCat films were frozen after exposure for 4 min (red and orange series) at the relevant potential, using the freeze-quench method. The solution used was 0.1 M KPi at pH 7 (red) or 1 M KOH at pH 13.8 (orange). The samples in the green series were exposed for different times (0, 0.5, 10 min) to alkaline electrolyte at 0.96 V_{RHE} applied potential. Dashed lines represent data simulations, consisting in the sum of two sigmoidal curves (Eq. 6.2), fitted parameters are reported in Table 7.3.

A third series of samples were frozen at different steps of the equilibration process (green series in Fig. 7.10, details in Fig. 7.6) and show an increase in oxidation state with time of exposure to alkaline electrolyte at 0.96 V_{RHE} applied potential. During 10 min the sample reaches an average oxidation state of 2.9.

Table 7.3: Midpoint potential for the $Co^{II} \rightleftharpoons Co^{III}$ and $Co^{III} \rightleftharpoons Co^{IV}$ reactions and the other parameters obtained from simulation of Co oxidation state at different applied potential with a modified Nernst equation (Eq. 6.2).[a, b]

	pH 7	**pH 14**
E_{m1} (V_{RHE})	1.39±0.03	0.99±0.02
E_{m2} (V_{RHE})	1.59±0.02	1.45±0.03
E_{I} (mV)	50±16	20±16
Y_{min1}	2.58±0.02	2.50±0.05
Y_{max2}	3.30±0.01	3.41±0.05

[a] The simulated data were obtained by XAS and are shown in Fig. 7.10.
[b] Errors represent one standard deviation.

The change in oxidation state in alkaline electrolytes can also be tracked by Raman spectroscopy, similarly to what happens in neutral electrolytes (see section 3.3.7). In the case of neutral electrolytes (reported in Fig. 3.12), the magnitude of the Raman bands decreases in intensity and the Raman spectral features are red-shifted for increasing potentials. In alkaline electrolytes (Fig. 7.11), the same decrease in bands magnitude is observed, but instead of a shift of the broad Raman features, a new Raman peak appears at low wavenumbers (473 cm^{-1}). Furthermore, the peak at 499 cm^{-1} increases, with respect to the main 629 cm^{-1} peak. The parallel with neutral electrolytes suggests that the peaks at low wavenumbers, which increase their intensity with potential, are linked to Co^{IV} species.

XANES spectra revealed a down-shift by 135 mV for the midpoint potential of the $Co^{III} \rightleftharpoons Co^{IV}$ reaction, upon change from neutral to alkaline electrolyte. This shift decreases the overpotential for Co^{IV} formation and thus, likely, the OER overpotential. The $Co^{II} \rightleftharpoons Co^{III}$ reaction is more strongly dependent on pH and its midpoint potential shifts by 390 mV, in fact Co^{III} formation is almost completed during the equilibration process, which is performed either at 0.96 V_{RHE} or in OCP (Fig. 7.3). In the Raman spectra, the oxidation state change is coupled with the appearance of a new peak at low wavenumbers, possibly linked to Co^{IV} species.

7.2.4 pH effect on the kinetic of oxidation state changes

The fixed-energy X-ray absorption spectroscopy method was used to track oxidation state changes operando and time-resolved during various electrochemical experiments. This method is extensively discussed in section 2.3. The study of the X-ray signal suggests that oxidation state changes are faster in alkaline in respect to neutral electrolyte. The CoCat sample in alkaline electrolyte was analyzed after the end of the equilibration process.

During cyclic voltammetry in neutral electrolyte the oxidation state varies from 2.6 to 3.1 and presents a strong hysteresis between forward and backward scans (Fig. 7.12). Whereas, in alkaline electrolyte, it shows no hysteresis and spans a smaller range, never decreasing below 3.0. The CV was started at a potential much lower than the first observed redox change, to ensure that the lowest oxidation state was reached. The reduced amount of oxidation state changes in alkaline electrolyte is confirmed by the X-ray edges measured just after the cyclic voltammetry

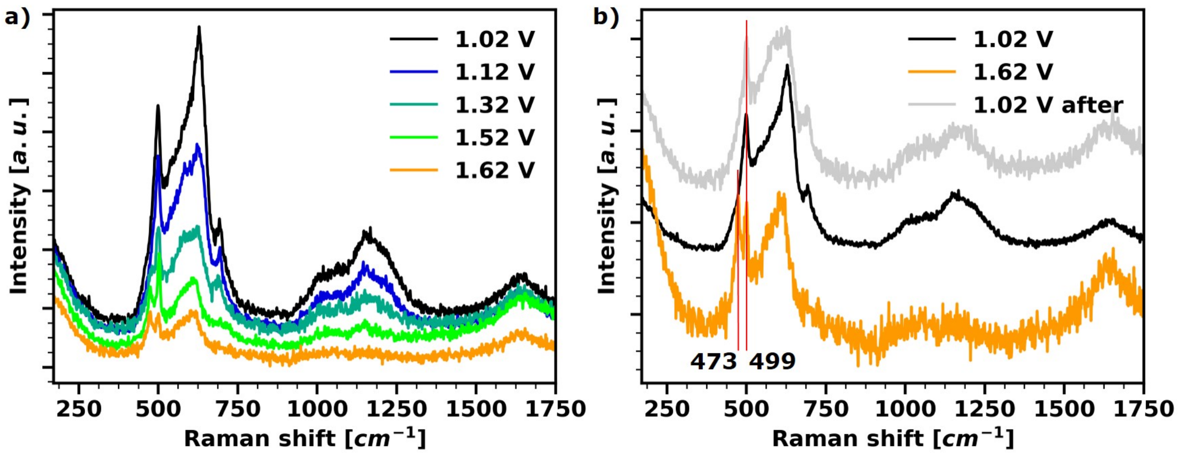

Figure 7.11: Raman spectra for CoCat, 40 mC cm^{-2} thick on Pt, operated in 1 M KOH after equilibration at OCP for 30 min. After equilibration, the sample was dried and then mounted in the Raman electrochemical cell. Raman spectra acquisition was initiated after 3 min exposure at the indicated potential. At each potential the average of 3 spectra collected for 1 min in at least two different sample positions is shown. Potentials are reported in the RHE scale. (a) Raman spectra during a potential stair experiment. The 1.32 V and 1.62 V spectra were up-scaled for clarity purposes. (b) Selected Raman spectra collected during the "potential stair" experiment and directly after it. After the "potential stair" experiment, the potential was lowered again (spectra denoted by "after"), to control the reversibility of the observed changes.

(Fig. 7.13). The presence of the hysteresis can be linked to a slow component of oxidation state changes, present only in neutral electrolyte. The CoCat appears stable in alkaline electrolyte, while in neutral electrolyte ca. 5 % of Co atoms are dissolved during 10 CVs, details on the dissolution phenomenon and the data correction procedure are reported in section 2.3.5.

The current density at high voltages presents a hysteresis in neutral electrolyte, with the current in the backward scan lower than in the forward scan. This is not explained by the hysteresis in the oxidation state, which, on the contrary, would suggest a higher current density in the backward scan. This effect can, most likely, be ascribed to the formation of a local acidic pH, due to the overrun of the phosphate buffer (as observed in section 4.2.2). In alkaline electrolyte, instead, no hysteresis is present, thanks to the high concentration of hydroxide ions, which favors proton transport mediated by the OH^-/H_2O couple, preventing the accumulation of protons at the film-electrolyte interface.

The derivative of the Co X-ray signal measures the rate of Co oxidation state changes and is proportional to the current needed to obtain those changes ("redox current", Fig. 7.14). The redox current can be derived from the fluorescence signal using equation 2.3, a dissolution factor ($diss = 0.6$) had to be added in the case of the film operated in neutral electrolyte. At both pHs, the redox current has the same shape as the recorded current density, if the catalytic activity is excluded. This confirms that the recorded current density is linked only to Co oxidation state changes or to processes that have the same potential dependence as Co oxidation state changes. It also supports the assignment of the oxidation waves, observed in the current recorded during a CV, to redox processes.

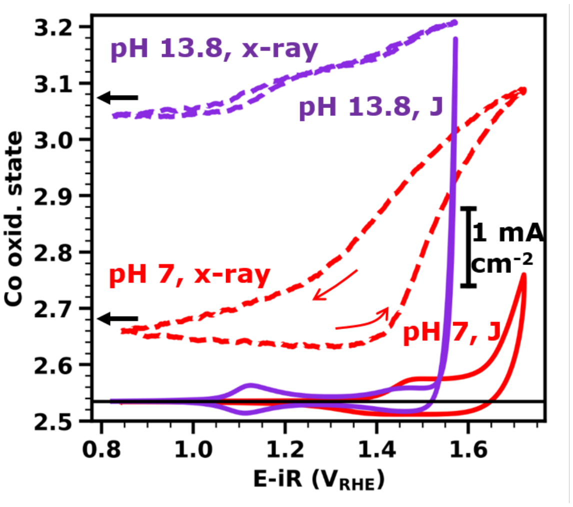

Figure 7.12: Operando time-resolved XAS during a CV (10 mV/s scan rate), for CoCat deposited on a GC substrate with a deposition charge of 25 mC cm^{-2}, in 0.1 M KPi pH 7 (red) and in 1 M KOH pH 13.8 (violet). The current density (full lines) is compared with the average oxidation state of Co (dotted lines), obtained from the X-ray signal using the method described in section 2.3.1. Samples were equilibrated with the electrolyte without potential (OCP) or at low potentials (0.96 V_{RHE}) for at least 15 min before being exposed to catalytic potentials. The average of 9 (neutral pH) and 14 (alkaline pH) CVs-repetitions are shown.

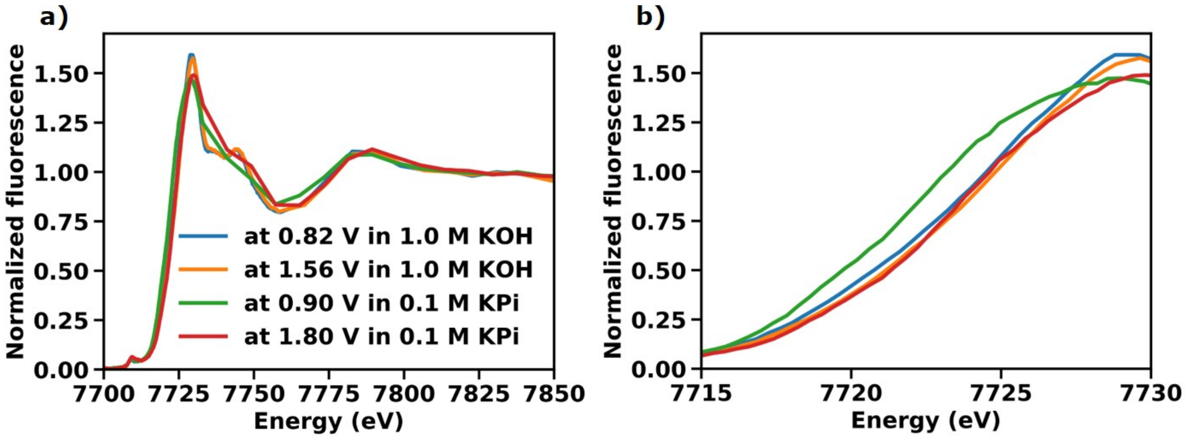

Figure 7.13: Co K-edges measured by operando XAS in 0.1 M KPi pH 7 or in 1 M KOH pH 13.8, at two different applied potentials (reported in the RHE scale) after a series of CVs (shown in Fig. 7.12). The CoCat samples were deposited on a GC substrate with a deposition charge of 25 mC cm^{-2}. Samples were equilibrated with the electrolyte without potential (OCP) or at low potentials (0.96 V_{RHE}) for at least 15 min before the CVs. (b) is a highlight of the XANES region taken from (a).

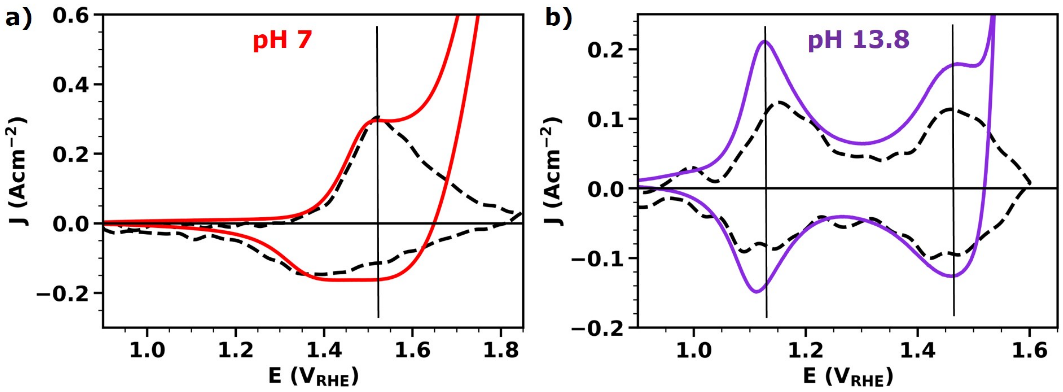

Figure 7.14: Operando time-resolved X-ray absorption spectroscopy during a CV (10 mV/s scan rate), for CoCat deposited on a GC substrate with a deposition charge of 25 mC cm^{-2}, in 0.1 M KPi pH 7 (a) and in 1 M KOH pH 13.8 (b). The measured current density (full line) is compared with the redox current density (i.e. component of the current responsible for oxidation state changes, dotted line). The redox current density was obtained from the derivative of the X-ray signal, using a dissolution factor of 0.6 and 1, in neutral and alkaline electrolyte respectively. Samples were equilibrated with the electrolyte without potential (OCP) or at low potentials (0.96 V$_{\mathrm{RHE}}$) for at least 15 min before being exposed to catalytic potentials. The average of 9 (neutral pH) and 14 (alkaline pH) CVs-repetitions are shown.

The absence of hysteresis in the oxidation state during the CV in alkaline electrolyte suggests that the Co redox reactions are faster than in neutral electrolyte. Further evidence is provided by a “potential jumps” experiment: the protocol consists in recording the Co fluorescence while stepping from a reducing to an oxidizing potential and vice versa (Fig. 7.15). When a reducing potential is applied, the X-ray signal increases, which corresponds to a reduction of Co average oxidation state. The increase is more than two times faster in alkaline electrolyte with a half-life of 160 ±30 ms compared to 370 ±30 ms in neutral. For the oxidation process the difference is higher: 130 ±10 ms in alkaline compared to 1190 ±10 ms in neutral electrolyte.

Furthermore, while the redox changes in alkaline electrolyte are completed in the time range of the experiment (20 s), this is not the case in neutral electrolyte, revealing the presence of a slower component. The slow component is also likely to cause the hysteresis observed during the CV.

In section 6.2.2, the kinetics of oxidation state changes in the 7 - 9 pH range is analyzed through visible absorption spectroscopy and a fast phase is identified, with a half-life of 100 ms for reduction and 400 ms for oxidation, which is independent of pH. The combined results suggest a rate-limiting step common at all pHs, i.e. electron transfer. In literature, two factors are proposed to influence the rate of electron transport in a Co-oxide film: the electron transfer between the Co-oxo clusters, which compose the catalyst, and the Co oxidation state; with higher Co$^{\mathrm{II}}$ concentration and smaller clusters being responsible for lower conductivity (Brodsky, 2018; Kwon, 2018; Costentin, 2016; Farrow, 2013). Our results in neutral electrolyte, consistently feature a reduction process faster than oxidation. A possible explanation is that the Co$^{\mathrm{II}} \rightleftharpoons$ Co$^{\mathrm{III}}$ transition is slower than the Co$^{\mathrm{III}} \rightleftharpoons$ Co$^{\mathrm{IV}}$ transition, due to the high concentration of Co$^{\mathrm{II}}$. During reduction the fast process is completed and, then, the slow begins. On the contrary, during oxidation, the slow process precedes and, thus, masks the fast one. In alkaline

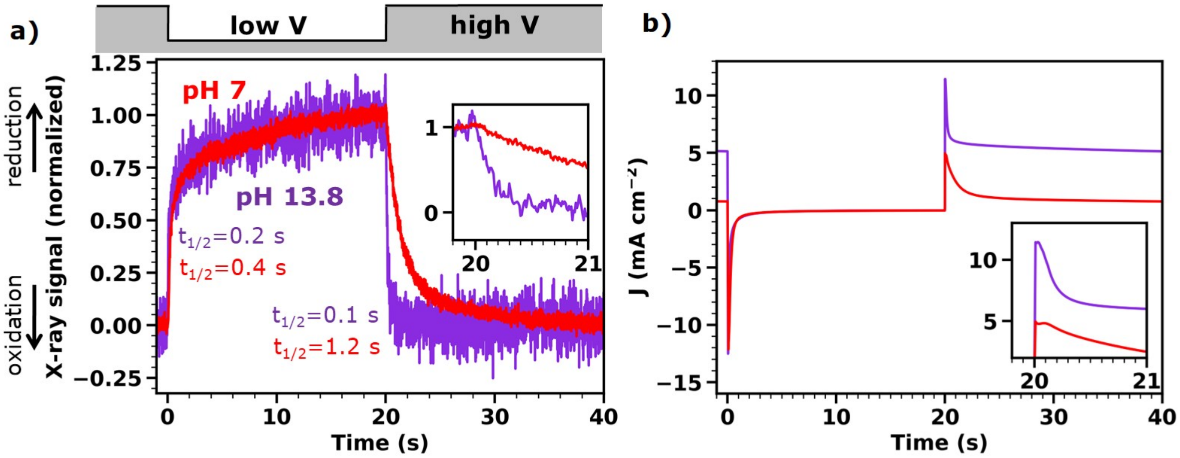

Figure 7.15: Operando time-resolved XAS during a potential jumps experiment, for CoCat deposited on a GC substrate with a deposition charge of 25 mC cm^{-2}. The electrolyte employed was either 0.1 M KPi pH 7 (red) or 1 M KOH pH 13.8 (violet), 1 M KNO_3 was added to 0.1 M KPi to ensure low solution resistance. The potential was alternated 30 times between 1.06 and 1.71 V_{RHE} (pH 7) or 0.86 and 1.71 V_{RHE} (pH 13.8) and the X-ray signal (fluorescence) from the Co was recorded, averaged over the different jumps and normalized, using the method described in section 2.3.1. Samples were equilibrated with the electrolyte without potential (OCP) or at low potentials (0.96 V_{RHE}) for at least 15 min before being exposed to catalytic potentials. (a) The normalized X-ray signal is shown as a function of time. The half-lives of the signal decay are reported ($t_{1/2}$) and, in the inset, a magnification of the short time region is shown. (b) Current density as a function of time.

electrolyte, the amount of Co^{II} is reduced and the size of the clusters is larger, facilitating inter-domain electron transfer. The increased cluster size explains the faster oxidation and reduction processes, while the reduced amount of Co^{II} explains the reduced difference between oxidation and reduction half-lives.

In alkaline electrolyte, the Co redox transitions are faster and span a smaller range than in neutral electrolyte. Moreover, a slow Co oxidation component (in the minutes' range) is detected in neutral electrolytes and likely causes hysteresis during the CV. The slower redox transitions are most likely linked to a higher Co^{II} concentration and smaller size of Co-oxo clusters in neutral electrolyte, which limits inter-domain electron transfer. These differences are not expected to affect the catalytic current, because at catalytic potentials Co^{II} is not present and electron transfer is not rate-limiting (Brodsky, 2018). The catalytic current in neutral electrolyte is most likely affected by the inefficient proton removal from the film-electrolyte interface, which causes hysteresis in the catalytic current during the CV. In alkaline electrolyte, protons are efficiently removed by OH^- anions and the hysteresis is not visible. The comparison of the derivative of the X-ray signal with the current suggests that, at non-catalytic potentials, the only process present is Co oxidation.

7.2.5 pH effect on the reaction mechanism

The Tafel slope is the increase in potential needed to obtain a ten-times increase in current density and it is often used to get information on the reaction rate-determining step (Bard, 2000b; Fletcher, 2008; Bockris, 1983; Shinagawa, 2015; Dunwell, 2018b). We introduce a new concept: the study of the dependence of current density from Co oxidation state, which reveals differences in reaction mechanism between neutral and alkaline pH.

Steady-state chronopotentiometry measurements in alkaline electrolyte revealed a more than 500-times increase in current density compared to neutral pH and a decrease in Tafel slope from 72 to 38 mV/dec (Fig. 7.16a), indicating improved conditions for catalysis and likely a change in the OER rate-limiting step.

The chronopotentiometry experiment was performed during operando X-ray measurements at a fixed energy (see section 2.3.3 for details), which provided an estimation of the Co oxidation state per each measured catalytic current.

At neutral pH, the current density has an exponential dependence on Co oxidation state. In chapter 6 and simlarly in Nong, 2020, the exponential dependence was explained with the formation of higher energy states, with a lower energy barrier for OER, as Co^{IV} accumulates within the catalyst material. At alkaline pH, the data suggest that there is no direct dependence of the current from the oxidation state, when a certain maximum oxidation state is reached the current density can increase driven by an increase in applied potential, without further change in the oxidation state. However, within the limit of data accuracy, a very steep exponential dependence of the current from Co oxidation state, similar to what happens in neutral electrolyte, cannot be excluded.

Steady-state chronoamperometry revealed higher current density in alkaline electrolyte in respect to neutral and a possible change in the reaction mechanism. Unlike in neutral, in alkaline electrolyte no accumulation of Co^{IV} species is observed and the OER could be directly driven by the applied potential, suggesting a change in the rate-determining step.

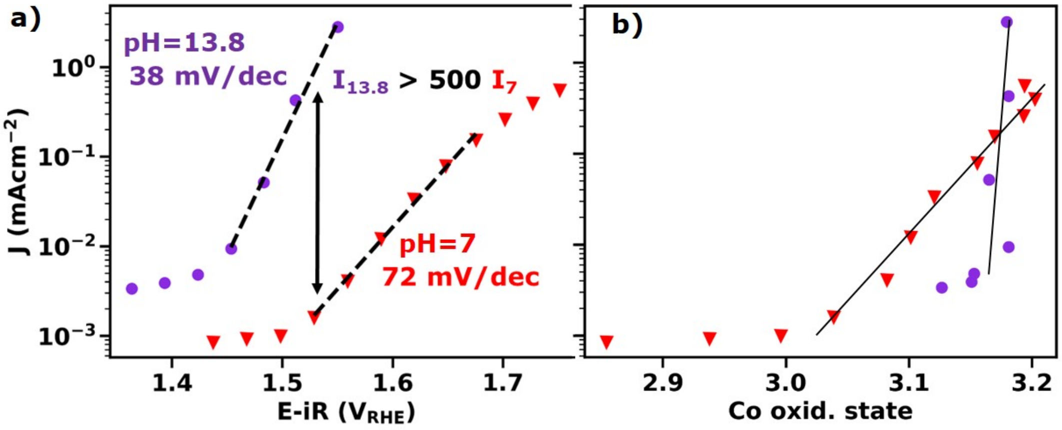

Figure 7.16: Chronopotentiometry measurements (values taken after 2-3 min equilibration) for CoCat deposited on GC substrates at pH 7 and tested in either 0.1 M KPi pH 7 (red triangles) or 1 M KOH pH 13.8 (violet circles). Samples were equilibrated with the electrolyte without potential (OCP) or at low potentials (0.96 V_{RHE}) for at least 15 min before being exposed to catalytic potentials. (a) Tafel plot, reporting the current density as a function of potential. Dotted lines are obtained by a fit of the linear region and the inverse of their slope is reported (Tafel slope). (b) Current density as a function of average Co oxidation state, obtained from the position of the Co K-edge, measured with operando XAS. Black lines were added to guide the eye.

7.2.6 Slow vs. fast Co oxidation in alkaline electrolytes

In section 7.2.2, the equilibration process is identified as a slow oxidation of the catalyst coupled with local ordering, which is driven by exposure to alkaline electrolyte in OCP or at low applied potentials. When, instead, the oxidation is driven by a catalytic potential, applied just after exposure of the catalyst to alkaline electrolyte, the oxidation is faster and a different non-ordered structure is obtained.

The two different equilibration processes are explained in Fig. 7.17. Two CoCat films were prepared by electrodeposition in pH 7 electrolyte on carbon fiber paper (CFP), which provides higher catalyst stability in respect to GC. Then, the films were dried and transferred in an electrochemical cell with 1 M KOH (pH 13.8) and exposed to an X-ray beam, which allowed to track the changes in Co oxidation state operando (black lines in the figure). One film was exposed to 1 M KOH without applying any potential for 1 h (panel a), during this time the average Co oxidation state increased and reached a stable state after 40 min. The second film was operated directly after exposure to 1 M KOH by performing two CVs. The application of a strongly oxidizing potential during the CV considerably accelerates the oxidation process (panel c), leading to different electrochemical behavior of the resulting catalyst film (compare panels b and d). In both cases the change in Co oxidation state was irreversible. The CV for the fast-equilibrated film (panel d) does not have a well-separated oxidation wave at low potential, which is visible for the slow-equilibrated film (panel b). In the fast-equilibrated film, the first oxidation wave is most likely merged with the second oxidation wave, like in neutral electrolytes, also the CV exhibit hysteresis in oxidation state changes as previously observed in neutral electrolytes (see Fig. 7.12). Reference edge scans were recorded before and after the CVs to exclude loss of material.

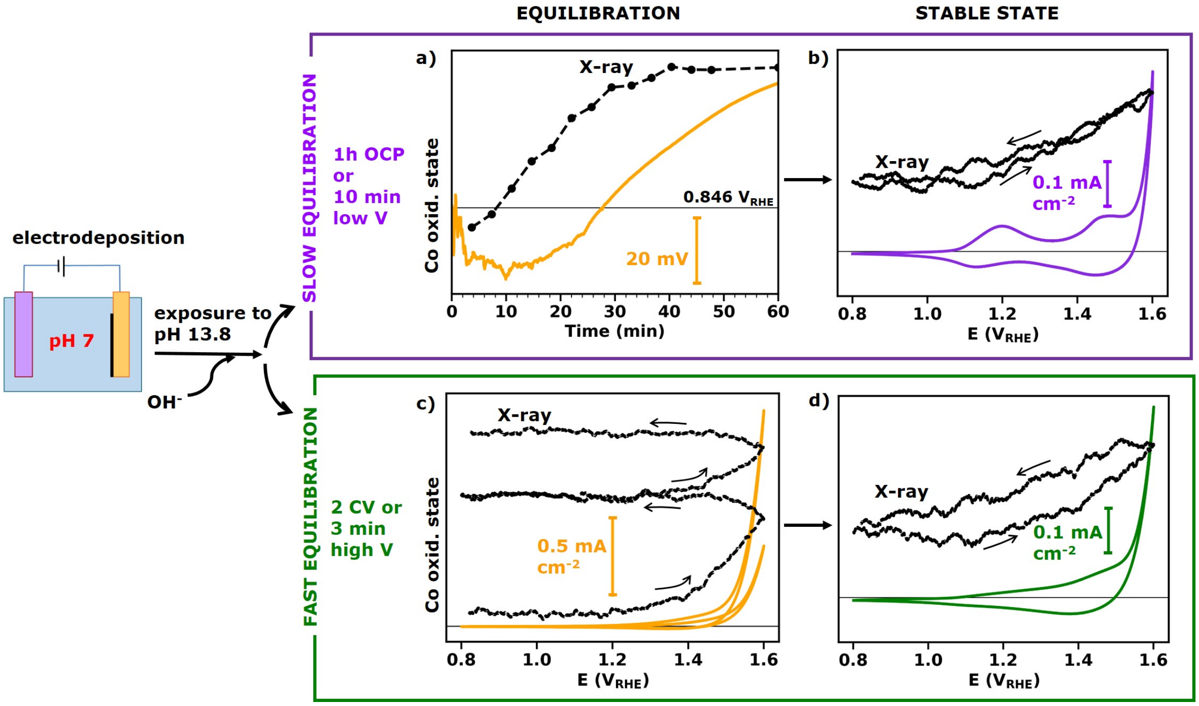

Figure 7.17: Scheme explaining the different electrochemical and redox behaviors stemming from different equilibration procedures in 1 M KOH for a CoCat film. The films were electrodeposited on a CFP substrate in 0.1 M KPi, with a deposition charge of 12.5 mC cm^{-2}. The colored lines represent the value of the open circuit potential in (a) and the current density in (b)-(d). The black lines represent the change in Co oxidation state obtained from the X-ray fluorescence, with the incoming beam energy fixed at 7722 eV. The black lines are shown on a reverse scale. In (a) each of the black points refers to a Co edge measured in OCP (full edges shown in Fig. 7.3d). In (b)-(d) the black lines were obtained during a CV experiment, for details see section 2.3. (a) Slow equilibration during exposure to OCP. (b) Stable behavior obtained after the slow equilibration. (c) Fast equilibration during the performance of two CVs. (d) Stable behavior obtained after the fast equilibration, followed by 1h exposure to OCP.

Raman spectra of the slow-equilibrated and fast-equilibrated films (prepared ex-situ) are compared in Fig. 7.18a, together with an as-deposited sample. In the case of the fast-equilibrated film, the structural change has begun (see the small peak at 497 cm^{-1}), but was most likely stopped by the fast oxidation. The resulting Raman spectrum is similar to the one of the as-deposited sample. In the 1000-1250 cm^{-1} region, the bands belonging to phosphate incorporated in the structure are not present. Thus, the fast-equilibration process involves the removal of phosphate species from CoCat interlayers, but it does not involve local ordering of the structure.

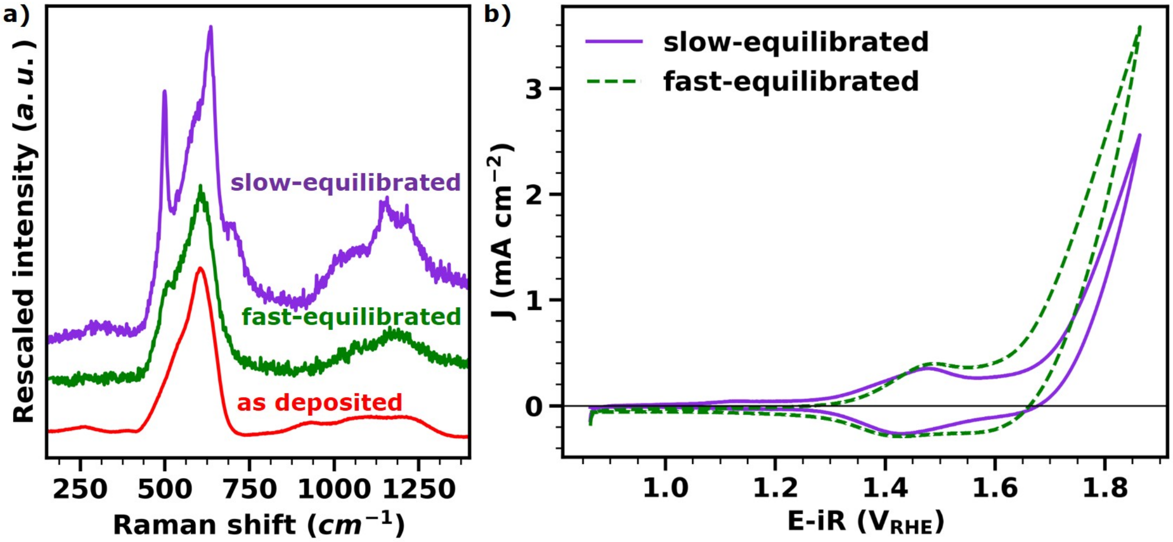

Figure 7.18: (a) Raman spectra for dry CoCat films measured: directly after deposition in neutral electrolyte (as-deposited), after exposure to 1 M KOH combined with catalytic potentials (fast-equilibrated) or after exposure to 1 M KOH combined with OCP (slow-equilibrated). After equilibration both the catalyst films were extensively operated in 1 M KOH, washed with MilliQ water, dried and measured with Raman spectroscopy. Samples were deposited on Pt with a deposition charge of 40 mC cm^{-2}. (b) CV (at 20 mV s^{-1} scan rate) in 0.1 M KPi at pH 7 for CoCat films after equilibration. Films were 40 mC cm^{-2} thick, deposited on Pt substrates. The CoCat films were deposited in 0.1 M KPi pH 7, then equilibrated in 1 M KOH, with either the slow-equilibration protocol (full line) or the fast equilibration (dotted line), extensively operated in 1 M KOH and transferred again to KPi at pH 7 to record the CVs shown in the figure. All CV features are reproducible.

The change in structure is not reverted when a sample, equilibrated in alkaline electrolyte, is transferred back to neutral electrolyte. Compared to a standard CV at pH 7, a CV on the slow-equilibrated sample has a more defined oxidation wave, indicating less variety between the local environments of Co atoms (Fig. 7.18b). Instead, the fast-equilibrated sample, transferred in a pH 7 electrolyte, does not differ from a standard CV at pH 7.

To exclude that the differences between fast- and slow-equilibrated catalysts are due to flawed adhesion to carbon substrates or to carbon corrosion (Gorlin, 2017; Yi, 2017), the CV experiment was repeated on a series of different substrates (Fig. 7.19), namely glassy carbon, carbon fiber paper, Pt and ITO on glass. The differences in redox waves between CVs on slow-equilibrated and fast-equilibrated catalysts were observed on all examined substrates. The CVs on fast-equilibrated catalysts presented consistently an earlier onset of the catalytic activity and a higher Tafel slope, although stability and activity changed according to the substrate. The cell resistance was slightly higher for the fast-equilibrated samples in respect to the slow-equilibrated, at parity of substrate, suggesting a worse adherence of the catalyst to the substrate.

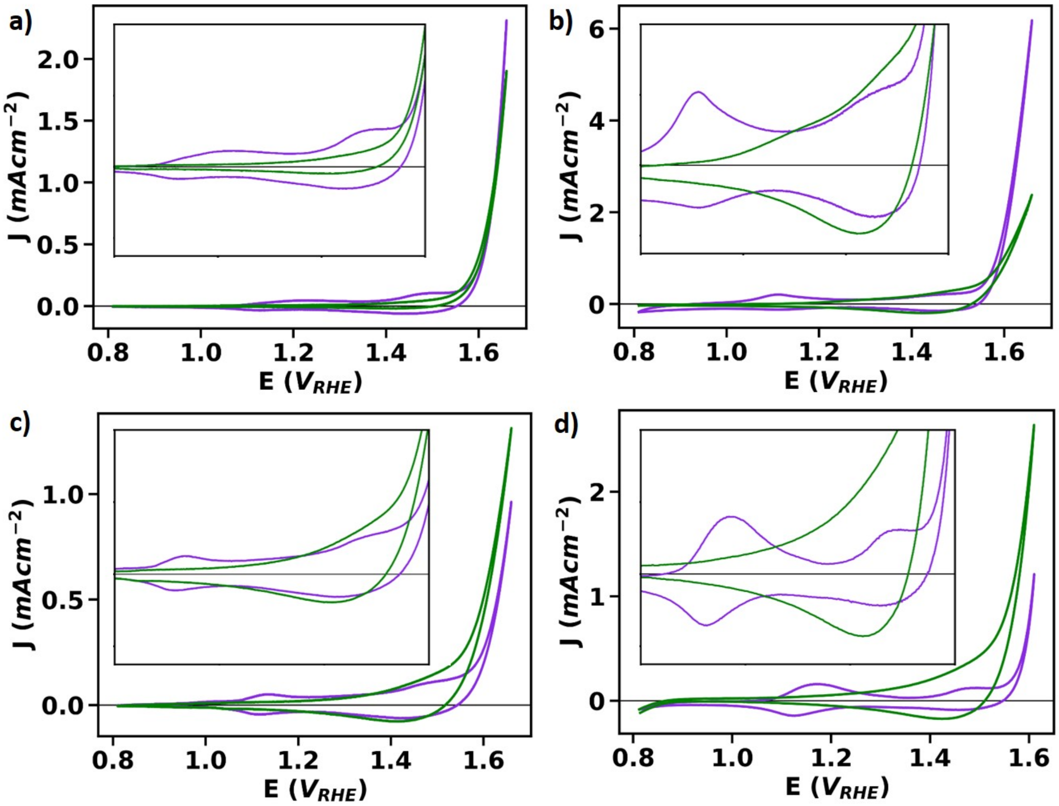

Figure 7.19: CVs (20 mV s^{-1} scan rate) started either directly after exposure to 1 M KOH (fast-equilibrated, green line) or after 1 h exposure to 1 M KOH in OCP (slow-equilibrated, violet line). The second CV is shown, the third CV does not differ significantly from the second. Different substrates were used: (a) carbon fiber paper, (b) glassy carbon, (c) ITO, (d) Pt. The deposition charge was 40 mC cm^{-2} on Pt and 10 mC cm^{-2} on the other substrates, because for a thin film on Pt it is not possible to obtain a fast-equilibration process.

Pt substrate provides good adhesion for the catalyst film and was used to study possible activation effects, resulting from prolonged catalyst activity. For the CV on a fast-equilibrated catalyst, we observe an increase in the redox area and in the catalytic properties after operation for 30 min at high catalytic current (Fig. 7.20, dashed lines). Furthermore, during the 30 min operation the overpotential required to drive OER is constantly decreasing. The same is not true for the CV on the slow-equilibrated catalyst, which presents an overpotential slightly increasing over time. Additional 30 min of operation (dotted lines) do not improve the activity further.

When the CoCat, prepared at neutral pH, is exposed to alkaline electrolyte, an irreversible oxidation process occurs. By applying a strong oxidative potential directly after sample exposure to the electrolyte, it was possible to drive the oxidation process to completion in few minutes (fast-equilibration). The fast-equilibration process, unlike the slow-equilibration, does not cause an ordering of the structure, in the resulting CV both redox waves are down-shifted in respect

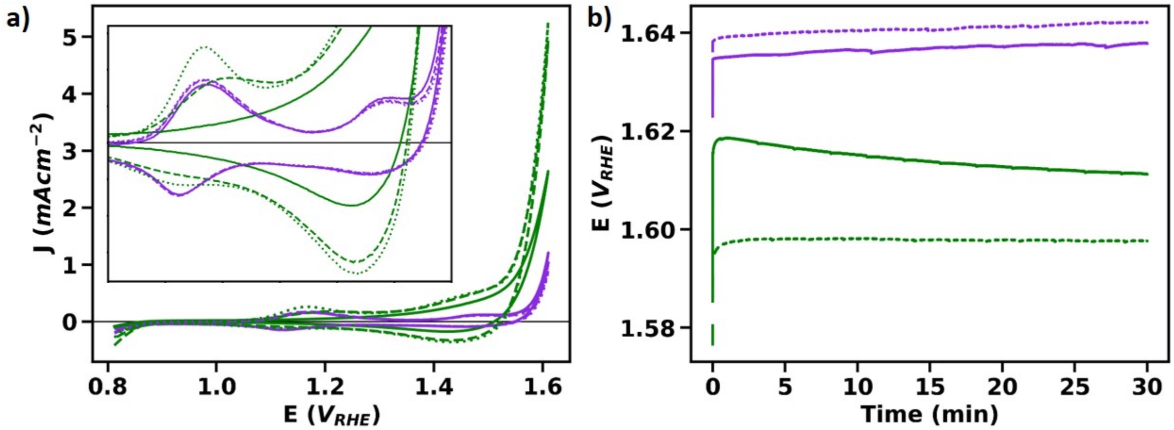

Figure 7.20: Activation process upon operation in 1 M KOH for a 40 mC cm^{-2} thick CoCat film deposited on Pt. An electrochemical protocol involving the alternation of 3 CVs (the second CV is shown) with 30 min chronopotentiometry was performed in purified 1 M KOH. The protocol was either preceded by 30 min equilibration in 1 M KOH (slow-equilibration, violet line) or started directly after exposure of the catalyst to alkaline electrolyte (fast-equilibration, green line). (a) CVs and (b) chronopotentiometry measurements (at 3 mA cm^{-2}), the first cycle is indicated by a full line, the second by a dashed line and the third by a dotted line. The behavior is reproducible.

to a CV in neutral electrolyte, but they are not separated, like they are after slow-equilibration. There is a difference in the catalytic properties, namely the fast-equilibrated catalyst has an earlier onset of OER but higher Tafel slope, in comparison to the slow-equilibrated. Operando XAS confirmed that the differences between the two catalysts are related to the speed of the irreversible oxidation process.

7.2.7 Universality of the equilibration phenomena

In the previous section, a simple protocol was developed to tune the level of crystallinity and electrochemical behavior of the Co oxide catalyst (anodically electrodeposited CoCat) in alkaline electrolyte. This was achieved by changing the speed of the oxidation process, which happens spontaneously when the catalyst is exposed to alkaline electrolyte. In this section, we study the universality of the observed behavior, by investigating differently prepared Co catalysts: the cathodic electrodeposition (Merrill, 2008) and the spin-coating (Smith, 2013a) methods were chosen for our analysis.

The "cathodically deposited catalyst" was electrodeposited from a neutral pH buffer using a short negative current pulse (1 s, -250 mA cm^{-2}), the negative current is used to produce molecular hydrogen, generating local alkalinization, which causes Co precipitation on the electrode. After deposition, the film was transferred in alkaline electrolyte and either equilibrated for 30 min at OCP (slow-equilibrated catalyst) or directly oxidized by performing a CV (fast-equilibrated catalyst), see Fig. 7.21b. The subsequent CVs present strong differences in the redox wave, namely the fast-equilibrated CV has a bigger redox area for the first oxidation wave and a slightly smaller redox area for the second oxidation wave. This is opposite to CoCat behavior (Fig. 7.21a), which has no low-potential redox features in the fast-equilibrated catalyst. To exclude that the difference is only a result of the longer time spent in alkaline electrolyte the fast-equilibrated film was left for 30 min in OCP before performing another CV series (Fig. 7.22a).

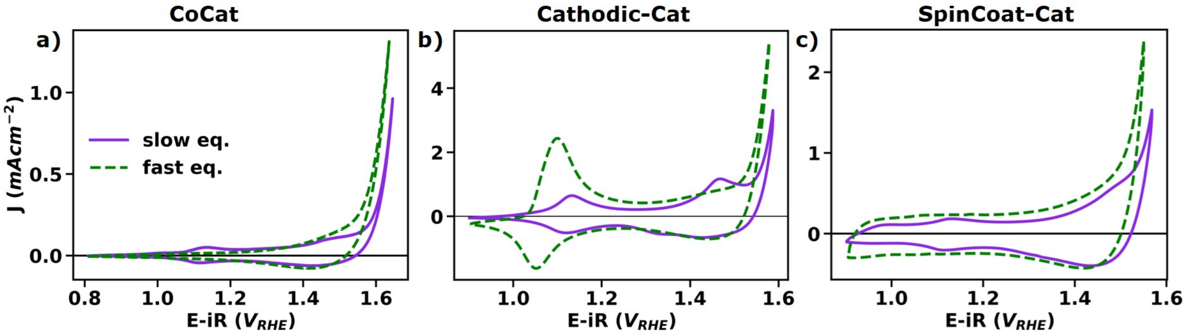

Figure 7.21: Cyclic voltammetry started either 2 s after exposure of a Co-oxide catalyst to 1 M KOH (green dotted line, fast-equilibration) or 30 min after exposure (violet line, slow-equilibration). The second CV is shown. The catalyst used was obtained either by (a) anodic electrodeposition (CoCat), (b) cathodic electrodeposition or (c) spin coating.

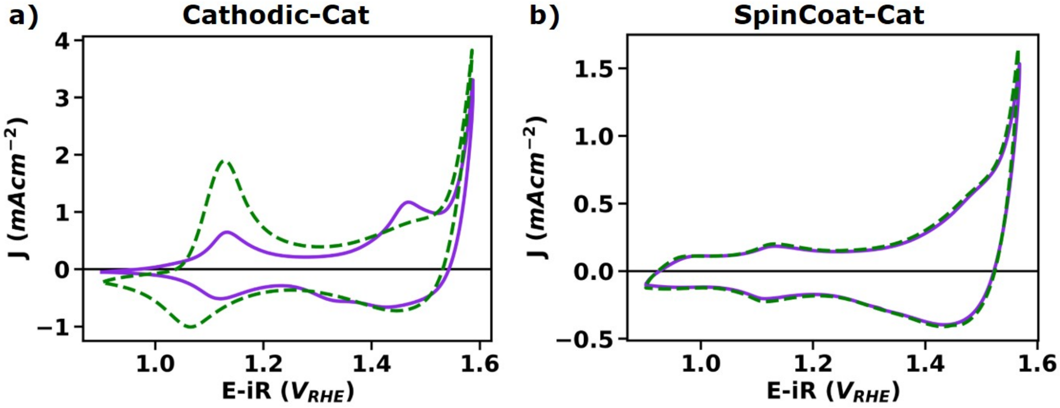

Figure 7.22: Irreversibility of the fast-equilibration process. Cyclic voltammetry for a Co-oxide catalyst in 1 M KOH started after 30 min at OCP for a fast-equilibrated (green dotted line) and a slow-equilibrated (violet line) catalyst. For the fast-equilibrated catalyst, 3 CVs were performed starting 2 s after exposure to 1 M KOH, then the film rested for 30 min at OCP and, then, 3 further CVs were performed (the second of this series is shown). For the slow-equilibrated catalyst, the protocol was similar but started directly with the 30 min resting time in OCP. The catalyst used was obtained either by (a) cathodic electrodeposition or (b) spin coating.

The “spin-coated catalyst” was prepared by spin-coating a drop of a metal-organic precursor and then using UV light to decompose the organic compound. To prepare the catalyst in the slow-equilibrated and fast-equilibrated state, three CVs were performed either directly after exposure to alkaline electrolyte or after 30 min in OCP. The slow-equilibrated catalyst presents more defined oxidation waves (Fig. 7.21c), which are almost not visible in the fast-equilibrated one, and lower catalytic activity. Unlike for the other catalyst types, when the fast-equilibrated film rests for 30 min in solution, it develops the same redox waves as the slow-equilibrated one (Fig. 7.22b).

Analysis of the Co K-edge positions, obtained by XANES, on the “cathodically deposited catalyst” indicates that the oxidation state changes, driven by the same applied potential, span a smaller range in the slow-equilibrated catalyst in respect to the fast-equilibrated (Fig. 7.23b). This is observed also in the case of CoCat (Fig. 7.23a) and “spin-coated catalyst” (Fig. 7.23a). As observed in the case of CoCat, in section 7.2.4, the magnitude of the redox waves in the CV do not fully mirror the measured change in oxidation state.

The three catalysts investigated have different local structures when examined directly after synthesis (compare "as prepared" in Figures 7.24, 7.25 and 7.26). Once exposed to alkaline electrolytes, however, they present very similar local structure, despite the differences in the CVs, as indicated by almost identical EXAFS features (Fig. 7.23). The structure of the slow-equilibrated catalysts has consistently a higher crystallinity level than the fast-equilibrated, indicated by higher peaks in the EXAFS, and resembles CoO(OH) (compare with Fig. 7.9a). It must be noted that the slow-equilibrated catalysts were dried in air after the equilibration process was completed and this could have an effect on XANES and EXAFS results, although a test performed for CoCat (Fig. 7.7) and the operando measurements suggest that this is not the case. The XANES and EXAFS spectra measured after conditioning at various potentials for CoCat, cathodically deposited and spin-coated catalysts are reported in Figures 7.24, 7.25 and 7.26, respectively.

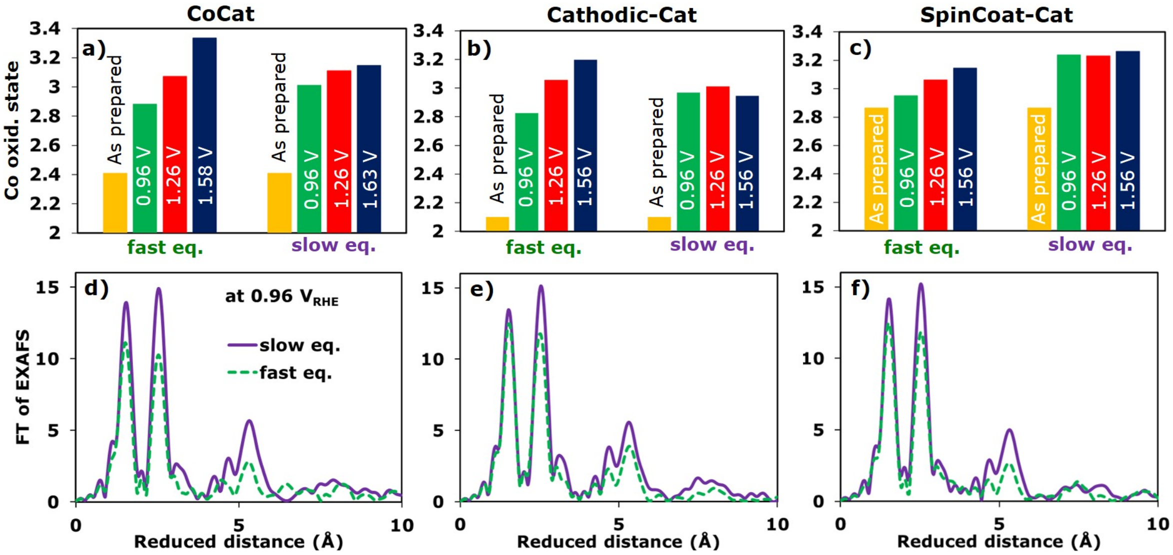

Figure 7.23: Effects of slow- and fast-equilibration processes on the oxidation state and the local structure of three differently prepared Co-oxide catalysts: (a) and (d) anodically electrodeposited (CoCat); (b) and (e) cathodically electrodeposited; (c) and (f) spin-coated. The catalysts were either: (1) exposed for 30 min in OCP in 1 M KOH, dried in air and then frozen after conditioning at the desired potential for 4 min (violet, slow-equilibration) or (2) conditioned for 1 min at a high potential just after exposure to 1 M KOH and then frozen after conditioning at the desired potential for 3 min (green, fast-equilibration). From XAS measurements (a-c) Co average oxidation states at different potentials derived from the Co K-edge position and (d-f) FT of the EXAFS at 0.96 V$_{\mathrm{RHE}}$.

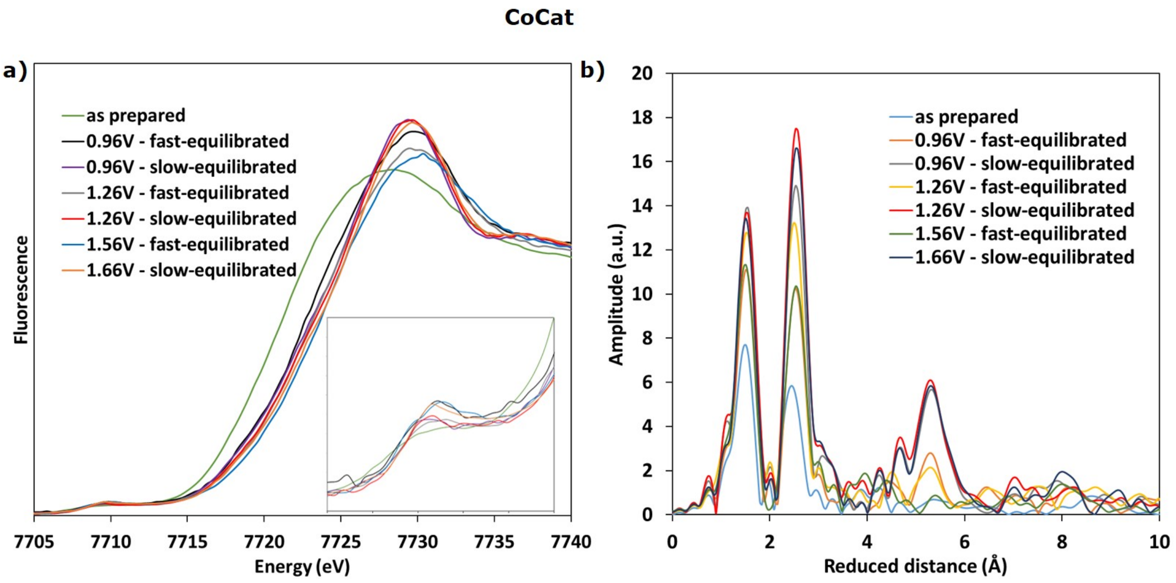

Figure 7.24: XAS measurements at the Co K-edge for an anodically electrodeposited catalyst (CoCat). The catalyst was either: (1) exposed for 30 min in OCP in 1 M KOH, dried in air and then frozen after conditioning at the desired potential for 4 min (slow-equilibration) or (2) conditioned for 1 min at a high potential just after exposure to 1 M KOH and then frozen after conditioning at the desired potential for 3 min (fast-equilibration). (a) XANES with inset showing the pre-edge region and (b) FT of the EXAFS at different potentials. Potentials are reported in the RHE scale.

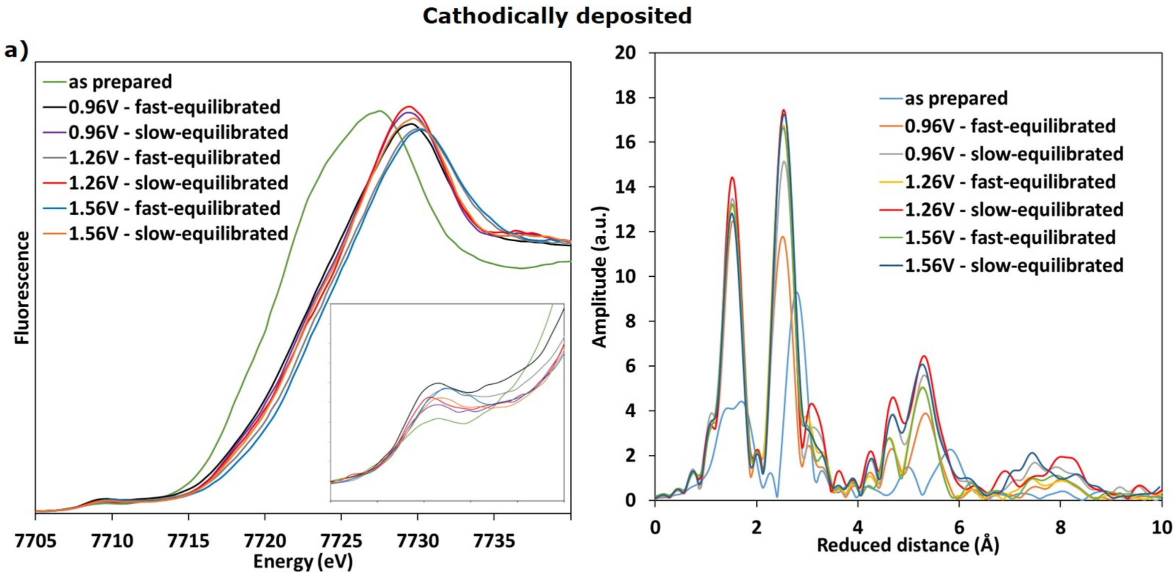

Figure 7.25: XAS measurements at the Co K-edge for a cathodically electrodeposited catalyst. The catalyst was either: (1) exposed for 30 min in OCP in 1 M KOH, dried in air and then frozen after conditioning at the desired potential for 4 min (slow-equilibration) or (2) conditioned for 1 min at a high potential just after exposure to 1 M KOH and then frozen after conditioning at the desired potential for 3 min (fast-equilibration). (a) XANES with inset showing the pre-edge region and (b) FT of the EXAFS at different potentials. Potentials are reported in the RHE scale.

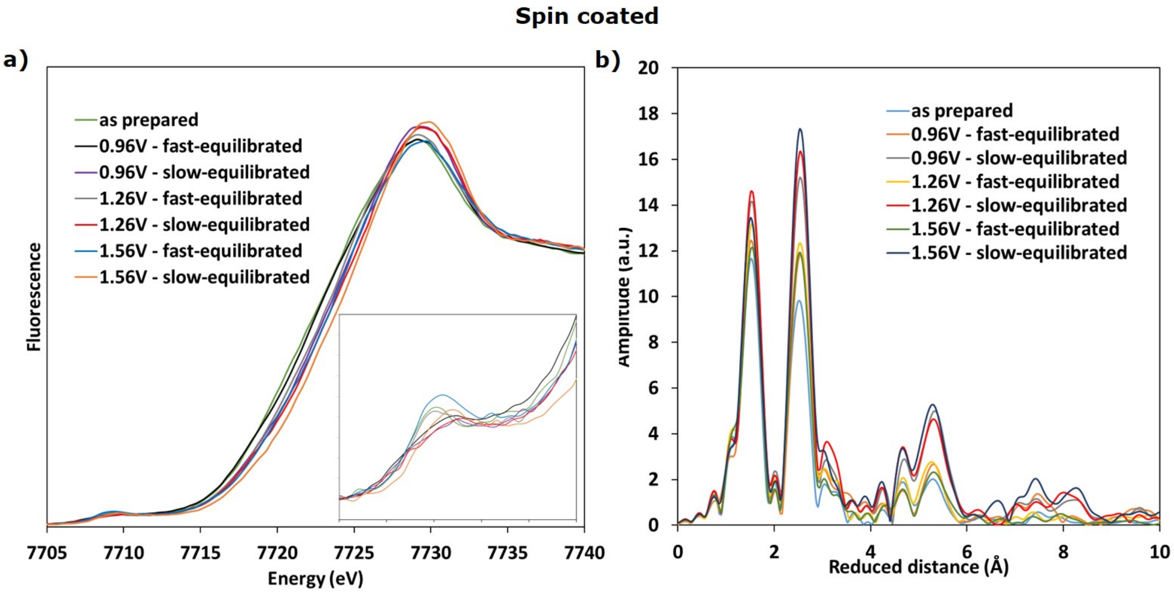

Figure 7.26: XAS measurements at the Co K-edge for a spin-coated catalyst. The catalyst was either: (1) exposed for 30 min in OCP in 1 M KOH, dried in air and then frozen after conditioning at the desired potential for 4 min (slow-equilibration) or (2) conditioned for 1 min at a high potential just after exposure to 1 M KOH and then frozen after conditioning at the desired potential for 3 min (fast-equilibration). (a) XANES with inset showing the pre-edge region and (b) FT of the EXAFS at different potentials. Potentials are reported in the RHE scale.

Comparison between three differently prepared Co catalysts highlighted the principal characteristics of the equilibration process. For all the examined catalysts, the oxidation state directly after synthesis is lower than their oxidation state at alkaline pH. Thus, exposure to alkaline pH involves an oxidation, which can happen through a slow or a fast process, resulting in two catalysts with different structural, redox and catalytic properties. The slow-equilibrated catalysts have a higher degree of local ordering and span a reduced range of oxidation states. The shape of the redox waves differs between CVs for fast- and slow-equilibrated catalysts and the fast-equilibrated presents slightly better activity at low overpotentials. These results strongly suggest that the equilibration process could be a key factor to determine the catalyst properties and structures, while the different preparation methods do not influence the final structure.

7.3 Discussion

7.3.1 Tailoring catalyst activity and degree of crystallinity

Three different Co-oxide catalysts were studied in this work (CoCat, cathodically deposited and spin-coated), for all of them we found that the as-prepared state is more reduced than their stable state in alkaline electrolyte (Fig. 7.23). Namely, Co average oxidation state changes from 2.4 to 3.0, 2.1 to 3.0 and 2.9 to 3.2 were observed, for the three catalysts respectively, during an irreversible oxidation process, which occurs when the catalyst is exposed to alkaline electrolyte. The process is most probably linked to the oxidation of Co^{II} sites to Co^{III}. The oxidation could either proceed fast, when driven by an oxidizing potential, or slow, when a low or open circuit potential is applied (Fig. 7.17), resulting in two different final catalyst structures. Co^{II} ions are reported to routinely leach in solution and can be redeposited following a $Co^{II} \rightarrow Co^{III}$ reaction (Surendranath, 2012; Costentin, 2017; Mohammadi, 2020), this characteristic makes Co^{II} ions highly mobile in the material. During the slow equilibration, mobile Co^{II} species support the formation of a structure with a higher degree of crystallinity (see also scheme 7.27). On the contrary, during the fast equilibration, Co^{II} species are converted to Co^{III}, before they can reorganize, thus blocking the catalyst in the disordered state. The blocking effect is irreversible, except for spin-coated catalysts. A similar protocol has been recently applied on a Co selenide precursor, where performing the slow equilibration, rather than the fast, lead to a more-ordered, not bulk active material (Hausmann, 2020).

When CoCat is kept in neutral electrolyte, reorganization of the Co sites is prevented by the presence of phosphate in the structure (Farrow, 2013; Kwon, 2018; Risch, 2012; King, 2017), which is expelled when the catalyst is exposed to alkaline electrolyte (Fig. 7.3 and 7.4). The equilibration process possibly affects a wide range of catalysts, not only the ones studied in this work, and should be taken into account when designing an electrochemical experiment. Differences in the electrochemical protocol or even in the time passed between set-up preparation and the effective start of an experiment could result in very different catalysts being examined, causing problems in experiment reproducibility and results interpretation. On the positive side, the slow or fast equilibration protocols can be exploited knowingly, as a new tool for tailoring catalysts structures with the desired electrochemical properties.

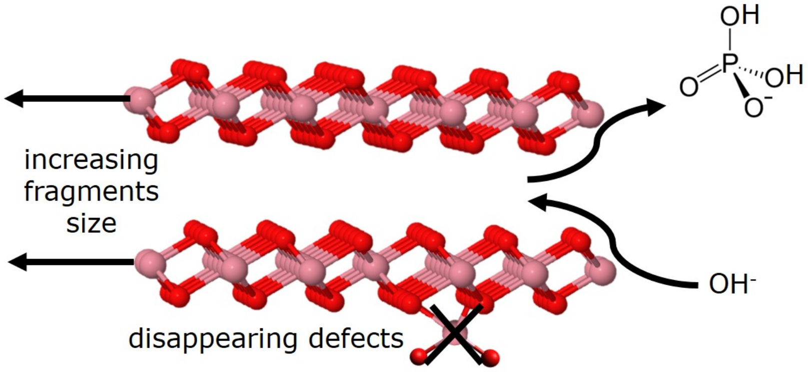

Figure 7.27: Scheme showing the effect of a slow equilibration in alkaline electrolyte for a CoCat film. The Co-oxide layers, which constitute the catalyst structure, increase their size, defects disappear and the phosphate present in the interlayer space is substituted by hydroxide ions.

After the slow equilibration, the three catalysts, prepared with three different methods, convert to the same structure (Fig. 7.23). The final structure is more ordered than each of the three initial ones and is almost identical to CoO(OH), apart from some degree of disorder, which is revealed by the broad feature in the Raman spectrum (Fig. 7.3). It is interesting to note that Raman spectra are more sensitive to the presence of defects, which cause the appearance of broad bands, in respect to EXAFS spectra. CoO(OH) was reported to form during OER (Bergmann, 2015; Yeo, 2011; Huang, 2016) and is considered favorable for catalytic performances (Favaro, 2017). In this work, we found that three different catalysts spontaneously transform to CoO(OH) through their bulk (XAS is a bulk technique), via exposure to alkaline electrolyte with low (just below the first redox transition) or no potential applied. Interestingly, even though the structure of the three equilibrated catalysts is the same, they still have different redox properties (Fig. 7.21), which could arise from differences linked to a minority of Co sites, not detectable by EXAFS.

Previously, it was shown that CoO(OH) nanosheets, with local structural distortions, have 20 times higher catalytic activity than bulk CoO(OH) (Huang, 2015). The structures obtained with the fast-equilibration protocol may be similar to the nanosheets, because they have a lower degree of order than the CoO(OH) structure (Fig. 7.23), resulting in a higher catalytic activity (Figures 7.21 and 7.20). For the CoCat, the fast-equilibration retains the catalyst amorphous structure and the small size of the Co-oxo cluster also in alkaline electrolyte (Fig. 7.18a). Since oxidation state changes and catalytic activity occur mostly at defect sites at the periphery of Co-oxo clusters (Kwon, 2018; Farrow, 2013; Risch, 2012; Bediako, 2015; Fester, 2017), they are enhanced by a smaller cluster size. The double-sided effects of smaller clusters have been introduced by studies comparing CoPi and CoBi (Kwon, 2018; Farrow, 2013), where disorder in the structure induced by phosphate had two parallel effects: from one side it increased the number of active Co ions and on the other side it decreased the bulk activity, which has been attributed to lower charge transport between Co clusters. The comparison between slow- and fast-equilibrated catalysts confirms this double effect. The fast-equilibrated catalyst shows an earlier onset of the catalytic activity, due to the higher number of active sites and the presence of defects, but the Tafel slope is higher, possibly due to slower proton or electron transfer kinetics, which introduces limitation at high turnover frequencies (more details in the next section).

Interestingly, the redox waves for the fast-equilibrated catalyst are similar to the redox waves for CoOx containing a large amount of Fe (Burke, 2015a). This similarity suggests that Fe could also act by blocking Co atoms ordering in alkaline electrolytes and, thus, improving catalytic performances. Available structural data (Enman, 2018; Smith, 2017) are not in contrast with this hypothesis, but a specific study is needed to provide evidence for it. Note that Fe was previously reported to hinder β- to γ-NiOOH transition (Klaus, 2015).

Finally, a parallel can be drawn between the β- and γ-NiOOH phases and the slow- and fast-equilibrated catalysts studied in this work. We argue that the catalyst prepared at neutral pH has similarities with the γ-NiOOH phase, due to its hydrated state, which allows bulk-activity, and the cations present inside the material (Surendranath, 2010; Klingan, 2014; Kanan, 2008). The slow-equilibration resembles the aging in alkaline electrolyte, which is reported to cause a transition from the γ- to the β-NiOOH phase (Bode, 1966; Doyle, 2013; Oliva, 1982; Klaus, 2015). Conversely, the fast-equilibration blocks the catalyst in the γ phase. The fast-equilibrated catalyst spans a larger range in oxidation state changes and has higher catalytic performances, which are characteristics typical of the γ-NiOOH phase (Bediako, 2012). Even issues in electrical contact with the substrate have been previously reported as a possible reason for decreased catalytic activity in the γ-NiOOH phase (Bediako, 2012) and are now revealed for the fast-equilibrated catalyst (higher cell resistance measured). However, although phase transition are reversible for Ni (Bode, 1966; Doyle, 2013; Oliva, 1982), the equilibration process for Co is irreversible (Fig. 7.18b). To validate the parallel between fast-equilibrated Co and γ-NiOOH and slow-equilibrated Co and β-NiOOH stronger experimental evidence is needed, including measurements of interlayer-spacing (XRD) and hydration levels (microgravimetry). It would also be interesting to clarify the role of carbon ligands by repeating the experiments in a controlled atmosphere and using substrates that do not contain carbon.

7.3.2 What causes improved activity in alkaline electrolytes?

The catalytic performances for CoCat in alkaline electrolyte are better than in neutral, due to an earlier onset of the catalytic activity and a lower Tafel slope (Figures 7.1 and 7.16). Improvements in catalytic current, linked to alkaline electrolytes, were reported for a large number of catalysts (Görlin, 2016; Grimaud, 2017; Gerken, 2011; Trześniewski, 2015; Takashima, 2012; Huynh, 2014; González-Flores, 2016). By comparing the fast- and slow-equilibrated catalysts in alkaline electrolyte with the catalyst in neutral electrolyte, we can differentiate between effects linked to the different electrolytes from effects linked to the different structures (fast-equilibrated and neutral electrolyte catalysts have the same structure). Since the fast-equilibrated catalyst has better performances than the slow-equilibrated, we assign the catalytic improvement directly to the different electrolyte.

In this work, three reasons were identified as possibly responsible for the observed improvement, each is explained in the following discussion.

1. The midpoint potential for oxidation state changes is down-shifted.
2. Proton and electron transports are faster.
3. The reaction mechanism and the rate-determining step are different.

1. The potential needed to achieve a small current density (10 µA cm^{-2}) is lowered by 130 mV in alkaline electrolyte (slow-equilibrated catalyst) and a similar shift is visible for the onset of the catalytic current during a CV (108 mV at 0.5 mA cm^{-2}). These values reflect the 135 mV shift in the midpoint potential for $\mathrm{Co^{III}} \rightleftharpoons \mathrm{Co^{IV}}$ (Fig. 7.10) suggesting that in alkaline electrolyte, as it happens in neutral electrolyte, a $\mathrm{Co^{IV}}$ intermediate is necessary for OER and its formation potential determines the onset of catalytic activity (see section 2.3.3; chapter 6 and Surendranath, 2010; Gerken, 2011; Kanan, 2010). Note that the reported shifts for the potential were calculated in the RHE-scale, which already takes into account the 59 mV/pH dependence of proton-electron transfer (a scheme in Fig. 7.2; see also Giordano, 2016).

The reason for the down-shift of $\mathrm{Co^{IV}}$ formation, which is observed for both slow- and fast-equilibrated catalysts is unclear. A hypothesis is the presence of new ligands of the Co, which could be one or more of the following:

- a different protonation state of Co bridging oxygen atoms, due to the different electrolyte pH;
- the removal of phosphate ligands. Phosphate direct bond to Co has been proposed based on a parallel with arsenate binding modes (Villalobos, 2019). The extrusion of internal phosphate in alkaline electrolyte is observed via Raman and TXRF measurements (Fig. 7.3 and 7.4);
- the formation of carbonate ligands. Carbonate is formed after CO_2 absorption by alkaline electrolyte exposed to air (Ko, 1983; Han, 1932) and previous works suggest an improved OER activity in the presence of carbonate (Hunter, 2016a; Aiso, 2017).

On the contrary, the midpoint potential for $\mathrm{Co^{II}} \rightleftharpoons \mathrm{Co^{III}}$ experiences a stronger down-shift by 390 mV, which is observed only for the slow-equilibrated catalyst. This is probably linked to the structural conversion to CoO(OH), because in the CoO(OH) crystal structure Co is present as Co^{III}. However, the shift of the $Co^{II} \rightleftharpoons Co^{III}$ reaction to lower potentials does not affect the catalytic performances.

2. In alkaline electrolyte, both proton and electron transport kinetics are favored. Electron transfer is the limiting factor for the kinetics of the redox reactions (see sections 6.2.2) and is itself limited by the presence of Co^{II} and by electron jumps between Co-oxo clusters (Brodsky, 2018; Kwon, 2018; Costentin, 2016; Farrow, 2013). In the slow-equilibrated catalyst, the size of the clusters is increased in comparison with the catalyst in neutral electrolyte (Fig. 7.9) and the average oxidation state is kept over 3 (Fig. 7.12). This explains the faster redox kinetics observed for the slow-equilibrated catalyst in respect to the neutral electrolyte catalyst (Fig. 7.15).

Although a contribution from proton transport inside the film cannot be excluded, proton transport is mostly limited by proton removal from the film into the electrolyte bulk (see section 4.2.4 and Brodsky, 2018; Klingan, 2014). Proton removal and transport is mediated by buffer species (Engasser, 1974; Engasser, 1980): the $HPO_4^{2-}/H_2PO_4^-$ couple in neutral electrolyte and the OH^-/H_2O couple in alkaline electrolyte. The elevated concentration of OH^- in alkaline electrolyte, together with their high mobility, efficiently removes the proton produced by OER, even at high current density. Thus, alkaline electrolyte prevents the formation of a local pH gradient, which is observed in neutral electrolyte close to the catalyst surface (see section 4.2.2).

Electron transfer is affecting redox kinetics but, since it is rate-limiting only in the presence of Co^{II}, the faster kinetics most likely does not have an influence on catalytic activity (Brodsky, 2018; Klingan, 2014). On the contrary, proton transfer has a direct influence on the catalytic activity at high turnover frequency and is probably responsible for the hysteresis observed in the current during CVs. The hysteresis in the current is visible in neutral electrolyte (Fig. 7.12) but not in alkaline (neither in the fast- nor in the slow-equilibrated structure, see Fig. 7.17) and is therefore assigned to the different electrolytes and to more efficient proton removal by OH^-.

3. The Tafel slope in alkaline electrolyte (slow-equilibrated catalyst) is lower than in neutral electrolyte (38 and 72 mV/dec, respectively, Fig. 7.16). A lower Tafel slope means a higher increase in catalytic current for the same increase in overpotential, which is beneficial for the catalytic performances. Since the Tafel slope value is determined by the reaction rate-limiting step, the change in Tafel slope corresponds to a change in the reaction mechanism with a new rate-limiting step.

In chapter 6, the reaction mechanism at neutral pH is investigated, revealing an accumulation of Co^{IV} within the catalyst material with increasing applied potential. A higher Co^{IV} concentration lowers the energy barrier for the rate-limiting step, which is oxygen-oxygen bond formation. As a result, the current density has an exponential dependence on Co oxidation state. On the contrary, at alkaline pH, the catalytic current does not seem to depend directly on the average oxidation state of the catalyst, but it seems to be directly driven by the applied potential (Fig. 7.16). A possible explanation is that the rate-limiting step at alkaline pH is electron transfer.

The observed changes are compatible with a new mechanism involving bulk water nucleophilic attack (BWNA), which can replace the intramolecular oxygen coupling observed in neutral electrolyte (Koroidov, 2015; Betley, 2008). The BWNA could be facilitated by the high concentration of OH^- in the electrolyte. In the case of BWNA, the oxygen-oxygen bond forms before the highest oxidation state is reached, thus it must be followed by a proton and electron transfer, which could become rate-limiting, causing the observed change in Tafel slope.

However, further studies are needed, possibly involving the fast-equilibrated catalyst and isotopic substitution, to propose a comprehensive reaction mechanism for alkaline electrolyte.

7.4 Summary

Co-oxide catalysts exposed to alkaline electrolyte at open circuit potential undergo structural modifications. The three catalysts investigated here (CoCat, cathodically deposited and spin-coated) convert spontaneously into a more ordered structure similar to CoOOH. The presence of high concentrations of $\mathrm{Co^{II}}$ in the as-prepared state is proposed to be crucial for structural ordering, because $\mathrm{Co^{II}}$ can dissolve in solution and be redeposited as $\mathrm{Co^{III}}$. We refer to the new structure as slow-equilibrated and draw a parallel with the aging process which leads to β-NiOOH formation. A method is proposed to maintain the structure amorphous by applying a catalytic potential directly after exposure of the catalyst to the electrolyte. The applied potential causes an irreversible oxidation which blocks the catalyst in the disordered state, enhancing its catalytic performances. The resulting catalyst is referred to as fast-equilibrated and has similarities with the γ-NiOOH phase. The comparison between slow- and fast-equilibrated catalysts highlights the importance of an amorphous structure, which increases the number of active sites and ensures higher catalytic performances at low overpotentials. However, in the fast-equilibrated catalyst charge transfer is decreased, resulting in a higher Tafel slope and possibly worst catalytic performances at higher potentials.

The differences between slow- and fast- equilibrated catalysts involve catalytic activity, redox properties and local structures. They are even bigger than the differences due to the catalyst preparation method and stem simply from the different time passed, between exposure of an electrode to solution and the application of an elevated potential. We stress the importance of taking into account the presence of these two phases when planning and executing an experiment, to have control of the studied material and ensure experiment reproducibility.

Both slow- and fast- equilibrated catalysts presented higher catalytic performances in respect to a catalyst operated at neutral pH, which consisted in lower overpotential for OER onset and lower Tafel slope. Thus, we can assign the catalytic improvement directly to the electrolyte and not to structural differences. Three reasons were proposed for the improvement of catalytic activity in alkaline electrolyte. The first reason is the down-shift of the midpoint potential for the $\mathrm{Co^{III}} \rightleftharpoons \mathrm{Co^{IV}}$ reaction. This shift is likely due to a change in Co coordination environment, which could include a change in oxygen atoms protonation state, removal of phosphate ligands and formation of carbonate ligands. The second reason is a more efficient removal of the protons produced during OER, due to the high concentration of $\mathrm{OH^-}$ in alkaline electrolyte. The third reason is a change in OER mechanism, which causes a lower Tafel slope and a reduced dependence of the catalytic current on Co oxidation state. In neutral electrolyte, the increase in $\mathrm{Co^{IV}}$ concentration drives the increase in catalytic current. In alkaline electrolyte, instead, the increase in catalytic current is directly driven by the applied potential, suggesting that electron transfer is the rate-determining step.

7.5 Experimental details

7.5.1 Materials

Five different types of substrates were used to match different experimental requirements: glassy carbon (GC), indium tin oxide (ITO), fluoride doped tin oxide (FTO), carbon fiber paper (CFP) and Pt sheets. GC sheets Sigradur K, 0.1 mm thick (Hochtemperatur-Werkstoffe GmbH), ITO (VisionTek Systems Ltd) and FTO TEC-7 (Solems S.A.) coated glass slides were cleaned with ethanol and MilliQ before use. CFP sheets 0.37 mm thick, 5% wet proofed (Toray Carbon Paper 120, FuelCellStore) were used as received. Pt sheets 0.1 mm thick, 99.95% purity (Labor-Platina Kft.) were sonicated for 10 minutes first in ethanol and then in MilliQ before use. Pt sheets were used multiple times and cleaned with 30% HCl after use. The alkaline electrolyte used was 1 M KOH at pH 13.8 (KOH 85%, Carl Roth), it was purified from Fe impurities by mixing and aging the solution with $Co(OH)_2$, as described previously (Trotochaud, 2014). Nevertheless, Fe was present during TXRF measurement (Fig. 7.4), possibly due to contamination during the TXRF measurement process. In any case, the Fe amount was always less than 5% of the Co amount and such a small quantity has no major effects on the catalyst activity (Burke, 2015a). All other chemicals were used as received, electrolyte solutions were prepared using MilliQ water (>18 MΩ cm). The reference electrodes used were Ag/AgCl (saturated, Metrohm) in neutral electrolyte and RHE (HydroFlex) in alkaline electrolyte, in neutral electrolyte the RHE scale potential was obtained by $E\ (V_{RHE}) = E\ (V_{NHE}) + 59\ mV \cdot pH = E\ (Ag/AgCl) + 200\ mV + 59\ mV \cdot pH$.

7.5.2 Films fabrication

CoCat films were anodically electrodeposited from an electrolyte solution containing 0.5 mM $Co(NO_3)_2$ in 0.1 M phosphate buffer (KPi) at pH 7 following an established protocol (Kanan, 2008). A potential of 1.05 V_{NHE} was applied until the accumulation of the desired charge, which was 10 mC cm^{-2} (when not otherwise specified). The potentiostat Interface 1000 (Gamry Instruments) was used with a single-compartment three-electrode cell, a Pt grid (2x2 cm2, 90% purity) as a counter electrode and an Ag/AgCl(saturated) as a reference electrode. Before exposing the film to a solution, it was dried in air for 1-2 days, thereby enhancing its stability in alkaline electrolyte. **Cathodically deposited films** were prepared via electrodeposition from an electrolyte solution containing 18 mM CoO_4S in 35 mM NH_4ClO_4 at pH 6.8, following an established protocol (Merrill, 2008). A constant current of 250 mA cm^{-2} was applied for 1 s. A SP-300 potentiostat (BioLogic) was used with a two-electrode cell, where the Pt grid counter electrode was parallel and 3 mm apart from the working electrode. **Spin-coated films** were prepared from a solution containing 0.3 M Co^{II} 2-ethyl hexanoate in ethanol, following an established protocol (Smith, 2013a). 10 µL of solution were dropped onto a FTO substrate, which was rotated at 3000 rpm and the resulting film was irradiated with UV light (Dinies Technologies GmbH, 18 Watt, no ozone filter) for 999 min.

7.5.3 Freeze-quench X-ray absorption spectroscopy

The freeze-quench method consists in freezing a sample during operation for subsequent analysis (Risch, 2015). The sample conditioning (4 min at a fixed potential) took place in a single-time use electrochemical cell (Fig. 6.20), containing 400 µL of solution with GC as working electrode and a thin Pt wire as counter electrode. A three-electrode configuration, with a Hg/Hg_2SO_4 (saturated) reference electrode, was used to determine the desired potential, then the reference electrode was removed and liquid nitrogen was poured on the cell. Further details on the procedure can be found in a previous work (Risch, 2015) and section 6.5. Sample deposition and equilibration occurred in a conventional electrochemical cell and samples were washed with MilliQ and dried in air before mounting them in the cell for conditioning. Spin-coated samples are not stable on GC and were prepared on FTO substrates, conditioned in a conventional electrochemical cell and frozen immediately after. X-ray absorption spectroscopy measurements at the Co K-edge were carried out at the BESSY synchrotron (Berlin) at beamlines KMC-1 and KMC-3 (Schaefers, 2007) in an Oxford He-flow cryostat (20 K), equipped with a 13-channel energy-resolving Ge detector (Canberra). The obtained spectra were processed and simulated in k-space using two home-developed software. The phase functions used in the simulation were obtained with the FEFF program, including a multiple scattering peak (Frenkel, 1993), the amplitude reduction factor ($S_0{}^2$) was 0.7. To extract the spectra edge-positions, the rise of the pre-edge was moved to 7708 eV (via a Gaussian fit of the derivative of the fluorescence) and the integral method (Dau, 2003) was applied. Different fit ranges gave rise to slightly different estimations for Co oxidation state, as discussed in section 2.3.2.

7.5.4 Operando X-ray absorption spectroscopy

The details about operando X-ray absorption measurements are extensively reported in section 2.3.

Compensation of the recorded potential for iR drop, when mentioned on the x-axis, was done during data analysis. A typical cell resistance was 4 Ω in alkaline and 35 Ω in neutral electrolytes, during potential jumps this value was lowered to 10 Ω by adding 1 M KNO_3. The working electrode material was GC in neutral electrolyte and CFP in alkaline (unless differently specified), which was necessary to improve the stability.

7.5.5 Elemental analysis

Total reflection X-ray fluorescence (TXRF) spectroscopy was used to analyze the composition of samples after electrochemical conditioning in alkaline electrolyte, using a Bruker S2 Picofox spectrometer at 40 kV. The catalyst film was removed from GC electrodes by 45 min exposure and sonication in HCl (34%, Carl Roth). Then 4 mg L^{-1} of Ga and 4 mg L^{-1} of Cs from standard solutions were added, to act as references for Co and Fe and for K and P quantifications, respectively. Error bars represent the standard error with a 95% confidence interval obtained from two distinct samples for the time series and from one sample for the equilibration-in-other-solutions series, three measurements were performed for each sample.

7.5.6 Raman spectroscopy

The details about operando Raman measurements are extensively reported in section 3.3.

In alkaline electrolyte the objective was protected by a thin Teflon film (13 μm, DuPont). Between the objective and the Teflon film, a water droplet ensured no variation in the refractive index. The excitation source was a 473 nm laser (YAG laser) and the focus on the sample had a line shape to reduce heating at the laser spot. Films used were 40 cm^{-2} thick and were deposited on a Pt substrate.

8 Key results

The first part of this thesis consists of the adaptation and application of novel operando techniques to an amorphous Co oxide catalyst (CoCat). The method advancements obtained have wide applicability in the study of transition metal catalysts and amorphous materials.

- Time-resolved X-ray absorption spectroscopy is established as an operando technique to track the oxidation state of the catalyst during electrochemical operation. A proof-of-concept experiment showed that a time-resolution of 10 milliseconds and an uncertainty range of ±0.09 oxidation state units are achievable for thin Co catalyst films using standard beam-line equipment. The method was used to: distinguish the redox and the catalytic components of the current, analyze the rate of oxidation state changes, investigate catalyst dissolution and study the relation between oxidation state and catalytic current, which sheds light on the factors controlling catalytic activity. *Chapter 2*
- Raman spectroscopy was established as a valid technique to study oxidation state changes and, unlike X-ray absorption, was proven able to distinguish the $Co^{II} \rightarrow Co^{III}$ from the $Co^{III} \rightarrow Co^{IV}$ oxidation. *Chapter 3*
- The Raman spectrum of an amorphous oxide (CoCat) was collected at various potentials and characterized with the use of isotope substitution and anion substitution. The presence of $H_2PO_4^-$ polymers, possibly functional for proton transport, in CoCat interlayers was revealed. Furthermore, the change in the Raman spectrum following the crystallization of the structure was observed in time. *Chapter 3 and 7*
- Operando Raman spectroscopy was established as a spatial and time-sensitive technique to measure the pH of an electrolyte. It revealed the acidification of the electrolyte close to the anode, even during operation at intermediate current densities and in the presence of a buffer. Such local pH changes have a strong effect on catalytic activity. *Chapter 4*
- Tafel slope values have a parabolic dependence on the pH of the electrolyte, with a minimum at the buffer pK_a. This is due to local acidification of the electrolyte and can result in wrong mechanistic interpretations. To reduce this effect buffers should be always used at a pH corresponding to their pK_a. *Chapter 4*
- Operando microscopy was employed to study the formation of oxygen bubbles. A rougher catalyst surface gives rise to smaller and more frequent bubbles, which are beneficial for catalysis. The major reason for catalyst deterioration, especially for catalyst films thicker than 2 µm, is the formation of microbubbles in the bulk of the catalyst, which can cause catalyst detachment from the substrate and catalyst destruction. *Chapter 5*

In the second part, these techniques are employed to investigate the mechanism of water oxidation at neutral and alkaline pH and the key factors that can enhance catalytic efficiency.

- The energetics of the precatalytic $\mathrm{Co}^{\mathrm{III/IV}}$ oxidation is regulated by a proton-electron transfer, while its kinetics is controlled by an electron transfer. Upon substitution of hydrogen with deuterium, an energetic isotope effect is observed, which up-shifts the Co redox potential and decreases the catalytic activity. *Chapter 6*

- A kinetic isotope effect on the catalytic activity is observed upon $^{16}\mathrm{O}/^{18}\mathrm{O}$ but not upon H/D substitution. Moreover, the catalytic activity is not directly influenced by the applied potential, suggesting that electron transfer is not rate-limiting. Thus, O-O bond formation is confirmed to be the rate-limiting step for water oxidation under neutral conditions. *Chapter 6*

- An exponential relationship is observed between catalytic currents and average Co oxidation state at neutral pH. This feature is proposed to arise due to an electronic coupling of cobalt sites, that increases the redox potential for $\mathrm{Co}^{\mathrm{III/IV}}$ oxidation as $\mathrm{Co}^{\mathrm{IV}}$ accumulates within the catalyst material and gives rise to higher energy states with a lower energy barrier for water oxidation. *Chapter 6*

- Several Co oxide catalysts are not stable when exposed to alkaline electrolyte, but undergo an irreversible oxidation process. By controlling the rate of this process, it is possible to tune the level of disorder in the catalyst. A faster oxidation, driven by the application of a catalytic potential, keeps the catalyst amorphous, influences its redox properties and is beneficial for catalytic activity. *Chapter 7*

- The presence of alkaline electrolyte improves the catalytic activity. Three factors possibly contribute to this improvement: the down-shift of the midpoint potential for the $\mathrm{Co}^{\mathrm{III/IV}}$ oxidation, likely due to a change in Co coordination environment; the more efficient removal of the protons produced during OER and a change in OER mechanism, which causes a lower Tafel slope and breaks the direct dependence of the catalytic current from Co oxidation state. *Chapter 7*

9 Appendix

9.1 Additional figures and tables

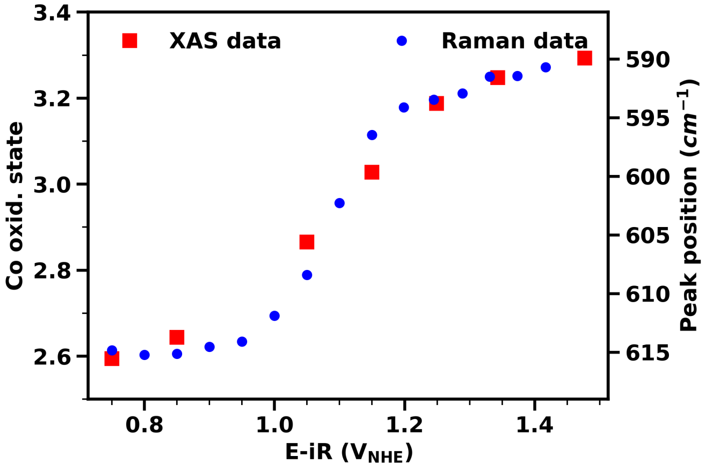

Figure 9.1: Analysis of the Raman spectra of CoCat (spectra in Fig. 3.12). The Raman spectra in the region 415 to 727 cm^{-1} were simulated with two Gaussian functions with varying positions. Comparison between the peak position for the first Gaussian function and the Co oxidation state at different potentials is shown. Co oxidation state is obtained by freeze-quench X-ray measurements.

Table 9.1: Parameters from the simulation of the CoCat Raman spectra obtained operando at different potentials in electrolytes (KPi, pL 7) made by water, deuterated water or normalized water. For each spectrum, two separated simulations were performed: one in the 415 to 714 cm^{-1} region, whose parameters are reported in (a) and one in the 766 to 1375 cm^{-1} region, whose parameters are reported in (b) and (c). (c) contains the parameters relating to the solution peaks.[a, b, c, d]

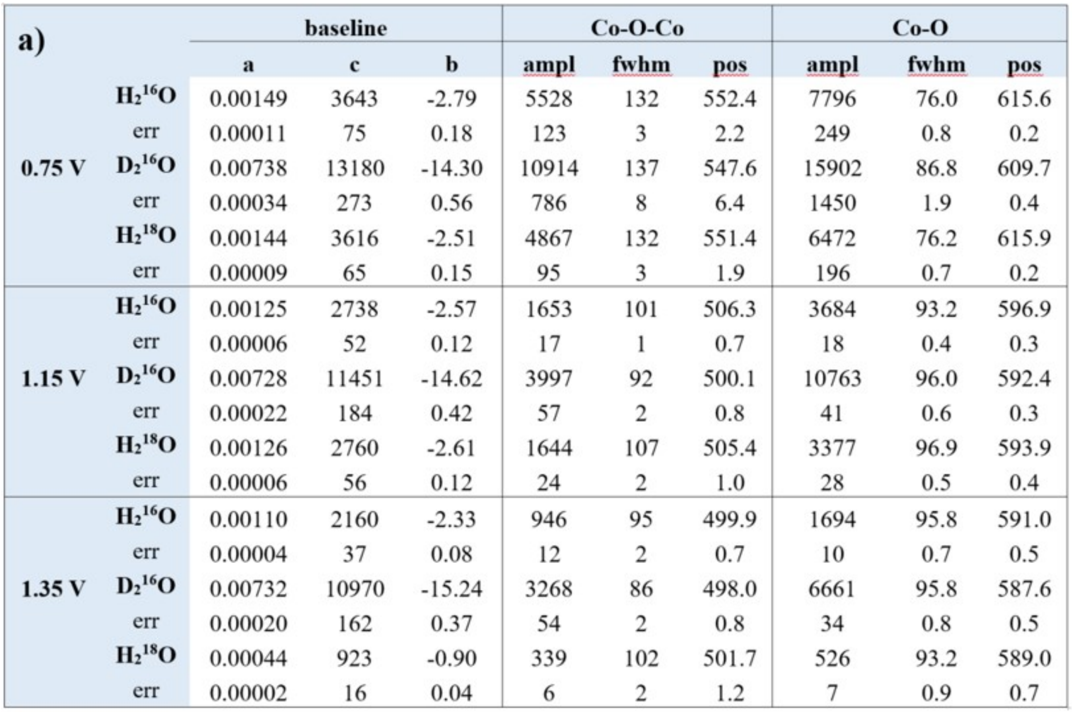

a)

		baseline			Co-O-Co			Co-O		
		a	c	b	ampl	fwhm	pos	ampl	fwhm	pos
0.75 V	$H_2{}^{16}O$	0.00149	3643	-2.79	5528	132	552.4	7796	76.0	615.6
	err	0.00011	75	0.18	123	3	2.2	249	0.8	0.2
	$D_2{}^{16}O$	0.00738	13180	-14.30	10914	137	547.6	15902	86.8	609.7
	err	0.00034	273	0.56	786	8	6.4	1450	1.9	0.4
	$H_2{}^{18}O$	0.00144	3616	-2.51	4867	132	551.4	6472	76.2	615.9
	err	0.00009	65	0.15	95	3	1.9	196	0.7	0.2
1.15 V	$H_2{}^{16}O$	0.00125	2738	-2.57	1653	101	506.3	3684	93.2	596.9
	err	0.00006	52	0.12	17	1	0.7	18	0.4	0.3
	$D_2{}^{16}O$	0.00728	11451	-14.62	3997	92	500.1	10763	96.0	592.4
	err	0.00022	184	0.42	57	2	0.8	41	0.6	0.3
	$H_2{}^{18}O$	0.00126	2760	-2.61	1644	107	505.4	3377	96.9	593.9
	err	0.00006	56	0.12	24	2	1.0	28	0.5	0.4
1.35 V	$H_2{}^{16}O$	0.00110	2160	-2.33	946	95	499.9	1694	95.8	591.0
	err	0.00004	37	0.08	12	2	0.7	10	0.7	0.5
	$D_2{}^{16}O$	0.00732	10970	-15.24	3268	86	498.0	6661	95.8	587.6
	err	0.00020	162	0.37	54	2	0.8	34	0.8	0.5
	$H_2{}^{18}O$	0.00044	923	-0.90	339	102	501.7	526	93.2	589.0
	err	0.00002	16	0.04	6	2	1.2	7	0.9	0.7

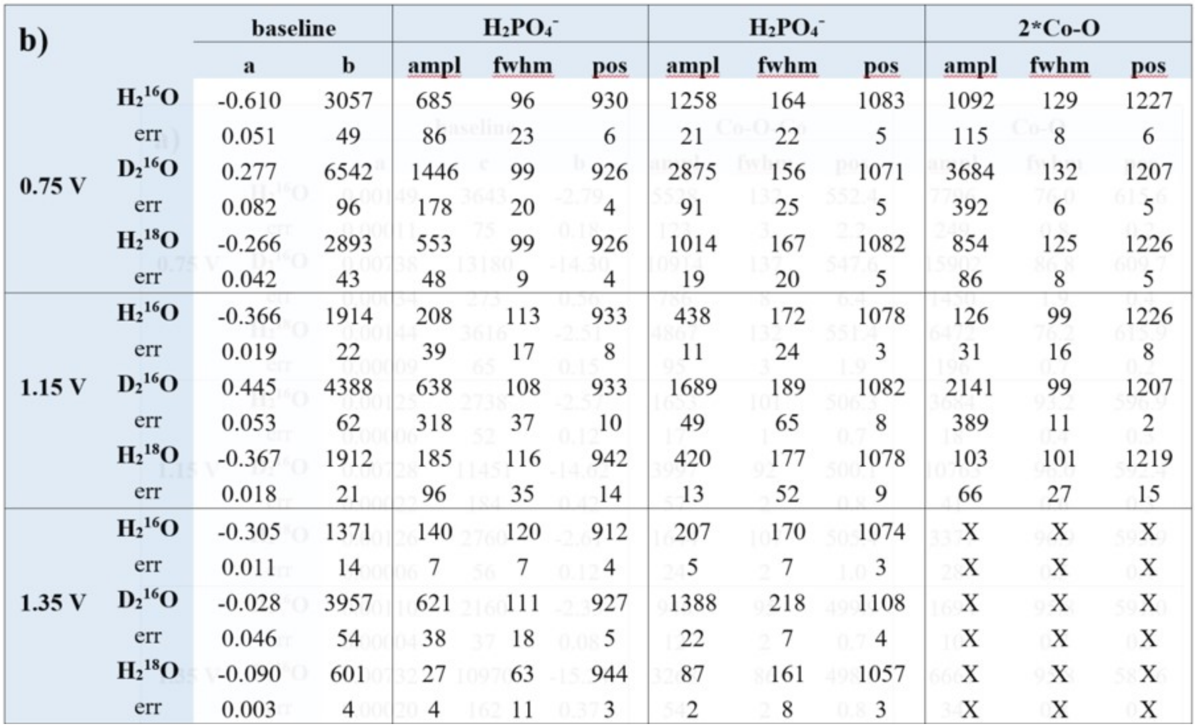

b)

		baseline		$H_2PO_4^-$			$H_2PO_4^-$			2*Co-O		
		a	b	ampl	fwhm	pos	ampl	fwhm	pos	ampl	fwhm	pos
0.75 V	$H_2{}^{16}O$	-0.610	3057	685	96	930	1258	164	1083	1092	129	1227
	err	0.051	49	86	23	6	21	22	5	115	8	6
	$D_2{}^{16}O$	0.277	6542	1446	99	926	2875	156	1071	3684	132	1207
	err	0.082	96	178	20	4	91	25	5	392	6	5
	$H_2{}^{18}O$	-0.266	2893	553	99	926	1014	167	1082	854	125	1226
	err	0.042	43	48	9	4	19	20	5	86	8	5
1.15 V	$H_2{}^{16}O$	-0.366	1914	208	113	933	438	172	1078	126	99	1226
	err	0.019	22	39	17	8	11	24	3	31	16	8
	$D_2{}^{16}O$	0.445	4388	638	108	933	1689	189	1082	2141	99	1207
	err	0.053	62	318	37	10	49	65	8	389	11	2
	$H_2{}^{18}O$	-0.367	1912	185	116	942	420	177	1078	103	101	1219
	err	0.018	21	96	35	14	13	52	9	66	27	15
1.35 V	$H_2{}^{16}O$	-0.305	1371	140	120	912	207	170	1074	X	X	X
	err	0.011	14	7	7	4	5	7	3	X	X	X
	$D_2{}^{16}O$	-0.028	3957	621	111	927	1388	218	1108	X	X	X
	err	0.046	54	38	18	5	22	7	4	X	X	X
	$H_2{}^{18}O$	-0.090	601	27	63	944	87	161	1057	X	X	X
	err	0.003	4	4	11	3	2	8	3	X	X	X

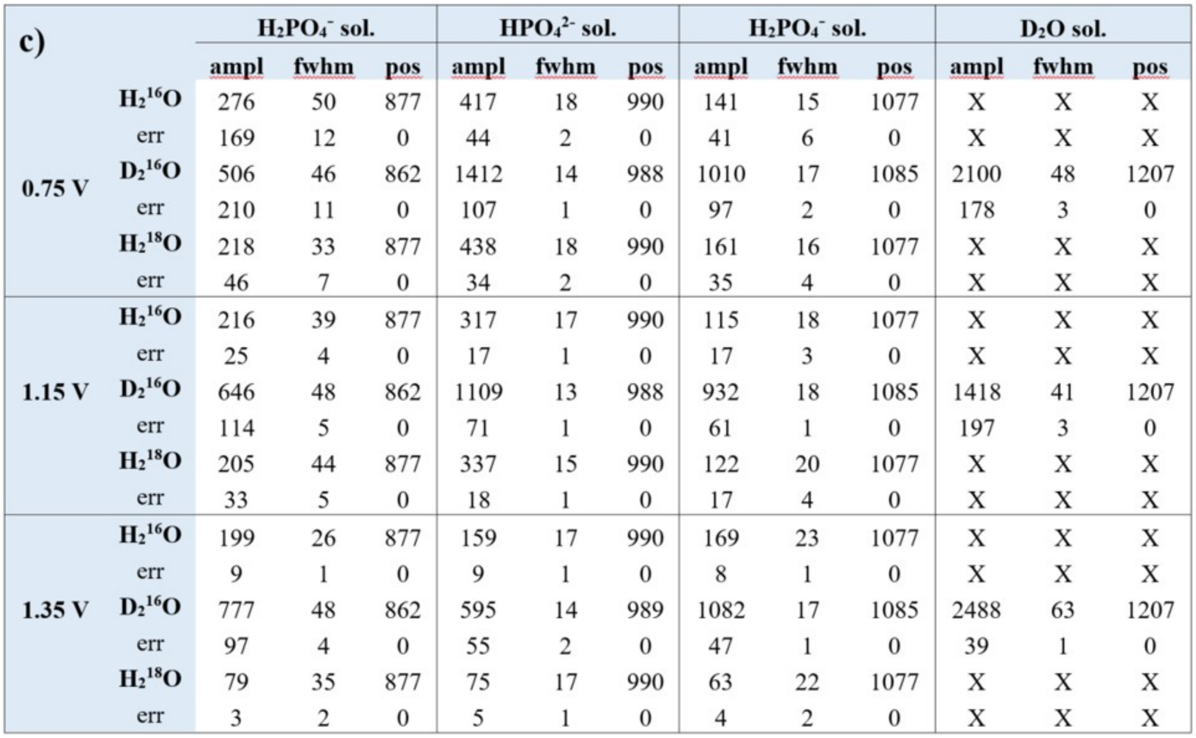

c)		$H_2PO_4^-$ sol.			HPO_4^{2-} sol.			$H_2PO_4^-$ sol.			D_2O sol.		
		ampl	fwhm	pos	ampl	fwhm	pos	ampl	fwhm	pos	ampl	fwhm	pos
0.75 V	**$H_2{}^{16}O$**	276	50	877	417	18	990	141	15	1077	X	X	X
	err	169	12	0	44	2	0	41	6	0	X	X	X
	$D_2{}^{16}O$	506	46	862	1412	14	988	1010	17	1085	2100	48	1207
	err	210	11	0	107	1	0	97	2	0	178	3	0
	$H_2{}^{18}O$	218	33	877	438	18	990	161	16	1077	X	X	X
	err	46	7	0	34	2	0	35	4	0	X	X	X
1.15 V	**$H_2{}^{16}O$**	216	39	877	317	17	990	115	18	1077	X	X	X
	err	25	4	0	17	1	0	17	3	0	X	X	X
	$D_2{}^{16}O$	646	48	862	1109	13	988	932	18	1085	1418	41	1207
	err	114	5	0	71	1	0	61	1	0	197	3	0
	$H_2{}^{18}O$	205	44	877	337	15	990	122	20	1077	X	X	X
	err	33	5	0	18	1	0	17	4	0	X	X	X
1.35 V	**$H_2{}^{16}O$**	199	26	877	159	17	990	169	23	1077	X	X	X
	err	9	1	0	9	1	0	8	1	0	X	X	X
	$D_2{}^{16}O$	777	48	862	595	14	989	1082	17	1085	2488	63	1207
	err	97	4	0	55	2	0	47	1	0	39	1	0
	$H_2{}^{18}O$	79	35	877	75	17	990	63	22	1077	X	X	X
	err	3	2	0	5	1	0	4	2	0	X	X	X

[a] Each peak was simulated with a Gaussian function. Lorentzian functions were tested but performed worse. For each Gaussian are reported the value of the amplitude, the FWHM (in cm^{-1}) and the position (in cm^{-1}). Each parameter has the corresponding error written in the table space below it.

[b] Solution peaks had fixed positions and have no corresponding error.

[c] An example of the simulation is shown in Fig. 3.15.

[d] The baseline is a quadratic function in (a) and a linear function in (b), with the form $y = ax^2 + bx + c$ and $y = ax + b$ respectively.

9.2 List of publications

I Author:

1. Pasquini, C.; Zaharieva, I.; González-Flores, D.; Chernev, P.; Mohammadi, M. R.; Guidoni, L.; Smith, R. D. L.; Dau, H. H/D isotope effects reveal factors controlling catalytic activity in Co-based oxides for water oxidation. *J. Am. Chem. Soc.* **2019**, *141*, 2938–2948, DOI: `10.1021/jacs.8b10002`
2. Pasquini, C.; D'Amario, L.; Zaharieva, I.; Dau, H. Operando Raman spectroscopy tracks oxidation-state changes in an amorphous Co oxide material for electrocatalysis of the oxygen evolution reaction. *J. Chem. Phys.* **2020**, *152*, 194202, DOI: `10.1063/5.0006306`
3. Pasquini, C.; Liu, S.; Chernev, P.; Gonzalez-Flores, D.; Mohammadi, M. R.; Kubella, P.; Jiang, S.; Loos, S.; Klingan, K.; Sikolenko, V.; Mebs, S.; Haumann, M.; Beyer, P.; D'Amario, L.; Smith, R. D. L.; Zaharieva, I.; Dau, H. Operando tracking of oxidation-state changes by coupling electrochemistry with time-resolved X-ray absorption spectroscopy demonstrated for water oxidation by a cobalt-based catalyst film. *Anal. Bioanal. Chem.* **2021**, DOI: `10.1007/s00216-021-03515-0`

II Author:

1. Smith, R. D. L.; Pasquini, C.; Loos, S.; Chernev, P.; Klingan, K.; Kubella, P.; Mohammadi, M. R.; González-Flores, D.; Dau, H. Spectroscopic identification of active sites for the oxygen evolution reaction on iron-cobalt oxides. *Nat. Commun.* **2017**, *8*, 2022, DOI: `10.1038/s41467-017-01949-8`
2. Smith, R. D. L.; Pasquini, C.; Loos, S.; Chernev, P.; Klingan, K.; Kubella, P.; Mohammadi, M. R.; González-Flores, D.; Dau, H. Geometric distortions in nickel (oxy)hydroxide electrocatalysts by redox inactive iron ions. *Energy Environ. Sci* **2018**, *11*, 2476–2485, DOI: `10.1039/c8ee01063c`
3. Dau, H.; Pasquini, C. Modelling the (essential) role of proton transport by electrolyte bases for electrochemical water oxidation at near-neutral pH. *Inorganics* **2019**, *7*, 20, DOI: `10.3390/inorganics7020020`

Others:

1. Zaharieva, I.; González-Flores, D.; Asfari, B.; Pasquini, C.; Mohammadi, M.; Klingan, K.; Zizak, I.; Loos, S.; Chernev, P.; Dau, H. Water oxidation catalysis – role of redox and structural dynamics in biological photosynthesis and inorganic manganese oxides. *Energy Environ. Sci.* **2016**, *9*, 2433–2443, DOI: `10.1039/C6EE01222A`
2. González-Flores, D.; Zaharieva, I.; Heidkamp, J.; Chernev, P.; Martinez-Moreno, E.; Pasquini, C.; Mohammadi, M. R.; Klingan, K.; Gernet, U.; Fischer, A.; Dau, H. Electrosynthesis of biomimetic manganese-calcium oxides for water oxidation catalysis - atomic structure and functionality. *ChemSusChem* **2016**, *9*, 379–387, DOI: `10.1002/cssc.201501399`
3. Klingan, K.; Kottakkat, T.; Jovanov, Z. P.; Jiang, S.; Pasquini, C.; Scholten, F.; Kubella, P.; Bergmann, A.; Roldan Cuenya, B.; Roth, C.; Dau, H. Reactivity determinants in electrodeposited Cu foams for electrochemical CO_2 reduction. *ChemSusChem* **2018**, *11*, 3449–3459, DOI: `10.1002/cssc.201801582`

4. González-Flores, D.; Klingan, K.; Chernev, P.; Loos, S.; Mohammadi, M. R.; Pasquini, C.; Kubella, P.; Zaharieva, I.; Smith, R. D. L.; Dau, H. Nickel-iron catalysts for electrochemical water oxidation – redox synergism investigated by in situ X-ray spectroscopy with millisecond time resolution. *Sustain. Energy Fuels* **2018**, *2*, 1986–1994, DOI: `10.1039/c8se00114f`

5. Villalobos, J.; González-Flores, D.; Klingan, K.; Chernev, P.; Kubella, P.; Urcuyo, R.; Pasquini, C.; Mohammadi, M. R.; Smith, R. D. L.; Montero, M. L.; Dau, H. Structural and functional role of anions in electrochemical water oxidation probed by arsenate incorporation into cobalt-oxide materials. *Phys. Chem. Chem. Phys.* **2019**, *21*, 12485–12493, DOI: `10.1039/c9cp01754b`

6. Jiang, S.; Klingan, K.; Pasquini, C.; Dau, H. New aspects of operando Raman spectroscopy applied to electrochemical CO_2 reduction on Cu foams. *J. Chem. Phys.* **2019**, *150*, 041718, DOI: `10.1063/1.5054109`

7. Meng, J.; Chernev, P.; Mohammadi, M. R.; Klingan, K.; Loos, S.; Pasquini, C.; Kubella, P.; Jiang, S.; Yang, X.; Cui, Z.; Zhu, S.; Li, Z.; Liang, Y.; Dau, H. Self-supported $Ni(OH)_2/MnO_2$ on CFP as a flexible anode towards electrocatalytic urea conversion: the role of composition on activity, redox states and reaction dynamics. *Electrochim. Acta* **2019**, *318*, 32–41, DOI: `10.1016/j.electacta.2019.06.013`

8. Abrashev, M. V.; Chernev, P.; Kubella, P.; Mohammadi, M. R.; Pasquini, C.; Dau, H.; Zaharieva, I. Origin of the heat-induced improvement of catalytic activity and stability of MnOx electrocatalysts for water oxidation. *J. Mater. Chem.A* **2019**, *7*, 17022–17036, DOI: `10.1039/c9ta05108b`

9. Muench, F.; El-Nagar, G. A.; Tichter, T.; Zintler, A.; Kunz, U.; Molina-Luna, L.; Sikolenko, V.; Pasquini, C.; Lauermann, I.; Roth, C. Conformal solution deposition of Pt-Pd titania nanocomposite coatings for light-assisted formic acid electro-oxidation. *ACS Appl. Mater. Interfaces* **2019**, *11*, 43081–43092, DOI: `10.1021/acsami.9b12783`

10. Mohammadi, M. R.; Loos, S.; Chernev, P.; Pasquini, C.; Zaharieva, I.; González-Flores, D.; Kubella, P.; Klingan, K.; Smith, R. D. L.; Dau, H. Exploring the limits of self-repair in cobalt oxide films for electrocatalytic water oxidation. *ACS Catal.* **2020**, *10*, 7990–7999, DOI: `10.1021/acscatal.0c01944`

9.3 List of presentations at international conferences

Oral presentations:

- 25-29.07.2016, 21st International Conference on Photochemical Conversion and Storage of Solar Energy, **St. Petersburg**, *Mechanistic study of amorphous Co-based oxide for water oxidation*

- 05-06.07.2017, International Solar Fuels Conference-2 Young, **San Diego**, *Water Oxidation in Neutral versus Alkaline Electrolyte: In-Situ X-Ray Absorption Study of an Amorphous Cobalt Oxide Catalyst*

— 10-14.09.2017, GDCh-Wissenschaftsforum Chemie 2017, **Berlin**, *Cobalt Oxide Catalysts for Water Oxidation: Neutral Versus Alkaline Electrolyte*

— 2-4.09.2019, International Workshop on Correlated Dynamics in Energy Conversion (IWCE), **Göttingen**, *H/D isotope effects reveal factors controlling catalytic activity in Co-based oxides for water oxidation*

— 4-8.11.2019, nanoGe Fall Meeting 2019, **Berlin**, *Redox Energetics and Kinetics of Water Oxidation in Neutral versus Alkaline Electrolyte: an In-Operando Time-Resolved X-Ray Absorption Study*

Posters:

— 27.07-01.08.2014, 20th International Conference on Conversion and Storage of Solar Energy, **Berlin**, *The role of protons in amorphous Co-based oxides for water oxidation*

— 14-17.09.2014, Annual Meeting of the German Biophysical Society, **Lübeck**, *The role of protons in water oxidation: a study of the kinetic isotope effect on a Co-based model catalyst*

— 18-21.01.2015, 3rd International Symposium on Chemistry for Energy Conversion and Storage (ChemEner), **Berlin**, *The role of protons in water oxidation in a Co-based model catalyst: H/D isotope effect investigated by combining electrochemistry, optical and X-ray spectroscopy*

— 16-18.09.2015, International Symposium on Protonation Dynamics in Redox Proteins, **Berlin**, *Water oxidation in a Co-based catalyst: H2O/D2O isotope effect studied by in-situ spectroscopy*

— 06-10.07.2017, International Solar Fuels Conference-2, **San Diego**, *Water Oxidation in Neutral versus Alkaline Electrolyte: Why are the current densities >100 times lower at pH 7?*

— 13-15.12.2017, BER II and BESSY II User Meeting, **Berlin**, *Insight in catalytic mechanisms by (quasi) in-situ X-ray absorption spectroscopy at metal K-edges (at KMC3): results on electrochemical water oxidation by freeze-quench experiments*

— 22-26.10.2018, nanoGe Fall Meeting 2018, **Malaga**, *Water oxidation in neutral versus alkaline electrolyte, combining electrochemistry with in-situ X-ray absorption and Raman spectroscopy*, **Best Poster Prize winner**

— 24-26.09.2018, Electrochemistry 2018 (GDCh), **Ulm**, *Water oxidation in neutral versus alkaline electrolyte, combining electrochemistry with in-situ X-ray absorption and Raman spectroscopy*

— 1-5.04.2019, International Bunsen-Discussion-Meeting, **Taormina**, *H/D isotope effects reveal factors controlling catalytic activity in Co-based oxides for water oxidation*, **Best Poster Prize winner**

9.4 Acknoweledgments

A Ph.D. in Physics is often a long journey, whose goal is to unravel a complicated question and push the bounds of knowledge a little step further. It requires learning a great deal of things on experimental techniques, on all the details of a particular system or reaction mechanism and on how to be a good scientist. I couldn't reach this far, learn, understand and achieve all that was needed to write this thesis without the guidance and the support of several people, which walked with me during a part of this journey. Thus, I would like to spend some words to thank some of them.

First I would like to thank Holger, who opened me the doors to the world of electrochemistry and welcomed me as one of his students. His ability to clearly explain complex concepts and his sincere passion for science were always an example for me. Discussing the interpretation of experimental results and possible reaction mechanisms with him was one of the most intellectually stimulating parts of my doctoral experience. The other person which guided my travel was Ivelina, thanks to Ivelina for introducing me to the synchrotron world, following all my first steps and helping me to improve my experiments. Thanks for supporting me in all the most delicate steps of my travel, from my first unexpected oral presentation in Russia to the last published paper.

Thanks to Diego, who was the one who taught a messy physics student about the clean world of chemistry and how a real chemist behaves in the lab. He took care of me, inside and outside the lab. I remember the time I wrote to him in a chaotic evening, one day before the start of my first beamtime, admitting that I wasn't any more sure what was the correct direction to mount the sample on the sample-holder, he answered after few minutes "Here is a picture of it, I took it in case you would forget". Thanks to Philipp, whose scientific spirit, commitment to science and intelligence were always an example for me. It was a pleasure to discuss with you every kind of scientific topic from the PSII cycle to the science behind astrological signs. I still remember the day I came to Berlin to visit the group, Diego and Philipp brought me to my first Berlin shore (in Treptower Park), it was the first of a long series of lake trips and made me feel welcome in this city.

Thanks to Leonardo, for believing in me, watching over my carrier, collaborating with me and being a friend and a guide. He introduced me to the fascinating concept of artificial photosynthesis, igniting the scientific drive that sustained me during this travel. Thanks to Rodney, for taking the time to spend hours with me in the lab discussing science from the mechanism of double-layer capacitance to a new scientific hypothesis. Thanks for taking the time to review and put your understanding on my first paper, for believing in its value and for teaching me how to write a high-level publication. Your time and support were fundamental! Your drive to always experiment with new ideas was always inspiring, be it a new way to use a spectroscopic method or a possible mechanistic proposal. You helped me remember how fun and attractive can scientific research be and why I love it.

Thanks to my family, which molded my scientific mindset and grew me to appreciate knowledge and scientific research as one of the maximum expressions of human intelligence. Thanks for being always there for supporting me, inspiring me and helping to put everything in the right perspective every time I needed it. Thanks to my flatmates, for believing in me, cooking for me in tough times and sharing fun recharging time with me.

Thanks to the SFB group, Mattia, Fede, Ema, Jovan, Sara and Paul, for all the lunches we eat together, for your friendship, for all the interesting scientific exchanges and good times we had together between scientific presentations and adventurous bonfire retreats. Thanks to my office team, Young, Paul and Ricardo, because we could find a way to laugh even in the most stressful times and switch from discussing science to political philosophy, to private life, thanks for your friendship, it made the travel lighter. Thanks to my colleagues Shan and Reza, traveling to conferences with you was always a fun adventure and comparing our different cultures and life views was very interesting and stimulating. Thanks to Luca, who arrived at the end of my travel and was of great support in times in which I was a bit lost, helping me understand life after a Ph.D. and supporting my work.

Thanks to Katharina, Stefan, Stefan and Michael, for the time spent working together in Bessy and in the lab and insightful exchanges on science and on life. Thanks to my students Tobias, Artem and Philip, for the good time we had together, guiding you in the first scientific steps allowed me to see things from a new perspective. Thanks to Robert, Neno, Prof. Abrashev and Prof. Hildebrandt, for opening me the doors of Raman spectroscopy and of their lab, helping me to master the technique and bring it back to my working group.

Thanks to all of you and to all the other people who accompanied me on this journey, you were the best part of it and what you have taught me and the nice experiences we had together will accompany me in all future steps.

9.5 Selbstständigkeitserklärung

Name: Pasquini
Vorname: Chiara

Ich erkläre gegenüber der Freien Universität Berlin, dass ich die vorliegende Dissertation selbstständig und ohne Benutzung anderer als der angegebenen Quellen und Hilfsmittel angefertigt habe. Die vorliegende Arbeit ist frei von Plagiaten. Alle Ausführungen, die wörtlich oder inhaltlich aus anderen Schriften entnommen sind, habe ich als solche kenntlich gemacht. Diese Dissertation wurde in gleicher oder ähnlicher Form noch in keinem früheren Promotionsverfahren eingereicht.

Mit einer Prüfung meiner Arbeit durch ein Plagiatsprüfungsprogramm erkläre ich mich einverstanden.

Datum: Unterschrift:

Bibliography

1 Abbott, D. Keeping the energy debate clean: how do we supply the world's energy needs? *Proc. IEEE* **2010**, *98*, 42–66, DOI: `10.1109/JPROC.2009.2035162`.

2 Abe, Y.; Hosono, H.; Akita, O.; Hench, L. L. Protonic conduction in phosphate glasses. *J. Electrochem. Soc.* **1994**, *141*, L64, DOI: `10.1149/1.2054988`.

3 Abrashev, M. V.; Chernev, P.; Kubella, P.; Mohammadi, M. R.; Pasquini, C.; Dau, H.; Zaharieva, I. Origin of the heat-induced improvement of catalytic activity and stability of MnOx electrocatalysts for water oxidation. *J. Mater. Chem.A* **2019**, *7*, 17022–17036, DOI: `10.1039/c9ta05108b`.

4 Achilli, E.; Vertova, A.; Visibile, A.; Locatelli, C.; Minguzzi, A.; Rondinini, S.; Ghigna, P. Structure and stability of a Copper(II) lactate complex in alkaline solution: a case study by energy-dispersive X-ray absorption spectroscopy. *Inorg. Chem.* **2017**, *56*, 6982–6989, DOI: `10.1021/acs.inorgchem.7b00553`.

5 Ahmet, I. Y.; Ma, Y.; Jang, J.-W.; Henschel, T.; Stannowski, B.; Lopes, T.; Vilanova, A.; Mendes, A.; Abdi, F. F.; van de Krol, R. Demonstration of a 50 cm^2 $BiVO_4$ tandem photoelectrochemical-photovoltaic water splitting device. *Sustain. Energy Fuels* **2019**, *3*, 2366–2379, DOI: `10.1039/c9se00246d`.

6 Ahn, H. S.; Bard, A. J. Surface interrogation of CoPi water oxidation catalyst by scanning electrochemical microscopy. *J. Am. Chem. Soc.* **2015**, *137*, 612–615, DOI: `10.1021/ja511740h`.

7 Aiso, K.; Takeuchi, R.; Masaki, T.; Chandra, D.; Saito, K.; Yui, T. Carbonate ions induce highly efficient electrocatalytic water oxidation by cobalt oxyhydroxide nanoparticles. *ChemSusChem* **2017**, *10*, 687–692, DOI: `10.1002/cssc.201601494`.

8 Anantharaj, S.; Ede, S. R.; Sakthikumar, K.; Karthick, K.; Mishra, S.; Kundu, S. Recent trends and perspectives in electrochemical water splitting with an emphasis on sulfide, selenide, and phosphide catalysts of Fe, Co, and Ni: a review. *ACS Catal.* **2016**, *6*, 8069–8097, DOI: `10.1021/acscatal.6b02479`.

9 Anderson, D.; Leach, M. Harvesting and redistributing renewable energy: on the role of gas and electricity grids to overcome intermittency through the generation and storage of hydrogen. *Energy Policy* **2004**, *32*, 1603–1614, DOI: `10.1016/s0301-4215(03)00131-9`.

10 Angeles-Boza, A. M.; Ertem, M. Z.; Sarma, R.; Ibañez, C. H.; Maji, S.; Llobet, A.; Cramer, C. J.; Roth, J. P. Competitive oxygen-18 kinetic isotope effects expose O-O bond formation in water oxidation catalysis by monomeric and dimeric ruthenium complexes. *Chem. Sci.* **2014**, *5*, 1141–1152, DOI: `10.1039/c3sc51919h`.

11 Armaroli, N.; Balzani, V. Towards an electricity-powered world. *Energy Environ. Sci* **2011**, *4*, 3193, DOI: `10.1039/c1ee01249e`.

12 Armaroli, N.; Balzani, V. Solar electricity and solar fuels: status and perspectives in the context of the energy transition. *Chem. - Eur. J.* **2016**, *22*, 32–57, DOI: `10.1002/chem.201503580`.

13 Ashley, D. C.; Brinkley, D. W.; Roth, J. P. Oxygen isotope effects as structural and mechanistic probes in inorganic oxidation chemistry. *Inorg. Chem.* **2010**, *49*, 3661–3675, DOI: `10.1021/ic901778g`.

14 Auinger, M.; Katsounaros, I.; Meier, J. C.; Klemm, S. O.; Biedermann, P. U.; Topalov, A. A.; Rohwerder, M.; Mayrhofer, K. J. J. Near-surface ion distribution and buffer effects during electrochemical reactions. *Phys. Chem. Chem. Phys.* **2011**, *13*, 16384, DOI: `10.1039/c1cp21717h`.

15 Bagger, A.; Ju, W.; Varela, A. S.; Strasser, P.; Rossmeisl, J. Electrochemical CO_2 reduction: a classification problem. *ChemPhysChem* **2017**, *18*, 3266–3273, DOI: `10.1002/cphc.201700736`.

16 Bard, A.; Faulkner, L. In; Wiley: 2000; Chapter Mass transfer by migration and diffusion, pp 137–155.

17 Bard, A.; Faulkner, L., *Electrochemical methods. Fundamentals and application*; Wiley: 2000.

18 Barnhart, C. J.; Dale, M.; Brandt, A. R.; Benson, S. M. The energetic implications of curtailing versus storing solar- and wind-generated electricity. *Energy Environ. Sci* **2013**, *6*, 2804, DOI: `10.1039/c3ee41973h`.

19 Baroutaji, A.; Wilberforce, T.; Ramadan, M.; Olabi, A. G. Comprehensive investigation on hydrogen and fuel cell technology in the aviation and aerospace sectors. *Renewable Sustainable Energy Rev.* **2019**, *106*, 31–40, DOI: `10.1016/j.rser.2019.02.022`.

20 Bediako, D. K.; Ullman, A. M.; Nocera, D. G. In *Solar Energy for Fuels*; Springer: 2015, pp 173–213.

21 Bediako, D. K.; Lassalle-Kaiser, B.; Surendranath, Y.; Yano, J.; Yachandra, V. K.; Nocera, D. G. Structure–activity correlations in a nickel–borate oxygen evolution catalyst. *J. Am. Chem. Soc.* **2012**, *134*, 6801–6809, DOI: `10.1021/ja301018q`.

22 Bediako, D. K.; Costentin, C.; Jones, E. C.; Nocera, D. G.; Savéant, J.-M. Proton–electron transport and transfer in electrocatalytic films. Application to a cobalt-based O_2-evolution catalyst. *J. Am. Chem. Soc.* **2013**, *135*, 10492–10502, DOI: `10.1021/ja403656w`.

23 Benson, P.; Briggs, G.; Wynne-Jones, W. The cobalt hydroxide electrode—I. Structure and phase transitions of the hydroxides. *Electrochim. Acta* **1964**, *9*, 275–280, DOI: `10.1016/0013-4686(64)80016-5`.

24 Bergmann, A.; Zaharieva, I.; Dau, H.; Strasser, P. Electrochemical water splitting by layered and 3D cross-linked manganese oxides: correlating structural motifs and catalytic activity. *Energy Environ. Sci* **2013**, *6*, 2745–2755, DOI: `10.1039/C3ee41194j`.

25 Bergmann, A.; Martinez-Moreno, E.; Teschner, D.; Chernev, P.; Gliech, M.; de Araujo, J. F.; Reier, T.; Dau, H.; Strasser, P. Reversible amorphization and the catalytically active state of crystalline Co_3O_4 during oxygen evolution. *Nat. Commun.* **2015**, *6*, 8625, DOI: `10.1038/ncomms9625`.

26 Bergmann, A.; Jones, T. E.; Moreno, E. M.; Teschner, D.; Chernev, P.; Gliech, M.; Reier, T.; Dau, H.; Strasser, P. Unified structural motifs of the catalytically active state of Co(oxyhydr)oxides during the electrochemical oxygen evolution reaction. *Nat. Catal.* **2018**, *1*, 711–719, DOI: `10.1038/s41929-018-0141-2`.

27 Bergmann, U.; Glatzel, P. X-ray emission spectroscopy. *Photosynth. Res.* **2009**, *102*, 255–266, DOI: `10.1007/s11120-009-9483-6`.

28 Betley, T. A.; Wu, Q.; Voorhis, T. V.; Nocera, D. G. Electronic design criteria for O-O bond formation via metal-oxo complexes. *Inorg. Chem.* **2008**, *47*, 1849–1861, DOI: `10.1021/ic701972n`.

29 Bigeleisen, J.; Wolfsberg, M. In, Prigogine, I., Ed., 1958; Chapter Theoretical and experimental aspects of isotope effects in chemical kinetics, pp 15–76.

30 Blankenship, R. E.; Tiede, D. M.; Barber, J.; Brudvig, G. W.; Fleming, G.; Ghirardi, M.; Gunner, M. R.; Junge, W.; Kramer, D. M.; Melis, A.; Moore, T. A.; Moser, C. C.; Nocera, D. G.; Nozik, A. J.; Ort, D. R.; Parson, W. W.; Prince, R. C.; Sayre, R. T. Comparing photosynthetic and photovoltaic efficiencies and recognizing the potential for improvement. *Science* **2011**, *332*, 805–809, DOI: `10.1126/science.1200165`.

31 Bockris, J. O.; Otagawa, T. Mechanism of oxygen evolution on perovskites. *J. Phys. Chem.* **1983**, *87*, 2960–2971.

32 Bode, H.; Dehmelt, K.; Witte, J. Zur kenntnis der nickelhydroxidelektrode—I.Über das nickel (II)-hydroxidhydrat. *Electrochim. Acta* **1966**, *11*, 1079–1087, DOI: `10.1016/0013-4686(66)80045-2`.

33 Bokhoven, J. A. V.; Lamberti, C., *X-ray absorption and X-ray emission spectroscopy*; John Wiley & Sons, Ltd: 2016, DOI: `10.1002/9781118844243`.

34 Brandon, N. P.; Kurban, Z. Clean energy and the hydrogen economy. *Philos. Trans. R. Soc. A: Math. Phys. Eng. Sci.* **2017**, *375*, 20160400, DOI: `10.1098/rsta.2016.0400`.

35 Brodsky, C. N.; Hadt, R. G.; Hayes, D.; Reinhart, B. J.; Li, N.; Chen, L. X.; Nocera, D. G. In situ characterization of cofacial Co(IV) centers in Co_4O_4 cubane: modeling the high-valent active site in oxygen-evolving catalysts. *Proc. Natl. Acad. Sci.* **2017**, *114*, 3855–3860, DOI: `10.1073/pnas.1701816114`.

36 Brodsky, C. N.; Bediako, D. K.; Shi, C.; Keane, T. P.; Costentin, C.; Billinge, S. J. L.; Nocera, D. G. Proton–electron conductivity in thin films of a cobalt–oxygen evolving catalyst. *ACS Appl. Energy Mater.* **2018**, *1*, 1–2, DOI: `10.1021/acsaem.8b00785`.

37 Bunsen, T.; Cazzola, P.; d'Amore, L.; Gorner, M.; Scheffer, S.; Schuitmaker, R.; Signollet, H.; Tattini, J.; Teter, J. *Global EV outlook 2019*; tech. rep., https://www.iea.org/reports/global-ev-outlook-2019; IEA, 2019.

38 Burdyny, T.; Graham, P. J.; Pang, Y.; Dinh, C.-T.; Liu, M.; Sargent, E. H.; Sinton, D. Nanomorphology-enhanced gas-evolution intensifies CO_2 reduction electrochemistry. *ACS Sustain. Chem. Eng.* **2017**, *5*, 4031–4040, DOI: `10.1021/acssuschemeng.7b00023`.

39 Burke, M. S.; Kast, M. G.; Trotochaud, L.; Smith, A. M.; Boettcher, S. W. Cobalt–iron (oxy)hydroxide oxygen evolution electrocatalysts: the role of structure and composition on activity, stability, and mechanism. *J. Am. Chem. Soc.* **2015**, *137*, 3638–3648, DOI: `10.1021/jacs.5b00281`.

40 Burke, M. S.; Zou, S.; Enman, L. J.; Kellon, J. E.; Gabor, C. A.; Pledger, E.; Boettcher, S. W. Revised oxygen evolution reaction activity trends for first-row transition-metal (oxy)hydroxides in alkaline media. *J. Phys. Chem. Lett.* **2015**, *6*, 3737–3742, DOI: `10.1021/acs.jpclett.5b01650`.

41 Carmo, M.; Fritz, D. L.; Mergel, J.; Stolten, D. A comprehensive review on PEM water electrolysis. *Int. J. Hydrogen Energy* **2013**, *38*, 4901–4934, DOI: `10.1016/j.ijhydene.2013.01.151`.

42 Catal, T.; Kavakli, H. In; Wiley: 2020; Chapter Hydrogen Production by Algae, pp 425–445, DOI: `10.1002/9781119152057.ch17`.

43 Chakthranont, P.; Kibsgaard, J.; Gallo, A.; Park, J.; Mitani, M.; Sokaras, D.; Kroll, T.; Sinclair, R.; Mogensen, M. B.; Jaramillo, T. F. Effects of gold substrates on the intrinsic and extrinsic activity of high-loading nickel-based oxyhydroxide oxygen evolution catalysts. *ACS Catal.* **2017**, *7*, 5399–5409, DOI: `10.1021/acscatal.7b01070`.

44 Ciamician, G. The photochemistry of the future. *Science* **1912**, *36*, 385–394.

45 Clark, A. H.; Steiger, P.; Bornmann, B.; Hitz, S.; Frahm, R.; Ferri, D.; Nachtegaal, M. Fluorescence-detected quick-scanning X-ray absorption spectroscopy. *J. Synchrotron Radiat.* **2020**, *27*, 681–688, DOI: `10.1107/s1600577520002350`.

46 Coehn, A.; Gläser, M. Studien über die Bildung von Metalloxyden I. Über das anodische Verhalten von Kobalt- und Nickel-Lösungen. *Z. Anorg. Allg. Chem.* **1902**, *33*, 9–24, DOI: `10.1002/zaac.19020330105`.

47 Corrigan, D. A. The catalysis of the oxygen evolution reaction by iron impurities in thin film nickel oxide electrodes. *J. Electrochem. Soc.* **1987**, *134*, 377–384, DOI: `10.1149/1.2100463`.

48 Costentin, C.; Robert, M.; Savéant, J. M. Concerted proton-electron transfer reactions in water. Are the driving force and rate constant depending on pH when water acts as proton donor or acceptor? *J. Am. Chem. Soc.* **2007**, *129*, 5870–5879, DOI: `10.1021/ja067950q`.

49 Costentin, C.; Robert, M.; Savéant, J.-M.; Teillout, A.-L. Concerted proton-coupled electron transfers in aquo/hydroxo/oxo metal complexes: electrochemistry of $[Os^{II}(bpy)_2py(OH_2)]^{2+}$ in water. *Proc. Natl. Acad. Sci. U.S.A.* **2009**, *106*, 11829–11836, DOI: `10.1073/pnas.0905020106`.

50 Costentin, C.; Porter, T. R.; Savéant, J.-M. Conduction and reactivity in heterogeneous-molecular catalysis: new insights in water oxidation catalysis by phosphate cobalt oxide films. *J. Am. Chem. Soc.* **2016**, *138*, 5615–5622, DOI: `10.1021/jacs.6b00737`.

51 Costentin, C.; Nocera, D. G. Self-healing catalysis in water. *Proc. Natl. Acad. Sci.* **2017**, *114*, 13380–13384, DOI: `10.1073/pnas.1711836114`.

52 Covington, A. K.; Paabo, M.; Robinson, R. A.; Bates, R. G. Use of the glass electrode in deuterium oxide and the relation between the standardized pD (paD) scale and the operational pH in heavy water. *Anal. Chem.* **1968**, *40*, 700–706, DOI: `10.1021/ac60260a013`.

53 Dau, H.; Liebisch, P.; Haumann, M. X-ray absorption spectroscopy to analyze nuclear geometry and electronic structure of biological metal centers—potential and questions examined with special focus on the tetra-nuclear manganese complex of oxygenic photosynthesis. *Anal. Bioanal.Chem.* **2003**, *376*, 562–583, DOI: `10.1007/s00216-003-1982-2`.

54 Dau, H.; Grundmeier, A.; Loja, P.; Haumann, M. On the structure of the manganese complex of photosystem II: extended-range EXAFS data and specific atomic-resolution models for four S-states. *Philos. Trans. R. Soc. B* **2007**, *363*, 1237–1244, DOI: `10.1098/rstb.2007.2220`.

55 Dau, H.; Limberg, C.; Reier, T.; Risch, M.; Roggan, S.; Strasser, P. The mechanism of water oxidation: from electrolysis via homogeneous to biological catalysis. *ChemCatChem* **2010**, *2*, 724–761, DOI: `10.1002/cctc.201000126`.

56 Dau, H.; Zaharieva, I.; Haumann, M. Recent developments in research on water oxidation by photosystem II. *Curr. Opin. Chem. Biol.* **2012**, *16*, 3–10, DOI: `10.1016/j.cbpa.2012.02.011`.

57 Dau, H.; Pasquini, C. Modelling the (essential) role of proton transport by electrolyte bases for electrochemical water oxidation at near-neutral pH. *Inorganics* **2019**, *7*, 20, DOI: `10.3390/inorganics7020020`.

58 David, M.; Ocampo-Martinez, C.; Sanchez-Peña, R. Advances in alkaline water electrolyzers: a review. *J. Energy Storage* **2019**, *23*, 392–403, DOI: `10.1016/j.est.2019.03.001`.

59 Deng, Y.; Yeo, B. S. Characterization of electrocatalytic water splitting and CO_2 reduction reactions using in situ/operando Raman spectroscopy. *ACS Catal.* **2017**, *7*, 7873–7889, DOI: `10.1021/acscatal.7b02561`.

60 Denholm, P.; Margolis, R. M. Evaluating the limits of solar photovoltaics (PV) in traditional electric power systems. *Energy Policy* **2007**, *35*, 2852–2861, DOI: `10.1016/j.enpol.2006.10.014`.

61 Diaz-Morales, O.; Ferrus-Suspedra, D.; Koper, M. T. M. The importance of nickel oxyhydroxide deprotonation on its activity towards electrochemical water oxidation. *Chem. Sci.* **2016**, *7*, 2639–2645, DOI: `10.1039/c5sc04486c`.

62 Dincă, M.; Surendranath, Y.; Nocera, D. G. Nickel-borate oxygen-evolving catalyst that functions under benign conditions. *Proc. Natl. Acad. Sci. U.S.A* **2010**, *107*, 10337–10341, DOI: `10.1073/pnas.1001859107`.

63 Doyle, R. L.; Godwin, I. J.; Brandon, M. P.; Lyons, M. E. G. Redox and electrochemical water splitting catalytic properties of hydrated metal oxide modified electrodes. *Phys. Chem. Chem. Phys.* **2013**, *15*, 13737, DOI: `10.1039/c3cp51213d`.

64 Du, P. W.; Kokhan, O.; Chapman, K. W.; Chupas, P. J.; Tiede, D. M. Elucidating the domain structure of the cobalt oxide water splitting catalyst by X-ray pair distribution function analysis. *J. Am. Chem. Soc.* **2012**, *134*, 11096–11099, DOI: `10.1021/ja303826a`.

65 Dunwell, M.; Yang, X.; Setzler, B. P.; Anibal, J.; Yan, Y.; Xu, B. Examination of near-electrode concentration gradients and kinetic impacts on the electrochemical reduction of CO_2 using surface-enhanced infrared spectroscopy. *ACS Catal.* **2018**, *8*, 3999–4008, DOI: `10.1021/acscatal.8b01032`.

66 Dunwell, M.; Luc, W.; Yan, Y.; Jiao, F.; Xu, B. Understanding surface-mediated electrochemical reactions: CO_2 reduction and beyond. *ACS Catal.* **2018**, *8*, 8121–8129, DOI: `10.1021/acscatal.8b02181`.

67 Engasser, J.-M.; Horvath, C. Buffer-facilitated proton transport. pH profile of bound enzymes. *Biochim. Biophys. Acta* **1974**, *358*, 178–192, DOI: `10.1016/0005-2744(74)90269-1`.

68 Engasser, J.-M.; Wilhelm-Despres, A.-M. The facilitation of proton transport by acids and bases. *Chem. Eng. Sci.* **1980**, *35*, 669–672, DOI: `10.1016/0009-2509(80)80017-0`.

69 Enman, L. J.; Stevens, M. B.; Dahan, M. H.; Nellist, M. R.; Toroker, M. C.; Boettcher, S. W. Operando X-ray absorption spectroscopy shows iron oxidation is concurrent with oxygen evolution in cobalt-iron (oxy)hydroxide electrocatalysts. *Angew. Chem. Int. Ed.* **2018**, *57*, 12840–12844, DOI: `10.1002/anie.201808818`.

70 Eom, C. J.; Suntivich, J. In situ stimulated Raman spectroscopy reveals the phosphate network in the amorphous cobalt oxide catalyst and its role in the catalyst formation. *J. Phys. Chem. C* **2019**, *123*, 29284–29290, DOI: `10.1021/acs.jpcc.9b10308`.

71 Esswein, A. J.; Surendranath, Y.; Reece, S. Y.; Nocera, D. G. Highly active cobalt phosphate and borate based oxygen evolving catalysts operating in neutral and natural waters. *Energy Environ. Sci.* **2011**, *4*, 499–504, DOI: `10.1039/c0ee00518e`.

72 Farmand, M.; Landers, A. T.; Lin, J. C.; Feaster, J. T.; Beeman, J. W.; Ye, Y.; Clark, E. L.; Higgins, D.; Yano, J.; Davis, R. C.; Mehta, A.; Jaramillo, T. F.; Hahn, C.; Drisdell, W. S. Electrochemical flow cell enabling operando probing of electrocatalyst surfaces by X-ray spectroscopy and diffraction. *Phys. Chem. Chem. Phys.* **2019**, *21*, 5402–5408, DOI: `10.1039/c8cp07423b`.

73 Farrow, C. L.; Bediako, D. K.; Surendranath, Y.; Nocera, D. G.; Billinge, S. J. L. Intermediate-range structure of self-assembled cobalt-based oxygen-evolving catalyst. *J. Am. Chem. Soc.* **2013**, *135*, 6403–6406, DOI: `10.1021/ja401276f`.

74 Favaro, M.; Drisdell, W. S.; Marcus, M. A.; Gregoire, J. M.; Crumlin, E. J.; Haber, J. A.; Yano, J. An operando investigation of (Ni–Fe–Co–Ce)ox system as highly efficient electrocatalyst for oxygen evolution reaction. *ACS Catal.* **2017**, *7*, 1248–1258, DOI: `10.1021/acscatal.6b03126`.

75 Fernández, D.; Maurer, P.; Martine, M.; Coey, J. M. D.; Möbius, M. E. Bubble formation at a gas-evolving microelectrode. *Langmuir* **2014**, *30*, 13065–13074, DOI: `10.1021/la500234r`.

76 Ferraro, J. R., *Introductory Raman spectroscopy*; Elsevier: 2003.

77 Fester, J.; García-Melchor, M.; Walton, A. S.; Bajdich, M.; Li, Z.; Lammich, L.; Vojvodic, A.; Lauritsen, J. V. Edge reactivity and water-assisted dissociation on cobalt oxide nanoislands. *Nat. Commun.* **2017**, *8*, 14169, DOI: `10.1038/ncomms14169`.

78 Filipponi, A.; Borowski, M.; Loeffen, P. W.; Panfilis, S. D.; Cicco, A. D.; Sperandini, F.; Minicucci, M.; Giorgetti, M. Single-energy x-ray absorption detection: a combined electronic and structural local probe for phase transitions in condensed matter. *J. Phys.: Condens. Matter* **1998**, *10*, 235–253, DOI: `10.1088/0953-8984/10/1/026`.

79 Finn, P.; Fitzpatrick, C.; Connolly, D. Demand side management of electric car charging: benefits for consumer and grid. *Energy* **2012**, *42*, 358–363, DOI: `10.1016/j.energy.2012.03.042`.

80 Fletcher, S. Tafel slopes from first principles. *J. Solid State Electrochem.* **2008**, *13*, 537–549, DOI: `10.1007/s10008-008-0670-8`.

81 Fracchia, M.; Ghigna, P.; Vertova, A.; Rondinini, S.; Minguzzi, A. Time-resolved X-ray absorption spectroscopy in (photo)electrochemistry. *Surfaces* **2018**, *1*, 138–150, DOI: `10.3390/surfaces1010011`.

82 Frenkel, A. I.; Stern, E. A.; Qian, M.; Newville, M. Multiple-scattering x-ray-absorption fine-structure analysis and thermal expansion of alkali halides. *Phys. Rev. B* **1993**, *48*, 12449–12458, DOI: `10.1103/physrevb.48.12449`.

83 Fujishima, A.; Honda, K. Electrochemical photolysis of water at a semiconductor electrode. *Nature* **1972**, *238*, 37–38, DOI: `10.1038/238037a0`.

84 Fukuzumi, S.; Hong, D. Homogeneous versus heterogeneous catalysts in water oxidation. *Eur. J. Inorg. Chem.* **2013**, *2014*, 645–659, DOI: `10.1002/ejic.201300684`.

85 Garg, S.; Li, M.; Weber, A. Z.; Ge, L.; Li, L.; Rudolph, V.; Wang, G.; Rufford, T. E. Advances and challenges in electrochemical CO_2 reduction processes: an engineering and design perspective looking beyond new catalyst materials. *J. Mater. Chem.A* **2020**, *8*, 1511–1544, DOI: `10.1039/c9ta13298h`.

86 Gerken, J. B.; McAlpin, J. G.; Chen, J. Y. C.; Rigsby, M. L.; Casey, W. H.; Britt, R. D.; Stahl, S. S. Electrochemical water oxidation with cobalt-based electrocatalysts from pH 0–14: the thermodynamic basis for catalyst structure, stability, and activity. *J. Am. Chem. Soc.* **2011**, *133*, 14431–14442, DOI: `10.1021/ja205647m`.

87 Giordano, L.; Han, B.; Risch, M.; Hong, W. T.; Rao, R. R.; Stoerzinger, K. A.; Shao-Horn, Y. pH dependence of OER activity of oxides: current and future perspectives. *Catal. Today* **2016**, *262*, 2–10, DOI: `10.1016/j.cattod.2015.10.006`.

88 González-Flores, D.; Sanchez, I.; Zaharieva, I.; Klingan, K.; Heidkamp, J.; Chernev, P.; Menezes, P. W.; Driess, M.; Dau, H.; Montero, M. L. Heterogeneous water oxidation: surface activity versus amorphization activation in cobalt phosphate catalysts. *Angew. Chem. Int. Ed.* **2015**, *54*, 2472–6, DOI: `10.1002/anie.201409333`.

89 González-Flores, D.; Zaharieva, I.; Heidkamp, J.; Chernev, P.; Martinez-Moreno, E.; Pasquini, C.; Mohammadi, M. R.; Klingan, K.; Gernet, U.; Fischer, A.; Dau, H. Electrosynthesis of biomimetic manganese-calcium oxides for water oxidation catalysis - atomic structure and functionality. *ChemSusChem* **2016**, *9*, 379–387, DOI: `10.1002/cssc.201501399`.

90 González-Flores, D. Electrochemical water oxidation with transition-metal based catalysts: structure-function relations by electrochemistry combined with X-ray absorption spectroscopy and UV-visible spectroscopy, Ph.D. Thesis, Freie Universität Berlin, 2016.

91 González-Flores, D.; Klingan, K.; Chernev, P.; Loos, S.; Mohammadi, M. R.; Pasquini, C.; Kubella, P.; Zaharieva, I.; Smith, R. D. L.; Dau, H. Nickel-iron catalysts for electrochemical water oxidation – redox synergism investigated by in situ X-ray spectroscopy with millisecond time resolution. *Sustain. Energy Fuels* **2018**, *2*, 1986–1994, DOI: `10.1039/c8se00114f`.

92 Gorlin, M.; de Araujo, J. F.; Schmies, H.; Bernsmeier, D.; Dresp, S.; Gliech, M.; Jusys, Z.; Chernev, P.; Kraehnert, R.; Dau, H.; Strasser, P. Tracking catalyst redox states and reaction dynamics in Ni-Fe oxyhydroxide oxygen evolution reaction electrocatalysts: the role of catalyst support and electrolyte pH. *J. Am. Chem. Soc.* **2017**, *139*, 2070–2082, DOI: `10.1021/jacs.6b12250`.

93 Görlin, M.; Gliech, M.; de Araújo, J. F.; Dresp, S.; Bergmann, A.; Strasser, P. Dynamical changes of a Ni-Fe oxide water splitting catalyst investigated at different pH. *Catal. Today* **2016**, *262*, 65–73, DOI: `10.1016/j.cattod.2015.10.018`.

94 Grimaud, A.; Diaz-Morales, O.; Han, B.; Hong, W. T.; Lee, Y.-L.; Giordano, L.; Stoerzinger, K. A.; Koper, M. T. M.; Shao-Horn, Y. Activating lattice oxygen redox reactions in metal oxides to catalyse oxygen evolution. *Nat. Chem.* **2017**, *9*, 457–465, DOI: `10.1038/nchem.2695`.

95 Gupta, N.; Gattrell, M.; MacDougall, B. Calculation for the cathode surface concentrations in the electrochemical reduction of CO_2 in $KHCO_3$ solutions. *J. Appl. Electrochem.* **2005**, *36*, 161–172, DOI: `10.1007/s10800-005-9058-y`.

96 Hadt, R. G.; Hayes, D.; Brodsky, C. N.; Ullman, A. M.; Casa, D. M.; Upton, M. H.; Nocera, D. G.; Chen, L. X. X-ray spectroscopic characterization of Co(IV) and metal–metal interactions in Co_4O_4: electronic structure contributions to the formation of high-valent states relevant to the oxygen evolution reaction. *J. Am. Chem. Soc.* **2016**, *138*, 11017–11030, DOI: `10.1021/jacs.6b04663`.

97 Han, B.; Stoerzinger, K. A.; Tileli, V.; Gamalski, A. D.; Stach, E. A.; Shao-Horn, Y. Nanoscale structural oscillations in perovskite oxides induced by oxygen evolution. *Nat. Mater.* **2016**, *16*, 121–126, DOI: `10.1038/nmat4764`.

98 Han, J. E. S.; Chao, T. Y. Carbonate content of volumetric sodium hydroxide solutions. *Ind. Eng. Chem. Anal. Ed* **1932**, *4*, 229–232, DOI: `10.1021/ac50078a030`.

99 Hashiba, H.; Weng, L.-C.; Chen, Y.; Sato, H. K.; Yotsuhashi, S.; Xiang, C.; Weber, A. Z. Effects of electrolyte buffer capacity on surface reactant species and the reaction rate of CO_2 in electrochemical CO_2 reduction. *J. Phys. Chem. C* **2018**, *122*, 3719–3726, DOI: `10.1021/acs.jpcc.7b11316`.

100 Haumann, M.; Müller, C.; Liebisch, P.; Iuzzolino, L.; Dittmer, J.; Grabolle, M.; Neisius, T.; Meyer-Klaucke, W.; Dau, H. Structural and oxidation state changes of the photosystem II manganese complex in four transitions of the water oxidation cycle (S0→ S1, S1→ S2, S2→ S3, and S3,4→ S0) characterized by X-ray absorption spectroscopy at 20 K and room temperature†. *Biochemistry* **2005**, *44*, 1894–1908, DOI: `10.1021/bi048697e`.

101 Hausmann, J. N.; Mebs, S.; Laun, K.; Zebger, I.; Dau, H.; Menezes, P. W.; Driess, M. Understanding the formation of bulk- and surface-active layered (oxy)hydroxides for water oxidation starting from a cobalt selenite precursor. *Energy Environ. Sci* **2020**, *13*, 3607–3619, DOI: `10.1039/d0ee01912g`.

102 Heighton, L. P.; Zimmerman, M.; Rice, C. P.; Codling, E. E.; Tossell, J. A.; Schmidt, W. F. Quantification of inositol hexa-kis phosphate in environmental samples. *Open J. Soil Sci.* **2012**, *2*, 55–63, DOI: `10.4236/ojss.2012.21009`.

103 Hisatomi, T.; Kubota, J.; Domen, K. Recent advances in semiconductors for photocatalytic and photoelectrochemical water splitting. *Chem. Soc. Rev.* **2014**, *43*, 7520–7535, DOI: `10.1039/c3cs60378d`.

104 Hoganson, C. W.; Babcock, G. T. A metalloradical mechanism for the generation of oxygen from water in photosynthesis. *Science* **1997**, *277*, 1953–1956, DOI: `10.1126/science.277.5334.1953`.

105 Hong, W. T.; Risch, M.; Stoerzinger, K. A.; Grimaud, A.; Suntivich, J.; Shao-Horn, Y. Toward the rational design of non-precious transition metal oxides for oxygen electrocatalysis. *Energy Environ. Sci* **2015**, *8*, 1404–1427, DOI: `10.1039/c4ee03869j`.

106 Hu, Y.; Zhan, F.; Wang, Q.; Sun, Y.; Yu, C.; Zhao, X.; Wang, H.; Long, R.; Zhang, G.; Gao, C.; Zhang, W.; Jiang, J.; Tao, Y.; Xiong, Y. Tracking mechanistic pathway of photocatalytic CO_2 reaction at Ni sites using operando, time-resolved spectroscopy. *J. Am. Chem. Soc.* **2020**, *142*, 5618–5626, DOI: `10.1021/jacs.9b12443`.

107 Huang, J.; Chen, J.; Yao, T.; He, J.; Jiang, S.; Sun, Z.; Liu, Q.; Cheng, W.; Hu, F.; Jiang, Y.; Pan, Z.; Wei, S. CoOOH nanosheets with high mass activity for water oxidation. *Angew. Chem. Int. Ed.* **2015**, *54*, 8722–8727, DOI: `10.1002/anie.201502836`.

108 Huang, J.; Liu, Q.; Yao, T.; Pan, Z.; Wei, S. XAFS study on structure-activity correlations of α-Co(OH)$_2$ nanosheets water oxidation catalysts. *J. Phys. Conf. Ser.* **2016**, *712*, 012128, DOI: `10.1088/1742-6596/712/1/012128`.

109 Hunter, B. M.; Hieringer, W.; Winkler, J. R.; Gray, H. B.; Muller, A. M. Effect of interlayer anions on [NiFe]-LDH nanosheet water oxidation activity. *Energy Environ. Sci* **2016**, *9*, 1734–1743, DOI: `10.1039/C6EE00377J`.

110 Hunter, B. M.; Blakemore, J. D.; Deimund, M.; Gray, H. B.; Winkler, J. R.; Müller, A. M. Highly active mixed-metal nanosheet water oxidation catalysts made by pulsed-laser ablation in liquids. *J. Am. Chem. Soc.* **2014**, *136*, 13118–13121, DOI: `10.1021/ja506087h`.

111 Hunter, B. M.; Gray, H. B.; Müller, A. M. Earth-abundant heterogeneous water oxidation catalysts. *Chem. Rev.* **2016**, *116*, 14120-14136, DOI: `10.1021/acs.chemrev.6b00398`.

112 Huynh, M. H. V.; Meyer, T. J. Proton-coupled electron transfer. *Chem. Rev.* **2007**, *107*, 5004–5064, DOI: `10.1021/cr0500030`.

113 Huynh, M.; Bediako, D. K.; Nocera, D. G. A functionally stable manganese oxide oxygen evolution catalyst in acid. *J. Am. Chem. Soc.* **2014**, *136*, 6002–6010, DOI: `10.1021/ja413147e`.

114 Inaba, M.; Iriyama, Y.; Ogumi, Z.; Todzuka, Y.; Tasaka, A. Raman study of layered rock-salt $LiCoO_2$ and its electrochemical lithium deintercalation. *J. Raman Spectrosc.* **1997**, *28*, 613–617, DOI: `10.1002/(sici)1097-4555(199708)28:8<613::aid-jrs138>3.0.co;2-t`.

115 Ismail, A. A.; Bahnemann, D. W. Photochemical splitting of water for hydrogen production by photocatalysis: a review. *Sol. Energy Mater. Sol. Cells* **2014**, *128*, 85–101, DOI: `10.1016/j.solmat.2014.04.037`.

116 Janssen, L. Mass transfer at gas evolving electrodes. *Electrochim. Acta* **1978**, *23*, 81–86, DOI: `10.1016/0013-4686(78)80101-7`.

117 Janssen, L.; Hoogland, J. The effect of electrolytically evolved gas bubbles on the thickness of the diffusion layer. *Electrochim. Acta* **1970**, *15*, 1013–1023, DOI: `10.1016/0013-4686(70)80041-x`.

118 Janssen, L.; Hoogland, J. The effect of electrolytically evolved gas bubbles on the thickness of the diffusion layer—II. *Electrochim. Acta* **1973**, *18*, 543–550, DOI: `10.1016/0013-4686(73)85016-9`.

119 Jiang, S.; Klingan, K.; Pasquini, C.; Dau, H. New aspects of operando Raman spectroscopy applied to electrochemical CO_2 reduction on Cu foams. *J. Chem. Phys.* **2019**, *150*, 041718, DOI: `10.1063/1.5054109`.

120 Jiao, Y.; Zheng, Y.; Jaroniec, M.; Qiao, S. Z. Design of electrocatalysts for oxygen- and hydrogen-involving energy conversion reactions. *Chem. Soc. Rev.* **2015**, *44*, 2060–2086, DOI: `10.1039/c4cs00470a`.

121 Jin, J.; Walczak, K.; Singh, M. R.; Karp, C.; Lewis, N. S.; Xiang, C. An experimental and modeling/simulation-based evaluation of the efficiency and operational performance characteristics of an integrated, membrane-free, neutral pH solar-driven water-splitting system. *Energy Environ. Sci* **2014**, *7*, 3371–3380, DOI: `10.1039/c4ee01824a`.

122 Jones, J. P.; Prakash, G. K. S.; Olah, G. A. Electrochemical CO_2 reduction: recent advances and current trends. *Isr. J. Chem.* **2014**, *54*, 1451–1466, DOI: `10.1002/ijch.201400081`.

123 Joya, K. S.; Sala, X. In situ Raman and surface-enhanced Raman spectroscopy on working electrodes: spectroelectrochemical characterization of water oxidation electrocatalysts. *Phys. Chem. Chem. Phys.* **2015**, *17*, 21094–21103, DOI: `10.1039/c4cp05053c`.

124 Julien, C. M. Lithium intercalated compounds - charge transfer and related properties. *Mater. Sci. Eng. R Rep.* **2003**, *40*, 47–102, DOI: `10.1016/S0927-796X(02)00104-3`.

125 Kanan, M. W.; Nocera, D. G. In situ formation of an oxygen-evolving catalyst in neutral water containing phosphate and Co^{2+}. *Science* **2008**, *321*, 1072–1075, DOI: `10.1126/science.1162018`.

126 Kanan, M. W.; Yano, J.; Surendranath, Y.; Dinca, M.; Yachandra, V. K.; Nocera, D. G. Structure and valency of a cobalt-phosphate water oxidation catalyst determined by in situ X-ray spectroscopy. *J. Am. Chem. Soc.* **2010**, *132*, 13692–13701, DOI: `10.1021/Ja1023767`.

127 Kang, Q.; Vernisse, L.; Remsing, R. C.; Thenuwara, A. C.; Shumlas, S. L.; McKendry, I. G.; Klein, M. L.; Borguet, E.; Zdilla, M. J.; Strongin, D. R. Effect of interlayer spacing on the activity of layered manganese oxide bilayer catalysts for the oxygen evolution reaction. *J. Am. Chem. Soc.* **2017**, *139*, 1863–1870, DOI: `10.1021/jacs.6b09184`.

128 Kasrai, M.; Fleet, M. E.; Bancroft, G. M.; Tan, K. H.; Chen, J. M. X-ray-absorption near-edge structure of alkali halides: the interatomic-distance correlation. *Phys. Rev. B* **1991**, *43*, 1763–1772, DOI: `10.1103/physrevb.43.1763`.

129 Kim, J. H.; Hansora, D.; Sharma, P.; Jang, J.-W.; Lee, J. S. Toward practical solar hydrogen production - an artificial photosynthetic leaf-to-farm challenge. *Chem. Soc. Rev.* **2019**, *48*, 1908–1971, DOI: `10.1039/c8cs00699g`.

130 King, H. J.; Bonke, S. A.; Chang, S. L. Y.; Spiccia, L.; Johannessen, B.; Hocking, R. K. Engineering disorder into heterogenite-like cobalt oxides by phosphate doping: implications for the design of water-oxidation catalysts. *ChemCatChem* **2017**, *9*, 511–521, DOI: `10.1002/cctc.201600983`.

131 King, H. J.; Fournier, M.; Bonke, S. A.; Seeman, E.; Chatti, M.; Jumabekov, A. N.; Johannessen, B.; Kappen, P.; Simonov, A. N.; Hocking, R. K. Photon-induced, timescale, and electrode effects critical for the in situ X-ray spectroscopic analysis of electrocatalysts: the water oxidation case. *J. Phys. Chem. C* **2019**, *123*, 28533–28549, DOI: `10.1021/acs.jpcc.9b06944`.

132 Klamt, A.; Schüürmann, G. COSMO: a new approach to dielectric screening in solvents with explicit expressions for the screening energy and its gradient. *J. Chem. Soc., Perkin Trans. 2* **1993**, 799–805, DOI: `10.1039/P29930000799`.

133 Klaus, S.; Cai, Y.; Louie, M. W.; Trotochaud, L.; Bell, A. T. Effects of Fe electrolyte impurities on $Ni(OH)_2/NiOOH$ structure and oxygen evolution activity. *J. Phys. Chem. C* **2015**, *119*, 7243–7254, DOI: `10.1021/acs.jpcc.5b00105`.

134 Klingan, K.; Ringleb, F.; Zaharieva, I.; Heidkamp, J.; Chernev, P.; González-Flores, D.; Risch, M.; Fischer, A.; Dau, H. Water oxidation by amorphous cobalt-based oxides: volume activity and proton transfer to electrolyte bases. *ChemSusChem* **2014**, *7*, 1301–1310, DOI: `10.1002/cssc.201301019`.

135 Klingan, K.; Kottakkat, T.; Jovanov, Z. P.; Jiang, S.; Pasquini, C.; Scholten, F.; Kubella, P.; Bergmann, A.; Roldan Cuenya, B.; Roth, C.; Dau, H. Reactivity determinants in electrodeposited Cu foams for electrochemical CO_2 reduction. *ChemSusChem* **2018**, *11*, 3449–3459, DOI: `10.1002/cssc.201801582`.

136 Ko, H.; Juang, H. Absorption of $C0_2$ by alkaline electrolyte and its effect on electrical discharge. *J. Appl. Electrochem.* **1983**, *13*, 725–730, DOI: `10.1007/BF00615821`.

137 Koningsber, P., *X-ray absorption*; John Wiley & Sons: 1988; 696 pp.

138 Kornienko, N.; Zhang, J. Z.; Sakimoto, K. K.; Yang, P.; Reisner, E. Interfacing nature's catalytic machinery with synthetic materials for semi-artificial photosynthesis. *Nat. Nanotechnology* **2018**, *13*, 890–899, DOI: `10.1038/s41565-018-0251-7`.

139 Koroidov, S.; Anderlund, M. F.; Styring, S.; Thapper, A.; Messinger, J. First turnover analysis of water-oxidation catalyzed by Co-oxide nanoparticles. *Energy Environ. Sci.* **2015**, *8*, 2492–2503, DOI: `10.1039/C5EE00700C`.

140 Koza, J. A.; Hull, C. M.; Liu, Y.-C.; Switzer, J. A. Deposition of $\beta - Co(OH)_2$ films by electrochemical reduction of tris(ethylenediamine)cobalt(III) in alkaline solution. *Chem. Mater.* **2013**, *25*, 1922–1926, DOI: `10.1021/cm400579k`.

141 Krishtalik, L. I. The mechanism of the proton transfer: an outline. *Biochim. Biophys. Acta* **2000**, *1458*, 6–27, DOI: `10.1016/S0005-2728(00)00057-8`.

142 Kwon, G.; Jang, H.; Lee, J.-S.; Mane, A.; Mandia, D. J.; Soltau, S. R.; Utschig, L. M.; Martinson, A. B. F.; Tiede, D. M.; Kim, H.; Kim, J. Resolution of electronic and structural factors underlying oxygen-evolving performance in amorphous cobalt oxide catalysts. *J. Am. Chem. Soc.* **2018**, *140*, 10710–10720, DOI: `10.1021/jacs.8b02719`.

143 Lazard Lazard's levelized cost of energy analysis - version 13.0, https://www.lazard.com/perspective/lcoe2019/, 2019.

144 Lazard Lazard's levelized cost of storage analysis - version 5.0, https://www.lazard.com/perspective/lcoe2019, 2019.

145 Lee, S. W.; Carlton, C.; Risch, M.; Surendranath, Y.; Chen, S.; Furutsuki, S.; Yamada, A.; Nocera, D. G.; Shao-Horn, Y. The nature of lithium battery materials under oxygen evolution reaction conditions. *J. Am. Chem. Soc.* **2012**, *134*, 16959–16962, DOI: `10.1021/ja307814j`.

146 Lewis, N. S.; Nocera, D. G. Powering the planet: chemical challenges in solar energy utilization. *Proc. Natl. Acad. Sci. U.S.A.* **2006**, *103*, 15729–15735, DOI: `10.1073/pnas.0603395103`.

147 Li, X.; Siegbahn, P. E. M. Water oxidation mechanism for synthetic Co-oxides with small nuclearity. *J. Am. Chem. Soc.* **2013**, *135*, 13804-13813, DOI: `10.1021/ja4053448`.

148 Li, Y.; Qiu, W.; Qin, F.; Fang, H.; Hadjiev, V. G.; Litvinov, D.; Bao, J. Identification of cobalt oxides with Raman scattering and Fourier transform infrared spectroscopy. *J. Phys. Chem. C* **2016**, *120*, 4511–4516, DOI: `10.1021/acs.jpcc.5b11185`.

149 Lin, P.-C.; Pakrasi, H. B. Engineering cyanobacteria for production of terpenoids. *Planta* **2018**, *249*, 145–154, DOI: `10.1007/s00425-018-3047-y`.

150 Lin, S.-C.; Chang, C.-C.; Chiu, S.-Y.; Pai, H.-T.; Liao, T.-Y.; Hsu, C.-S.; Chiang, W.-H.; Tsai, M.-K.; Chen, H. M. Operando time-resolved X-ray absorption spectroscopy reveals the chemical nature enabling highly selective CO_2 reduction. *Nat. Commun.* **2020**, *11*, DOI: `10.1038/s41467-020-17231-3`.

151 Loos, S.; Zaharieva, I.; Chernev, P.; Lißner, A.; Dau, H. Electromodified NiFe alloys as electrocatalysts for water oxidation: mechanistic implications of time-resolved UV/Vis tracking of oxidation state changes. *ChemSusChem* **2019**, *12*, 1966–1976, DOI: `10.1002/cssc.201802737`.

152 Lu, Z.; Zhu, W.; Yu, X.; Zhang, H.; Li, Y.; Sun, X.; Wang, X.; Wang, H.; Wang, J.; Luo, J.; Lei, X.; Jiang, L. Ultrahigh hydrogen evolution performance of under-water "superaerophobic" MoS_2 nanostructured electrodes. *Adv. Mater.* **2014**, *26*, 2683–2687, DOI: `10.1002/adma.201304759`.

153 Luna, P. D.; Hahn, C.; Higgins, D.; Jaffer, S. A.; Jaramillo, T. F.; Sargent, E. H. What would it take for renewably powered electrosynthesis to displace petrochemical processes? *Science* **2019**, *364*, eaav3506, DOI: `10.1126/science.aav3506`.

154 Lutterman, D. A.; Surendranath, Y.; Nocera, D. G. A self-healing oxygen-evolving catalyst. *J. Am. Chem. Soc.* **2009**, *131*, 3838–3839, DOI: `10.1021/ja900023k`.

155 Mahajan, S.; Cole, R. M.; Speed, J. D.; Pelfrey, S. H.; Russell, A. E.; Bartlett, P. N.; Barnett, S. M.; Baumberg, J. J. Understanding the surface-enhanced Raman spectroscopy “background”. *J. Phys. Chem. C* **2009**, *114*, 7242–7250, DOI: `10.1021/jp907197b`.

156 Mai, T.; Wiser, R.; Sandor, D.; Brinkman, G.; Heath, G.; Denholm, P.; Hostick, D.; Darghouth, N.; Schlosser, A.; Strzepek, K. *Exploration of high-penetration renewable electricity futures. Vol. 1 of renewable electricity futures study*; tech. rep. NREL/TP-6A20-52409-1; National Renewable Energy Laboratory, 2012.

157 Man, I. C.; Su, H.-Y.; Calle-Vallejo, F.; Hansen, H. A.; Martínez, J. I.; Inoglu, N. G.; Kitchin, J.; Jaramillo, T. F.; Nørskov, J. K.; Rossmeisl, J. Universality in oxygen evolution electrocatalysis on oxide surfaces. *ChemCatChem* **2011**, *3*, 1159–1165, DOI: `10.1002/cctc.201000397`.

158 Marken, F.; Neudeck, A.; Bond, A. M. In, Scholz, F., Ed.; Springer: 2010; Chapter Cyclic voltammetry, pp 57–106.

159 Masson-Delmotte, V.; Zhai, P.; Pörtner, H.-O.; Roberts, D.; Skea, J.; Shukla, P.; Pirani, A.; Moufouma-Okia, W.; Péan, C.; Pidcock, R.; Connors, S.; Matthews, J.; Chen, Y.; Zhou, X.; Gomis, M.; Lonnoy, E.; Maycock, T.; Tignor, M.; Waterfield, T. In; World Meteorological Organization, Geneva, Switzerland: 2018; Chapter IPCC, 2018: Summary for Policymakers. P 32.

160 Matsuda, Y.; Kuwata, N.; Okawa, T.; Dorai, A.; Kamishima, O.; Kawamura, J. In situ Raman spectroscopy of $LiCoO_2$ cathode in $Li/Li_3PO_4/LiCoO_2$ all-solid-state thin-film lithium battery. *Solid State Ion.* **2019**, *335*, 7–14, DOI: `10.1016/j.ssi.2019.02.010`.

161 Mattioli, G.; Risch, M.; Bonapasta, A. A.; Dau, H.; Guidoni, L. Protonation states in a cobalt-oxide catalyst for water oxidation: fine comparison of ab initio molecular dynamics and X-ray absorption spectroscopy results. *Phys. Chem. Chem. Phys.* **2011**, *13*, 15437, DOI: `10.1039/c1cp21776c`.

162 Mattioli, G.; Giannozzi, P.; Amore Bonapasta, A.; Guidoni, L. Reaction pathways for oxygen evolution promoted by cobalt catalyst. *J. Am. Chem. Soc.* **2013**, *135*, 15353-15363, DOI: `10.1021/ja401797v`.

163 May, K. J.; Carlton, C. E.; Stoerzinger, K. A.; Risch, M.; Suntivich, J.; Lee, Y.-L.; Grimaud, A.; Shao-Horn, Y. Influence of oxygen evolution during water oxidation on the surface of perovskite oxide catalysts. *J. Phys. Chem. Lett* **2012**, *3*, 3264–3270, DOI: `10.1021/jz301414z`.

164 McAlpin, J. G.; Surendranath, Y.; Dincă, M.; Stich, T. A.; Stoian, S. A.; Casey, W. H.; Nocera, D. G.; Britt, R. D. EPR evidence for Co(IV) species produced during water oxidation at neutral pH. *J. Am. Chem. Soc.* **2010**, *132*, 6882–6883, DOI: `10.1021/ja1013344`.

165 McAlpin, J. G.; Stich, T. A.; Ohlin, C. A.; Surendranath, Y.; Nocera, D. G.; Casey, W. H.; Britt, R. D. Electronic structure description of a $[\mathrm{Co(III)_3Co(IV)O_4}]$ cluster: a model for the paramagnetic intermediate in cobalt-catalyzed water oxidation. *J. Am. Chem. Soc.* **2011**, *133*, 15444–15452, DOI: `10.1021/ja202320q`.

166 McCrory, C. C. L.; Jung, S.; Peters, J. C.; Jaramillo, T. F. Benchmarking heterogeneous electrocatalysts for the oxygen evolution reaction. *J. Am. Chem. Soc.* **2013**, *135*, 16977–16987, DOI: `10.1021/ja407115p`.

167 McKone, J. R.; Lewis, N. S.; Gray, H. B. Will solar-driven water-splitting devices see the light of day? *Chem. Mater.* **2014**, *26*, 407–414, DOI: `10.1021/cm4021518`.

168 Meng, J.; Chernev, P.; Mohammadi, M. R.; Klingan, K.; Loos, S.; Pasquini, C.; Kubella, P.; Jiang, S.; Yang, X.; Cui, Z.; Zhu, S.; Li, Z.; Liang, Y.; Dau, H. Self-supported $Ni(OH)_2/MnO_2$ on CFP as a flexible anode towards electrocatalytic urea conversion: the role of composition on activity, redox states and reaction dynamics. *Electrochim. Acta* **2019**, *318*, 32–41, DOI: `10.1016/j.electacta.2019.06.013`.

169 Merrill, M. D.; Dougherty, R. C. Metal oxide catalysts for the evolution of O_2 from H_2O. *J. Phys. Chem. C* **2008**, *112*, 3655–3666, DOI: `10.1021/Jp710675m`.

170 Minguzzi, A.; Lugaresi, O.; Locatelli, C.; Rondinini, S.; D'Acapito, F.; Achilli, E.; Ghigna, P. Fixed energy X-ray absorption voltammetry. *Anal. Chem.* **2013**, *85*, 7009–7013, DOI: `10.1021/ac401414v`.

171 Mohammadi, A.; Mehrpooya, M. A comprehensive review on coupling different types of electrolyzer to renewable energy sources. *Energy* **2018**, *158*, 632–655, DOI: `10.1016/j.energy.2018.06.073`.

172 Mohammadi, M. R.; Loos, S.; Chernev, P.; Pasquini, C.; Zaharieva, I.; González-Flores, D.; Kubella, P.; Klingan, K.; Smith, R. D. L.; Dau, H. Exploring the limits of self-repair in cobalt oxide films for electrocatalytic water oxidation. *ACS Catal.* **2020**, *10*, 7990–7999, DOI: `10.1021/acscatal.0c01944`.

173 Mora-diez, N.; Egorova, Y.; Plommer, H.; Tremaine, P. R. Theoretical study of deuterium isotope effects on acid – base equilibria under ambient and hydrothermal conditions. *RSC Adv.* **2015**, *5*, 9097–9109, DOI: `10.1039/C4RA14087G`.

174 Muench, F.; El-Nagar, G. A.; Tichter, T.; Zintler, A.; Kunz, U.; Molina-Luna, L.; Sikolenko, V.; Pasquini, C.; Lauermann, I.; Roth, C. Conformal solution deposition of Pt-Pd titania nanocomposite coatings for light-assisted formic acid electro-oxidation. *ACS Appl. Mater. Interfaces* **2019**, *11*, 43081–43092, DOI: `10.1021/acsami.9b12783`.

175 Müller, O.; Nachtegaal, M.; Just, J.; Lützenkirchen-Hecht, D.; Frahm, R. Quick-EXAFS setup at the SuperXAS beamline for in-situX-ray absorption spectroscopy with 10 ms time resolution. *J. Synchrotron Radiat.* **2016**, *23*, 260–266, DOI: `10.1107/s1600577515018007`.

176 Munuera, L.; Fukui, H. *Tracking energy integration 2019*; tech. rep., https://www.iea.org/reports/tracking-energy-integration-2019; Paris: IEA, 2019.

177 Nagasaka, M.; Yuzawa, H.; Kosugi, N. Development and application of in situ/operando soft X-ray transmission cells to aqueous solutions and catalytic and electrochemical reactions. *J. Electron Spectrosc. Relat. Phenom.* **2015**, *200*, 293–310, DOI: `10.1016/j.elspec.2015.05.012`.

178 Neese, F. The ORCA program system. *WIREs Comput. Mol. Sci.* **2012**, *2*, 73–78, DOI: `10.1002/wcms.81`.

179 Neese, F.; Wennmohs, F.; Hansen, A.; Becker, U. Efficient, approximate and parallel Hartree-Fock and hybrid DFT calculations. A 'chain-of-spheres' algorithm for the Hartree-Fock exchange. *Chem. Phys.* **2009**, *356*, 98–109, DOI: `10.1016/j.chemphys.2008.10.036`.

180 Nelson, N.; Yocum, C. F. Structure and function of photosystems I and II. *Annu. Rev. Plant Biol.* **2006**, *57*, 521–565, DOI: `10.1146/annurev.arplant.57.032905.105350`.

181 Newville, M. Fundamentals of XAFS. *Rev. Mineral. Geochem.* **2004**, *78*, 33–74, DOI: `10.2138/rmg.2014.78.2`.

182 Nguyen, A. I.; Ziegler, M. S.; Oña-Burgos, P.; Sturzbecher-Hohne, M.; Kim, W.; Bellone, D. E.; Tilley, T. D. Mechanistic investigations of water oxidation by a molecular cobalt oxide analogue: evidence for a highly oxidized intermediate and exclusive terminal oxo participation. *J. Am. Chem. Soc.* **2015**, *137*, 12865–12872, DOI: `10.1021/jacs.5b08396`.

183 Nocera, D. G. The artificial leaf. *Acc. Chem. Res.* **2012**, *45*, 767–776, DOI: `10.1021/ar2003013`.

184 Nong, H. N.; Falling, L. J.; Bergmann, A.; Klingenhof, M.; Tran, H. P.; Spöri, C.; Mom, R.; Timoshenko, J.; Zichittella, G.; Knop-Gericke, A.; Piccinin, S.; Pérez-Ramírez, J.; Cuenya, B. R.; Schlögl, R.; Strasser, P.; Teschner, D.; Jones, T. E. Key role of chemistry versus bias in electrocatalytic oxygen evolution. *Nature* **2020**, *587*, 408–413, DOI: `10.1038/s41586-020-2908-2`.

185 Obata, K.; van de Krol, R.; Schwarze, M.; Schomäcker, R.; Abdi, F. F. In situ observation of pH change during water splitting in neutral pH conditions: impact of natural convection driven by buoyancy effects. *Energy Environ. Sci* **2020**, *13*, 5104–5116, DOI: `10.1039/d0ee01760d`.

186 Oliva, P.; Leonardi, J.; Laurent, J.; Delmas, C.; Braconnier, J.; Figlarz, M.; Fievet, F.; Guibert, A. Review of the structure and the electrochemistry of nickel hydroxides and oxy-hydroxides. *J. Power Sources* **1982**, *8*, 229–255, DOI: `10.1016/0378-7753(82)80057-8`.

187 Park, J. E.; Karuppannan, M.; Kwon, O. J.; Cho, Y.-H.; Sung, Y.-E. Development of high-performance membrane-electrode assembly in unitized regenerative fuel cells. *J. Ind. Eng. Chem.* **2019**, *80*, 527–534, DOI: `10.1016/j.jiec.2019.08.029`.

188 Parkin, G. Temperature-dependent transitions between normal and inverse isotope effects pertaining to the interaction of H - H and C - H bonds with transition metal centers. *Acc. Chem. Res.* **2009**, *42*, 315–325, DOI: `10.1021/ar800156h`.

189 Pascarelli, S.; Neisius, T.; Panfilis, S. D. Turbo-XAS: dispersive XAS using sequential acquisition. *J. Synchrotron Radiat.* **1999**, *6*, 1044–1050, DOI: `10.1107/s0909049599004513`.

190 Pasquini, C.; Zaharieva, I.; González-Flores, D.; Chernev, P.; Mohammadi, M. R.; Guidoni, L.; Smith, R. D. L.; Dau, H. H/D isotope effects reveal factors controlling catalytic activity in Co-based oxides for water oxidation. *J. Am. Chem. Soc.* **2019**, *141*, 2938–2948, DOI: `10.1021/jacs.8b10002`.

191 Pasquini, C.; D'Amario, L.; Zaharieva, I.; Dau, H. Operando Raman spectroscopy tracks oxidation-state changes in an amorphous Co oxide material for electrocatalysis of the oxygen evolution reaction. *J. Chem. Phys.* **2020**, *152*, 194202, DOI: `10.1063/5.0006306`.

192 Pasquini, C.; Liu, S.; Chernev, P.; Gonzalez-Flores, D.; Mohammadi, M. R.; Kubella, P.; Jiang, S.; Loos, S.; Klingan, K.; Sikolenko, V.; Mebs, S.; Haumann, M.; Beyer, P.; D'Amario, L.; Smith, R. D. L.; Zaharieva, I.; Dau, H. Operando tracking of oxidation-state changes by coupling electrochemistry with time-resolved X-ray absorption spectroscopy demonstrated for water oxidation by a cobalt-based catalyst film. *Anal. Bioanal. Chem.* **2021**, DOI: `10.1007/s00216-021-03515-0`.

193 Pavlovic, Z.; Ranjan, C.; van Gastel, M.; Schlögl, R. The active site for the water oxidising anodic iridium oxide probed through in situ Raman spectroscopy. *Chem. Commun.* **2017**, *53*, 12414–12417, DOI: `10.1039/c7cc05669a`.

194 Pellow, M. A.; Emmott, C. J. M.; Barnhart, C. J.; Benson, S. M. Hydrogen or batteries for grid storage? A net energy analysis. *Energy Environ. Sci* **2015**, *8*, 1938–1952, DOI: `10.1039/c4ee04041d`.

195 Penner-Hahn, J. E. X-ray absorption spectroscopy in coordination chemistry. *Coord. Chem. Rev.* **1999**, *190-192*, 1101–1123, DOI: `10.1016/S0010-8545(99)00160-5`.

196 Polo da Fonseca, C. N.; De Paoli, M.-. A.; Gorenstein, A. Electrochromism in cobalt oxide thin films grown by anodic electroprecipitation. *Sol. Energy Mater. Sol. Cells* **1994**, *33*, 73–81, DOI: `10.1016/0927-0248(94)90291-7`.

197 Preston, C. M.; Adams, W. A. A laser Raman spectroscopic study of aqueous orthophosphate salts. *J. Phys. Chem.* **1979**, *83*, 814–821, DOI: `10.1021/j100470a011`.

198 Qiu, J.; Hajibabaei, H.; Nellist, M. R.; Laskowski, F. A. L.; Oener, S. Z.; Hamann, T. W.; Boettcher, S. W. Catalyst deposition on photoanodes: the roles of intrinsic catalytic activity, catalyst electrical conductivity, and semiconductor morphology. *ACS Energy Lett.* **2018**, *3*, 961–969, DOI: `10.1021/acsenergylett.8b00336`.

199 Ralon, P.; Taylor, M.; Ilas, A.; Diaz-Bone, H.; Kairies, K.-P. *Electricity storage and renewables: costs and markets to 2030*; tech. rep., ISBN 978-92-9260-038-; International Renewable Energy Agency, Abu Dhabi: IRENA, 2017.

200 Rashchi, F.; Finch, J. Polyphosphates: a review their chemistry and application with particular reference to mineral processing. *Miner. Eng.* **2000**, *13*, 1019–1035, DOI: `10.1016/s0892-6875(00)00087-x`.

201 Regmi, Y. N.; Peng, X.; Fornaciari, J. C.; Wei, M.; Myers, D. J.; Weber, A. Z.; Danilovic, N. A low temperature unitized regenerative fuel cell realizing 60% round trip efficiency and 10 000 cycles of durability for energy storage applications. *Energy Environ. Sci* **2020**, *13*, 2096–2105, DOI: `10.1039/c9ee03626a`.

202 Reier, T.; Nong, H. N.; Teschner, D.; Schlögl, R.; Strasser, P. Electrocatalytic oxygen evolution reaction in acidic environments - reaction mechanisms and catalysts. *Adv. Energy Mater.* **2016**, *7*, 1601275, DOI: `10.1002/aenm.201601275`.

203 REN21 Renewables 2019 global status report, https://www.ren21.net/reports/global-status-report/, 2019.

204 Risch, M.; Khare, V.; Zaharieva, I.; Gerencser, L.; Chernev, P.; Dau, H. Cobalt-oxo core of a water-oxidizing catalyst film. *J. Am. Chem. Soc.* **2009**, *131*, 6936–6937, DOI: `10.1021/Ja902121f`.

205 Risch, M.; Klingan, K.; Ringleb, F.; Chernev, P.; Zaharieva, I.; Fischer, A.; Dau, H. Water oxidation by electrodeposited cobalt oxides - role of anions and redox-inert cations in structure and function of the amorphous catalyst. *ChemSusChem* **2012**, *5*, 542–549, DOI: `10.1002/cssc.201100574`.

206 Risch, M.; Ringleb, F.; Kohlhoff, M.; Bogdanoff, P.; Chernev, P.; Zaharieva, I.; Dau, H. Water oxidation by amorphous cobalt-based oxides: in situ tracking of redox transitions and mode of catalysis. *Energy Environ. Sci* **2015**, *8*, 661–674, DOI: `10.1039/C4ee03004d`.

207 Risch, M. Structure-function relations in water-oxidizing cobalt oxides investigated by X-ray absorption spectroscopy, Ph.D. Thesis, Freie Universität Berlin, 2011.

208 Risch, M.; Klingan, K.; Heidkamp, J.; Ehrenberg, D.; Chernev, P.; Zaharieva, I.; Dau, H. Nickel-oxido structure of a water-oxidizing catalyst film. *Chem. Commun.* **2011**, *47*, 11912, DOI: `10.1039/c1cc15072c`.

209 Risch, M.; Klingan, K.; Zaharieva, I.; Dau, H. In *Molecular Water Oxidation Catalysts*, Llobet, A., Ed.; Wiley-VCH: 2014.

210 Rivas-Murias, B.; Salgueiriño, V. Thermodynamic $CoO - Co_3O_4$ crossover using Raman spectroscopy in magnetic octahedron-shaped nanocrystals. *J. Raman Spectrosc.* **2017**, *48*, 837–841, DOI: `10.1002/jrs.5129`.

211 Roberts, J. A. S.; Bullock, R. M. Direct determination of equilibrium potentials for hydrogen oxidation/production by open circuit potential measurements in acetonitrile. *Inorg. Chem.* **2013**, *52*, 3823–3835, DOI: `10.1021/ic302461q`.

212 Robinson, R.; Paabo, M.; Bates, R. G. Deuterium isotope effect on the dissociation of weak acids in water and deuterium oxide. *J. Res. Natl. Bur. Stand. A Phys. Chem.* **1969**, *73A*, 299–308, DOI: `10.1139/v76-407`.

213 Roger, I.; Shipman, M. A.; Symes, M. D. Earth-abundant catalysts for electrochemical and photoelectrochemical water splitting. *Nat. Rev. Chem.* **2017**, *1*, 0003, DOI: `10.1038/s41570-016-0003`.

214 Rögner, M. Metabolic engineering of cyanobacteria for the production of hydrogen from water. *Biochem. Soc. Trans.* **2013**, *41*, 1254–1259, DOI: `10.1042/bst20130122`.

215 Ronge, E.; Lindner, J.; Ross, U.; Melder, J.; Ohms, J.; Roddatis, V.; Kurz, P.; Jooss, C. Atom surface dynamics of manganese oxide under oxygen evolution reaction-like conditions studied by in situ environmental transmission electron microscopy. *J. Phys. Chem. C* **2021**, *125*, 5037–5047, DOI: `10.1021/acs.jpcc.0c09806`.

216 Roth, J. P. Oxygen isotope effects as probes of electron transfer mechanisms and structures of activated O_2. *Acc. Chem. Res* **2009**, *42*, 399–408, DOI: `10.1021/ar800169z`.

217 Rougier, A.; Nazri, G. A.; Julien, C. Vibrational spectroscopy and electrochemical properties of $LiNi_{0.7}Co_{0.3}O_2$ cathode material for rechargeable lithium batteries. *Ionics* **1997**, *3*, 170–176, DOI: `10.1007/BF02375613`.

218 Ryu, J.; Wuttig, A.; Surendranath, Y. Quantification of interfacial pH variation at molecular length scales using a concurrent non-Faradaic reaction. *Angew. Chem. Int. Ed.* **2018**, *57*, 9300–9304, DOI: `10.1002/anie.201802756`.

219 Sayeed, M. A.; O'Mullane, A. P. Electrocatalytic water oxidation at amorphous trimetallic oxides based on FeCoNiOx. *RSC Adv.* **2017**, *7*, 43083–43089, DOI: `10.1039/c7ra07995h`.

220 Schaefers, F.; Mertin, M.; Gorgoi, M. KMC-1: a high resolution and high flux soft X-ray beamline at BESSY. *Rev. Sci. Instrum.* **2007**, *78*, 123102.

221 Schalenbach, M.; Tjarks, G.; Carmo, M.; Lueke, W.; Mueller, M.; Stolten, D. Acidic or alkaline? Towards a new perspective on the efficiency of water electrolysis. *J. Electrochem. Soc.* **2016**, *163*, F3197–F3208, DOI: `10.1149/2.0271611jes`.

222 Schalenbach, M.; Zeradjanin, A. R.; Kasian, O.; Cherevko, S.; Mayrhofer, K. J. A perspective on low-temperature water electrolysis – challenges in alkaline and acidic technology. *Int. J. Electrochem. Sci.* **2018**, 1173–1226, DOI: `10.20964/2018.02.26`.

223 Schlücker, S. Surface-enhanced Raman spectroscopy: concepts and chemical applications. *Angew. Chem. Int. Ed.* **2014**, *53*, 4756–4795, DOI: `10.1002/anie.201205748`.

224 Schwendke, P. Protonen in der wasserspaltung durch kobaltoxide, MA thesis, Freie Universität Berlin, 2018.

225 Seddon, J. R. T.; Lohse, D. Nanobubbles and micropancakes: gaseous domains on immersed substrates. *J. Phys.: Condens. Matter* **2011**, *23*, 133001, DOI: `10.1088/0953-8984/23/13/133001`.

226 Seh, Z. W.; Kibsgaard, J.; Dickens, C. F.; Chorkendorff, I.; Nørskov, J. K.; Jaramillo, T. F. Combining theory and experiment in electrocatalysis: insights into materials design. *Science* **2017**, *355*, 4998–5009, DOI: `10.1126/science.aad4998`.

227 Shaner, M. R.; Atwater, H. A.; Lewis, N. S.; McFarland, E. W. A comparative technoeconomic analysis of renewable hydrogen production using solar energy. *Energy Environ. Sci* **2016**, *9*, 2354–2371, DOI: `10.1039/c5ee02573g`.

228 Sheehy, J. A.; Gil, T. J.; Winstead, C. L.; Farren, R. E.; Langhoff, P. W. Correlation of molecular valence- and K-shell photoionization resonances with bond lengths. *J. Chem. Phys.* **1989**, *91*, 1796–1812, DOI: `10.1063/1.457085`.

229 Shinagawa, T.; Garcia-Esparza, A. T.; Takanabe, K. Insight on Tafel slopes from a microkinetic analysis of aqueous electrocatalysis for energy conversion. *Sci. Rep.* **2015**, *5*, 13801, DOI: `10.1038/srep13801`.

230 Shinagawa, T.; Ng, M. T.-K.; Takanabe, K. Boosting the performance of the nickel anode in the oxygen evolution reaction by simple electrochemical activation. *Angew. Chem. Int. Ed.* **2017**, *56*, 5061–5065, DOI: `10.1002/anie.201701642`.

231 Shinagawa, T.; Ng, M. T.-K.; Takanabe, K. Electrolyte engineering towards efficient water splitting at mild pH. *ChemSusChem* **2017**, *10*, 4155–4162, DOI: `10.1002/cssc.201701266`.

232 Shinagawa, T.; Takanabe, K. Towards versatile and sustainable hydrogen production through electrocatalytic water splitting: electrolyte engineering. *ChemSusChem* **2017**, *10*, 1318–1336, DOI: `10.1002/cssc.201601583`.

233 Siebert, F.; Hildebrandt, P., *Vibrational spectroscopy in life science*; Wiley: 2007, DOI: `10.1002/9783527621347`.

234 Singh, M. R.; Papadantonakis, K.; Xiang, C.; Lewis, N. S. An electrochemical engineering assessment of the operational conditions and constraints for solar-driven water-splitting systems at near-neutral pH. *Energy Environ. Sci* **2015**, *8*, 2760–2767, DOI: `10.1039/c5ee01721a`.

235 Smith, R. D. L.; Pasquini, C.; Loos, S.; Chernev, P.; Klingan, K.; Kubella, P.; Mohammadi, M. R.; González-Flores, D.; Dau, H. Spectroscopic identification of active sites for the oxygen evolution reaction on iron-cobalt oxides. *Nat. Commun.* **2017**, *8*, 2022, DOI: `10.1038/s41467-017-01949-8`.

236 Smith, R. D. L.; Prévot, M. S.; Fagan, R. D.; Zhang, Z.; Sedach, P. A.; Kit, M.; Siu, J.; Trudel, S.; Berlinguette, C. P. Photochemical route for accessing amorphous metal oxide materials for water oxidation catalysis. *Science* **2013**, *340*, 60–63, DOI: `10.1126/science.1233638`.

237 Smith, R. D. L.; Prévot, M. S.; Fagan, R. D.; Trudel, S.; Berlinguette, C. P. Water oxidation catalysis: electrocatalytic response to metal stoichiometry in amorphous metal oxide films containing iron, cobalt, and nickel. *J. Am. Chem. Soc.* **2013**, *135*, 11580–11586, DOI: `10.1021/ja403102j`.

238 Smith, R. D. L.; Berlinguette, C. P. Accounting for the dynamic oxidative behavior of nickel anodes. *J. Am. Chem. Soc.* **2016**, *138*, 1561–1567, DOI: `10.1021/jacs.5b10728`.

239 Smith, R. D. L.; Pasquini, C.; Loos, S.; Chernev, P.; Klingan, K.; Kubella, P.; Mohammadi, M. R.; González-Flores, D.; Dau, H. Geometric distortions in nickel (oxy)hydroxide electrocatalysts by redox inactive iron ions. *Energy Environ. Sci* **2018**, *11*, 2476–2485, DOI: `10.1039/c8ee01063c`.

240 Song, F.; Bai, L.; Moysiadou, A.; Lee, S.; Hu, C.; Liardet, L.; Hu, X. Transition metal oxides as electrocatalysts for the oxygen evolution reaction in alkaline solutions: an application-inspired renaissance. *J. Am. Chem. Soc.* **2018**, *140*, 7748–7759, DOI: `10.1021/jacs.8b04546`.

241 Spoeri, C.; Kwan, J. T. H.; Bonakdarpour, A.; Wilkinson, D. P.; Strasser, P. The stability challenges of oxygen evolving catalysts: towards a common fundamental understanding and mitigation of catalyst degradation. *Angew. Chem. Int. Ed.* **2017**, *56*, 5994–6021, DOI: `10.1002/anie.201608601`.

242 Stamenkovic, V. R.; Strmcnik, D.; Lopes, P. P.; Markovic, N. M. Energy and fuels from electrochemical interfaces. *Nat. Mater.* **2017**, *16*, 57–69, DOI: `10.1038/NMAT4738`.

243 Suen, N.-T.; Hung, S.-F.; Quan, Q.; Zhang, N.; Xu, Y.-J.; Chen, H. M. Electrocatalysis for the oxygen evolution reaction: recent development and future perspectives. *Chem. Soc. Rev.* **2017**, *46*, 337–365, DOI: `10.1039/c6cs00328a`.

244 Surendranath, Y.; Dinca, M.; Nocera, D. G. Electrolyte-dependent electrosynthesis and activity of cobalt-based water oxidation catalysts. *J. Am. Chem. Soc.* **2009**, *131*, 2615–2620, DOI: `10.1021/ja807769r`.

245 Surendranath, Y.; Kanan, M. W.; Nocera, D. G. Mechanistic studies of the oxygen evolution reaction by a cobalt-phosphate catalyst at neutral pH. *J. Am. Chem. Soc.* **2010**, *132*, 16501–16509, DOI: `10.1021/Ja106102b`.

246 Surendranath, Y.; Lutterman, D. A.; Liu, Y.; Nocera, D. G. Nucleation, growth, and repair of a cobalt-based oxygen evolving catalyst. *J. Am. Chem. Soc.* **2012**, *134*, 6326–6336, DOI: `10.1021/ja3000084`.

247 Suter, S.; Cantoni, M.; Gaudy, Y. K.; Pokrant, S.; Haussener, S. Linking morphology and multi-physical transport in structured photoelectrodes. *Sustain. Energy Fuels* **2018**, *2*, 2661–2673, DOI: `10.1039/c8se00215k`.

248 Symes, M. D.; Surendranath, Y.; Lutterman, D. A.; Nocera, D. G. Bidirectional and unidirectional PCET in a molecular model of a cobalt-based oxygen-evolving catalyst. *J. Am. Chem. Soc.* **2011**, *133*, 5174–5177, DOI: `10.1021/ja110908v`.

249 Takashima, T.; Hashimoto, K.; Nakamura, R. Mechanisms of pH-dependent activity for water oxidation to molecular oxygen by MnO_2 electrocatalysts. *J. Am. Chem. Soc.* **2012**, *134*, 1519–1527, DOI: `10.1021/ja206511w`.

250 Takata, T.; Jiang, J.; Sakata, Y.; Nakabayashi, M.; Shibata, N.; Nandal, V.; Seki, K.; Hisatomi, T.; Domen, K. Photocatalytic water splitting with a quantum efficiency of almost unity. *Nature* **2020**, *581*, 411–414, DOI: `10.1038/s41586-020-2278-9`.

251 Thomas, C. Fuel cell and battery electric vehicles compared. *Int. J. Hydrogen Energy* **2009**, *34*, 6005–6020, DOI: `10.1016/j.ijhydene.2009.06.003`.

252 Thompson, A.; Attwood, D.; Gullikson, E.; Howells, M.; Kim, K.-J.; Kirz, J.; Kortright, J.; Lindau, I.; Pianetta, P.; Robinson, A.; Scofield, J.; Underwood, J.; Vaughan, D.; Williams, G.; Winick, H., *X-ray data booklet*; Lawrence Berkeley National Laboratory, University of California: Berkeley, 2001.

253 Trotochaud, L.; Mills, T. J.; Boettcher, S. W. An optocatalytic model for semiconductor-catalyst water-splitting photoelectrodes based on in situ optical measurements on operational catalysts. *J. Phys. Chem. Lett.* **2013**, *4*, 931–935, DOI: `10.1021/jz4002604`.

254 Trotochaud, L.; Young, S. L.; Ranney, J. K.; Boettcher, S. W. Nickel–iron oxyhydroxide oxygen-evolution electrocatalysts: the role of intentional and incidental iron incorporation. *J. Am. Chem. Soc.* **2014**, *136*, 6744–6753, DOI: `10.1021/ja502379c`.

255 Trześniewski, B. J.; Diaz-Morales, O.; Vermaas, D. A.; Longo, A.; Bras, W.; Koper, M. T. M.; Smith, W. A. In situ observation of active oxygen species in Fe-containing Ni-based oxygen evolution catalysts: the effect of pH on electrochemical activity. *J. Am. Chem. Soc.* **2015**, *137*, 15112–15121, DOI: `10.1021/jacs.5b06814`.

256 Tse, E. C. M.; Hoang, T. T. H.; Varnell, J. A.; Gewirth, A. A. Observation of an inverse kinetic isotope effect in oxygen evolution electrochemistry. *ACS Catal.* **2016**, *6*, 5706–5714, DOI: `10.1021/acscatal.6b01170`.

257 Ullman, A. M.; Brodsky, C. N.; Li, N.; Zheng, S.-l.; Nocera, D. G. Probing edge site reactivity of oxidic cobalt water oxidation catalysts. *J. Am. Chem. Soc.* **2016**, *138*, 4229-4236, DOI: `10.1021/jacs.6b00762`.

258 Van Oversteeg, C. H. M.; Doan, H. Q.; de Groot, F. M. F.; Cuk, T. In situ X-ray absorption spectroscopy of transition metal based water oxidation catalysts. *Chem. Soc. Rev.* **2017**, *46*, 102–125, DOI: `10.1039/C6CS00230G`.

259 Victoria, M.; Zhu, K.; Brown, T.; Andresen, G. B.; Greiner, M. The role of storage technologies throughout the decarbonisation of the sector-coupled European energy system. *Energy Convers. Manage.* **2019**, *201*, 111977, DOI: `10.1016/j.enconman.2019.111977`.

260 Villalobos, J.; González-Flores, D.; Klingan, K.; Chernev, P.; Kubella, P.; Urcuyo, R.; Pasquini, C.; Mohammadi, M. R.; Smith, R. D. L.; Montero, M. L.; Dau, H. Structural and functional role of anions in electrochemical water oxidation probed by arsenate incorporation into cobalt-oxide materials. *Phys. Chem. Chem. Phys.* **2019**, *21*, 12485–12493, DOI: `10.1039/c9cp01754b`.

261 Vogt, H. The actual current density of gas-evolving electrodes—Notes on the bubble coverage. *Electrochim. Acta* **2012**, *78*, 183–187, DOI: `10.1016/j.electacta.2012.05.124`.

262 Walrafen, G. E. Raman spectral studies of water structure. *J. Chem. Phys.* **1964**, *40*, 3249–3256, DOI: `10.1063/1.1724992`.

263 Wang, H.-Y.; Hung, S.-F.; Hsu, Y.-Y.; Zhang, L.; Miao, J.; Chan, T.-S.; Xiong, Q.; Liu, B. In situ spectroscopic identification of μ-OO bridging on spinel Co_3O_4 water oxidation electrocatalyst. *J. Phys. Chem. Lett* **2016**, *7*, 4847–4853, DOI: `10.1021/acs.jpclett.6b02147`.

264 Wang, L.-P.; Van Voorhis, T. Direct-coupling O_2 bond forming a pathway in cobalt oxide water oxidation catalysts. *J. Phys. Chem. Lett* **2011**, *2*, 2200–2204, DOI: `10.1021/jz201021n`.

265 Wang, L.; Nitopi, S. A.; Bertheussen, E.; Orazov, M.; Morales-Guio, C. G.; Liu, X.; Higgins, D. C.; Chan, K.; Nørskov, J. K.; Hahn, C.; Jaramillo, T. F. Electrochemical carbon monoxide reduction on polycrystalline copper: effects of potential, pressure, and pH on selectivity toward multicarbon and oxygenated products. *ACS Catal.* **2018**, *8*, 7445–7454, DOI: `10.1021/acscatal.8b01200`.

266 Weinberg, D. R.; Gagliardi, C. J.; Hull, J. F.; Murphy, C. F.; Kent, C. A.; Westlake, B. C.; Paul, A.; Ess, D. H.; McCafferty, D. G.; Meyer, T. J. Proton-coupled electron transfer. *Chem. Rev.* **2012**, *112*, 4016–4093, DOI: `10.1021/cr200177j`.

267 Wilson, E. B.; Decius, J. C.; Cross, P. C., *Molecular vibrations: the theory of infrared and Raman vibrational spectra*; Dover Publications: Mineola, NY, 1955.

268 Wolfsberg, M. Theoretical evaluation of experimentally observed isotope effects. *Acc. Chem. Res.* **1972**, *5*, 225–233, DOI: `10.1021/ar50055a001`.

269 Wood, R. M.; Palenik, G. J. Bond valence sums in coordination chemistry: a simple method for calculating the oxidation state of cobalt in complexes containing only Co-O bonds. *Inorg. Chem.* **1998**, *37*, 4149–4151, DOI: `10.1021/ic980176q`.

270 Xu, D.; Stevens, M. B.; Cosby, M. R.; Oener, S. Z.; Smith, A. M.; Enman, L. J.; Ayers, K. E.; Capuano, C. B.; Renner, J. N.; Danilovic, N.; Li, Y.; Wang, H.; Zhang, Q.; Boettcher, S. W. Earth-abundant oxygen electrocatalysts for alkaline anion-exchange-membrane water electrolysis: effects of catalyst conductivity and comparison with performance in three-electrode cells. *ACS Catal.* **2019**, *9*, 7–15, DOI: `10.1021/acscatal.8b04001`.

271 Yang, J.; Liu, H.; Martens, W. N.; Frost, R. L. Synthesis and characterization of cobalt hydroxide, cobalt oxyhydroxide, and cobalt oxide nanodiscs. *J. Phys. Chem. C* **2010**, *114*, 111–119, DOI: `10.1021/jp908548f`.

272 Yang, J.; Cooper, J. K.; Toma, F. M.; Walczak, K.; Favaro, M.; Beeman, J.; Hess, L.; Wang, C.; Zhu, C.; Gul, S.; Yano, J.; Kisielowski, C.; Schwartzberg, A.; Sharp, I. A multifunctional biphasic water splitting catalyst tailored for integration with high-performance semiconductor photoanodes. *Nat. Mater.* **2016**, *16*, 335–341, DOI: `10.1038/nmat4794`.

273 Yang, K.; Kas, R.; Smith, W. A. In situ infrared spectroscopy reveals persistent alkalinity near electrode surfaces during CO_2 electroreduction. *J. Am. Chem. Soc.* **2019**, *141*, 15891–15900, DOI: `10.1021/jacs.9b07000`.

274 Yeo, B. S.; Bell, A. T. Enhanced activity of gold-supported cobalt oxide for the electrochemical evolution of oxygen. *J. Am. Chem. Soc.* **2011**, *133*, 5587–5593, DOI: `10.1021/ja200559j`.

275 Yi, Y.; Weinberg, G.; Prenzel, M.; Greiner, M.; Heumann, S.; Becker, S.; Schlögl, R. Electrochemical corrosion of a glassy carbon electrode. *Catal. Today* **2017**, *295*, 32–40, DOI: `https://doi.org/10.1016/j.cattod.2017.07.013`.

276 Zaffran, J.; Stevens, M. B.; Trang, C. D. M.; Nagli, M.; Shehadeh, M.; Boettcher, S. W.; Toroker, M. C. Influence of electrolyte cations on Ni(Fe)OOH catalyzed oxygen evolution reaction. *Chem. Mater.* **2017**, *29*, 4761–4767, DOI: `10.1021/acs.chemmater.7b00517`.

277 Zaharieva, I.; Chernev, P.; Risch, M.; Klingan, K.; Kohlhoff, M.; Fischer, A.; Dau, H. Electrosynthesis, functional and structural characterization of a water-oxidizing manganese oxide. *Energy Environ. Sci* **2012**, *5*, 7081–7089, DOI: `doi:10.1039/C2EE21191B`.

278 Zaharieva, I.; González-Flores, D.; Asfari, B.; Pasquini, C.; Mohammadi, M.; Klingan, K.; Zizak, I.; Loos, S.; Chernev, P.; Dau, H. Water oxidation catalysis – role of redox and structural dynamics in biological photosynthesis and inorganic manganese oxides. *Energy Environ. Sci.* **2016**, *9*, 2433–2443, DOI: `10.1039/C6EE01222A`.

279 Zaharieva, I.; Najafpour, M. M.; Wiechen, M.; Haumann, M.; Kurz, P.; Dau, H. Synthetic manganese–calcium oxides mimic the water-oxidizing complex of photosynthesis functionally and structurally. *Energy Environ. Sci* **2011**, *4*, 2400, DOI: `10.1039/c0ee00815j`.

280 Zeng, K.; Zhang, D. Recent progress in alkaline water electrolysis for hydrogen production and applications. *Prog. Energy Combust. Sci.* **2010**, *36*, 307–326, DOI: `10.1016/j.pecs.2009.11.002`.

281 Zeng, Z.-C.; Hu, S.; Huang, S.-C.; Zhang, Y.-J.; Zhao, W.-X.; Li, J.-F.; Jiang, C.; Ren, B. Novel electrochemical Raman spectroscopy enabled by water immersion objective. *Anal. Chem.* **2016**, *88*, 9381–9385, DOI: `10.1021/acs.analchem.6b02739`.

282 Zeradjanin, A. R.; Topalov, A. A.; Overmeere, Q. V.; Cherevko, S.; Chen, X.; Ventosa, E.; Schuhmann, W.; Mayrhofer, K. J. J. Rational design of the electrode morphology for oxygen evolution – enhancing the performance for catalytic water oxidation. *RSC Adv.* **2014**, *4*, 9579, DOI: `10.1039/c3ra45998e`.

283 Zhang, M.; de Respinis, M.; Frei, H. Time-resolved observations of water oxidation intermediates on a cobalt oxide nanoparticle catalyst. *Nat. Chem.* **2014**, *6*, 362–367, DOI: `10.1038/Nchem.1874`.

284 Zhang, W.; Burgess, I. J. Kinetic isotope effects in proton coupled electron transfer. *J. Electroanal. Chem.* **2012**, *668*, 66–72, DOI: `10.1016/j.jelechem.2011.12.014`.

285 Zhong, D. K.; Gamelin, D. R. Photoelectrochemical water oxidation by cobalt catalyst ("Co-Pi")/α-Fe_2O_3 composite photoanodes: oxygen evolution and resolution of a kinetic bottleneck. *J. Am. Chem. Soc.* **2010**, *132*, 4202–4207, DOI: `10.1021/ja908730h`.

286 Zhu, K.; Zhu, X.; Yang, W. Application of in situ techniques for the characterization of NiFe-based oxygen evolution reaction (OER) electrocatalysts. *Angew. Chem. Int. Ed.* **2018**, *58*, 1252–1265, DOI: `10.1002/anie.201802923`.

287 Zizak, I.; Gaal, P. The KMC-3 XPP beamline at BESSY II. *Journal of large-scale research facilities* **2017**, *3*, DOI: `10.17815/jlsrf-3-112`.

288 Zou, S.; Burke, M. S.; Kast, M. G.; Fan, J.; Danilovic, N.; Boettcher, S. W. Fe (oxy)hydroxide oxygen evolution reaction electrocatalysis: intrinsic activity and the roles of electrical conductivity, substrate, and dissolution. *Chem. Mater.* **2015**, *27*, 8011–8020, DOI: `10.1021/acs.chemmater.5b03404`.